Analysis of the external quantum efficiency of quantum dot-enhanced multijunction solar cells

by

Olivier Thériault

Thesis submitted to the
Faculty of Graduate and Postdoctoral Studies
In partial fulfillment of the requirements
For the Ph.D. degree in Physics

Ottawa-Carleton Intitute of Physics
Department of Physics
University of Ottawa

Abstract

This thesis focuses on the analysis of the external quantum efficiency of quantum dot-enhanced multi-junction solar cells. Divided in four major parts, it uses the experimental methodology developed in the SUNLAB. At first, a model is introduced to calculate the external quantum efficiency of single and multi-junction solar cells. This model takes into account the semiconductor physics governing the electrical property of the solar cell. It furthermore takes into account the optical transmission and reflection in the semiconductor structure using a transfer matrix method. The calculated curve fits a single junction GaAs solar cell's external quantum efficiency to a high degree of precision. Finally, an InGaP/GaAs/Ge solar cell's external quantum efficiency is calculated and it reproduces accurately the behavior of a measured cell.

Second, the reflectivity of a solar cell is studied. An analysis technique involving using the fast Fourier transform of the oscillation in the reflectivity is introduced. This technique extracts the thicknesses of the top and middle subcells. The reflectivity is subsequently calculated using the transfer matrix method and it reproduces the behavior of the measured samples.

Third, the effect of the addition of quantum dots in the middle subcell is studied. It is demonstrated that they extend the absorption range of the middle subcell. This is completed by first modeling the quantum mechanical behavior of the electrons and holes in the nanostructure. Their emission and absorption properties are derived. Those derived properties are verified by experimentally measured photoluminescence and electroluminescence of the nanostructures. The resulting model is then compared to experimentally measured external quantum efficiencies of single junction and multi-junction quantum dot-enhanced solar cells.

Finally, a study of the bottom subcell artifact is completed. Using the fill-factor bias experiment, each of the contribution of the light coupling and the internal voltage biasing is decoupled. For the measured sample, an optimal voltage of 2.1 V is found to minimize the artifact. At this point, the internal voltage biasing creates an artifact of 1 % and the light coupling artifact is 8 %.

Statement of Originality

Except where otherwise stated, the results presented in the current thesis were obtained during the period of the author's Ph.D. research project. This was completed under the supervision of Dr. Karin Hinzer. To the best of the author's knowledge, the results are original. These include :

- Developing the methodology for the measurement of the external quantum efficiency of multi-junction solar cells,
- Modeling of the external quantum efficiency of InGaP/GaAs/Ge solar cells using an analytical semiconductor model,
- Calculation of the thicknesses of the top and middle subcells in a multi-junction solar cell using the Fourier transform of the reflectivity,
- Measurement and modelling of the emission and absorption properties of quantum dots embedded in solar cells,
- Deconvolution of the effects of the internal voltage coupling and the light coupling in the bottom subcell's artifact.

The measured samples came from multiple sources. The standard MJSC structure (MJSC-S) was obtained from a commercial vendor. The single junction GaAs samples (SJ-ref, SJ-A and SJ-B) were grown by Dr. Jihène Zribi at the Université de Sherbrooke as part of her Ph.D. research. The quantum dot enhanced multi-junction solar cells were grown and fabricated by Cyrium Technologies and graciously given by Dr. Simon Fafard. Fabrication processes to enhance the photoluminescence of these samples was completed by Dr. Artur Turala at the Nanofabrication and nanocharacterization research center at the Université de Sherbrooke.

All of the external quantum efficiency, reflectivities, photoluminescence and electroluminescence measurements presented in this thesis were completed by the author. The transmission electron microscopy images of the quantum dots were completed by Dr. Jihène Zribi. The fill-factor bias J-V curve measurements were completed first by the author, and then subsequently re-measured by Normand Amyotte, Michael Kelly, Robert

Li and Patrick White. They built a prototype of the fill-factor bias apparatus and completed these measurements as part of their final year engineering project.

The above work has led to the following papers and conference proceedings:

- **O. Thériault**, P. White, M. Yandt, K. Hinzer. "Decoupling light coupling and internal voltage biasing in the bottom subcell artifact", In preparation.
- A. W. Walker, **O. Thériault**, K. Hinzer. "Carrier Dynamics in Quantum-Dot Multijunction Solar Cells Under Concentration", *IEEE Journal of Photovoltaics*, 4(4), pp. 1095-1099, 2014.
- A. W. Walker, **O. Thériault**, and K. Hinzer. "Positioning and doping effects on quantum dot enhanced multi-junction solar cell performance", *Progress in Photovoltaics: Research and Application*. DOI: 10.1002/pip. 2487, 2014.
- A. W. Walker, **O. Thériault**, and K. Hinzer. "The dependence of multi-junction solar cell performance on the number of quantum dot layers", *IEEE Journal of Quantum Electronics*. 50(3), pp. 198-203, 2014.
- A. W. Walker, **O. Thériault**, J. F. Wheeldon, K. Hinzer. "The effects of absorption and recombination in quantum dot multi-junction solar cell device efficiency", *Journal of Photovoltaics*, 3(3), pp. 1118-1124, 2013.
- **O. Thériault**, A. Walker, J. F. Wheeldon, K. Hinzer. "Effects of quantum dot layers on the behaviour of mulit-junction solar cell operation under concentration", Oral presentation and proceeding at the *8th International Conference on Concentrating Photovoltaics*, Toledo, Spain, 2012.
- M. D. Yandt, J. F. Wheeldon, J. Cook, R. Beal, A. W. Walker, **O. Thériault**, H. Schriemer, T.J. Hall and K. Hinzer. "Estimating Cell Temperature In A Concentrating Photovoltaic System", Poster and proceeding at the *8th International Conference on Concentrating Photovoltaics*, Toledo, Spain, 2012.
- A. W. Walker, J. F. Wheeldon, **O. Thériault**, M. D. Yandt, K. Hinzer. "Temperature dependent external quantum efficiency simulations and experimental measurement of lattice matched quantum dot enhanced multi-junction solar cells", Poster and proceeding at the *37th IEEE Photovoltaics Specialist Conference*, Seattle, WA, USA, 2011.

- **O. Thériault**, J. F. Wheeldon, A. W. Walker, P. Bitar, M. D. Yandt, C. E. Valdivia, K. Hinzer. "Temperature-dependent external quantum efficiency of quantum dot enhanced multi-junction solar cells", Poster and proceeding at the *7th International Conference on Concentrating Photovoltaic Systems*, Las Vegas, USA, 2011.

- J. F. Wheeldon, A. Walker, C. E. Valdivia, S. Chow, **O. Thériault**, R. Beal, M. Yandt, F. Proulx, D. Masson, B. Riel, D. McMeekin, N. Puetz, S. G. Wallance, V. Aimez, R. Ares, T. J. Hall, S. Fafard, K. Hinzer. "Efficiency measurements and simulations of GaInP/InGaAs/Ge quantum dot solar cells at up to 1000-suns under flash and continuous concentration", Poster and proceeding at the *7th International Conference on Concentrating Photovoltaic Systems*, Las Vegas, USA, 2011.

- **O. Thériault**, A.J. SpringThorpe, J.F. Wheeldon, C.E. Valdivia, A. Walker, B.J. Riel and K. Hinzer. "Study of InGaAs/GaAs quantum dot saturation level for the design of concentrated multi-junction solar cells", Oral presentation and proceeding at the *Photovoltaics Canada First National Scientific Conference: Photonics North 2010*, proceedings of SPIE, 7750, 77502T, 2010.

Portions of the results were presented in the following conferences:

- **O. Thériault**, K. Hinzer. "Bandgap engineering of multi-junction solar cells using nanostructures for enhanced performance under concentration", Oral presentation at the *Ottawa-Carleton Institute for Physics seminars*, May 2013.

- **O. Thériault**, K. Hinzer. "Non-destructive thickness measurement of solar cell layers", Oral presentation at *Next generation solar-Photovoltaics Canada*, Montréal, Canada, May 2013.

- A. W. Walker, **O. Thériault**, J. F. Wheeldon, K. Hinzer. "Bandgap engineering of multi-junction solar cells using nanostructures for enhanced performance under concentration", Oral presentation at the *Ottawa-Carleton Institute for Physics seminars*, May 2013

- **O. Thériault**, S. Fafard. "Semiconductor bandgap-engineering of III-V multi-junction solar cell devices for concentrated photovoltaic (CPV) applications", Oral presentation at the *Symposium on advanced materials for application in energy, health, electronics and photonics*, Montréal, Canada, November 2012.

- **O. Thériault**, S. Fafard. "Low-cost high-performance concentrated photovoltaic solar cell production and optimization using III-V quantum dot material band-gap engineering", Oral presentation at the *OSA Renewable energy & the environment*, Eindhoven, Netherlands, November 2012.

- **O. Thériault**, A. W. Walker, J. F. Wheeldon, K. Hinzer. "Simulated quantum dot enhanced multijunction solar cell for increased efficiency over concentration", Oral presentation at *Next generation solar-Photovoltaics Canada*, Montréal, Canada, May 2012.

- **O. Thériault**, J. F. Wheeldon, K. Hinzer. "Solar cell characterization laboratory", Poster presentation at the *Canada research chair conference series*, Toronto, Canada, November 2010.

Contributions not related to this thesis:

- A. W. Walker, **O. Thériault**, M. Wilkins, J. F. Wheeldon, K. Hinzer. "Tunnel junction limited multi-junction solar cell performance under concentration", *Journal of selected topics in quantum electronics: Numerical Simulation of Optoelectronic Devices*, 19(5), 2013.

- B. Paquette, M. DeVita, G. Kolhatkar, A. Turala, A. Boucherif, J. F. Wheeldon, A. W. Walker, **O. Thériault**, K. Hinzer, C. E. Valdivia, S. G. Wallace, S. Fafard, V. Aimez and R. Ars. "Chemical Beam Epitaxy Growth of AlGaAs/GaAs Tunnel Junctions using Trimethyl Aluminum for Multijunction Solar Cells", Oral presentation and proceeding at the *9th International Conference on Concentrating Photovoltaics*, Miyazaki, Japan, April 2013.

- A. W. Walker, A. Coathup, **O. Thériault**, H. M. Myers, J. F. Wheeldon, S. Park, Z. Mi, I. Shih, K. Hinzer. "Modeling Cu(In,Ga)Se2 solar cells for applications in multi-junction solar cell technologies", Oral presentation at the *Next generation solar-Photovoltaics Canada*, Montréal, Canada, 2012.

- A. W. Walker, J. F. Wheeldon, **O. Thériault**, G. Arbez, K. Hinzer. "Understanding Synopsys TCAD Sentaurus by Simulating a P-N Junction". *CMC Application Note*, 2010.

Part of this work was performed as part of the Semiconductor Using Nanostructures for Record Increases in Solar-Cell Efficiency (SUNRISE) project, supported by NSERC.

The research project was furthermore completed as part of project 11 of the Photovoltaic Innovation Network (PVIN) supported by NSERC, MRI, CFI and CRC. Finally, research completed as part of this thesis contributed to the research project '4CPV: Materials and processes for quad-junction concentrated photovoltaic (CPV) solar cells with conversion efficiencies in the 45-50 % range, grown by chemical beam epitaxy', supported by NSERC, MRI, CFI and CRC. The author would like to thank the University of Ottawa as well as the NSERC postgraduate doctoral scholarship program for financial support.

Acknowledgements

J'aimerais, en premier lieu, remercier ma superviseure, Dr. Karin Hinzer. Son enthousiasme continuel et sa supervision dévouée a créé un environnement propice à la découverte scientifique. Je me souviendrai toujours de son rire contagieux que l'on peut entendre du bout du couloir. Ce qui a été le plus important dans ces 5 années de recherche, c'est la confiance en moi qu'elle ma apporté. Grace à elle, j'ai eu la chance de voyager et de présenter ma recherche dans plusieurs endroits dans le monde. Sans ces opportunités, je ne serais pas le scientifique que je suis devenu aujourd'hui.

I would like to furthermore thank Dr. Jeff Wheeldon and Dr. Chris Valdivia for their continous supervision. Their critical insights and thorough reviews of my work improved my scientific ethics. Without them, the young student would have never become rigourous enough to enter the scientific world.

I would like to highlight the contributions of the 3001 group to this thesis. Dr. Alex Walker, Mark Yandt and Ahmed Gabr have been a huge part of this scientific adventure, be it with interesting answers to unsolved problems or with the necessary chess games. I was lucky enough to have these 3 friends along with me, to help with the motivation and to keep me on track.

J'aimerais aussi remercier les correcteurs de cette thèse. Merci à Alexandre Bouchard d'avoir pris le temps de la lire. Mais surtout, merci à Alex Walker d'avoir pris le temps de la réviser en profondeur. Son aide a été primordiale dans l'écriture et surtout la correction des nombreuses erreurs. Alex est un scientifique de qualité, et je suis extrêmement chanceux d'avoir eu la chance de collaborer avec lui.

J'aimerais remercier Dr. Simon Fafard, de Cyrium. Simon a généreusement donné les échantillons de cellules solaires qui ont été instrumentaux dans la réussite de ma recherche. J'ai eu aussi la chance de présenter en son nom, ce qui est une marque de confiance et de respect que j'apprécie profondément.

J'aimerais aussi remercier Dr. Artur Turala et Dr. Jihène Zribi de l'Université de Sherbrooke. Artur a gracieusement fabriqué les échantillons pour la mesure de la photoluminescence et Jihène a effectué la croissance des cellules solaires à simple jonction qui ont été analysés dans la thèse. Je suis reconnaissant d'avoir eu la chance de pouvoir collaborer avec ces deux scientifiques de haut niveau.

Je voudrais aussi remercier ma famille. Mes parents, Sylvie Bérubé et Normand Thériault, qui m'ont toujours encouragé à foncer et faire ce que j'aime. Je suis heureux d'avoir des merveilleux frère et soeurs, Simon, Camille et Valérie. Leurs joies et leur compagnie ont toujours été essentielles a ce que je garde un bel équilibre dans ma vie.

Finalement, le merci de la fin revient à ma copine, Roxanne Piché. Sans elle, je n'aurais jamais pu passer au travers de la jungle qu'est l'écriture de la thèse.

Contents

List of Tables

List of Figures

Acronyms

$JDOS$ joint density of states. 104

J_{sc} short-circuit current density. 14, 30, 137, 149

V_{oc} open circuit voltage. 15, 27, 87, 149, 156

FF fill factor. 15

J-V current density-voltage curve. 10, 14, 27, 154

R reflectivity. 39

AC oscillating current. 22

AFM atomic force microscopy. 112

ARC anti-reflection coating. 62, 64, 69, 79

bsf back surface field. 66, 81, 83

CBO conduction band offset. 92, 108

CCD charge coupled device. 123, 125, 128

CdTe cadmium telluride. 2

CIGS copper indium gallium selenide. 2, 9

CPV concentrated photovoltaics. 3, 6, 162

DC continuous current. 22

EL electroluminescence. 108, 110, 116, 120, 138

EQE external quantum efficiency. 11, 13, 14, 17, 26, 40, 62, 77, 91, 117, 119, 121, 123, 130, 139, 141, 147, 161

FF-bias fill-factor bias. 12, 139, 148, 152

FFT fast Fourier transform. 74, 75, 77

fsf front surface field. 51, 65, 81, 83

FWHM full width at half-maximum. 19, 75

IQE internal quantum efficiency. 17

LED light-emitting diode. 1, 150, 151

MBE molecular beam epitaxy. 70

MJSC multijunction solar cell. 3, 5, 12, 15, 26, 60, 66, 81, 87, 121, 124, 127, 139

MOCVD metal-organic chemical vapor deposition. 10

MSE mean squared error. 52, 155

NREL National Renewable Energy Laboratory. 6

OD optical density. 121, 123, 152

PL photoluminescence. 109, 121–124

PV photovoltaic. 1, 2, 13

QD quantum dot. 12, 13, 86, 89, 95, 98, 103, 106, 111, 113, 116, 118, 120, 121, 125, 127

QW quantum well. 113, 120, 127

RHEED reflection high energy electron diffraction. 70

Si silicon. 1, 2

SRH Schockley-Read-Hall. 37, 42

SRV surface recombination velocity. 39, 53

TEM transmission electron microscopy. 70, 88, 112, 121

TMM transfer matrix method. 39, 47, 49, 57, 62, 68, 71, 77

TTL transistor-transistor logic. 24, 26

VBO valence band offset. 92, 108

WL wetting layer. 105

wvf wavefunction. 98

Sample list

- **MJSC-S** is a standard lattice matched InGaP/GaAs/Ge multi-junction solar cell. It was obtained from a commercial vendor. The measured external quantum efficiency of this standard design is shown in Figure 2.24, page 59 The measured reflectivity of this sample is shown in Figure 3.1, page 63 and Figure 3.13, page 82.

- **SJ-ref** is a single junction GaAs solar cell. It was grown by Dr. Jihène Zribi at the Université de Sherbrooke. It consists of a n++ GaAs cap layer, an AlGaAs front surface field, and a GaAs p-i-n junction. Its design is shown in Section 2.4.4, page 51. The measured quantum efficiency is shown in pages 52 and 54 and was used to demonstrate the capacity of the quantum efficiency model to accurately reproduce the results. The measured reflectivity is shown in Figure 3.10, page 78 and was used to verify the Fourier transform technique for the measurement of semiconductor thicknesses in the solar cell. The electroluminescence is shown in Figure 4.11, page 111.

- **SJ-A** is a quantum dot enhanced single junction GaAs solar cell. It was grown by Dr. Jihène Zribi at the Université de Sherbrooke. It consists of the same structure as SJ-ref, but with 20 layers of InAs quantum dots positioned inside the intrinsic region of the solar cell. Those quantum dots had an indium flush applied after the deposition of 2.5 nm of GaAs. The measured external quantum efficiency is shown in Figure 4.2, page 90 and in Figure 4.16, page 119. A transmission electron microscopy of a single quantum dot in this solar cell is shown in Figure 4.13, page 113. The associated absorption coefficient of these nanostructures is shown in Figure 4.14a, page 114. The measured electroluminescence of this sample is shown in Figure 4.15a, page 117.

- **SJ-B** is a quantum dot enhanced single junction GaAs solar cell. It was grown by Dr. Jihène Zribi at the Université de Sherbrooke. It consists of the same structure as SJ-ref and SJ-A, with 20 layers of InAs quantum dots positioned inside the intrinsic region of the solar cell. Those quantum dots had an indium flush applied after the deposition of 5 nm of GaAs. The measured external quantum efficiency

is shown in Figure 4.2, page 90 and in Figure 4.17, page 120. The associated absorption coefficient of these nanostructures is shown in Figure 4.14b, page 114. The measured electroluminescence of this sample is shown in Figure 4.15b, page 117.

- **MJSC-920** is a quantum dot enhanced InGaP/GaAs/Ge multijunction solar cell. Quantum dots that absorb in the wavelength region of 920 nm are grown in the intrinsic region of the GaAs subcell. It was grown and fabricated by Cyrium Technologies and graciously given by Dr. Simon Fafard. The measured external quantum efficiency is shown first to enumerate the focus of this thesis in Figure 1.7, page 11. It was then subsequently shown in Figure 4.2, page 90 and in Figure 4.26, page 137. The measured reflectivity of this sample is shown in Figure 3.14, page 84. The calculated absorption coefficient of the quantum dots is shown in Figure 4.10, page 109. The measured intensity dependant photoluminescence spectra are shown in Figure 4.20, page 132. The temperature dependent photoluminescence spectra are shown in Figure 4.21, page 135. The bottom subcell's artifact correction procedure is demonstrated on this sample in Figure 5.6, page 149. The measured fill-factor bias experiment is completed on this sample in Figures 5.9 and 5.10 in pages 154 and 156.

- **MJSC-970** is a quantum dot enhanced InGaP/GaAs/Ge multijunction solar cell. Quantum dots that absorb in the wavelength region of 970 nm are grown in the intrinsic region of the GaAs subcell. It was grown and fabricated by Cyrium Technologies and graciously given by Dr. Simon Fafard. The measured external quantum efficiency is shown in figure 4.2, page 90 and in Figure 4.25, 136. The measured intensity dependant photoluminescence spectra are shown in Figure 4.20, page 126. The temperature dependent photoluminescence spectra are shown in Figure 4.21, page 129.

Chapter 1

Introduction

1.1 Photovoltaics

Even though the photovoltaic effect was first reported in 1839 by Becquerel [1], it was not until much later that the solar cell begun its way in the research world. More than 100 years later, in 1954, the first silicon solar cell was created by Chapin, Fuller and Pearson [2]. With its mere 6% efficiency, it was far from being capable of generating enough electricity to be a technology that one would consider to power their home. The actual cell, with its 2 cm^2 area [3], would generate just enough power under sunlight to light up a small, green light-emitting diode (LED).

Photovoltaics (PVs) have gone a long way since then. It is now a major electricity source, with 100 GW installed worldwide [4]. Albeit this renewable energy is not yet cost-competitive compared to more conventional sources of energy, such as the carbon emission heavy coal plants, it is approaching what is called grid parity. This happens when the cost of electricity created by photovoltaics is equivalent to the one sold in the grid. It is expected to happen at different times in different countries, due to different costs of electricity. The European Photovoltaic Industry Association predicts that it should happens in 2020 for the majority of Europe [5]. Hence, as pressing energy needs grow and the quantity of oil starts decreasing, photovoltaics will have to play a major role in this energy crisis.

For a long time, the technology was limited to silicon (Si) solar panels. This technology, referred as the first generation of photovoltaics, is based on the very well known silicon material. Since Si is an indirect semiconductor, it has a low absorption coefficient at the bandedge. Si cells need to be very thick, increasing the amount of material needed

Figure 1.1: Arnprior solar plant, made out of 319 000 CdTe panels. Photo courtesy of Mark Yandt.

to create a good solar cell. Hence, the Si solar panel is relatively costly. However, Si material has been used for a long time in the transistor technology, creating a strong industrial and manufacturing infrastructure. It is more convenient and cost effective to create a panel from a known technology. For these reasons, Si solar cells dominate the current market, with 85 % of produced PV in 2010 being Si [6].

The second generation of solar cells, appearing 25 years ago [7], is made out of thin-film material. These new materials, such as cadmium telluride (CdTe) or copper indium gallium selenide (CIGS), have a very high absorption coefficient, leading to a very thin cell. With much less material needed for each cell, this technology is significantly cheaper than its Si counterpart. It also means that the cells will be much lighter, making the installation easier. However, it is very difficult to grow high quality thin film cells, leading to devices with a lower efficiency. Therefore, these thin-film cells are tailored for large area applications. The Arnprior solar plant, shown in Figure 1.1, is one of the major photovoltaic plants in Ontario, Canada and has 97 MW worth of CdTe panels installed [8].

Another technology that falls in the second generation category is organic photovoltaics [9]. Made out of fully organic material, these cells are the cheapest of all technologies. Completely different physics govern their behavior compared to their semiconductor based counterpart. Again, due to a high absorption coefficient, only a thin layer

of material is needed for the operation of the device. But, due to the hopping mechanism necessary for the transport of carriers in the material, high recombination rates are seen and therefore low efficiencies are measured. The organic nature of the material makes it susceptible to oxygen and water contamination from the environment. This makes their lifetime very short, and render their use for long-term projects problematic. Larger scale implementation is particularly hard.

The third generation of solar cells, the high efficiency solution, tackles the problem in a different way. Instead of trying to decrease the price of the device, the new generation of cells aims at significantly increasing the efficiencies. Multiple solutions have been proposed, such as the intermediate band solar cell concept [10] or up-conversion [11], but the solution that has achieved commercial interest due to its high efficiencies is the multijunction solar cell (MJSC) [12]. This type of solar cell uses III-V semiconductor material grown epitaxially, creating multiple sub-cells stacked on top of each other to collectively absorb greater than 95 % of the incident solar spectrum. They are used in concentrated photovoltaics (CPV) systems to further reduce costs and improve efficiencies. Under concentrated sunlight, the efficiency of these devices reaches over 40 %, with 44.4 % being the current record [13].

Those three generations of solar cells have received commercial interest to a various degree. One of the most important factors that dictate their implementation in the field is the efficiency. Figure 1.2 presents the typical module, the best research cell and the theoretical maximal efficiencies for each type of solar cell described previously. The first generation, the widespread Si technology, has a record efficiency that is very close to the theoretical maximum efficiency, with only an 8 % difference. Si is a very well known material, and therefore most of its properties are well understood. No significant improvement can be expected in terms of the record efficiencies. Furthermore, because the Si solar cell industry can be considered mature, the module production has efficiencies that are close to the record cell. This means that for this type of technology, most of the work that needs to be done is on the industrial implementation side, to make costs lower. On the other hand, the third generation presents a different behavior. Its maximal attainable efficiency is very high, and the current world record is far from this value, with a 30 % difference. This demonstrates that the CPV technology is still very young, and that much improvement in efficiency is attainable. One could expect that a significant investment in research and development should repay significantly.

The current CPV industry gains a lot from research and development. Only by gaining significant knowledge in the operation, the design and the science of the multijunction

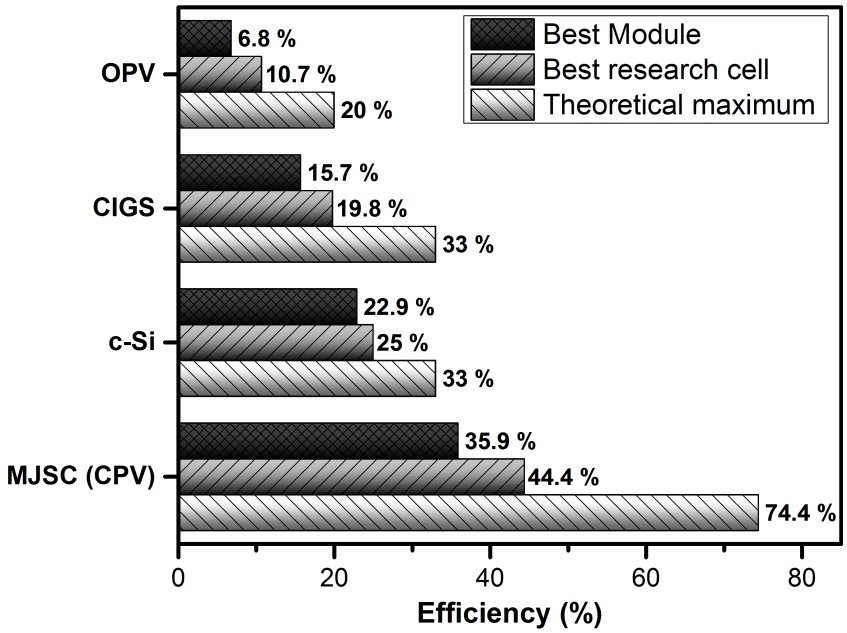

Figure 1.2: Comparison of the efficiencies for a sample of technologies. The theoretical maximum for concentrated photovoltaics (CPV), crystalline silicon (c-Si) and CIGS were obtained from the detailed balance model [9, 14]. The theoretical maximum for CPV was obtained for an infinite number of subcells. The theoretical maximum for organic photovoltaic (OPV) was obtained by estimation of the exciton dissociation efficiency [15]. The record module efficiency as well as the record cell efficiency for each technology were obtained from the 43$^{\text{rd}}$ solar cell efficiency table [13].

solar cell, the photovoltaic community can hope to further increase the efficiency of these products. Increasing the efficiency is the best way to render this renewable energy marketable. In this context, the importance of the research in the current thesis falls into place.

1.2 Multijunction solar cells

The most widespread solar cell uses a single semiconductor: silicon. All photons that are of an energy higher than its bandgap of 1.1 eV can be absorbed in the material. As shown in Figure 1.3a, the solar cell will absorb a large part of the solar spectrum. However, the voltage of the cell will be limited to its bandgap. A general approximation to obtain the open circuit voltage (V_{oc}) of a cell is $V_{oc} = E_g/q - 0.4V$, where E_g is the bandgap

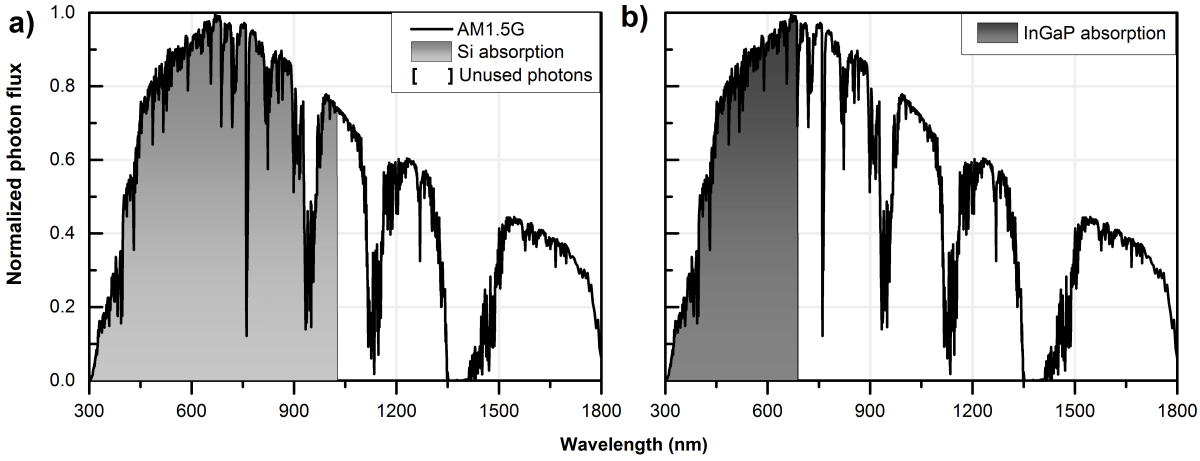

Figure 1.3: The possible absorption of the global solar spectrum (AM1.5G) by a single junction solar cell. a) The absorption of Si, starting at 1.1 eV (1127 nm), absorbs alot of photons, but has a lower bandgap. b) The absorption of InGaP, starting at 1.8 eV (689 nm), absorbs a small number of photons, but has a high bandgap.

of the semiconductor [16]. As seen in figure 1.3b, if one uses Indium-Gallium-Phosphide ($In_{0.49}Ga_{0.51}P$) with its bandgap of approximately 1.9 eV, it will absorb less photons while giving a higher possible V_{oc}. Because the power output of a solar cell will be given by its current multiplied by voltage, the maximization of the power is an optimization problem. With a high bandgap, the semiconductor absorbs less photons but creates a high voltage; with a small bandgap, the semiconductor absorbs more photons but creates a low voltage.

Instead of harnessing the solar spectrum in an inefficient way, a solution would be to use multiple different semiconductors instead of a single one. This is the proposed solution of the MJSC. As seen in Figure 1.4, by choosing three different semiconductors, you can absorb 3 different parts of the spectrum in a more efficient way. The highest bandgap semiconductor is placed on top, so that it absorbs all the light that is of higher energy than its bandgap and lets all the lower energy photons go through the subsequent layers. Each subcell is connected in series by tunnel junctions and the total voltage of the device is given approximately by the addition of the voltage of each subcell. Those tunnel junctions are made out of highly doped layers that allows the carrier to tunnel through the bandgap, starting in the conduction band of one subcell to the valence band of the subsequent subcell. This tunnel junction allows the connection in series of each subcell with minimal voltage drop. With adequate design, the current output is

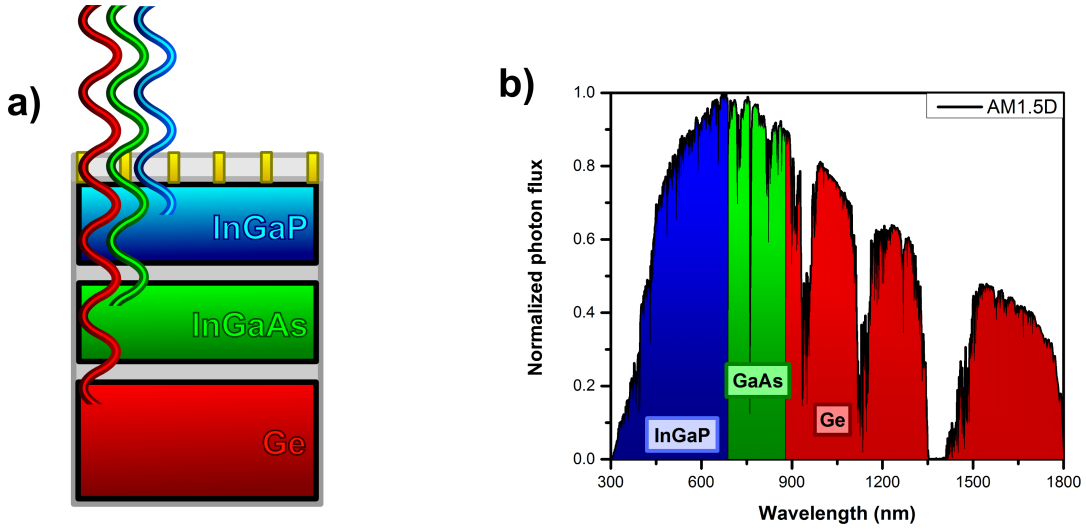

Figure 1.4: a) Schematic of the MJSC's design b) Absorption of each part of the AM1.5D solar spectrum by the three different semiconductors.

maximised and the three single subcell's voltages are added. This leads to a significant increase in efficiency compared to the single junction equivalent.

As mentioned before, the MJSC is a relatively young technology. The National Renewable Energy Laboratory (NREL) began the study and growth of MJSC in 1985 [17, 18]. Less than five years afterwards, a 27.3 % efficient dual junction solar cell, under one sun AM1.5G spectrum, was obtained [19]. This device contained an InGaP top subcell and a GaAs bottom subcell on a GaAs substrate. Even though it was considered too costly for a ground based application at the time, it quickly found a niche market in the space industry. For satellites, the biggest driving factor is weight and size, not cost. Hence, for a solar based energy system in space, the cells with the highest efficiency is often the best solution. For example, the Landsat Data Continuity Mission satellite is powered by four lattice matched MJSC solar panels from the company EMCORE [20].

After considerable research in possible implementations, the CPV solution gained commercial interest. By using a concentrating system, the need for a large area of costly semiconductor is removed. Furthermore, the higher the photon flux, the higher the efficiency [9]. By using concentrators, the cost of a panel was significantly reduced and the efficiency increased. The CPV industry has grown from that idea. A CPV demonstrator, built by a collaboration pioneered by SUNLAB can be seen in Figure 1.5 [21].

Figure 1.5: The SUNRISE demonstrator, operating at the National Research Council in Ottawa.

1.3 Quantum dots

In what will be referred to as the 'standard design' [17], the MJSC is composed from 3 lattice matched semiconductors : Indium-Gallium-Phosphide ($In_{0.49}Ga_{0.51}P$), Indium-Gallium-Arsenide ($In_{0.01}Ga_{0.99}As$) and Germanium (Ge). Even though the middle subcell is made out of InGaAs, this thesis will now refer to it with its more common denominator, GaAs, ignoring the 1 % of In. The convention refers to each subcell as the Top, Middle and Bottom subcells. As mentioned in section 1.2, each subcell is connected in series. The voltage of each subcell is added, but the output current is given by the subcell that produces the least amount. If a particular cell produces a very low current, the whole device will be current limited. In the standard design, the top and middle subcells commonly create similar levels of current, while the bottom subcell produces over 1.5 times more current. These currents are calculated using the external quantum efficiency, as will be described in the next section. The additional amount of absorbed photons is lost, and would be much better used if they could be redistributed in the top or middle subcell.

To increase the efficiency of the cell, a good solution would be to use a semiconductor

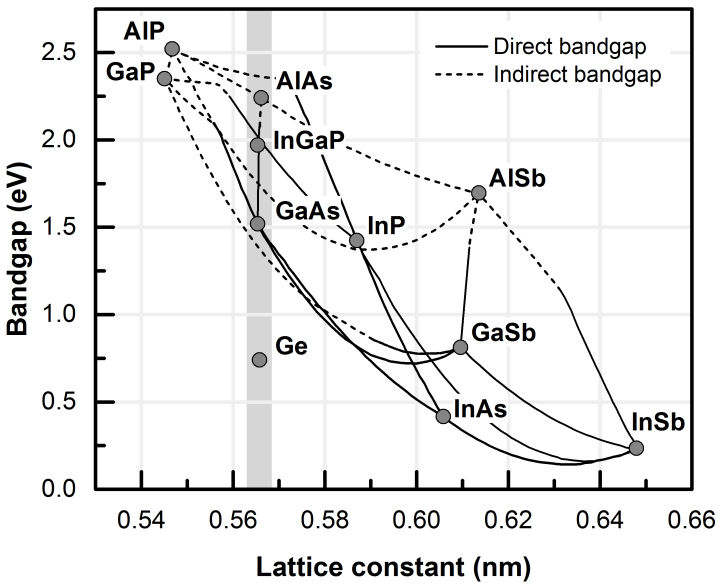

Figure 1.6: The lattice constant and bandgap of III-V semiconductors. The lines between the semiconductors are the tertiary material that can be grown between each binary semiconductor. The grey area depicts the semiconductors that are within 0.5% of the lattice constant of germanium. Data from [22].

with a lower bandgap for the middle subcell. From detailed balance calculations, the best bandgaps leading to the highest efficiency are 0.58 eV, 1.1 eV and 1.75 eV [14]. If it would be possible to grow any type of semiconductor on top of Ge, the problem would be solved. However, since MJSCs are grown epitaxially, the lattice constant must be very similar between each material. The lattice constant, the distance between each adjacent atoms in the crystalline structure, varies depending on the semiconductor. The majority of known semiconductors, their bandgaps and their lattice constant are shown in Figure 1.6. Growing a semiconductor of a different lattice constant on top of the substrate would be like trying to stack legos of different sizes on top of each other. This growth is actually possible, but it creates a large amount of dislocations and recombination centers, rendering the structure unusable. The choice of material is confined to a small number of semiconductors, depicted in Figure 1.6 as the grey area. In this range of available materials, there is no available semiconductor with a bandgap lower than GaAs.

New designs have been proposed to overcome this problem and increase the efficiency of MJSCs.

- *The metamorphic approach.* In this design, a graded layer of InGaAs is grown on

top of the Ge substrate with an increasing lattice constant. On top of this layer is then grown the top two cells, with a larger lattice constant than usual. Because of the larger lattice constant, it is possible to grow a lower bandgap middle subcell made out of InGaAs. The dislocations and recombination centers are located in an electrically inactive region [23]. This approach has reached up to 41.1 % efficiency [24].

- *The inverted metamorphic approach.* In this design, the top two cells are grown on a GaAs substrate. The cell is then flipped and the GaAs substrate removed. Again, a graded layer is grown, with an InGaAs bottom subcell then grown on top [25]. Again, this approach has been favored by a few companies, and has reached up to 44.4 % efficiency [13].

- *The dilute nitride subcell.* In this design, the bottom subcell is a GaInNAs cell grown on top of a GaAs substrate. The nitride in the GaAs semiconductor effectively lowers its bandgap whereas the In maintains the lattice matching criterion. Because the bandgap of the bottom subcell is higher than Ge, this leads to a better current matching between the three subcells. This design has led to the highest efficiency in the world in 2012, with 44 % efficiency [13]. Furthermore, the possibility of creating a quadruple junction solar cell if grown on top of Ge renders this design very interesting.

- *The porous Si.* In this design proposed by the APECS collaboration which the SUNLAB is the main investigator, the substrate is Si instead of Ge. The topmost layer of Si is porosified to render the growth of GaAs possible. The lattice mismatch requirement is relaxed by the porosity and the flexibility of the Si layer [26]. Because the Si bottom subcell's bandgap is higher than Ge, the cell is better current matched and possibly of a higher efficiency.

- *The CIGS approach.* This design, proposed by the PVIN project 11 of which SUNLAB is the principal investigator, uses CIGS as the bottom subcell of the MJSC. CIGS is more commonly used as a thin-film solar cell. However, it is possible to obtain a CIGS semiconductor of the same lattice constant as GaAs [27]. In the proposed design, an InGaP top subcell and a GaAs mid subcell are grown on top of a GaAs substrate. Then the CIGS bottom subcell is grown at the bottom of the substrate. The CIGS bandgap is tuneable by the amount of Indium incorporated, leading to a possible current matched bottom subcell [28].

- *The quantum well approach.* The Imperial College research group has proposed the addition of quantum wells in the middle subcell as far back as 1999 [29]. The addition of InGaAs quantum wells allows the absorption of photons that are of energies lower than the bandgap of GaAs. This redistributes the photons from the bottom Ge subcell to the middle subcell. This type of design has been commercialised by a university spin-off, QuantaSol, which is now part of JDSU [30].

The number of propositions is rich and varied. This is a clear proof that the MJSC community can be considered young. Even though multiple Ph.D. theses could be spent on each of these solutions, the current text will concentrate on another novel solution. The proposed solution is the *quantum dot-enhanced solar cell* (QDEC), commercialised by Cyrium Technologies [31]. Similar to the quantum well solar cell, the QDEC contains nanostructures in the intrinsic region of the middle subcell. Those quantum dots extend the absorption range of the middle subcell, absorbing photons that would otherwise be absorbed by the bottom subcell. Those InGaAs quantum dots form automatically by the Stranski-Krastanov growth process [32]. Because they can be grown in a metal-organic chemical vapor deposition (MOCVD) reactor, they don't significantly decrease the growth speed. The structure is nearly free of dislocations and does not need strain compensation layers due to rapid thermal anneal and the indium flush technique [33, 34]. The GaAs subcell is still lattice matched to the germanium layer. Because the absorption of these quantum dots depends on their size, it is possible to achieve a better current matching by tuning the quantum dot properties [35].

These quantum dot-enhanced solar cells are complex structures. A complete understanding of the behavior of these structures necessitates the application of Schrödinger's equation coupled to various semiconductor physic models. One of the goals of this thesis is to understand and explain various effects that these quantum dots can have on the solar cell. A physicist point of view, with a strong engineering background, is considered to be a perfect suit for the study of these structures.

1.4 Experimental measurements

The SUNLAB is a premier solar cell characterization facility in Canada. The experimental characterization of research devices is an essential step in the creation of novel devices. The most important test in solar cell research is the measurement of the current density-voltage curve (J-V) curve. This measurement is essential to demonstrate the

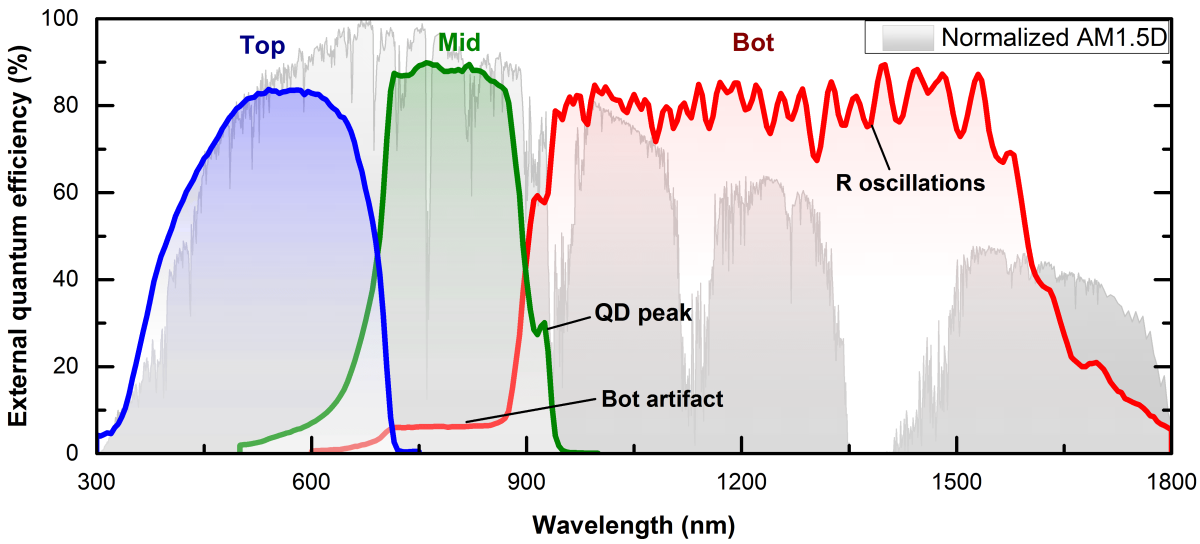

Figure 1.7: The quantum dot-enhanced MJSC's EQE (sample MJSC-920). The top, middle and bottom subcells' EQE are shown in blue, green and red respectively. The normalized photon flux of the standard direct solar spectrum (AM1.5D) is shown in the background, in grey. The reflectivity oscillations (R oscillations), quantum dot peak (QD peak) and bottom subcell artifact (Bot artifact) are features of the EQE that will be studied in depth in the thesis.

potential efficiency of a device. However, it is particularly hard to extract information on the device directly from the J-V curve. Hence, to completely characterize a solar cell, especially a multijunction solar cell, the illuminated J-V curve is not sufficient.

The most important experimental measurement of a solar cell for design purpose is the external quantum efficiency (EQE). The EQE, given in percentage (%), is the measurement of the number of electrons (or holes) being extracted for each photon incident on the device [36]. This is done for each wavelength of incident light. By scanning the whole wavelength range of the solar spectrum, the EQE can give the current output of the solar cell. If the J-V measurement is a single curve where most of the properties of the internal layers in the device are hidden, the EQE measurement is the opposite. When analysed thoroughly, the EQE of a multijunction solar cell is incredibly rich, giving insights in the design of multiple layers in the structure. Such measurement and analysis, when coupled to simulation, can lead to important design improvements.

Figure 1.7 shows an example of a measured quantum dot-enhanced MJSC's EQE, from the sample MJSC-920. The top, middle and bottom subcells each absorb their part of the solar spectrum. As can be seen from the solar spectrum outlined in grey,

the bottom subcell has the potential to absorb much more photons than the two other subcells. Centered around 920 nm, the quantum dots absorb photons that would be otherwise absorbed by the bottom subcell and increases the overall current of the device. This absorption peak demonstrates the redistribution of photons that was mentioned before.

There are multiple components in the EQE figure that are important to analyse. The oscillations seen in the bottom subcell, labeled as the 'R oscillations' in Figure 1.7, are due to the internal reflectivity of the complete structure. These ripples in the reflectivity originate from the etalon effect, or constructive and destructive interference inside the different layers in the structure. By carefully measuring the period of these oscillations, it is possible to obtain insightful information on the thicknesses of the different layers in the device. Using Maxwell's equation, the importance of the reflectivity measurement will be demonstrated, and the internal structure of all the layers of the solar cell will be uncovered.

The shape of the bandedge, located in the longer wavelength region of each subcell, is dictated by the absorption coefficient of the subcell. In this thesis, photoluminescence and electroluminescence spectroscopy will be used to correlate the middle subcell's emission to its absorption coefficient. By using such emission, it is possible to estimate the absorption coefficient of the nanostructures and study their state-filling properties. These measurements will be used to analyse the quantum dot (QD) peak in the EQE. After analysing most of the properties of these quantum dots under emission spectroscopy, this thesis will give the reader a better overview of the role played by the nanostructures inside the device.

One last, but important part of the EQE is what will be refered to as the 'bottom subcell artifact' in Figure 1.7. This artifact is the non-zero signal of the bottom subcell's EQE in the middle subcell region. The amplitude of this artifact is different for each MJSC, with its range of amplitude being from 0 to 20 %. In the sample MJSC-920, the amplitude of the artifact is 7 %. This artifact is considered to be due to internal voltage biasing between each subcell during the measurement [37]. However, the origin of this artifact is still subject to debate. It is believed that a part of the artifact, if not the entirety, is due to photon coupling between the middle and the bottom subcell [38]. This thesis aims to use the fill-factor bias (FF-bias) experiment, proposed by Cyrium Technologies [39], to shed new light on the problem.

1.5 Thesis overview

As mentioned before, this thesis will be concentrating on multijunction solar cells, and more specifically on the quantum dot-enhanced solar cell. Simulation of such cells is very useful in understanding the behavior and importance of each layers. However, a strong simulation always requires verification with experimental measurements. This is why the current thesis is an important complement to another portion of the SUNLAB's expertise, which is numerical simulation and design of novel solar cells. The Ph.D. thesis of Dr. Alex Walker, on the numerical simulation of multijunction solar cell [40], is an important complementary study to the current thesis.

Concentrated photovoltaic is a very young industrial sector. There are plenty of efficiency increases that can still be made. Scientific research plays a vital role in this new field. Furthermore, MJSCs are one of the most promising technology in PV, leading to the highest efficiency to date. The added flexibility that the QDs gives them makes them a worthwhile technology.

Because of its incredible richness in information, the EQE is considered to be one of the most important measurement for this type of device. Hence, the goal of this thesis will be to understand and analyze all possible information that can be obtained from the EQE of a quantum dot-enhanced solar cell. The thesis is divided in four major parts.

Chapter 2 derives most of the important equations and theory needed to fully understand the electrical behavior of the MJSC. A particular attention is given to the derivation of equations estimating the EQE. The expected effect of changes in most layers in the structure are demonstrated in the EQE. **Chapter 3** studies the reflectivity of the MJSC structure. A transfer matrix method is used to simulate the reflectivity of the structure, with all layers incorporated in the calculation. With the help of this method, a rapid technique to estimate the various thicknesses in the solar cell using the etalon effect is used. Then, in **chapter 4**, the emission spectroscopy of the quantum dot-enhanced solar cell is studied. The quantum dot energy levels are first simulated using a finite element method simulation. The absorption coefficient and the emission properties are obtained and compared to experimental measurements. They are then used to obtain the simulated EQE which is then compared to the experimental measurements. In **chapter 5**, the bottom subcell artifact is analyzed. A model to estimate the intensity of the artifact is first developed. Then, using the FF-bias measurements, the correlation between the internal J-V curves of the solar cell and the said artifact is demonstrated.

Chapter 2

External quantum efficiency

The EQE of a solar cell is the incident photon to converted electron ratio, measured over different wavelength of light. Because it is directly related to the short-circuit current of the solar cell, it is an excellent diagnostic tool to improve efficiency.

In this chapter, the foundations necessary to study the important parts of EQE are built. The main equations and guiding principles of this measurement are reviewed, as these will serve as a guideline for the subsequent sections. The experimental system that was used throughout the thesis is described thoroughly. Each component of the setup is reviewed and linked to its purpose. Finally, a mathematical framework is built to simulate the EQE of various types of solar cells. Using semiconductor physics and the transport equations governing p-n junctions, the model is linked to important design principles of solar cell growth. The results of the two main parts of this chapter, the experimental setup and the EQE calculation, will be used throughout the thesis.

2.1 Current-Voltage curve

The semiconductor solar cell is a p-n junction designed to create current from the absorption of photon. The J-V curve of a solar cell represents the relationship between the current created by a solar cell and the applied voltage. It is a combination of the diode-like behavior of the p-n junction and the current created from the absorption of the light. The dark current density, J_0, is the current created by the applied voltage in the reverse biased p-n junction. The short-circuit current density (J_{sc}) created by the light, flows in the opposite direction. The general formula of the J-V curve is

$$J = J_{sc} - J_0 \left(\mathrm{e}^{\frac{qV}{nk_{\mathrm{B}}T}} - 1 \right) \tag{2.1}$$

where J is the measured current density, n is the ideality factor, q is the electron charge, T is the temperature and k_{B} is the Boltzmann constant. An example of an illuminated J-V curve of a typical single junction solar cell is shown in Figure 2.1.

For single junction solar cells, the ideality factor lies between $n = 1$ and $n = 2$. It is determined by the recombination mechanisms in the solar cell and will have an effect on the shape of the curvature of the J-V curve. For the case of the simplified formula for the J-V curve in Equation 2.1, the open circuit voltage (V_{oc}) is given by

$$V_{oc} = \frac{nk_{\mathrm{B}}T}{q} \ln\left(\frac{J_{sc}}{J_0} + 1\right). \tag{2.2}$$

The delivered power of the solar cell is given by the multiplication of the current and the voltage, as in $P = JV$. The desired solar cell's operating point occurs at the maximum power point, which occurs at a certain V_{max} and a J_{max}. The efficiency (η) of the solar cell is then given by

$$\eta = \frac{P_{max}}{P_{in}} = \frac{V_{max}J_{max}}{P_{in}} \tag{2.3}$$

where P_{in} is the incident power of the light.

The fill factor (FF) is defined as the ratio

$$FF = \frac{V_{max}J_{max}}{V_{oc}J_{sc}}, \tag{2.4}$$

and describes the shape of the diode curve. A high FF is necessary for a good efficiency of the solar cell. A fill factor of 100% would give a perfectly rectangular curve.

In a MJSC, each subcell is connected in series. Hence, at a particular current, their voltages are added together. This is highlighted in Figure 2.2a, where the J-V curve of a simple dual junction solar cell is shown. The J-V curves were calculated using Equation 2.1. The first solar cell's J-V curve, which approximates an InGaP subcell behavior, was calculated using J_{sc} =12.2 mA/cm^{-2}, $J_0 = 4.88 \cdot 10^{-11}$ mA/cm^{-2} and $n = 1$. The second solar cell's J-V curve, which approximates a GaAs subcell behavior, was calculated using $J_{sc} = 12.2$ mA/cm^{-2}, $J_0 = 3.72 \cdot 10^{-26}$ mA/cm^{-2} and $n = 2$. In this case, the J_{sc} of the full structure is equivalent to the J_{sc} of each subcell while the V_{oc} is given by the sum of each subcell's, giving $V_{oc} = 2.4V$. These values were chosen to qualitatively reproduce the behavior of the two subcells.

Figure 2.2b demonstrates their behavior when the subcells are not current matched. The curve of the top solar cell was kept the same while the current created by the GaAs subcell was doubled. As can be seen in the total solar cell's J-V curve, the J_{sc} is limited by the top subcell while the V_{oc} is still the sum of the two subcell's V_{oc}. These figures demonstrates the complex electrical interaction between the subcells in a MJSC.

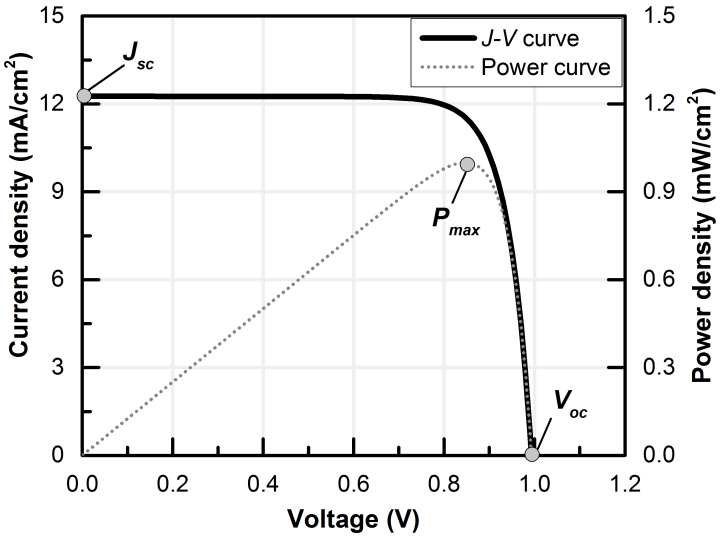

Figure 2.1: Single junction J-V curve of a solar cell calulated with the diode equation.

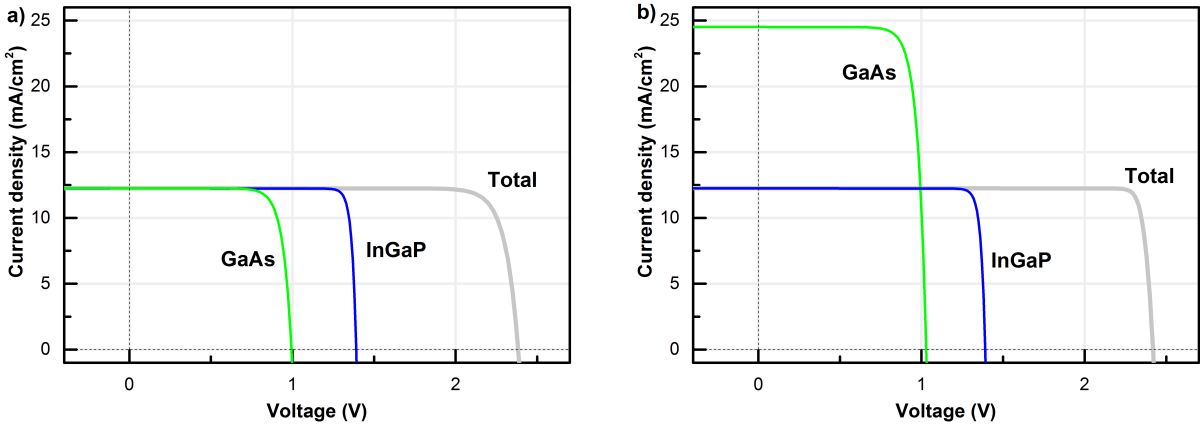

Figure 2.2: Dual junction J-V curve of an InGaP/GaAs solar cell calculated with the diode equation. Subfigure a) demonstrates the resulting J-V curve when the two subcells are current matched while b) demonstrates the J-V curve when the GaAs subcell overproduces current.

2.2 Main quantum efficiency equations

The external quantum efficiency is defined as the ratio, at a specific wavelength, of the number of carriers collected to the number of incident photons. Hence, if the cell collects a current I for an incident photon beam of f photons, the EQE is given by

$$EQE\left(\lambda\right) = \frac{I}{q \cdot f}, \tag{2.5}$$

where q is the electric charge. This ratio is by definition taken when no voltage is applied on the solar cell. It is then possible to obtain the J_{sc} created by the solar cell under any spectrum, by integrating both quantities such as

$$J_{sc} = \int EQE\left(\lambda\right) b_{\lambda} d\lambda, \tag{2.6}$$

where b_{λ} is the incoming spectrum in photon flux (N_{λ}/m^2).

Another important quantity is the internal quantum efficiency (IQE). The IQE is the ratio of the collected carriers to the number of photons that are actually absorbed by the solar cell. As a formula, it is given by

$$IQE\left(\lambda\right) = \frac{EQE\left(\lambda\right)}{1 - R\left(\lambda\right)}, \tag{2.7}$$

where $R\left(\lambda\right)$ is the reflectivity of the solar cell. The IQE is an indication of the capacity of the active layers of the solar cell to make good use of the absorbed photons. It is always higher than the EQE, but should never exceed 100 %, with the exception of multi-exciton generation.

2.3 The external quantum efficiency measurement

The measurements of the EQE and IQE presented in this thesis were all completed using the IQE200 from Oriel [41]. A complete schematic, along with a picture of the instrument, is shown in Figure 2.3. As mentioned before in Equation 2.5, the principle of the EQE is to count the proportion of carriers extracted out of the cell to the numbers of photons impinging on the surface. To do so, it is necessary to shine a monochromatic light on the cell, with controllable wavelength, while measuring the current. By definition, this current needs to be measured at $V = 0$. Furthermore, it is necessary to measure the reflectivity of the cell to calculate the IQE. The description of the operation of the

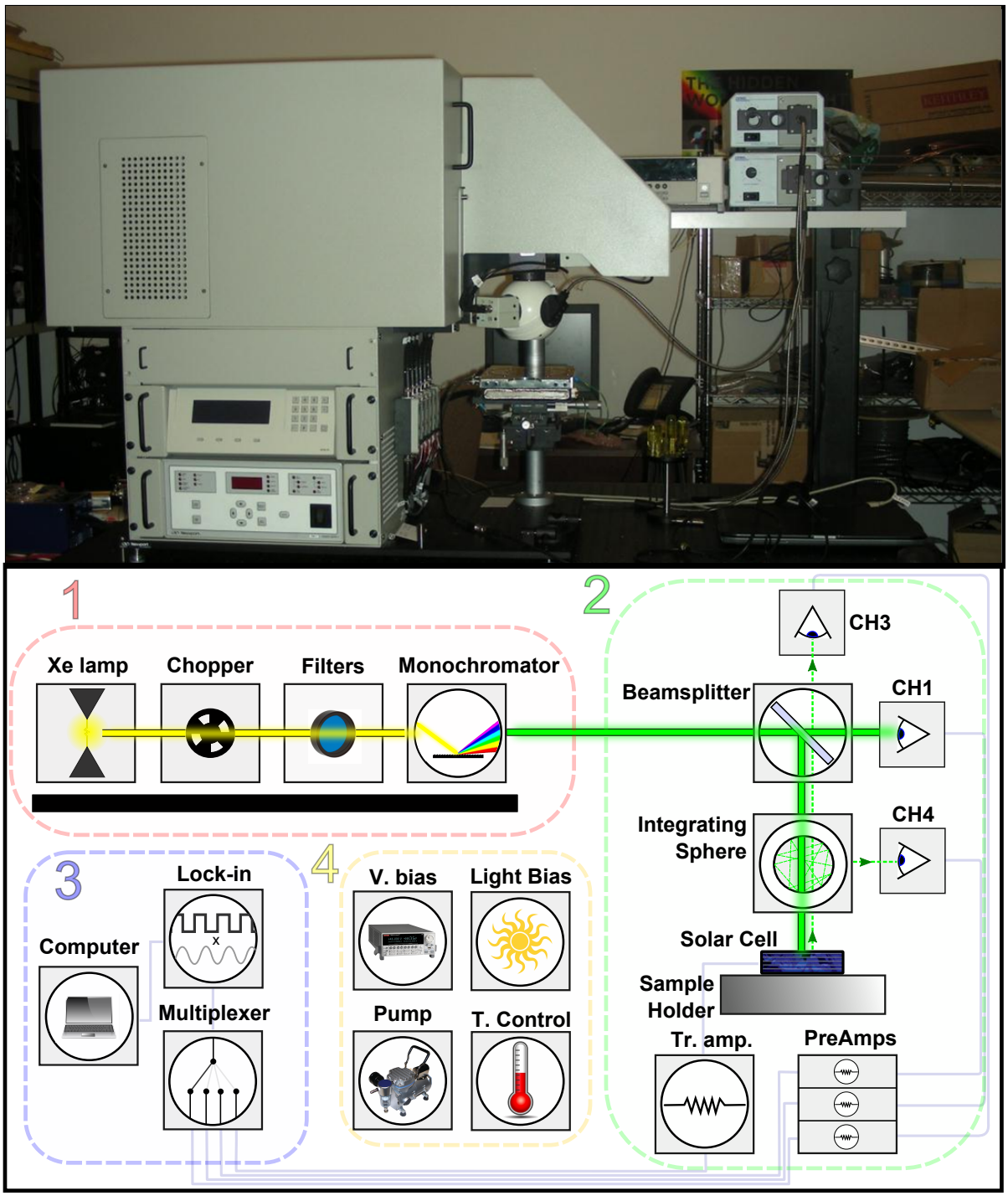

Figure 2.3: The picture and schematic of the IQE200 by Oriel. The IQE is divided in four main parts; 1-the tunable monochromatic light source, 2-the electro-optical measurement, 3-the digital conversion of the measured values and 4-the external biasing functionality.

instrument is divided in four parts. First is the creation of the tuneable monochromatic light source, second is the electro-optical measurement, third, the digital conversion of the measured values, and finally, the external biasing sources.

2.3.1 The monochromatic light source

The first part of the system, the monochromatic light source, is circled as red number 1 in Figure 2.3. A 300 W Xenon light source (Model 66485) provides a light source with an extended spectrum from 300 to more than 1800 nm [42]. The light emitted from the arc of the lamp is collected by a collimating lens and then directed towards an optical chopper. This rotating disk with open slits modulates the light in a square wave. Its purpose is to modulate the light and to couple the useful signal to a lock-in amplifier, which is placed in the Section 3 of the experimental setup. In all experiments, the light is modulated at a 30 Hz frequency, to avoid coupling with the 60 Hz power line frequency. The light is then directed towards a filter holder, in which 3 possible filters can be used. The three possible options are either no filter, a 550 nm long-wave pass filter or a 1000 nm long wave pass filter. These filters are used to remove the higher order diffraction peaks from the grating in the following monochromator.

The light is then directed into a Cornerstone 130 1/8m spectrometer (Model 74004). Figure 2.4 shows a schematic of the inside of the monochromator. The light is focused on the entrance slit, and then collected by the collimating mirror. It is important to note that the focal ratio (f#) of the lens needs to be matched to the focal ratio of the spectrometer, to ensure that the light beam fully encompasses the first mirror [43]. Otherwise, the light would either overfill the mirror and create stray light, or underfill the grating, leading to a less efficient diffraction. After hitting the mirror, the white light is directed towards a diffraction grating, which separates the incoming white light into a rainbow of color. Now that each color of the light is spatially separated by the grating, it is collected by the focusing mirror and directed towards the exit slit. This exit slit blocks most of the incoming light and allows only the required wavelength to exit the monochromator. The light that exits the instrument is quasi-monochromatic. Because the diffracted light is spatially separated, the exit slit size will control the width of the spectral dispersion of the output beam. For the used instruments and the available gratings, the dispersion is 13 nm/mm. This means that for the output slit size used in all the experiments inside this thesis, of 0.25 mm, the exit beam has a 3.3 nm wide full width at half-maximum (FWHM) spectrum [41].

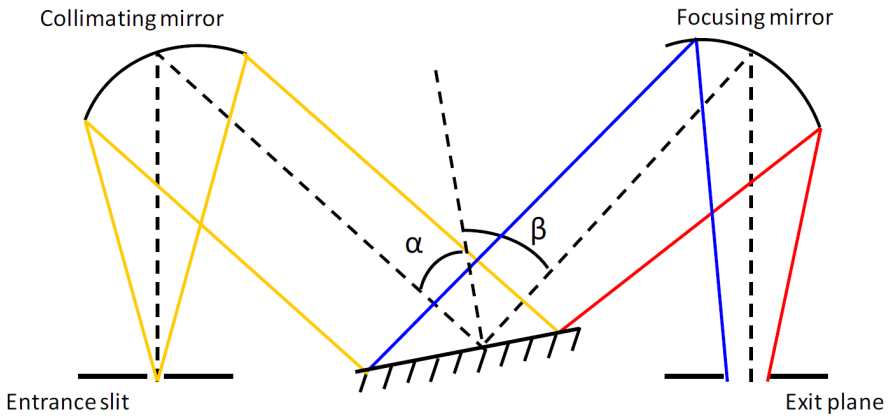

Figure 2.4: The optical configuration inside the monochromator. Focused light enters the monochromator through the entrance slit, and is redirected by the collimating mirror towards the grating. This grating diffracts the light towards the focusing mirror, which then redirects the chosen wavelength towards the exit slit. Figure taken from [43, 44].

A diffraction grating consists of a periodic structure of equally spaced grooves along its surface. These grooves, which are of dimensions similar to the wavelength of light of interest, diffract the light and redirect each wavelength in a different direction. According to the Huygens-Fresnel principle [45], if a wavefront of light hits a grating surface, each point on the surface will act as a point source. Hence, when a plane wave of wavelength λ hits the grating, each plateau acts as a point source. Since each of these point sources are at a distance d from each other, at any point in space the sources will either constructively or destructively interfere. A diffraction grating will diffract an incoming monochromatic light source according to the grating equation [43]

$$d\,(\sin\alpha + \sin\beta) = m\lambda, \tag{2.8}$$

where α is the incoming wavefront angle with respect to the grating, β is the diffracted light angle and m is any integer, including zero. It is interesting to note that if $m = 0$, the grating acts as a purely reflective component. In principle, all of the refractive orders m are present, but the design of the grating and the spectrometer is usually optimized for $m = 1$. When the grating equation for the diffracted angle is solved,

$$\beta = \arcsin\left(\frac{m\lambda}{d} - \sin\alpha\right), \tag{2.9}$$

the dependence of the outgoing angle with the wavelength λ becomes clear. For an incoming white light, the diffraction grating will split each wavelength onto different

angles. To obtain a monochromatic light source, it is possible to put an exit slit at the correct angle from the diffraction grating. A rotating motor is installed to allow the grating to turn and to pick different wavelengths for a fixed exit slit.

The diffraction efficiency of the grating changes over different wavelengths depending on the material used and the shape of the grooves. One method to change the diffraction efficiency of a grating is by transforming the rectangular shapes that was assumed earlier into pyramidal shapes. The different angles of each facet, referred to as the blazing angle, will change the efficiency of diffractions for different wavelengths [43, 46]. Gratings that are optimized for green light will be specified as having a blaze at 555 nm. For a long wavelength range such as the one under consideration (300 to 1800 nm), a single diffraction grating is not enough. If a grating that is adequate for visible light is chosen, it will not be efficient enough in the infrared. This is why, in the used monochromator, two different gratings are used. Grating 1 has 600 grooves/mm, 400 nm blaze, and is usable from 250 to 1300 nm. Grating 2 has 600 grooves/mm, 1 µm blaze, and is usable from 600 to 2500 nm. To achieve the highest light intensity in the system, the monochromator switches between gratings at 720 nm.

It is important to note that in the grating equation, for a single set of diffracting angles, there are multiple wavelength solutions. For example, if a light source that extends from 300 to 1800 nm is used, and an angle that would allow the 900 nm diffracted beam to go through the exit slit is picked, there is one other wavelength that would be diffracted towards the same angle. Looking at the grating equation, the other solution is $m = 2$ and 450 nm. Even though the intensity of the higher order diffracted beam is significantly lower than the first order, it would still be present and add uncertainty in the measurement. For this reason it is important to use order sorting filters.

These long-wave pass filters cut all of the incoming light of wavelength below a threshold, allowing only the first diffraction peak to be created. Because the light source emits light of wavelengths longer than 300 nm, the exit slit will see only the first order peak in the wavelengths between 300 and 600 nm. Then, at wavelengths of over 600 nm, the light that would allow a $m = 2$ diffracted beam to go through the monochromator needs to be removed. Three possible filter options are available. The no filter option for the wavelength range of 300 to 560 nm, the long-wave pass 550 nm for the wavelength range of 560 to 1040 nm and the long-wave pass 1000 nm for the wavelength range of 1040 to 1800 nm. By using these filters, the monochromator outputs only the useful $m = 1$ peak.

2.3.2 Electro-optical measurement

The electro-optical measurement part of the IQE200 system is highlighted as the green number 2 in Figure 2.3. It encompasses the solar cell sample, the sample holder, the various light detectors and the attached amplifiers. This is the stage where the incoming light and collected electrons are measured. Both of these quantities are used to calculate EQE according to Equation 2.5.

The first part of the IQE200 system was used to create a quasi-monochromatic light source. This light beam is now directed towards a beamsplitter, which reflects half of the light towards the solar cell sample, and transmits the other half towards a detector, referred to as channel 1 (CH1). The first half of the light is focused 10.16 cm (4 inches) below the beamsplitter assembly using a focusing lens. The solar cell sample is placed in the focal plane of the beam with the help of a temperature controlled sample holder. The solar cell sample is electrically connected using test probes, alligator clips, or BNC cables depending on the available contacts. The wires are then connected to a trans-impedance amplifier (Tr. amp., Model 70714) that transforms the current into an amplified voltage value [47]. This amplifier is capable of independently amplifying the continuous current (DC) and the oscillating current (AC) components of the input current. A wide range of gain values are possible, from 10^2 to 10^4 V/A for the DC component and 10 to 10^3 for the AC component. The settings used for all measurements in the current thesis are 10^2 V/A for the DC and 10^3 V/A for the AC. This means that if the solar cell creates a continuous current of 1 mA and an oscillating current of 1 μA, the transimpedance amplifier will give as output 100 mV in the DC component and 1 mV in the AC component. Because the incoming light is chopped in an oscillatory behavior, the AC value will be the important number to take into account. This number will be used to measure the current created by the incoming light, or in other words to count the number of electrons created. On the system, and in further discussion in this thesis, the AC component of the transimpedance amplifier will be referred to as channel 2 (CH2) of the IQE200.

The DC value can be important to evaluate the polarity of the connections. Because the transimpedance amplifier cannot accept significant negative current, it is necessary to connect the solar cell sample with the correct polarity. This value can also be used to estimate the amount of continuous light bias applied either from the light in the room or by the external light component in the system, as explained later in this section.

The second half of the light is directed towards the CH1 detector, and is used to measure the light intensity coming out of the monochromator. It will be used to count the

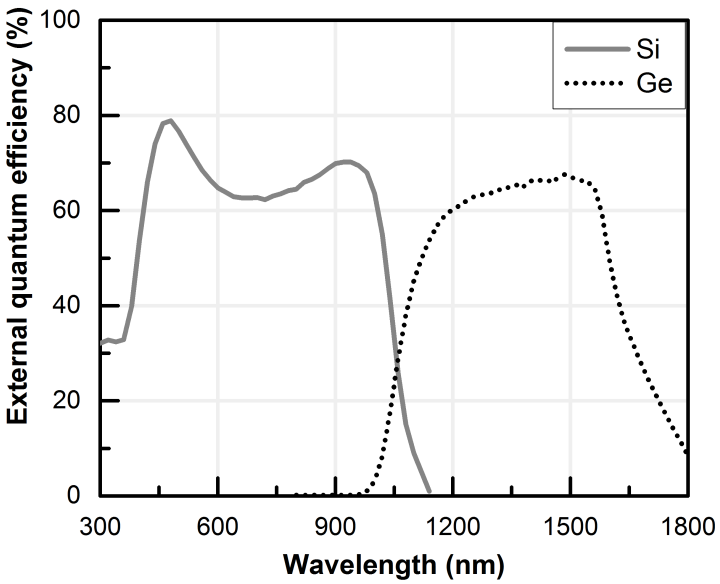

Figure 2.5: External quantum efficiency of the sandwiched photodiodes used in CH1, CH3 and CH4.

number of photons directed towards the solar cell. The detector is a Silicon-Germanium (Si-Ge) sandwiched photodiode that covers the wavelength range of interest. Figure 2.5 shows the EQE of each detector. Because the two photodiodes are stacked mechanically on top of each other, it is possible to obtain two independent outputs depending on the wavelength measured.

Another Si-Ge detector, referred to as channel 3 (CH3), is placed on top of the beamsplitter. Its active area is pointed vertically towards the solar cell sample. This detector measures the direct (specular) reflection of the light from the solar cell surface. Initially, the reflected light is collected by the focusing lens. Half of it then passes through the beamsplitter and is collected by the detector. The CH3 detector is similar to the CH1, with 2 independent outputs, one being the Si diode and the other being the Ge diode.

The last Si-Ge detector, channel 4 (CH4), is attached to an integrating sphere (Newport 70671). The integrating sphere, installed over the solar cell sample, collects all the diffuse reflection of the light from the solar cell surface. The interior of the sphere is coated by a highly reflective white material. The diffuse reflected light follows multiple reflections from the interior surface before being directed towards the CH4 detector. Even though the diffuse reflection from solar cells can be a very important and interesting measurement, it will not be studied in the current thesis.

	CH1		CH3		CH4	
	Si	Ge	Si	Ge	Si	Ge
Gain	10^4	10^4	10^5	10^5	10^6	10^6
Time	fast	fast	fast	fast	fast	fast

Table 2.1: The gain and time settings on each of the detectors used in the system.

The three detectors (CH1, CH3 and CH4) give six different current values (Si and Ge values for each channel) depending on the light intensity hitting the photodiodes. These six outputs are electrically connected to six preamplifiers (Model 70710) that transform the current into a more convenient voltage value. Each preamplifier has a wide range of amplifying values, covering 10^4 to 10^8. The gain values must be chosen to create an output voltage that is suitable for the subsequent measurement stages of the system. Values in the mV range for each channel (CH1, CH3 and CH4) were chosen by the author. This removes the possibility of creating too high voltages when in the range of the Xenon spikes in the lamp, and allows a good range to detect smaller component in the μV range. Table 2.1 enumerates the various settings on the pre-amplifiers used in the current thesis.

Using the settings shown in Table 2.1, the voltages of a common measurement of a Si cell are shown in Figure 2.6. The spectrum of the light and the EQE of each channel strongly influence the shape of the curves. The Xenon spikes, in the 900 to 1100 nm region, can be clearly seen in the three channels. A proportional comparison amongst the channels yields the values that are needed to calculate the EQE.

2.3.3 Digital conversion of measurements

This section of the system takes the voltages given by the preamplifiers and the transimpedance amplifier, imports it in the computer software and then calculates the external quantum efficiency. Circled as the blue number 3 in Figure 2.3, it encompasses the computer and its software, the lock-in amplifier (Merlin lock-in, Model 70100), the multiplexer and the three transistor-transistor logic (TTL) switches. The electrical connections are shown in light purple.

First, the six preamplifier voltage outputs are connected to three TTL switches. These switches are standard logic gates that allow switching between two channels depending on the voltage that is applied to it. When 0 V is applied to its gate, the switch gives the

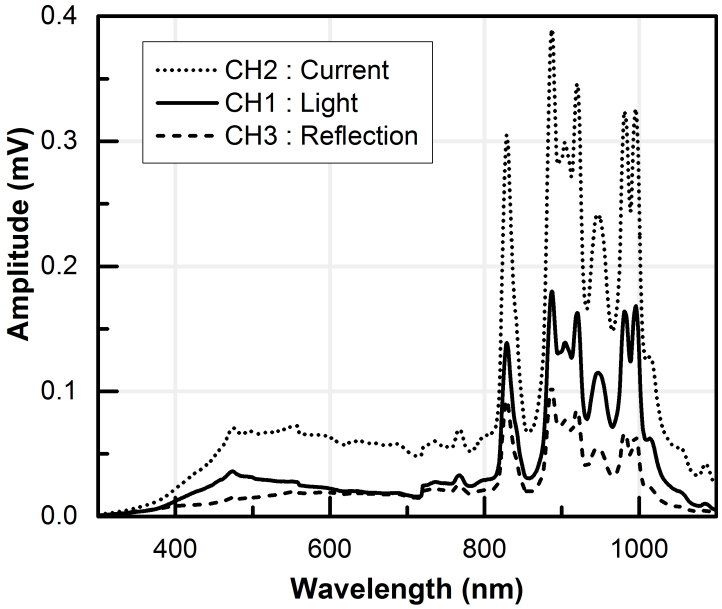

Figure 2.6: Typical voltage values on each channels for a Si solar cell measurement.

value from the Si detector. If 5 V is applied to its gate, the output from the switch is the value from the Ge detector. The switches are all connected together to the computer, which decides whether the Si of the Ge detector is used. For all the measurements done in this thesis, Si detectors were used for the wavelength range of 300 to 1099 nm, while Ge detectors were used for the rest of the range, 1100 to 1800 nm.

The three outputs from the switches, as well as the CH2 output from the transimpendance amplifier, are connected to a multiplexer. This multiplexer is similar to the switches, as it allows us to choose a single output from the four inputs available. It does not change the actual value of the voltage. The multiplexer is connected to the computer through a USB port. Hence, for a single point in the measurement, the multiplexer cycles sequentially through each of the four channels one at a time. The single output of the multiplexer is then connected to the Merlin lock-in amplifier.

The purpose of the lock-in amplifier is to receive the noisy oscillatory voltage from the multiplexer, and obtain the precise amplitude value of the useful signal [48]. It does so by picking only that component of the signal whose frequency is equal to the frequency of the optical chopper, 30 Hz in our case. The instrument receives two inputs, the first being a square wave given by the optical chopper of the right frequency and the second being the input signal from the multiplexer, coming either from the detectors or from the solar cell sample.

The working principle of the lock-in amplifier is simple to understand. Let's first assume that the reference signal coming from the chopper as well as the signal from the measurement are both sinusoids instead of square waves. The lock-in takes the multiplication of the two components and integrates the resulting values for a long time. The value of the integration is going to be directly proportional to the amplitude of the signal at the exact frequency of the reference signal. This principle is highlighted by one important property of the integration of a sinusoid,

$$\lim_{T\to\infty} \frac{1}{T} \int_0^T \sin\omega_1 t \sin\omega_2 t dt = \frac{\delta_{\omega_1,\omega 2}}{2}, \tag{2.10}$$

where δ is the Kronecker delta. For a long enough period of integration T, the integrated signal will give a value that is directly proportional to the amplitude of the measured signal of frequency (ω_2) that is of the exact frequency of the chopper signal (ω_1). All of the other frequencies components, even the constant DC signal, will give an integration that is equal to zero. Due to this, the lock-in amplifier is capable of obtaining accurate measurement in an extremely noisy signal.

The lock-in amplifier output is read by the computer through a USB port. The computer controls the complete process by manipulating six of the instruments mentioned beforehand; the chopper, the filter holder, the monochromator, the TTL switches, the multiplexer and the lock-in amplifier. After setting the filters and the monochromator, it measures in cycle each of the four channels. It then cycles trough wavelengths, storing the voltage values in the computer. The IQE200 software then uses these four channel values at each wavelength, applies post-processing calibration data and equations, and finally obtains the EQE, the IQE, the direct reflectivity (R_s), and the diffuse reflectivity (R_d). The post-processing will be discussed in depth in the subdivision 2.3.5 of the current section.

2.3.4 External biasing source

Light Biasing

The IQE200 comes with two light biasing sources that are necessary to measure the MJSC's EQE. Since each of the subcells of a MJSC are connected in series, measuring the EQE of a single subcell without light bias is not possible. Say, for example, a beam of green light (555 nm) is shone on a standard MJSC. The top sub-cell (InGaP) would absorb the light and create carriers, while the other two subcells (GaAs and Ge) would

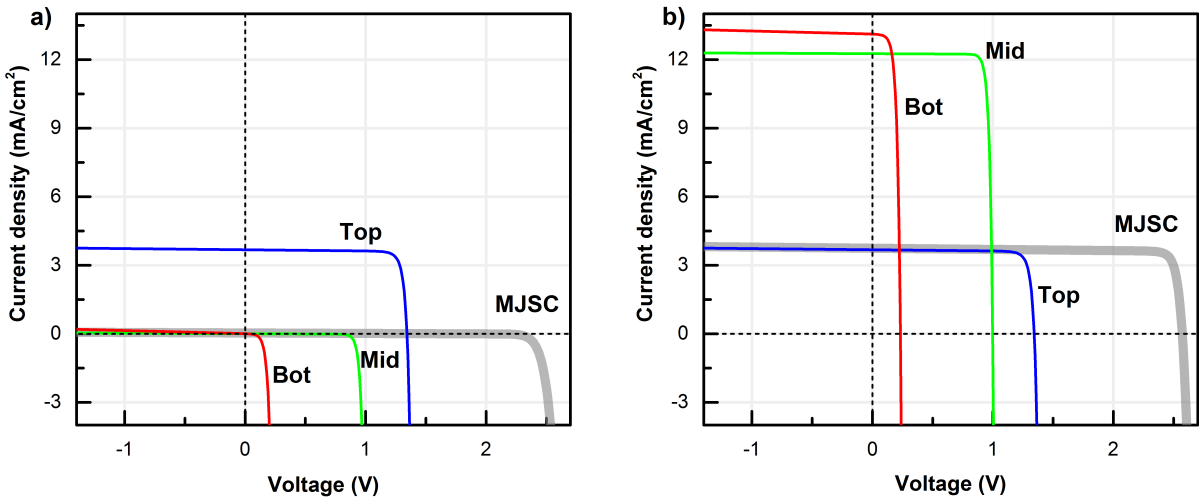

Figure 2.7: Internal J-V curves of each subcell during an EQE measurement when; a) no light bias is applied on the bottom and middle subcell, blocking the current of the top subcell, b) light bias is applied on the bottom and middle subcell, allowing the current of the top subcell to be measured on the MJSC J-V curve.

absorb little to nothing. Since the three junctions are connected in series, the Kirchhoff laws state that the current is the same for the three subcells while their voltages are added together. If two subcells are creating no current, then the current from the top subcell will be blocked. This case is demonstrated in Figure 2.7a, where the J-V curves of each of the subcell and the full MJSC are shown. This model has been created using a two-diode model for each subcell, which will be described and studied in chapter 5.

If the amount of current created by the green light needs to be measured, the effect of the two other subcells on the photocurrent should be eliminated. This is done by light biasing the subcells that are not measured. In this case, a small amount of green light (555 nm) is directed towards the cell while shining a large amount of light that is absorbed by the middle and bottom subcell (from 700 to 1800 nm). The two lower subcells are said to be light biased. This case can be seen in Figure 2.7b. The two lower subcells absorb a large amount of photocurrent while the top subcell is current limiting. When the current in the full device is measured, it is limited by the current absorbed by the top subcell, while the other two subcells are almost at their V_{oc}. Hence, to measure the top subcell EQE, a large amount of constant light on the middle and bottom subcells needs to be applied to the cell while shining a small amount of light that is scanned through the wavelength range of interest (300 to 700 nm). As mentioned

Slot #	①	②	③
Top Light	10-CGA-695 (top)	SWF-650 (mid)	SWF-900 + KG1 (bot)
Bot Light	empty	LWF-900 (mid)	SWF-900 + KG1 (bot)

Table 2.2: Filter configuration for the light bias on the IQE200.

before, this light is chopped to be measured precisely by the lock-in amplifier. A very similar procedure, where light bias on the two subcells that are not of interest is applied, can be used to measure the middle and bottom subcell [36].

This light biasing procedure is done using two quartz-tungsten light sources (model 66088) with six available slots for filters. After passing through the filters, the light of these two sources is guided towards the solar cell sample trough a fiber optic bundle. To measure the top subcell, a 700 nm long-wave pass filter is used. This filter blocks all wavelengths below 700 nm while passing light that is over 700 nm, effectively biasing the middle and bottom subcells. To measure the middle subcell, a 650 nm short-wave pass filter on one of the light sources and a 900 nm long-wave pass filter on the second light source are used. The first filter and light combination biases the top subcell by blocking all wavelengths over 650 nm while the second combination biases the bottom subcell by shining light of 900 nm and over. To measure the bottom subcell, the two light sources are equipped with a 900 nm short-wave pass filter and a KG1 glass. The short-wave pass filter blocks all the light that is of wavelength over 900 nm, effectively biasing the top and middle subcells. The KG1 is a glass with a broad transition range in the visible and a very good infrared rejection profile. Since the 900 nm short-wave pass filter has a non-negligible amount of infrared light (over 1200 nm) that leaks through, the KG1 glass is necessary to ensure an adequate spectrum. The two light sources are equipped with these filters to allow a larger range of available light intensities. The filter configuration used for the EQE is shown in Table 2.2. The possible arrangements of these filters allows us to create various spectra, which are shown in Figure 2.8 along with a standard EQE. The ASDi FieldSpec 3 spectroradiometer has been used to obtain these calibrated spectra.

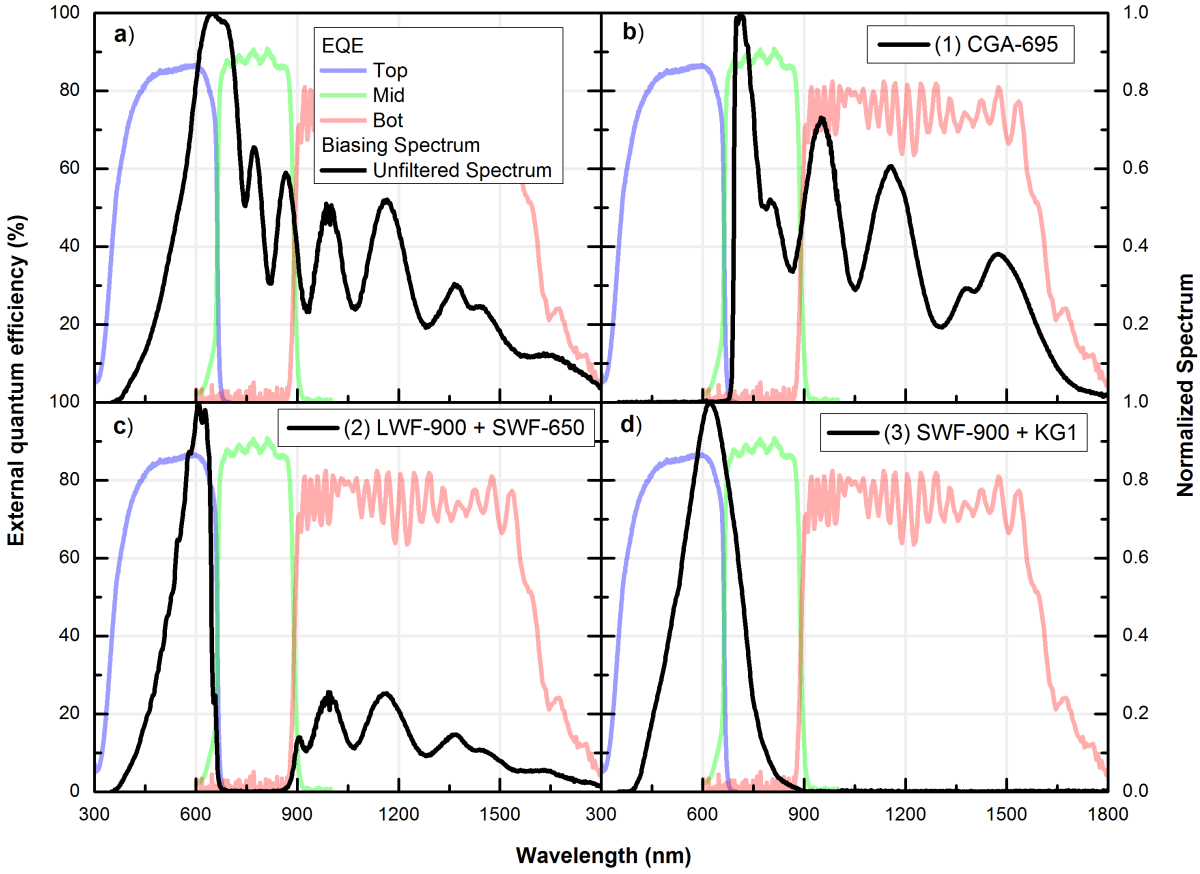

Figure 2.8: The available light biasing spectra in the IQE200, with a) the unfiltered spectrum of the QTH lamp passing through the fibre bundle, b) the spectrum used to bias the middle and bottom subcells, c) the spectrum used to bias the top and bottom subcells and finally, in d) the spectrum used to bias the top and middle subcells. The used filters are shown in the legend of each subfigure.

	Top	Mid	Bot
V_{oc}	1.3 V	0.9 V	0.2 V
Applied V	1.1 V	1.5 V	2.2 V

Table 2.3: Values of the voltage that needs to be applied on the MJSC during an EQE measurement.

Voltage Biasing

While the EQE of a subcell needs to be measured at its own J_{sc}, it is not necessarily at the J_{sc} of the MJSC. The full J-V curve is a combination of the three subcells, and it is not possible to individually measure each component. In a configuration where one subcell receives a low amount of light while the other 2 are fully light biased and the full MJSC is at $V = 0$, such as in Figure 2.7, the measured subcell is actually reverse biased, at $V_{top} \approx -1.1$ in this case. This is because the other two subcells operate near their V_{oc} and the sum of the voltages needs to be equal to zero. To measure the said subcell at $V_{top} = 0$, a voltage of $V \approx 1.1$ needs to be applied on the cell.

The standard values of V_{oc} of each subcell in a lattice-matched MJSC at 1 sun were obtained from numerical simulation [40]. These values are used to estimate the amount of voltage that needs to be applied to measure the EQE, as shown in Table 2.3. However, in most cells, the internal V_{oc} of each subcell is unknown, and these values are used as an estimate. Even though it is measurable, the voltage dependence of the EQE of the top and middle subcell is negligible [37]. This is why in most cases, no voltage is applied for the top and middle subcell measurement. This voltage dependance shall be studied in the chapter 5 of this thesis.

On the other hand, the measurement of the EQE of the bottom subcell is much more dependent on the applied voltage. The portion of the J-V curve of the Ge subcell in reverse bias is not always linear, and oftentimes non-negligible shunting appears. This either creates a non-linear response to photocurrent, or internal voltage biasing creates an artifact in the EQE measurements [37]. For the bottom subcell, it is of utmost importance to apply the correct voltage. Since the voltage of the top two subcells are unknown, there are multiple ways of choosing the right voltage. For a rapid measurement, applying $V = 2$ V is a good estimate. This voltage minimizes the measurement artifact to a low enough degree, achieving less than 1 % difference compared to the optimal voltage measurement. Otherwise, to obtain the optimal voltage, one needs to maximize

the value of the EQE in the infrared region. This is done experimentally by choosing a wavelength that is absorbed by the bottom subcell, and changing the voltage while measuring the CH2 on the lock-in amplifier. The optimal voltage, near 2 V in most cases, will maximize the CH2 value. After the correct voltage is obtained, the bottom subcell EQE can be obtained. A further study of the interaction of each subcell's J-V curve during the measurement of the EQE will be discussed in chapter 5.

The possibility of adding an additional voltage source to the IQE200 is possible through the transimpedance amplifier. A Keithley 2601 sourcemeter is used to apply a voltage ranging from 0 to 3 V to the pins 2 and 3 of the amplifier [47]. The amplifier applies the DC voltage to the solar cell while amplifying the current adequately. It is important to note that applying the Keithley source directly on the solar cell would disrupt the measurement, since the current would be picked up by the Keithely and not the amplifier.

2.3.5 Post-processing and calibration

As mentioned in Equation 2.5, the EQE is calculated by measuring the number of collected carriers going out of the solar cell divided by the number of photons incident on the cell. In the measurements, the CH1 voltage is directly proportional to the incoming photon flux, while the CH2 voltage is directly proportional to the collected current. Hence, it is possible to obtain the number of incident photons by using a simple conversion factor in $f = C_1 V_{CH1}$ and to obtain the number of carriers from CH2 by using a simple conversion factor in $I/q = C_2 V_{CH2}$. The transmitivity and the reflectivity of the beamspliter, the transmitivity of the focusing lenses in front of the sample and detector, the gain of the CH1 preamplifier, the spectral response of the CH1 detector and the conversion factor of the lock-in amplifier are all factors affecting the C_1 constant. The gain of the transimpedance amplifier, as well as the conversion factor of the lock-in amplifier are factors affecting the C_2 constant. It is important to note that since the transmitivity and reflectivity of the beamspliter, the transmitivity of the focusing lenses, and the responsivity of the CH1 detector are all wavelength dependent, the C_1 constant will be wavelength dependent as well. The EQE will be proportional to the division of the two channels, as in

$$EQE\,(\lambda) = \frac{I}{q \cdot f} = \frac{C_2 V_{CH2}}{C_1 V_{CH1}} = C_{cal}\,(\lambda)\,\frac{V_{CH2}}{V_{CH1}}, \tag{2.11}$$

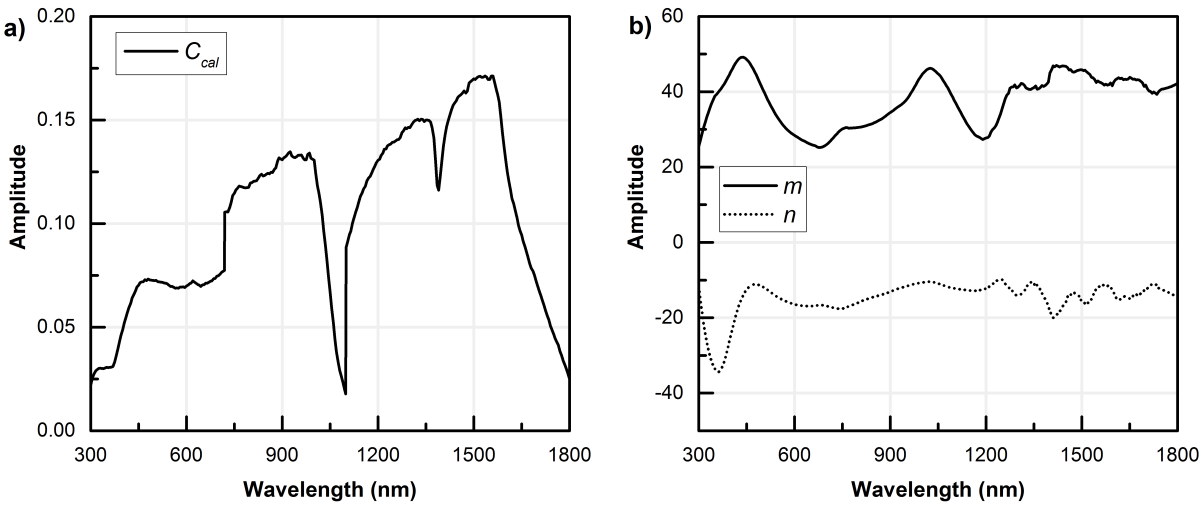

Figure 2.9: Calibration factors used in the calculation of the EQE and the reflectivity. a) The value of C_{cal}, where the switching point between the two detectors at 1100 nm is seen by the steep change in the factor. b) The values of m and n used in the calculation of the reflectivity.

where $C_{cal}(\lambda)$ is the calibrated conversion factor that is currently unknown. This factor will be obtained through a calibration procedure, and will be subsequently used for all measurements.

The calibration process for the measurement of the EQE is used to obtain the value of $C_{cal}(\lambda)$. It is done using a pre-calibrated cell with a known EQE (EQE_{ref}), such as the NREL calibrated Si cell (model 91150V) or the Newport calibrated Si and Ge detectors (IQE-SAMPLE-SI and GE). These calibrated cells are NIST traceable. They were cross-calibrated using working standard detectors which were themselves cross-calibrated initially using the Primary Optical Watt Radiometer (PWOR) at the SIRCUS facility at the NIST in Maryland. The PWOR system is a cryogenic electrical substitution radiometer, which uses a cryogenic temperature of 2 K and electrical substitution radiometry to obtain an uncertainty of less than 0.02 % [49].

The $C_{cal}(\lambda)$ value is obtained by reversing the Equation 2.11 and measuring the calibrated detector channel values, giving

$$C_{cal}(\lambda) = EQE_{ref}(\lambda)\frac{V_{CH1}}{V_{CH2}}. \tag{2.12}$$

Figure 2.9a shows an example of the value of the calibration factor.

It is important to ensure that during the calibration run, the settings for the various integration times and gains are exactly the same as in the measurement taken. The

calibration methodology assumes multiple things. It first assumes that the detectors have a linear response. This is a good approximation for Si-Ge sandwich photodiodes in the operational range under consideration, from approximately 0 to 30 μW [50]. It further assumes that no cross-talk is present between channels. Potential cross-talk is eliminated by the fact that the memory buffer of the lock-in amplifier is cleared between each channel measurement. It assumes as well that the detectors have no dark current, so they give a zero voltage value when no light is incident on them.

The calibration process for the measurement of the reflectivity is similar, but has some significant differences. Reflectivity is given by dividing the reflected photon flux f_R by the incoming photon flux f. It is calculated using the voltage values of CH3 and CH1. Using a similar notation, the photon quantity incident on the solar cell is obtained using $f = C_1 V_{CH1}$, while the number of photons reflected from the solar cell is obtained using $f_R = C_3 V_{CH3}$. The transmitivity of the beamspliter, the transmitivity of the focusing lenses in front of the sample and the detector, the gain of the CH3 preamplifier, the spectral response of the CH3 detector as well as the conversion factor of the lock-in amplifier are all factors contained inside the C_3 constant. The C_3 constant will be wavelength dependent as well. Because the gain setting is set to a higher value in this channel, the dark current value will be non-negligible for this detector. This dark value comes from multiple noise sources in the experiment, such as light bias, light in the room or electrical noise. It is for this reason that the dark value from the channel is subtracted in order to obtain the correct photon count, $f_R = C_3 \left(V_{CH3} - V3_{dark}\right)$. This $V3_{dark}$ will be independent of wavelength. Hence, to calculate the reflectivity, the reflected photon flux needs to be divided by the incoming photon flux,

$$R = \frac{f_R}{f} = \frac{C_3 \left(V_{CH3} - V3_{dark}\right)}{C_1 V_{CH1}} = m\frac{V_{CH3}}{V_{CH1}} + n, \tag{2.13}$$

where the equation has been reworked to match the IQE200 manual's terminology [41]. In this case, the calibration prefactors which are wavelength dependent are given by $m = \frac{C_3}{C_1}$ and $n = -m\frac{V_{dark}}{V_{CH1}}$.

The calibration is done in a two step process. Since there are two unknowns for each wavelength, m and n, two reflectivity standards are needed. The first measurement is done using a high reflectance standard (90%, model 20D20AL.2), while the second measurement is done using a low reflectance standard (0.01%, model FSQ-OD400). Figure 2.10a shows the reflectivity curve for each standard used. Since the exact reflectivity value is known for each standard, it is possible to plot the reflectivity as a function of the $\frac{V_{CH3}}{V_{CH1}}$ proportion. For each wavelength, a linear regression of the two points give the

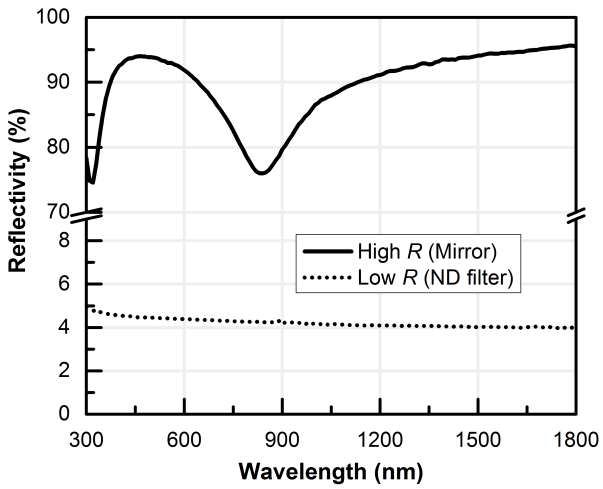

Figure 2.10: Reflectivity of the standard used in the specular reflectivity calibration procedure

slope (m) and the origin (n) for the calibration. Figure 2.9b shows the values of the two factors over wavelength for a typical calibration run. The n factor is significantly important at small reflectance values. Of particular importance is the fact that n is dependent on the light intensity, CH1. This means that for different light intensity, the value of n will change, and the calibration for low reflectivity values will not be correct. However, if the light intensity is constant between the calibration and the measurement, the n values will be very accurate.

2.4 Modeled quantum efficiency

The p-n junction used in semiconductor photovoltaics is a physics problem that has been studied extensively in the literature. This thesis assumes that the reader has a good knowledge of semiconductor physics. Even though most of the principles will be properly introduced, the results discussed in the derived model necessitate some knowledge of the energy band diagram, carrier transport phenomena and Fermi-Dirac statistics.

The band diagram of a p-n junction is shown in Figure 2.11. The free carriers from the p and the n region travel through the junction in a diffusion process, and create the space-charge region. The concentration of free carriers in this region is negligible, and a static charge is created. From the static charge, a directed electric field is created, leading to the creation of a built-in voltage. Due to this change in potential inside the junction, any new electron-hole pair can be separated and a current can be generated.

To create one pair, a photon needs to be absorbed. This pair has to diffuse to the electric field region where it gets separated. Then each carrier is collected at its own contact, being the n side for the electrons and the p side for the holes.

In this section, the quantum efficiency of a p-n homojunction is derived using standard semiconductor physics. The quantum efficiency will depend on key material parameters, such as the bandgap, the absorption coefficient and the lifetime and mobility of carriers. It will depend as well on the solar cell architecture and growth parameters, such as the layer thickness, the doping levels and the surface recombination velocities.

2.4.1 Coupled set of equations

Carrier transport in a p-n homojunction is governed by five coupled set of equations. If we assume a only one dimension in x, the transport equation for the electrons and holes is given by

$$\frac{\partial n}{\partial t} = \frac{1}{q}\frac{\partial}{\partial x}J_n + G_n - U_n, \tag{2.14}$$

$$\frac{\partial p}{\partial t} = -\frac{1}{q}\frac{\partial}{\partial x}J_p + G_p - U_p, \tag{2.15}$$

as well as the Poisson's equation

$$\frac{\partial^2}{\partial x^2}\phi = \frac{q}{\varepsilon_s}\left(N_A^- - N_D^+ + n - p\right), \tag{2.16}$$

and finally the current equations

$$J_n = qD_n\frac{\partial}{\partial x}n + q\mu_n\varepsilon_s n, \tag{2.17}$$

$$J_p = -qD_p\frac{\partial}{\partial x}p + q\mu_p\varepsilon_s p. \tag{2.18}$$

Throughout those equations, the electronic charge is given by q, the minority carrier (electrons or holes) concentrations are given by n and p, the diffusion coefficient of the carriers is given by D, the mobility is given by μ and the permittivity of the semiconductor is given by ε_s. The ionized acceptor doping concentration as well as the donor doping concentration are defined as N_A^- and N_D^+ respectively.

In the transport Equations 2.14 and 2.15, the carrier concentrations' variation over time is dictated by the current J, the generation term G and the recombination term U. In the case of a solar cell, the generation term is assumed to be solely dictated by

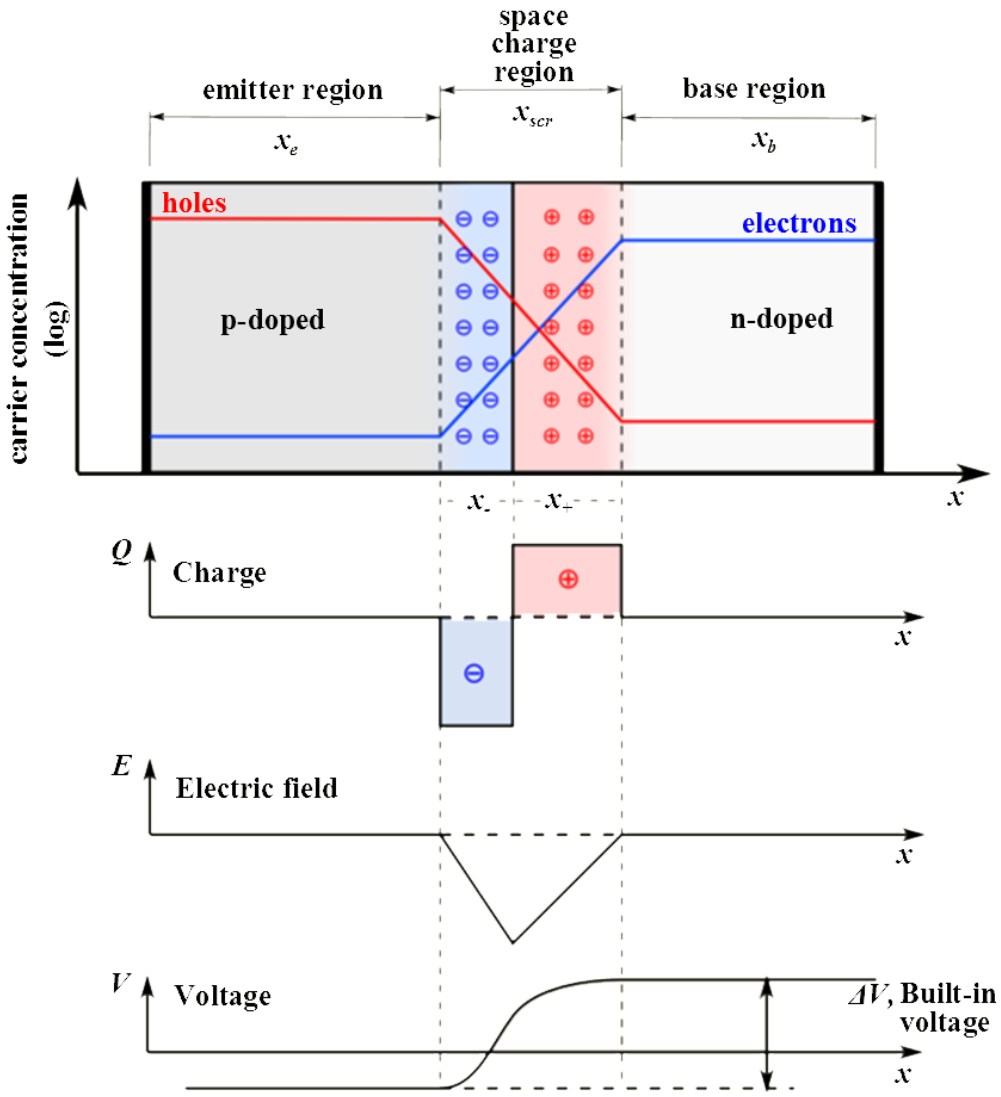

Figure 2.11: The p-n junction diagram, modified from Wikipedia Commons©. As shown in the carrier concentration in the p-n junction, free carriers diffuse at the junction and creates a region of fixed charge. The three main regions have their thicknesses defined as x_e being the emitter region, x_{scr} being the space-charge region and x_b being the base region. The three next graphs are the electric charge, the electric field present in the space-charge region and the voltage present in the junction. A negative charge is formed in the p-doped region, with a thickness of x_- , and a positive charge is created in the n-doped region, with a thickness of x_+.

the photon absorption. It is given by the photon flux inside the structure, b and the absorption coefficient of the semiconductor, α

$$G(x) = \int b(E,x)\alpha(E,x)dE, \tag{2.19}$$

where E is the energy of the photons. On the other hand, the recombination term is given by multiple components. In the semiconductor structure, there are four different paths to recombination for carriers. The recombinations are the radiative (U_{rad}), the Schockley-Read-Hall (SRH), (U_{SRH}), the Auger (U_{Aug}) and surface (U_s) recombinations. In a non-degenerate doped material, the U_{rad}, U_{SRH}, and U_{Aug} can each be associated to a lifetime. For example, for a p-doped semiconductor, the recombination mechanisms for minority carriers are given by

$$U_{rad} = \frac{\Delta n}{\tau_{n,rad}}, \qquad U_{SRH} = \frac{\Delta n}{\tau_{n,SRH}}, \qquad U_{Aug} = \frac{\Delta n}{\tau_{n,Aug}}, \tag{2.20}$$

where $\tau_{n,rad}$, $\tau_{n,SRH}$ and $\tau_{n,Aug}$ are the radiative, SRH and Auger recombination lifetime respectively. To obtain the total recombination rate, the three recombination rates are added together. This gives the total recombination lifetime of the carriers τ_{tot}, which is

$$\frac{1}{\tau_{tot}} = \frac{1}{\tau_{rad}} + \frac{1}{\tau_{SRH}} + \frac{1}{\tau_{Aug}}. \tag{2.21}$$

The fourth recombination path, the surface recombination U_s, is calculated using the surface recombination velocity (SRV), given in units of speed (m/s). This recombination mechanism is primarly due to defects due to broken bonds at the surface of a semiconductor. These can be created by impurities that are concentrated at the interfaces between layers. For these reasons, a surface recombination velocity is used instead of a typical recombination flux. The SRV is highly dependent on the quality of the interfaces between the semiconductor. A very good SRV between a subcell and its front surface field can go down to less than 6000 cm/s [51].

Using these coupled equations and the p-n junction architecture, it is possible to analytically solve them under certain assumptions. The two main approximations that need to be made are the depletion approximation and the linearity of the recombination mechanism. The recombination approximation states that the recombination mechanism in the semiconductor follows the relations shown in Equation 2.21. The depletion approximation assumes multiple things. It revolves around the depletion region created between the p and the n semiconductors. It assumes that it is a region completely free of free carriers, that the potential step and the electric field is given only by the fixed

charge present in the region and that outside of this region no electric field is present. After assuming this, the five coupled equations become solvable analytically. A complete derivation of these can be found in Physics of solar cells [9]. If the p-n junction is illuminated by a photon flux of b_λ and is biased by an applied voltage V, the general solution for the current J in the solar cell is given by

$$J = J_e + J_b + J_{scr}, \tag{2.22}$$

where J_e, J_b and J_{scr} are the total currents in the emitter, the base and the space-charge region respectively. The solution for the current in the emitter is given by [9]

$$\begin{aligned} J_e = \int & q b_\lambda \left(1 - R\left(\lambda\right)\right) f_\alpha \left(L_e\right) \\ & \cdot \left(\frac{\alpha(\lambda) L_e + \ell_e - \mathrm{e}^{-\alpha(\lambda) x_e} \cdot \left(\ell_e \cosh \frac{x_e}{L_e} + \sinh \frac{x_e}{L_e} \right)}{\ell_e \sinh \frac{x_e}{L_e} + \cosh \frac{x_e}{L_e}} - \alpha(\lambda) L_e \mathrm{e}^{-\alpha(\lambda) x_e} \right) d\lambda \\ & + \frac{q D_e N_e (\mathrm{e}^{\frac{qV}{k_\mathrm{B} T}} - 1)}{L_e} \left(\frac{\ell_e \cosh \frac{x_e}{L_e} + \sinh \frac{x_e}{L_e}}{\ell_e \sinh \frac{x_e}{L_e} + \cosh \frac{x_e}{L_e}} \right), \end{aligned} \tag{2.23}$$

while the current in the space-charge region is given by

$$J_{scr} = \int q b_\lambda \left(1 - R\left(\lambda\right)\right) \mathrm{e}^{-\alpha(\lambda) x_{scr}} d\lambda - \frac{q n_i x_{scr}}{\sqrt{\tau_n \tau_p}} \frac{2 \sinh \left(\frac{qV}{2 k_\mathrm{B} T} \right)}{q \frac{V_{bi} - V}{k_\mathrm{B} T}} \frac{\pi}{2}, \tag{2.24}$$

and the solution for the current in the base is

$$\begin{aligned} J_b = \int & q b_\lambda (1 - R\left(\lambda\right)) f_\alpha \left(L_b\right) \mathrm{e}^{-\alpha(\lambda)(x_e + x_{scr})} \\ & \cdot \left(\frac{\mathrm{e}^{-\alpha(\lambda) x_e} \cdot (\alpha(\lambda) L_b + \ell_b) - \left(\ell_b \cosh \frac{x_b}{L_b} + \sinh \frac{x_b}{L_b} \right)}{\ell_b \sinh \frac{x_b}{L_b} + \cosh \frac{x_b}{L_b}} + \alpha(\lambda) L_b \right) d\lambda \\ & + \frac{q D_b N_b (\mathrm{e}^{\frac{qV}{k_\mathrm{B} T}} - 1)}{L_b} \left(\frac{\ell_b \cosh \frac{x_b}{L_b} + \sinh \frac{x_b}{L_b}}{\ell_b \sinh \frac{x_b}{L_b} + \cosh \frac{x_b}{L_b}} \right). \end{aligned} \tag{2.25}$$

Multiple new quantities have been introduced in those equations. Quantities that have already been defined, namely the charge q, the reflectivity of the structure $R(\lambda)$, the diffusion coefficient of the minority carriers D, the incident solar photon flux b_λ, the

wavelength of the light λ, the total lifetime of the carriers τ and the absorption coefficient of the material α are all present. As seen in Figure 2.11, the thicknesses are defined as the emitter x_e, the space charge region x_{src} and the base x_b. The surface recombination length is given by $\ell = \frac{SRV \cdot L}{D}$. The diffusion length L, the surface recombination velocity (SRV) and the active doping value N is defined for each material, be it emitter ($_e$) or base ($_b$). The diffusion coefficients D are obtained by the Einstein relationship, while the absorption function f_α and the diffusion lengths L can be obtained using [9]

$$D = \frac{\mu k_{\mathrm{B}} T}{q}, \qquad f_\alpha(L) = \frac{\alpha L}{\alpha^2 L^2 - 1}, \text{ and} \qquad L = \sqrt{\tau D}. \tag{2.26}$$

The reflectivity (R) will be given by a calculation using the transfer matrix method (TMM). This will be derived in Section 2.4.3. The other quantities that needs to be calculated are the space-charge region length, x_{scr} as well as the depth of the space-charge region within the emitter and base. These can be seen in the Figure 2.11. They can be calculated by using the formulas [9]

$$x_{scr} = \sqrt{\frac{2\varepsilon_s}{q}\left(\frac{1}{N_e} + \frac{1}{N_b}\right) V_{bi}}, \tag{2.27}$$

where V_{bi} is the built-in bias created by the p-n junction and ε_s is the material's permittivity. The built-in bias is dependent on the semiconductor doping following

$$V_{bi} = \frac{k_{\mathrm{B}} T}{q} \log\left(\frac{N_e N_b}{n_i^2}\right) \tag{2.28}$$

where n_i is the intrinsic doping of the semiconductor. The base and emitter thicknesses are calculated by removing the depleted part from each of them, following the equations

$$x_e = w_e - \frac{1}{N_e}\sqrt{\frac{2\varepsilon_s V_{bi}}{q\left(\frac{1}{N_e} + \frac{1}{N_b}\right)}}, \tag{2.29}$$

and

$$x_b = w_b - \frac{1}{N_b}\sqrt{\frac{2\varepsilon_s V_{bi}}{q\left(\frac{1}{N_e} + \frac{1}{N_b}\right)}}, \tag{2.30}$$

where w_e and w_b are the actual grown thicknesses of the emitter and base layer.

Since each of the Equations 2.23, 2.24 and 2.25 have an exponential dependence over voltage, it is possible to compare them to the common two-diode equation. This two diode equation, with no series or shunt resistances, is given by

$$J = J_L - J_0\left(\mathrm{e}^{\frac{qV}{k_{\mathrm{B}}T}} - 1\right) - J_{02}\left(\mathrm{e}^{\frac{qV}{2k_{\mathrm{B}}T}} - 1\right), \tag{2.31}$$

where J_L is the photocurrent, J_0 is the radiative recombination current density and J_{02} is the recombination current density in the space charge region. The first two coefficients are straightforward to associate between the two sets of equations. First, the photocurrent J_L is given by adding all the coefficients that are voltage independent and contains the photon flux b_λ. These coefficients will be used further in the next section. Second, the recombination current J_0 is given by all the components that vary with the exponential decay given by $\left(\mathrm{e}^{\frac{qV}{k_\mathrm{B}T}}-1\right)$. These factors are related to an ideality factor of $n=1$. Given these assumptions, the recombination current is given by

$$J_0 = \frac{qD_eN_e}{L_e}\left(\frac{\ell_e\cosh\frac{x_e}{L_e}+\sinh\frac{x_e}{L_e}}{\ell_e\sinh\frac{x_e}{L_e}+\cosh\frac{x_e}{L_e}}\right)+\frac{qD_bN_b}{L_b}\left(\frac{\ell_b\cosh\frac{x_b}{L_b}+\sinh\frac{x_b}{L_b}}{\ell_b\sinh\frac{x_b}{L_b}+\cosh\frac{x_b}{L_b}}\right). \tag{2.32}$$

The obtained equations have no terms directly proportional to $\left(\mathrm{e}^{\frac{qV}{2k_\mathrm{B}T}}-1\right)$, corresponding to the second recombination term. However, assuming forward bias only, the hyperbolic sinusoidal term $2\sinh\left(\frac{qV}{2k_\mathrm{B}T}\right)$ seen in Equation 2.24 can be approximated as $\left(\mathrm{e}^{\frac{qV}{2k_\mathrm{B}T}}-1\right)$. Given the assumption that the sinh term behaves similarly to the exponential, the space-charge region recombination current is defined as

$$J_{02} = \frac{\pi n_i}{2\sqrt{\tau_n\tau_p}}\frac{x_{scr}}{\frac{V_{bi}-V}{k_\mathrm{B}T}}. \tag{2.33}$$

Hence, given those equations, it is possible to estimate the J-V curve of a homojunction solar cell.

2.4.2 The quantum efficiency equations

Now that the derivation for the current in the cell has been obtained, it is possible to obtain the EQE of the said cell. The EQE is obtained by using the Equations 2.23, 2.24 and 2.25 at $V=0$ and by removing the integrals over wavelength. Applying $V=0$ ensures that the calculation is done at J_{sc} and the removal of the integral ensures that the values are wavelength dependent. The central solution for the EQE is then given by

$$\mathrm{EQE} = \mathrm{EQE_e} + \mathrm{EQE_b} + \mathrm{EQE_{scr}}, \tag{2.34}$$

where the solution for the EQE in the emitter is given by

$$\mathrm{EQE}_e(\lambda) = (1-R(\lambda))f_\alpha(L_e) \cdot\left(\frac{\alpha(\lambda)L_e+\ell_e-\mathrm{e}^{-\alpha(\lambda)x_e}\cdot\left(\ell_e\cosh\frac{x_e}{L_e}+\sinh\frac{x_e}{L_e}\right)}{\ell_e\sinh\frac{x_e}{L_e}+\cosh\frac{x_e}{L_e}}-\alpha(\lambda)L_e\mathrm{e}^{-\alpha(\lambda)x_e}\right), \tag{2.35}$$

the solution for the EQE in the space-charge region is

$$\mathrm{EQE}_{scr}(\lambda) = q\left(1 - R\left(\lambda\right)\right)\mathrm{e}^{-\alpha(\lambda)x_{scr}}, \tag{2.36}$$

and finally the solution for the EQE in the base is

$$\begin{aligned}\mathrm{EQE}_b(\lambda) = {} & \left(1 - R\left(\lambda\right)\right) f_\alpha\left(L_b\right)\mathrm{e}^{-\alpha(\lambda)(x_e + x_{scr})} \\ & \cdot \left(\frac{\mathrm{e}^{-\alpha(\lambda)x_e} \cdot \left(\alpha(\lambda)L_b + \ell_b\right) - \left(\ell_b \cosh\frac{x_b}{L_b} + \sinh\frac{x_b}{L_b}\right)}{\ell_b \sinh\frac{x_b}{L_b} + \cosh\frac{x_b}{L_b}} + \alpha(\lambda)L_b \right).\end{aligned} \tag{2.37}$$

In these equations, the various quantities are the same as defined earlier.

Now that all the equations needed are defined, it is possible to distinguish the parameters that are variable and the parameters given by the semiconductor properties. The variable parameters are the doping, N_e and N_b, the various thicknesses in the solar cell, w_e and w_b and the temperature T. For the remainder of the thesis, the temperature will be set constant at $T = 300K$. It is possible to add an intrinsic region w_i by simply replacing the x_{scr} by $w_i + x_{scr}$. The parameters that are growth dependent, but will be varied, are the surface recombination velocities (SRV) of the contact-emitter and the contact-base surfaces. These are present in the surface recombination length, $\ell = \frac{SRV \cdot L}{D}$.

The parameters that are dependent on the semiconductor properties are the mobilities μ_e and μ_b, the total recombination lifetimes τ_e and τ_b, the intrinsic doping n_i, the permittivity ε_s and the absorption coefficient α. These are present in the diffusion coefficient $D = \frac{\mu k_\mathrm{B} T}{q}$, in the diffusion length $L = \sqrt{\tau D}$ and the absorption function $f_\alpha = \frac{\alpha L}{\alpha^2 L^2 - 1}$.

2.4.3 The semiconductor parameters

The semiconductors that are used in the standard lattice-matched multi-junction solar cell design are materials that have been extensively studied in the scientific literature. In this section, the valuable quantities that will be used in the simulation of the EQE shall be summarized.

The lifetimes

The first semiconductor parameters that are defined are the recombination lifetimes. As seen in Equation 2.21, the total lifetime is given by the reciprocal addition of each of

the individual lifetimes. To obtain the total lifetime, each of the individual lifetimes of the minority carriers need to be found. These lifetimes can vary widely over doping concentration.

The radiative lifetime varies as the inverse of the doping density, as in

$$\tau_{rad} = \frac{1}{B_{rad}N}, \tag{2.38}$$

where B_{rad} is the radiative recombination coefficient [9]. This recombination process happens when electrons spontaneously recombine with a hole and emit a photon. It is important to note that the radiative recombination is for the minority carrier in the material. If the emitter is n-doped with a donor density N_D, the radiative lifetime will be defined for the holes, as in τ_p. For higher doping, the radiative lifetime will be smaller, giving a recombination rate that will be faster. This is expected, since the higher concentration of the majority carrier will allow the minority carrier to recombine more often.

The other main recombination mechanism in solar cells, the SRH recombination, has a lifetime that behaves following the equation

$$\tau_{SRH} = \frac{\tau_{SRH,max}}{1 + \left(\frac{N}{N_{ref}}\right)^{\gamma}}, \tag{2.39}$$

where $\tau_{SRH,max}$, N_{ref} and γ are material dependent constants. This recombination mechanism involves deep traps inside the bandgap, where electrons or holes can be captured and subsequently recombine non-radiatively. Because it involves traps inside the semiconductor, this recombination process will be directly related to the quality of the material.

The third recombination process, that is negligible in solar cell operation, is the Auger recombination. It happens when an electron in the conduction band recombines with a hole and transfers its energy through scattering with another electron. The transfer of kinetic energy to the excited electron is then relaxed by the emission of phonons. Because it involves a three particle process, the Auger recombination rate is often negligible. It varies as the inverse square of the doping, with

$$\tau_{Auger} = \frac{1}{A_{Auger}N^2}, \tag{2.40}$$

where A_{Auger} is a material dependant parameter.

The three main semiconductors used in the MJSC, GaAs, InGaP and Ge all have significantly different lifetimes. The parameters obtained from the literature are shown

Material	Doping type	Minority carriers	B_{rad} (cm^{-3})	$\tau_{SRH,max}$ (s)	N_{ref} (cm^{-3})	γ	A_{Auger} (s)
InGaP	p	e	$2.4 \cdot 10^{-10}$	$2 \cdot 10^{-7}$	10^{19}	1	$3 \cdot 10^{-30}$
	n	h	$2.4 \cdot 10^{-10}$	$2 \cdot 10^{-7}$	10^{19}	1	$3 \cdot 10^{-30}$
GaAs	p	e	10^{-10}	10^{-4}	10^{16}	1	$3 \cdot 10^{-30}$
	n	h	10^{-10}	$2 \cdot 10^{-8}$	10^{18}	3	$3 \cdot 10^{-30}$
Ge	p	e	$5.2 \cdot 10^{-14}$	$2 \cdot 10^{-5}$	10^{17}	1	$2.8 \cdot 10^{-31}$
	n	h	$5.2 \cdot 10^{-14}$	$4 \cdot 10^{-5}$	$3 \cdot 10^{16}$	1	$8 \cdot 10^{-32}$

Table 2.4: Parameters used in the calculation of the InGaP, GaAs and Ge minority carrier lifetimes. The values comes from [26].

in Table 2.4. Figure 2.12 shows the recombination lifetimes over doping for electrons in GaAs. The lifetime is dominated by radiative processes at higher doping concentration, while at lower doping the SRH and radiative processes both contribute. For all dopings, the Auger recombination process is negligible.

The resulting total recombination lifetime for both electrons and holes are shown in figure 2.13. The recombination lifetime decreases at higher doping. It is interesting to note that at doping higher than 10^{17} cm^{-3}, the carrier lifetime for both InGaP and GaAs are similar.

In the EQE model, the doping for each layer, namely the emitter and base for each of the three subcells, are defined initially. Then the recombination lifetimes are calculated using the previously defined equations. Those recombination lifetimes are subsequently used in the main EQE Equations 2.35, 2.36 and 2.37.

The mobility

The second important semiconductor parameter is the mobility, μ. The mobility of carriers in semiconductor varies depending on the doping level N, similarly to the SRH lifetime. The doping dependence follows the Sotoodeh model [52],

$$\mu = \mu_{min} + \frac{\mu_{max} - \mu_{min}}{1 + \left(\frac{N}{N_{ref}}\right)^{\lambda}} \tag{2.41}$$

where μ_{min}, μ_{max}, N_{ref} and λ are material dependant parameters. Each of these components have different values depending on the minority carrier types, being either electrons

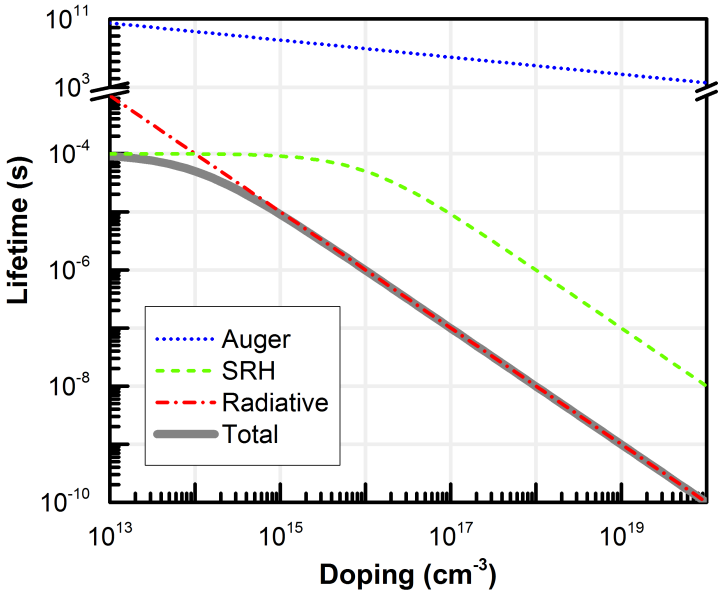

Figure 2.12: The different electron lifetimes over doping concentration in GaAs, calculated using Equations 2.38, 2.39 and 2.40 and the parameters in Table 2.4.

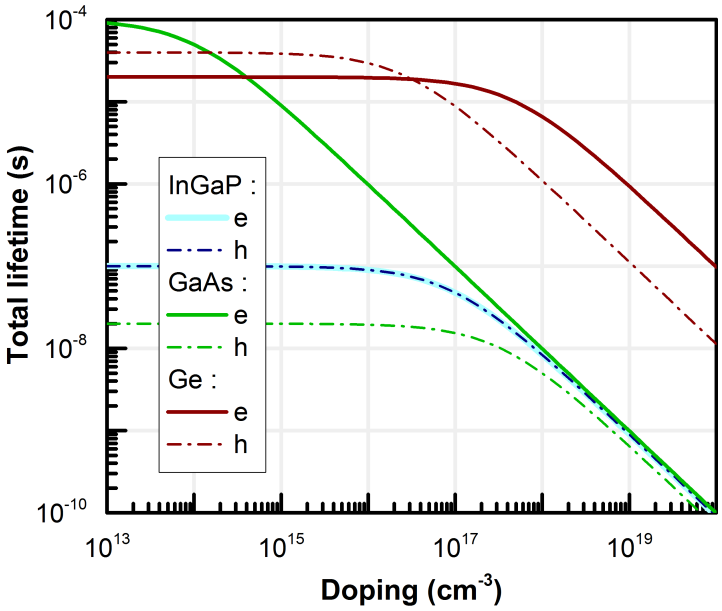

Figure 2.13: The total lifetimes of electrons (e) and holes (h) for the three standard semiconductors in MJSC, namely InGaP, GaAs and Ge obtained by the reciprocal addition of each of the individual lifetimes in Equation 2.21.

Material	Doping type	Minority carriers	μ_{max} (cm^2/Vs)	μ_{min} (cm^2/Vs)	N_{ref} (cm^{-3})	λ
InGaP	p	e	4300	400	$2.0 \cdot 10^{16}$	0.70
	n	h	150	15	$1.5 \cdot 10^{17}$	0.80
GaAs	p	e	9400	500	$6.0 \cdot 10^{16}$	0.39
	n	h	491.5	20	$1.5 \cdot 10^{17}$	0.38
Ge	p	e	3895	641	$6.1 \cdot 10^{16}$	1.04
	n	h	2505	175	$9.3 \cdot 10^{16}$	0.9

Table 2.5: Parameters used in the calculation of the InGaP, GaAs and Ge minority carrier mobilities. The values were obtained from [52] and from [53].

(e) or holes (h). Here, it is important to note that λ is not the wavelength, but a number on the order of 1 that controls the steepness of the curve. Following this equation, the mobility will change between its minimum and maximum value depending on the doping levels. The parameters used to obtain the total mobility for minority carriers in the EQE model are obtained from the literature, and shown in Table 2.5. The resulting total mobilities for both electrons and holes are shown in Figure 2.14.

The complex refractive index

The light propagation inside the semiconductor is dictated by the complex refractive index, $\tilde{n}$. It is given by

$$\tilde{n} = n - ik, \tag{2.42}$$

where n is the refractive index of the material and k is the extinction coefficient. The refractive index indicates the phase speed of light inside the material while k indicates the amount of loss when light passes through the material. Both of them are unitless. This complex refractive index is used in the plane wave expression of light propagation through matter,

$$E = E_0 \mathrm{e}^{-2\pi i(n-ik)z/\lambda + i\omega t}, \tag{2.43}$$

where E is the propagating electric field, E_0 is the field amplitude, ω is the light frequency and λ is the wavelength.

The absorption coefficient used in the Equations 2.35, 2.36 and 2.37 can be obtained

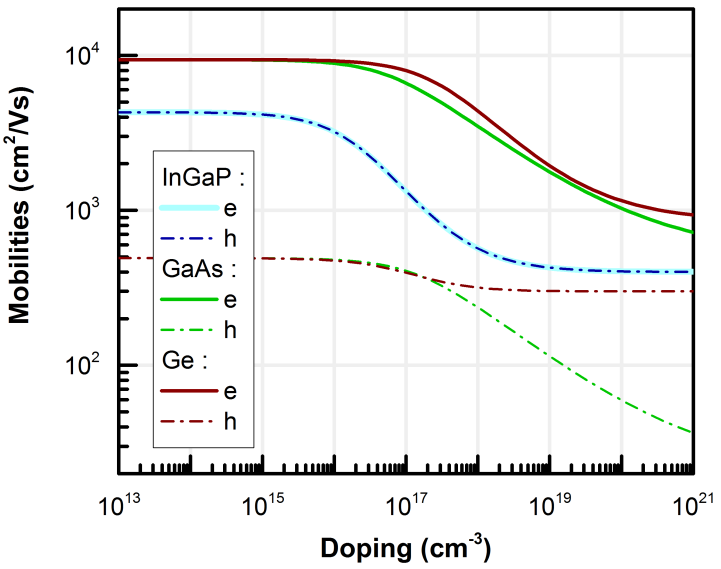

Figure 2.14: The InGaP, GaAs and Ge carrier mobilities over doping concentration obtained by the Sotoodeh model in Equation 2.41 and the semiconductor parameters in Table 2.5.

from the extinction coefficient, by

$$\alpha = \frac{4\pi k}{\lambda}. \tag{2.44}$$

The three absorption coefficient, InGaP, GaAs and Ge, used in the model are shown in Figure 2.15. Their different absorption edges, at 685, 890 and 1800 nm respectively, corresponds to their bandgap. Because of these different absorption coefficients, they each absorb a different part of the solar spectrum.

Reflectivity calculation

The calculation of the reflectivity will be studied in depth in chapter 3 but the technique is introduced here. The reflectivity of the solar cell is highly dependent on the various refractive indexes of the materials. A good approximation of the reflectivity can be obtained by taking into account only the first few layers. For example, if a 100 nm layer of SiO_2 material deposited on top of a non-absorbing InGaP semi-infinite wafer is considered, the reflectivity is given by

$$R = \frac{(n_0 - n_2)^2 + \left(\frac{n_0 n_2}{n_1} - n_1\right)^2 \tan^2 \delta_1}{(n_0 + n_2)^2 + \left(\frac{n_0 n_2}{n_1} + n_1\right)^2 \tan^2 \delta_1}, \tag{2.45}$$

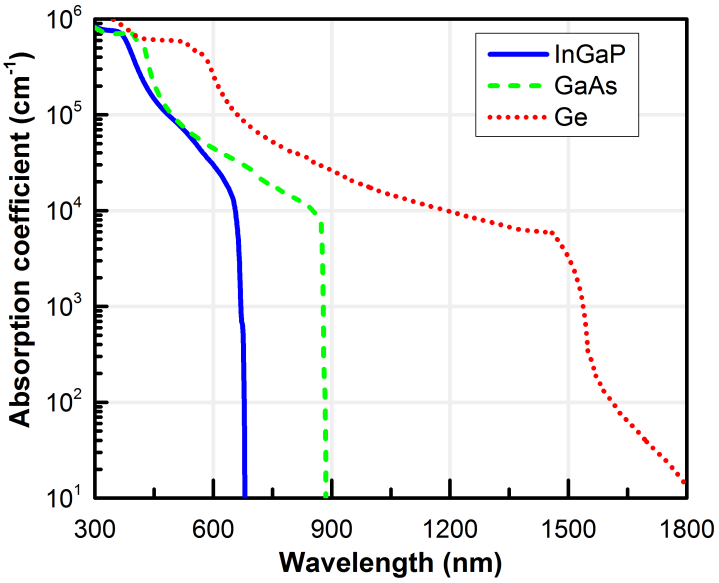

Figure 2.15: The absorption coefficient of InGaP, GaAs and Ge, taken from [54], [55] and [56].

where n_0, n_1 and n_2 are the refractive index of air, SiO_2 and InGaP respectively, $\delta_1 = \frac{2\pi}{\lambda} dn_1$ is the optical path of the light inside the SiO_2 layer and d is the thickness of the layer. The refractive index of SiO_2 and InGaP are obtained from references [57] and [54] respectively. The reflectivity calculated from this formula is shown in Figure 2.16, labeled as the 'Simplified calculation' curve.

However, in the complex structure of a MJSC, each layers will have an effect on the reflectivity. The simple Equation 2.45 will not be adequate to obtain the full reflectivity. For this purpose, a transfer matrix method (TMM) is developed. Using the method developed by Harbecke [58], the reflection and transmission at each interface is taken into account. The total reflectivity is given by

$$R = |r|^2 + R_{sub}, \tag{2.46}$$

where r is the complex reflectance from all of the layers in the structure and R_{sub} is the reflection of light from the back of the substrate. The complex reflectance is given by

$$r = \frac{M_{(2,1)}}{M_{(1,1)}}, \tag{2.47}$$

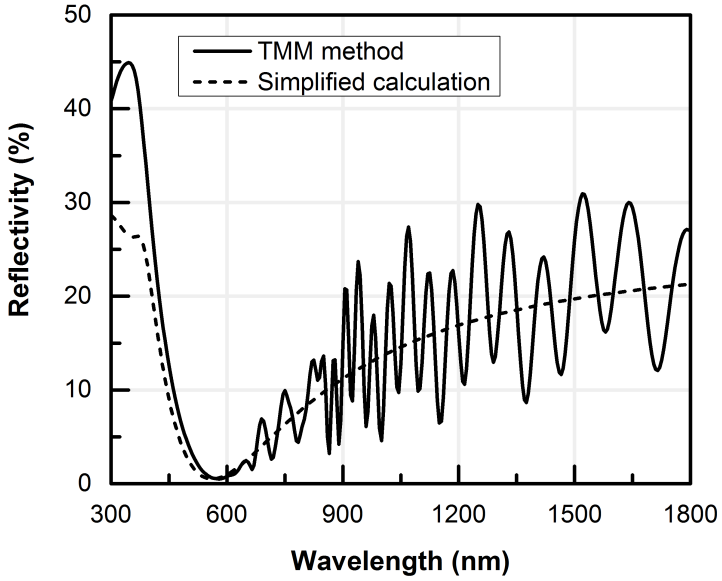

Figure 2.16: Reflectivity of the simplified solar cell structure, comparing the transfer matrix method to the analytical reflectivity formula.

where,

$$M = \left[\prod_{i=1}^{m} \frac{1}{2\tilde{n}_{i-1}} \begin{pmatrix} \tilde{n}_{i-1}+\tilde{n}_i & \tilde{n}_{i-1}-\tilde{n}_i \\ \tilde{n}_{i-1}-\tilde{n}_i & \tilde{n}_{i-1}+\tilde{n}_i \end{pmatrix} \cdot \begin{pmatrix} e^{i\delta_i} & 0 \\ 0 & e^{i\delta_i} \end{pmatrix}\right] \cdot \begin{pmatrix} \tilde{n}_m+\tilde{n}_{sub} & \tilde{n}_m-\tilde{n}_{sub} \\ \tilde{n}_m-\tilde{n}_{sub} & \tilde{n}_m+\tilde{n}_{sub} \end{pmatrix}, \tag{2.48}$$

where $\tilde{n}_i$ is the complex refractive index of the ith layer, $\tilde{n}_{sub}$ is the complex refractive index of the substrate. δ_i is the optical path traveled by light inside each layer, given by $\delta = 2\pi\tilde{n}_i d_i/\lambda$ and d_i is the thickness of the ith layer. The multiplication is done from the first layer ($i = 1$) to the last layer before the substrate ($i = m$). The first matrix takes into account the reflection and transmission at each interface between materials of different index of refraction. The second matrix takes into account the interference between incoming and reflected light beams. The last matrix is the reflection and transmission from the last layer and the substrate. The reflection from the back of the wafer is not considered into the interference patterns. The main reason is that the period of the oscillations created by the reflection of the wafer is smaller than the resolution of the apparatus. For a 500 µm thick germanium wafer of refractive index of $n \approx 4.1$, oscillation of a period of 0.8 nm at 1800 nm light is expected. As mentioned in Section 2.3.1, the instrument resolution is 3.3 nm. Hence, these oscillations are smeared out, and only the reflection from the back of the wafer, without the interference effect, is taken into

account.

The reflection from the substrate, R_{sub}, is taken into account by using the incoherent reflection method introduced by Harbecke [58]. It is given by

$$r_{sub} = \frac{\tilde{n}_{sub} - n_{air}}{\tilde{n}_{sub} + n_{air}}, \tag{2.49}$$

which then comes into

$$R_{sub} = |t_{ab} t_{ba} r_{sub}|^2 \frac{\mathrm{e}^{-2\alpha_{sub} d_{sub}}}{1 - |r_{sub} r_{ba}| \, \mathrm{e}^{-2\alpha_{sub} d_{sub}}}, \tag{2.50}$$

where $\tilde{n}_{sub}$, α_{sub} and d_{sub} are the complex index of refraction, the absorption coefficient and the thickness of the substrate respectively. The transitivity and reflectivity quantities, t_{ab}, t_{ba} and r_{ba}, are the complex matrix coefficient of the TMM matrix M, defined as

$$t_{ab} = \frac{1}{M_{(1,1)}}, \qquad t_{ba} = \frac{M_{(1,1)} \cdot M_{(2,2)} - M_{(1,2)} \cdot M_{(2,1)}}{M_{(1,1)}}, \text{ and} \qquad r_{ba} = -\frac{M_{(1,2)}}{M_{(1,1)}}. \tag{2.51}$$

To calculate the total reflectivity of the structure, the complex refractive indexes, $\tilde{n}_i$, and the thickness d_i of all of the ith layers are needed.

Using the transfer matrix method, it is then possible to calculate the reflectivity of a full MJSC structure. Using the TMM method, the reflectivity of a simplified MJSC structure of 100 nm of SiO_2, 1 µm of InGaP, 2 µm of GaAs and 500 µm of Ge is calculated and shown in Figure 2.16. The differences between the TMM method and the simplified reflectivity are highlighted in the differences between the curves in the UV-blue (300-400 nm) and the red-IR (700-1800 nm) regions. In the UV-blue region, the difference between the two curves arises because the TMM method takes into account the extinction coefficient k. The InGaP absorption in this region is high enough to have a significant effect on the reflectivity. In the red-IR region, the two reflectivities follow the same trend. However, the reflectivity calculated by the TMM method shows strong oscillation over wavelength. These oscillations are due to the creation of optical cavities in the structure, namely the InGaP and the GaAs layers. The transmission and reflection of the light inside those cavities creates constructive and destructive interferences, leading to those oscillations. It is clear that to accurately calculate the reflectivity pattern in a full structure, the TMM method is necessary.

The refractive indexes and the extinction coefficients of all the material used in this thesis are shown in Figure 2.17. The extinction coefficients of InGaP, GaAs and Ge correspond to the absorption coefficients shown in Figure 2.15. These complex refractive

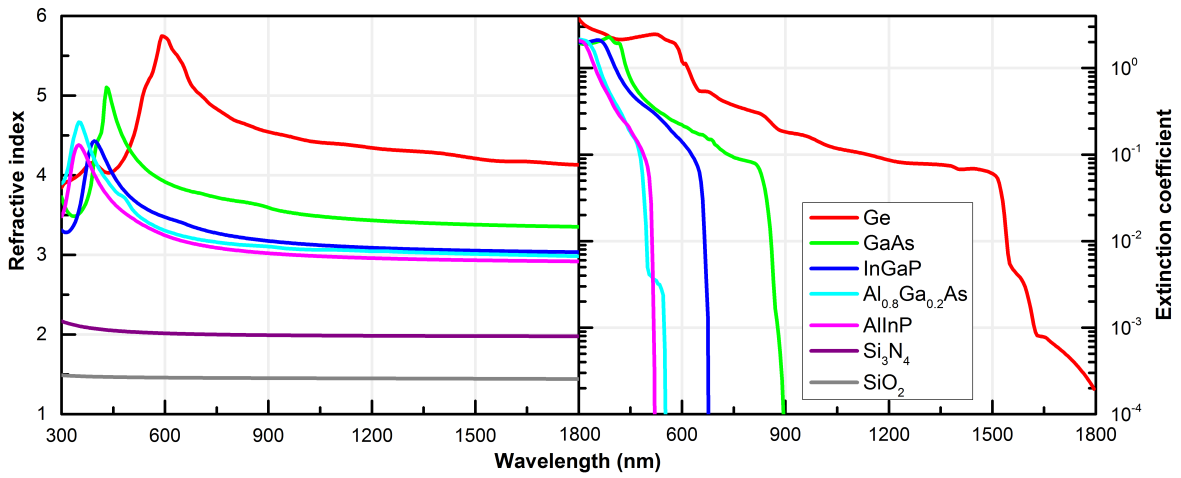

Figure 2.17: The refractive index and extinction coefficient of the materials in solar cell EQE simultation. (Ge [56], GaAs [55], InGaP [54], AlGaAs [61], AlInP [60], SiO_2 [57] and Si_3N_4 [59])

indexes come from multiple sources in the literature. The dielectric materials, namely SiO_2 and Si_3N_4 are from [57] and [59]. The extinction coefficient of these dielectric material are not visible in Figure 2.17, since they are equal to zero in this wavelength range. The semiconductor materials shown in the figure are AlInP [60], AlGaAs [61], InGaP [54], GaAs [55], and Ge [56]. In this thesis, the material and thicknesses profile will be listed for all simulations and these complex refractive indexes will be used to calculate the reflectivity of the structure.

The intrinsic parameters

The two remaining parameters used in the EQE equations that haven't been discussed yet are the permittivity ε_s and the intrinsic carrier density n_i. Those 2 quantities are used only in the calculation of the built-in bias, V_{bi}, in Equation 2.28. The permittivity is related to the refractive index, given by $\varepsilon_s = n^2$, when no absorption in the material is considered. The values of the permittivity of the three material is given in Table 2.6.

The intrinsic carrier density, n_i, is the quantity of free carriers present in an undoped semiconductor material. They are related to the available carriers in the semiconductor without any external excitation. These are shown in Table 2.6.

Material	Intrinsic carrier density n_i (cm^{-3})	Permittivity ε_s
InGaP	$1.2 \cdot 10^3$	11.8
GaAs	$2 \cdot 10^6$	12.9
Ge	$2.5 \cdot 10^{13}$	16

Table 2.6: Intrinsic carrier density and the semiconductor permitivities used in the EQE simulation. The permittivity is obtained from [62]. The InGaP, GaAs and Ge intrinsic carrier density are obtained from [63], [64] and [65] respectively.

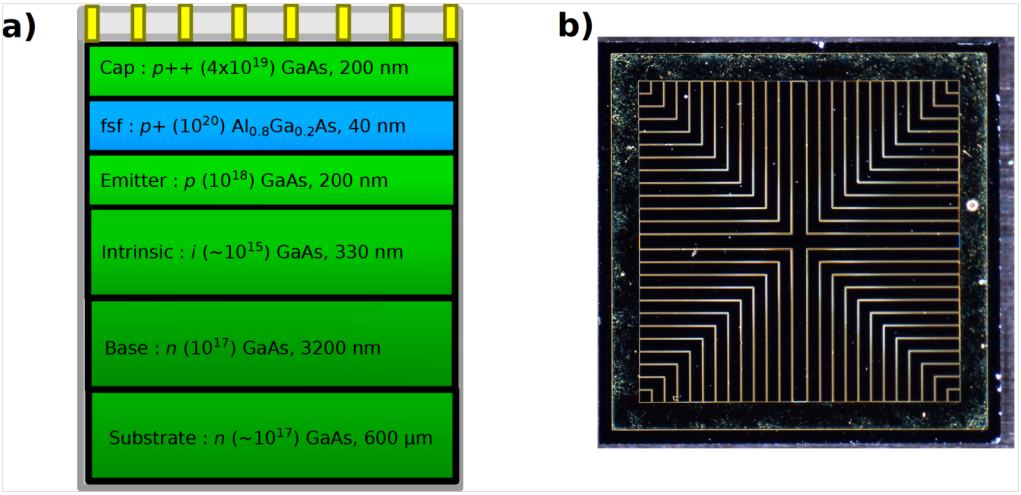

Figure 2.18: a) Single junction GaAs (sample SJ-ref) design used in the EQE simulation. b) Picture of single junction GaAs cell epitaxially grown at the Université de Sherbrooke.

2.4.4 The single junction GaAs cell

All the semiconductor parameters that are needed to simulate the EQE of a single junction EQE have now been defined. A standard single junction GaAs (sample SJ-ref) will first be studied. The simulated EQE is compared to an experimentally measured EQE of a *n-i-p* structure grown at Université de Sherbrooke. Figure 2.18 shows the design and a picture of the studied solar cell. No anti-reflection coating has been deposited on the solar cell. An AlGaAs front surface field (fsf) is grown to reduce the front surface recombination velocity.

The calculated and measured EQE are shown in Figure 2.19. Values of 10^5 cm/s for the front and back surface recombination velocities (SRV) were used. Typical values for

an unpassivated GaAs layer are 10^6 to 10^7 cm/s [66]. The n++ GaAs cap layer and the AlGaAs fsf layers were considered in the reflectivity calculation, but were assumed to contribute no current in the EQE. This means that the EQE was calculated using Equations 2.35, 2.36 and 2.37, multiplied by the transmitted light intensity given in the TMM method, t_{ab}, in Equation 2.51. The finger shading was measured to be 7.4 % [67].

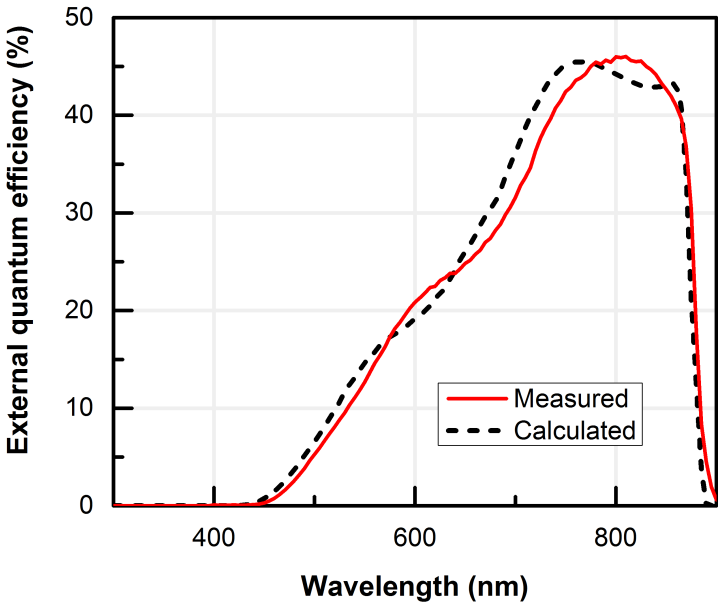

Figure 2.19: The simulated and measured single junction GaAs EQE, sample Sj-ref from the Université de Sherbrooke.

The similarity between the two EQEs is very strong, with most of the main features reproduced between the two. The difference between the two curves is calculated using the mean squared error (MSE), given by

$$\mathrm{MSE} = \frac{1}{N_{tot}} \sum_{i=1}^{N_{tot}} \left| y_{meas} - y_{calc} \right|^2 , \tag{2.52}$$

where N_{tot} is the total number of points in the measurement, y_{meas} and y_{calc} are the measured and calculated values. Using those initial values for the calculation of the single junction EQE, we obtain a MSE of 3.25.

The longer wavelength edges of each EQE, around 880 nm, are both present. The slow rising of the EQE, starting at 450 nm, is similar for both EQE, and is due to the non-used absorption in the cap and fsf. The shoulder in both EQEs, placed at $\sim$ 600 nm, is due to interference effects in the reflectivity. The said shoulder is placed at different

position for the two curves, and is due to a non-negligible uncertainty in the thicknesses of the cap and fsf layers.

As mentioned before, there are multiple variables that we can control to simulate the EQE of this single junction solar cell. Changing these quantities will help obtain a better fit and lower the MSE. The first quantity that we will study is the SRV of the front and the back of the solar cell. Figure 2.20a shows the evolution of the single junction GaAs EQE when the front SRV is varied between 10^3 and 10^8 cm/s. The subset of the figure shows the evolution of the J_{sc} over SRV for an AM1.5G illumination using Equation 2.6. It demonstrates the continuous decrease of the EQE for increasing front SRV, although at higher values, 10^7 cm/s and more, the EQE stabilizes. It demonstrates as well that the change of EQE for SRV lower than 10^4 cm/s is negligible.

Comparatively, the second part of Figure 2.20a shows the evolution of the single junction GaAs EQE when the back SRV is varied between 10^2 and 10^7 cm/s. Similar to the front SRV, the EQE decreases for higher SRV values. It stabilizes for values of 10^7 cm/s and more or 10^4 cm/s and less. Interestingly, the effect of the back SRV on the J_{sc} is much less pronounced. This demonstrates the importance of having a good growth of the front surface field, while the back surface field is less important.

Since the structure and the doping of the solar cell is given, it is not possible to vary them in our equations. However, the available values of the SRV create a calculated EQE that does not fit to the measured EQE to a satisfactory value. In the structure, the highest uncertainty lies in the thickness of the cap layer. It can vary by more than 10 % depending on the structure. Figure 2.20b demonstrates the effect of the variation of the thickness of the cap layer on the single junction cell EQE. This layer has multiple effects on the EQE. It absorbs a non-negligible amount of light, especially in the smaller wavelength region. Furthermore, since it is the first layer on the top of the structure, it has a strong effect on the reflectivity. Normally, the cap layer is etched away apart from under the contacts to remove its parasitic absorption.

Having this additional quantity to vary, it is possible to fit the EQE of the measured cell. To fit the EQE and obtain the optimal parameters, the MSE is minimized. Calculating a three dimensional matrix of EQEs, the minimal value of the MSE is found. The MSE of the initial guess was 3.25, using a front SRV of 10^5 cm/s, a back SRV of 10^5 cm/s and a cap layer thickness of 200 nm. It was brought down to a minimum of 2.0 using a front SRV of $3 \cdot 10^4$ cm/s, a back SRV of $2 \cdot 10^6$ cm/s and a cap layer thickness of 220 nm. Figure 2.20c shows the optimized calculated EQE along with the measured EQE. Those values will now be considered standard for the single junction GaAs structure.

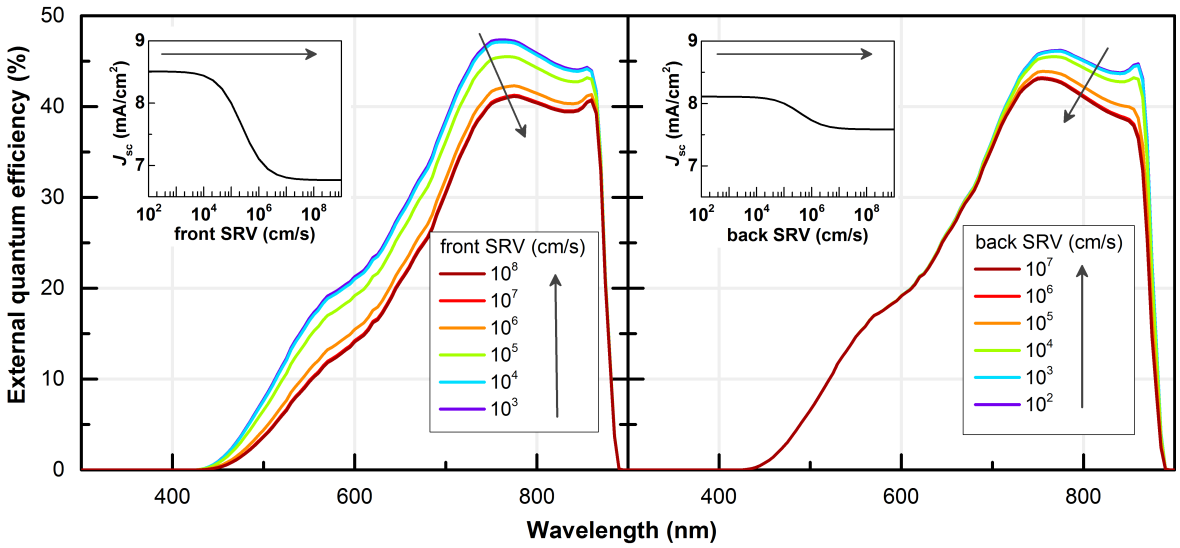

(a) The simulated GaAs EQE for different front and back SRV. The insets show the short circuit current of the device under 1 sun illumination of AM1.5G as a function of SRV. The EQE was calculated using the structure in Figure 2.18.

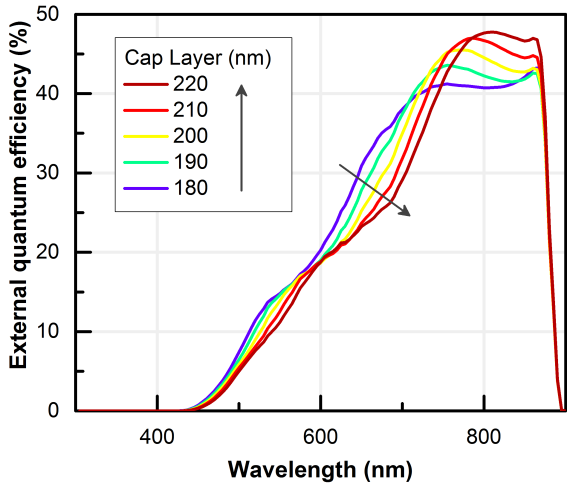

(b) The simulated GaAs EQE for different thicknesses of the cap layer.

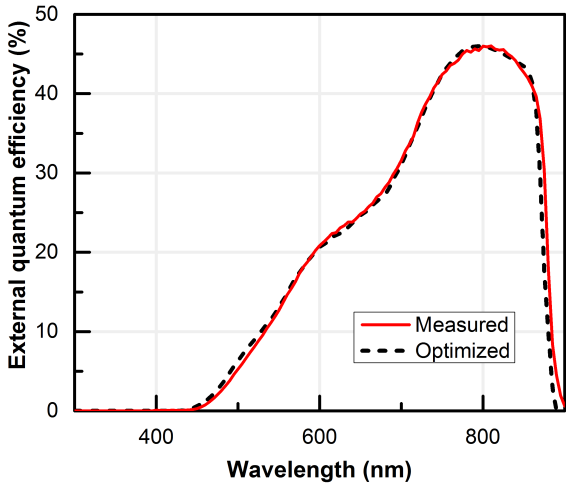

(c) The optimized and measured single junction GaAs EQE.

Figure 2.20: Variation of the available parameters in the EQE calculation to optimize the fit with the measured EQE of the SJ-ref GaAs solar cell.

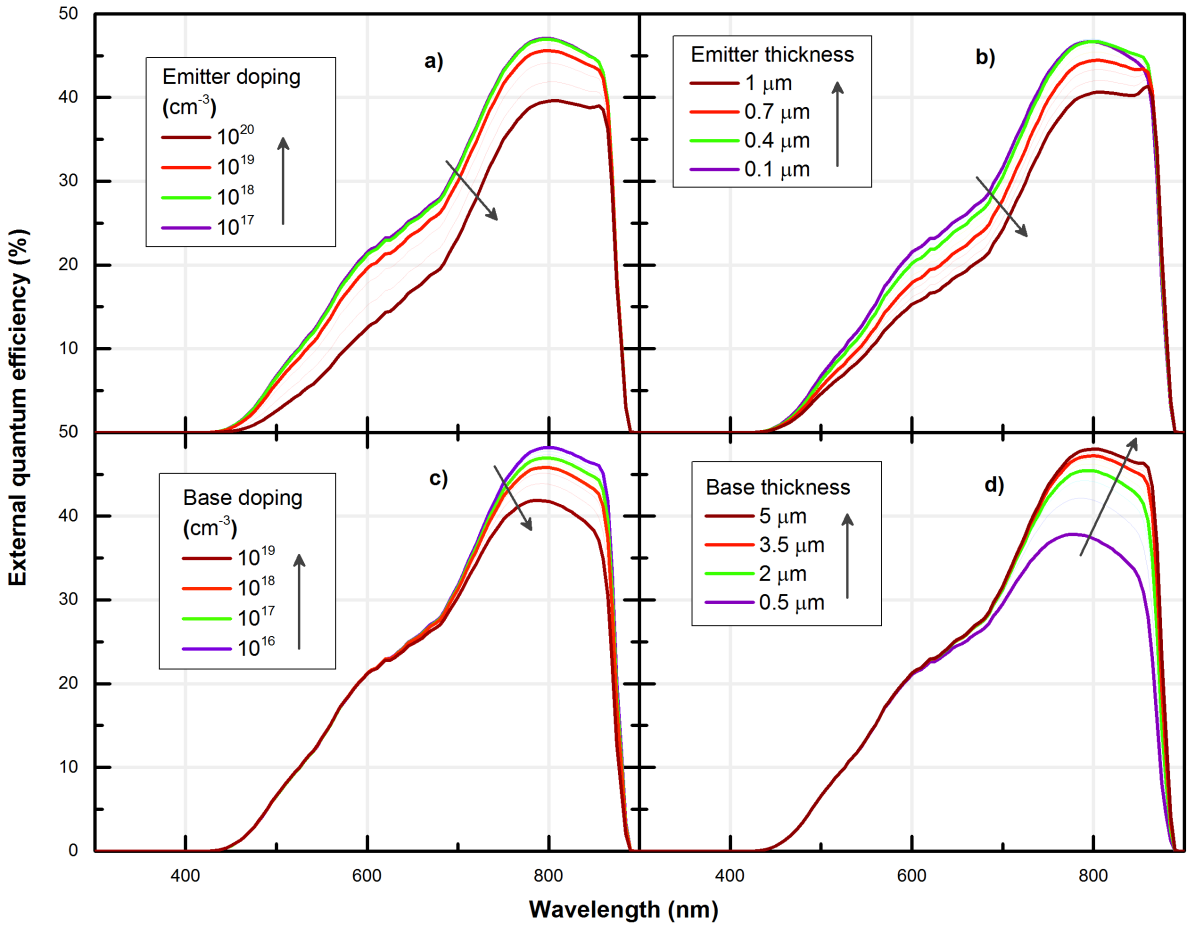

Figure 2.21: Variation of the layer properties in a single junction GaAs solar cell EQE. The parameters are varied from a) 10^{17} to 10^{20} cm^{-3} for the emitter doping, b) 0.1 to 1 µm for the emitter thickness c) 10^{16} to 10^{19} cm^{-3} for the base doping and d) 0.5 to 15 µm for the base thickness. The arrows show increasing doping or increasing thickness.

Now that an EQE that matches the experimental results has been obtained, the available variable parameters are studied to optimize the current production of the solar cell. The four parameters that are accessible are the thicknesses and doping of the emitter and the base. Even though the addition of an anti-reflection coating and the removal of the cap layer are two other key points to improve the solar cell performance, it shall be studied further in the Chapter 3 of this thesis. Figure 2.21 demonstrates the variation of the EQE for various values of the thickness and doping of the solar cell layers.

Figure 2.21a shows the variation of the EQE for emitter doping increasing from 10^{17} to 10^{20} cm^{-3}. It is important to note that for doping of 10^{19} cm^{-3} and higher, Fermi-Dirac statistic becomes important and the Boltzmann approximation used in the EQE Equations 2.35, 2.36 and 2.37 is not accurate anymore [68]. However, these values are kept nonetheless to demonstrate the trend in the EQE changes. For doping values between 10^{17} to 10^{18} cm^{-3}, the EQE does not change significantly. As soon as doping of 10^{19} cm^{-3} and higher are reached, the EQE decrease significantly throughout the whole wavelength range. This is because the recombination lifetime in the emitter becomes fast enough to significantly increase the recombination rate of the carriers. It is also due to smaller mobilities of carriers in the heavily doped region of the emitter. This means that the diffusion length itself is too short for carriers to reach the depletion region. This can be seen in Figure 2.12, where the GaAs lifetimes are dropping to lower values in the higher doping region as well in Figure 2.14, where the GaAs electron mobilites are lower at higher doping values. Hence, to get the highest EQE, one would want to use the lowest emitter doping possible, to ensure long recombination lifetime and high values of mobilities.

Figure 2.21b shows the variation of the EQE for emitter thicknesses increasing from 0.1 to 1 μm. The emitter had a fixed doping of 10^{18} cm^{-3}. The trend in the EQE is similar to the one in figure 2.21a, where the doping was varied. The EQE decreases for increasing emitter thickness. This is due to the small recombination lifetime (4.1 ns) and mobility (174 cm^2/Vs) of electrons in the highly doped emitter. The longer the emitter is, the longer the carriers have to diffuse before being separated at the space-charge region. Hence, the carriers have a higher chance of recombining before reaching the region where most of the electric field is present. For design purpose, the emitter has to be the smallest possible. In this case, the used thickness of 0.2 μm can be considered optimal since it is similar to the highest EQE of this graph.

Similarly to Figure 2.21a, Figure 2.21c shows the variation of the EQE for base doping increasing from 10^{16} to 10^{19} cm^{-3}. Again, as the doping increases, the EQE is reduced,

due to the lowering recombination lifetime and carrier mobility. The drop in EQE is located especially in the longer wavelength region, because the 400 to 700 nm region is dominated by the emitter characteristics. Again, the doping value of 10^{17} cm^{-3} is one of the highest EQE possible, showing that the experimental design uses near-optimal values.

Similarly to Figure 2.21b, Figure 2.21d shows the variation of the EQE for base thicknesses increasing from 0.5 to 5 μm. Contrarily to the emitter graph, the EQE now increases for increasing thickness of the base. This is because the light is incompletely absorbed by the GaAs cell structure. Since it is assumed that all the light absorbed in the substrate is not contributing to the photocurrent, the 0.5 μm base thick design absorbs only 70 % of 850 nm light. Hence, to get a good EQE, one must ensure that the base is thick enough to absorb the incoming light. The used base thickness, of 3.2 μm, is of the highest EQE possible, showing that the experimental design uses near-optimal values.

One can conclude from this study that to obtain the highest EQE possible, the front and back SRV's needs to be lowered. This is commonly done either by growing a doped layer of higher bandgap in the front and in the back. For simpler designs, especially in single junction solar cell, a layer of highly doped material is grown instead. The other parameters that were tested are the layer doping and thicknesses.

2.4.5 The multijunction external quantum efficiency

Using the model to calculate the EQE, it is now possible to extend it to the calculation of a MJSC's EQE. The necessary parameters includes the lifetimes, mobilities and optical constants for the three main semiconductors in the structure that have been defined in Section 2.4.3.

Because the solar cells are grown on top of each other, each of the semiconductor layers will affect the light propagation through the cell. The reflectivity will be calculated using the TMM method, with all the layers taken into account. It is important to note that in the TMM method, the wavelength dependence of the refractive index is taken into account. This is featured in Figure 2.22, where the refractive index is shown as a function of wavelength and as a function of depth inside the MJSC. The various semiconductor and thicknesses of each layers used in the EQE calculation are shown in Table 2.7. The structure is a standard MJSC design, used extensively in the SUNLAB for numerical simulation [40]. The important variation of the refractive index, highlighted by the

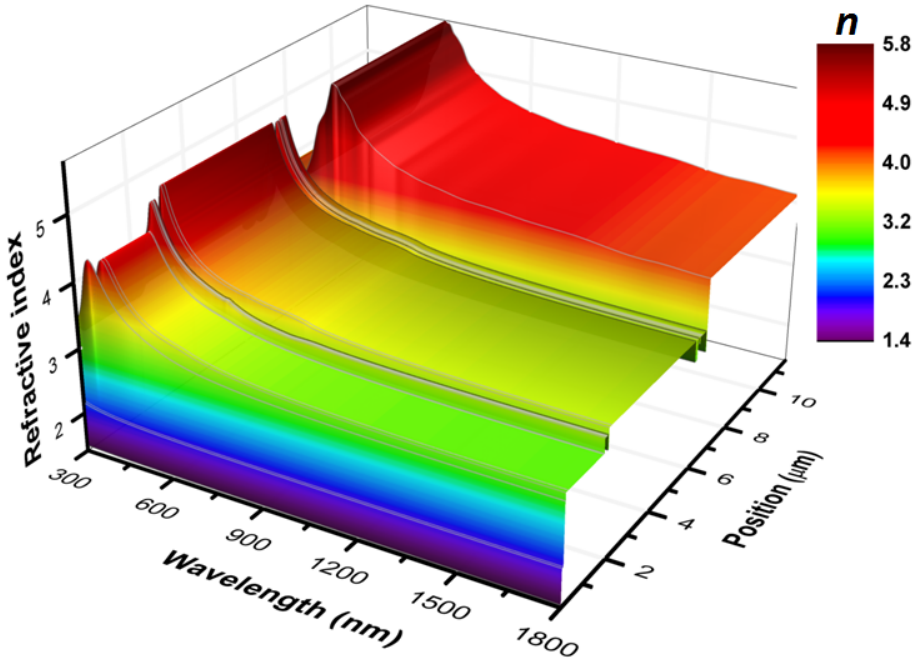

Figure 2.22: Refractive index of the material as a function of wavelength and position inside the solar cell. The top subcell starts at 0.14 μm, the middle at 1.9 μm and the bottom at 6.3 μm. The materials and their thicknesses are taken from Table 2.7.

differences in the short wavelength region compared to the long wavelength region, is essential in the accuracy of the model.

The absorption inside each layer before the active subcells has to be calculated. Similarly to the previous section, the light absorbed before the electrically active regions (emitter and base) will not contribute to the subcell in question. The light hitting each subcell will be reduced by the absorption from the cells above it. This is highlighted in Figure 2.23, where the extinction coefficient as a function of wavelength and as a function of depth inside the MJSC is shown. For example, to calculate the middle subcell's EQE, the incoming light will be reduced by the absorption from the top subcell and the top tunnel junction. Hence, in the calculation, the EQE of the middle and bottom subcell is multiplied by the transmitted portion of the upper layers. In the TMM method, it is given by t_{ab}, in Equation 2.51. Each layer is taken into account using this method.

The calculated triple junction solar cell EQE is shown in Figure 2.24. The various semiconductor and thicknesses of each layers used in the EQE calculation are shown in Table 2.7. The dopings used in the calculation of the lifetimes and mobilities are shown

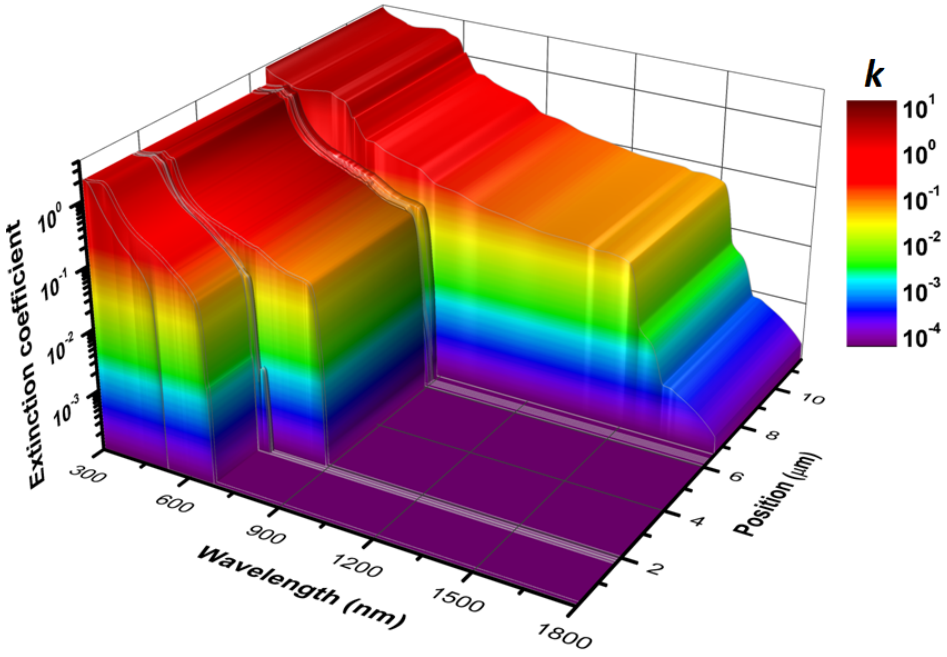

Figure 2.23: Extinction coefficient of the material as a function of wavelength and position inside the solar cell. The top subcell starts at 0.14 μm, the middle at 1.9 μm and the bottom at 6.3 μm. The materials and their thicknesses are taken from Table 2.7.

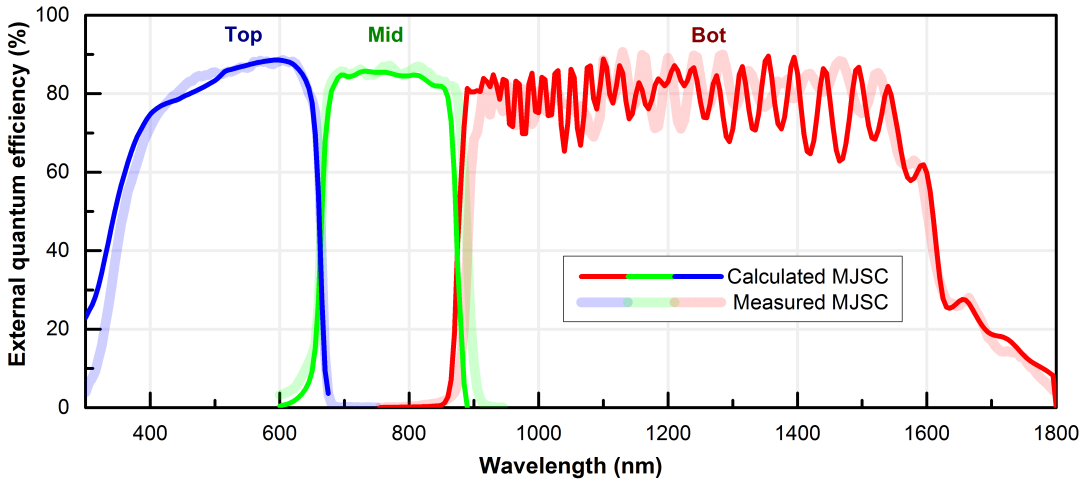

Figure 2.24: Calculated multijunction solar cell external quantum efficiency compared to an experimentally measured multijunction lattice matched solar cell (MJSC-S).

for each subcell. The front and back SRV's of the top, middle and bottom subcell are 10^2 and 10^2 cm/s, $5 \cdot 10^5$ and 10^5 cm/s, 10^7 and 10^5 cm/s respectively. These values have been chosen to minimize the error between the two curves. An additional 5 % of shading coming from the contact shading has been added. The experimentally measured EQE of sample MJSC-S, a standard lattice matched MJSC, is shown in Figure 2.24 as the lighter curves. The fit between the calculated and experimental curves is surprisingly accurate, especially since the complete structure of the experimental sample is unknown, as this information is under protection of intellectual property. The MSE between the two curves, of 3.2, is very low for a measurement of the full EQE.

This model is a first step to completely understand the EQE of a lattice matched MJSC. It clearly demonstrates the distribution of the EQE throughout the three subcells. It demonstrates as well the importance of the quality of the electrically active region of each subcell, the emitter and the base, since these directly contribute to the calculated EQE.

2.5 Conclusion

Now that a model has been developed to explain the EQE of a MJSC, it is possible to extend this study to the more complex behavior of the EQE. The oscillations in the bottom subcell's EQE, as can be seen in Figure 2.24, are explained by the reflectivity calculated with the TMM method. The behavior of the top subcell's responsivity in the blue-UV region (300-400 nm) is described as well by the reflectivity. These topics shall be studied further in the next chapter.

In this calculated EQE, two important features are not yet present; the bottom subcell artifact and the QD absorption peak. Comparing the simulation in Figure 2.24 and the measured QD-enhanced EQE in Figure 1.7, these differences become apparent. The bottom subcell artifact should be seen as a non-zero value in the bottom subcell's EQE in the middle subcell wavelength range (600-900 nm), while the QD absorption peak should be seen as an EQE peak below the middle subcell band-edge, in the 920 nm region. The developed model is not yet complete enough to incorporate those quantities. This is why in Figure 2.24, the calculated EQE was compared to a standard MJSC, with no QD and with the bottom subcell artifact removed using a correction factor. Experimental measurements and a further development of the model will be demonstrated for both features in Chapters 4 and 5. But before that, as much information as possible from the simple reflectivity measurement shall be gathered.

Subcell	Layer	Material	Thickness (nm)	Doping (cm^{-3})
ARC	-	SiO_2	79	-
	-	Si_3N_4	59	-
Top	fsf	AlInP	10	-
	emitter	InGaP	100	$3 \cdot 10^{18}$
	base	InGaP	1500	$5 \cdot 10^{17}$
	bsf	InGaP	30	-
Tunnel diode	buffer	AlGaAs	50	-
	p++	AlGaAs	20	-
	n++	AlGaAs	20	-
	buffer	AlGaAs	50	-
Middle	fsf	InGaP	20	-
	emitter	GaAs	100	$5 \cdot 10^{18}$
	base	GaAs	4000	$5 \cdot 10^{17}$
	bsf	InGaP	100	-
Tunnel diode	buffer	GaAs	50	-
	p++	AlGaAs	50	-
	n++	GaAs	50	-
	buffer	GaAs	50	-
Bottom	buffer	GaAs	200	-
	fsf	InGaP	20	-
	emitter	Ge	100	10^{19}
	base	Ge	170 µm	$2 \cdot 10^{17}$

Table 2.7: Standard multijunction solar cell design used in the calculation of the external quantum efficiency, modified from [40].

Chapter 3

Reflectivity

3.1 Motivation

The reflectivity is a common measurement done in conjunction with the EQE. One of the most important contributions of this measurement is to demonstrate the importance of the addition of anti-reflection coatings (ARCs) on solar cells. Furthermore, by substracting the reflectivity values from the EQE, the internal quantum efficiency (IQE) is obtained. This quantity gives the conversion from photons to collected carrier efficiency for photons that are actually absorbed in the solar cell. The IQE gives direct insight into the quality of the semiconductor layers, as well as the quality of the junctions. Doing this kind of analysis directly from the EQE can sometimes be cumbersome, especially in the UV region where the reflection at the surface typically hides important features such as the front surface field recombination rate. This is why the reflectivity is measured: to allow a more in-depth analysis of the EQE.

In this chapter, the analysis of the reflectivity of the solar cell is explored. First the effect of each component in the multi-junction solar cell on the reflectivity is studied. This is done using the transfer matrix method introduced in the previous chapter. Important features can be extracted from the reflectivity, and further help the design of these solar cells. In the second part of this chapter, a method derived from the thin film technology to obtain the thicknesses in the solar cell is proposed. The method is first studied using the calculated TMM reflectivity, and then applied to various experimentally measured reflectivities of solar cells.

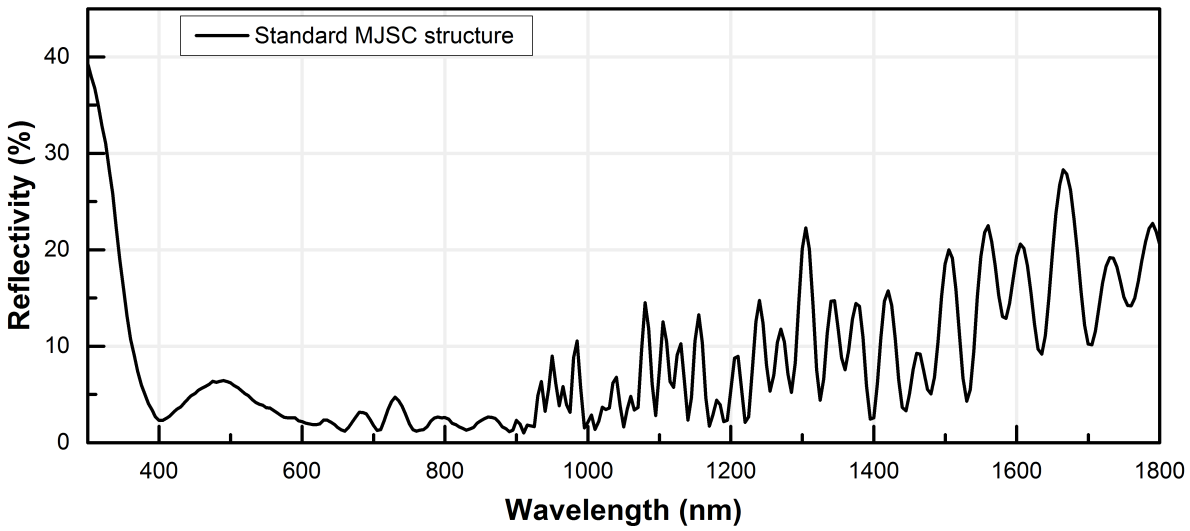

Figure 3.1: Measured reflectivity of sample MJSC-S over wavelength.

3.2 Multijunction solar cell reflectivity

3.2.1 Experimental measurement

As shown in Section 2.3, the experimental measurement of the reflectivity of a solar cell is done using the IQE200. Figure 3.1 shows a measurement of the reflectivity of a MJSC from 300 to 1800 nm, at 5 nm steps. This reflectivity is measured on sample MJSC-S. The goal of this current section is to demonstrate that the model developed in Section 2.4 is capable of reproducing the important features seen in the reflectivity. With the model in hand, the effect of each component of the solar cell on the reflectivity can now be explained.

3.2.2 Calculated reflectivities

The calculation of the reflectivity is done using the TMM method. This method was introduced extensively in Section 2.4.3. The importance of using the complete TMM method, along with the complex refractive index of each material has been highlighted in Figure 2.16. Using the standard MJSC structure introduced in Table 2.7, the calculated reflectivity is shown in Figure 3.2. The curve is divided in 3 colors, each corresponding to its subcell of interest. Since this reflectivity curve corresponds to the standard structure, it should qualitatively correspond to the experimentally measured curve in Figure 3.1. All further MJSC reflectivities are going to be compared to this standard structure.

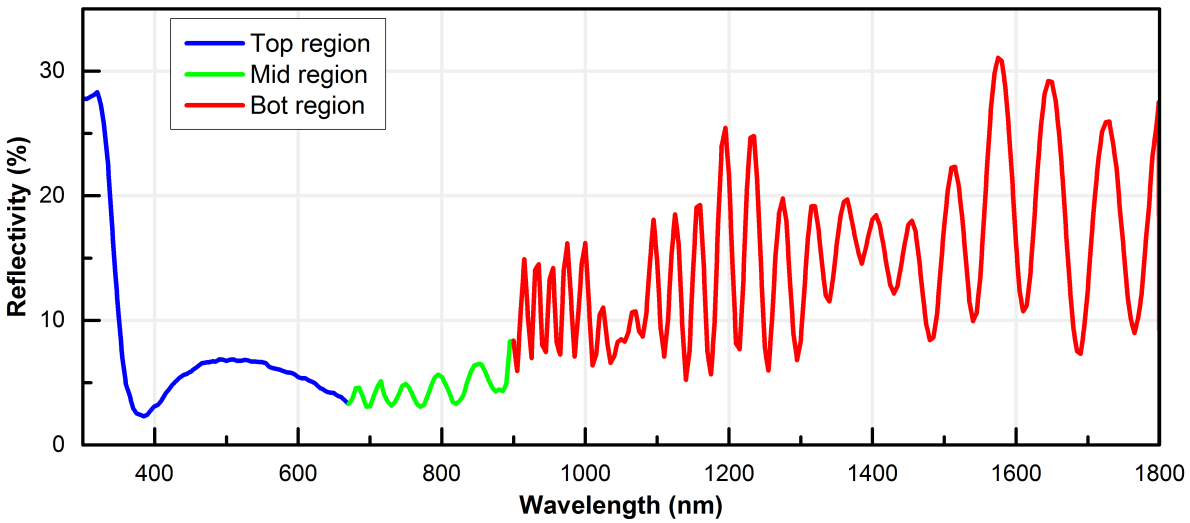

Figure 3.2: Calculated reflectivity of the MJSC structure over wavelength. The colors, blue, green and red, are placed to correspond to the subcell of interest.

Impact of the antireflection coating

The reflectivity of the solar cell is dependent on each layer. The first few layers of material will, however, have a major impact on the overall reflectivity of the structure. By looking at the MJSC's EQE in Figure 2.24, one might wonder why the EQE values of each subcell lies considerably higher than the GaAs single junction EQE, shown in Figure 2.20c. This is a result of the addition of an ARC on the MJSC. The GaAs solar cell, having no coatings on its surface, has a significant reflection of light over the wavelength range of 400 to 900 nm, where it would absorb sunlight. The reason why this reflection is so high is because the first layer of material the light encounters is a semiconductor. The photons have to pass from a medium of refractive index of 1 to one of over 3.4 at a wavelength of 800 nm. This leads to a reflectivity of over 54 % at this particular wavelength. By adding a lower refractive index material on top of the semiconductor, the reflection at the surface is significantly decreased. The antireflection coating, by careful design, lowers the reflection of light over the whole spectrum and increases the absorbed portion of the light by the solar cell.

Figure 3.3 demonstrates the difference between the reflectivity of the standard MJSC with and without an ARC. Let's first have a look at the reflectivity in the top subcell's wavelength region (300 to 670 nm). In the standard structure, the light first enters the cell by going through the ARC, a 79 nm layer of SiO_2 and a 59 nm layer of Si_3N_4, and then goes through the fsf made of 10 nm of AlGaAs and finally gets absorbed by the

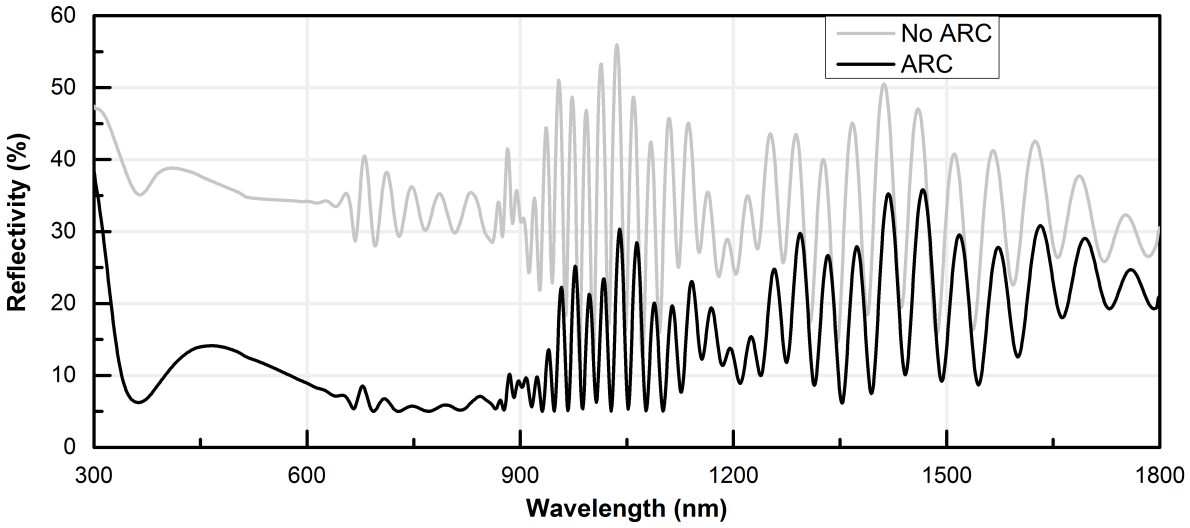

Figure 3.3: Calculated reflectivity of the MJSC with and without the ARC.

electrically active InGaP. The light that is not absorbed by the InGaP active layers then continues in the structure, either being reflected or absorbed in the subsequent layers. In the structure without an ARC, the light enters the cell by going through the fsf made of 10 nm of AlGaAs and then gets absorbed by the electrically active InGaP. The differences in the reflectivity are notable.

The double layered ARC was designed to decrease reflectivity over the complete wavelength range. This figure demonstrates that the ARC has a significant importance in the solar cell reflectivity. The overall shape of the reflectivity is determined by the ARC. Hence, in the complete range of wavelength, from 300 to 1800 nm, the MJSC's reflectivity is dependent on the ARC composition. For this reason, it is of upmost importance to optimize the ARC of a solar cell.

Figure 3.4 demonstrates the effect of changing the material of the fsf on the reflectivity of the MJSC. The material of the fsf was changed from AlInP to Ge. Even though this change is not feasible for growth, it was done in the calculation to demonstrate the effect of the fsf on the reflectivity. This modification of the structure significantly changes the refractive index of the material that the light encounters when it enters the structure. Changing this 10 nm layer has an effect on the wavelength range of 600 to 1800 nm. The reflectivity increases by a few percent over the full range. However, it has an important effect on the top subcell's behavior. The curvature and amplitude have changed. Those changes in the reflectivity can be explained by the significant difference of their refractive indexes, as can be seen in Figure 2.17. Hence, the reflectivity of the full structure will be

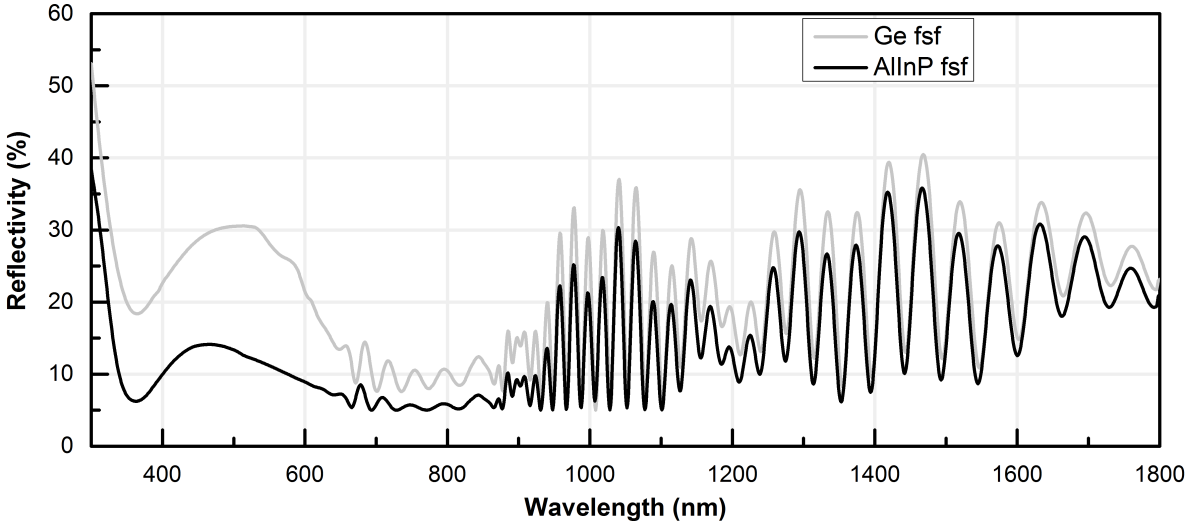

Figure 3.4: Calculated reflectivity of the MJSC with a top subcell fsf made of AlInP or Ge.

dependent not only on the ARC design, but on the composition of the first semiconductor layer as well.

Impact of optical cavities inside the solar cell

As discussed in Section 2.4.3 and shown in Figure 2.16, the complex structure of a MJSC is capable of creating optical cavities. These cavities create significant interference effects that can be seen in the solar cell's reflectivity. Figure 3.5 shows the refractive index at 1200 nm throughout the standard MJSC. The refractive index changes from 3.7 in the top subcell to 3.9 in the middle subcell and to 5.7 in the bottom subcell. The smaller changes near the interfaces of each subcell come from either the fsf, the back surface field (bsf) or the tunnel junctions. At each interface, the light is either reflected or transmitted. The larger the difference in refractive index, the larger the quantity that will be reflected. This way, each subcell can act as an optical cavity, creating either destructive or constructive interferences at different wavelengths.

A good way of viewing the problem is by going back and having a look at the reflectivity of a two layer system. A 100 nm layer of SiO_2 material deposited on top of a non-absorbing InGaP semi-infinite wafer was considered in Chapter 2. Equation 2.45,

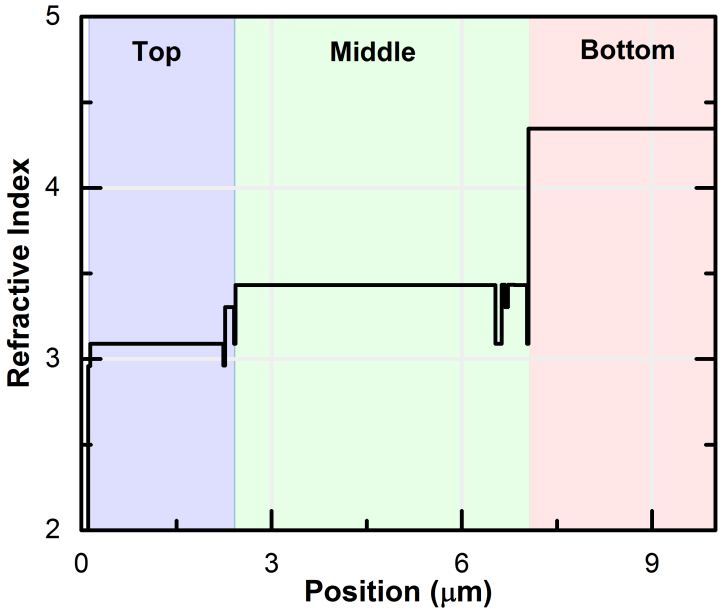

Figure 3.5: Refractive index of the material as a function of depth inside the MJSC, at 1200 nm. The colors, blue, green and red, are placed to correspond to the subcell of interest.

written as

$$R = \frac{(n_0 - n_2)^2 + \left(\frac{n_0 n_2}{n_1} - n_1\right)^2 \tan^2 \delta_1}{(n_0 + n_2)^2 + \left(\frac{n_0 n_2}{n_1} + n_1\right)^2 \tan^2 \delta_1},$$

approximated the reflectivity of the layered structure. Assuming that the refractive indices are wavelength independant, the reflectivity will vary over the optical path, $\delta = \frac{2\pi}{\lambda} d n_1$. In this scenario, the reflectivity will be maximal at $\delta = m\pi$ and minimal at $\delta = \frac{\pi}{2} + m\pi$, where m is an integer. The maximum and minimum reflectivity are given by

$$R_{max} = \frac{(n_0 - n_2)^2}{(n_0 + n_2)^2}, \qquad R_{min} = \frac{\left(\frac{n_0 n_2}{n_1} - n_1\right)^2}{\left(\frac{n_0 n_2}{n_1} + n_1\right)^2}. \tag{3.1}$$

The amplitude of the oscillations will be dependant on the proportion between the refractive indexes of the layers creating the optical cavity.

Assuming that the index of refraction is constant, the difference between two maxima (m and $m+1$) are going to be approximately given by

$$\delta_1 - \delta_2 = m\pi - (m+1)\pi = \frac{2\pi n d}{\lambda_1} - \frac{2\pi n d}{\lambda_2}. \tag{3.2}$$

This simplifies to

$$-\frac{1}{2nd} = \frac{1}{\lambda_1} - \frac{1}{\lambda_2}. \tag{3.3}$$

For large wavelength and small difference between λ_1 and λ_2, the approximate formula for the period of the oscillations is given by

$$\Delta\lambda = \frac{\lambda^2}{2nd}, \tag{3.4}$$

where n is the index of refraction of the studied material at wavelength λ. This period will be inversely proportional to the index of refraction of the optical cavity and to its thickness. For a thicker cavity, the oscillation will have a smaller period, and vice-versa for the thinner cavity. It is important to note that these equations are derived only as a proof of concept. They are an approximations to the more complete calculations of the TMM method. Because the index of refraction varies over wavelength, the period of the oscillation shall then change over wavelength as well. The period of the oscillations calculated here is used only as a means to approximate an expected result.

Figure 3.6 demonstrates the implication of varying the first optical cavity, the top subcell, on the reflectivity of the MJSC. In the standard structure, the top subcell has a total thickness of 1.63 μm of InGaP, while the second structure has a total thickness of InGaP that was changed to 0.63 μm. The top subcell's region of the reflectivity, from 300 to 600 nm, remains unchanged. Afterwards, the oscillations present in the middle subcell's region, from 600 to 900 nm, are affected. The period of the variation increases in the cell that has a smaller InGaP thickness. According to Equation 3.4, using the refractive index of InGaP at 700 nm, $n = 3.33$, the oscillations of the reflectivity at 700 nm should have a period of approximately $\Delta\lambda = 45$ nm for the standard cell. Similarly, in the second structure the reflectivity should have a period of approximatively $\Delta\lambda = 117$ nm. These changes are quantitatively seen in the figure. The distance between the two maxima around 700 nm for the standard MJSC is 31 nm and is 105 nm for the 0.63 μm top subcell.

The period of the oscillations in the bottom subcell's region, from 900 to 1800 nm, changes as well. In this structure, as seen in Table 2.7, the InGaP's thickness is 1.63 μm while the GaAs thickness is 4.1 μm. Since the GaAs thickness is larger, one would then expect the oscillations present in the bottom subcell to be due to interference created inside the middle subcell. If this is true, the frequency of the oscillations present in the bottom subcell's region should not change when the top subcell's thickness is altered. The refractive index of InGaP at 1400 nm is 3.06 while it is 3.39 for GaAs. Using the

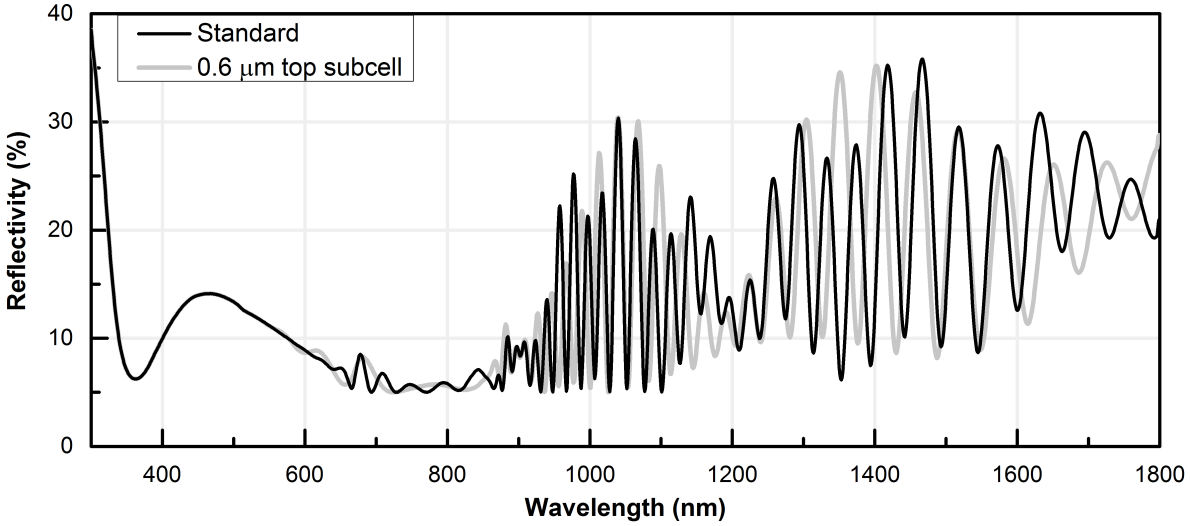

Figure 3.6: Calculated reflectivity of the MJSC with a different top subcell thickness. The standard MJSC structure has a total InGaP thickness of 1.63 μm, while the modified structure has a total InGaP thickness of 0.63 μm.

approximated method to calculate the oscillations period in the reflectivity, a period of $\Delta\lambda = 71$ nm at 1400 nm for the oscillations created by the 4.1 μm middle subcell is obtained. From Figure 3.6, this does not correspond to the oscillations observed. The approximate period of the oscillations at 1400 nm is 44 nm for the standard MJSC and 51 nm for the 0.63 μm top subcell. If the oscillations can be created by the optical cavity created by both the InGaP and the GaAs layers together, a period of $\Delta\lambda = 52$ nm and $\Delta\lambda = 62$ nm at 1400 nm are obtained for the two aforementionned MJSC designs. This corresponds more accurately to the observed trend in the figure.

The oscillations present in the bottom subcell are of multiple origins. The higher frequency oscillations are created by the large optical cavity composed by the top and middle subcell. The envelope is then a multiplication of the oscillations created by the middle subcell alone and the top subcell alone and other possible structures in the cell such as front or back surface fields. As demonstrated earlier in Figure 2.16, the base variation is governed mainly by the ARC. This means that the bottom subcell's reflectivity is an amalgam of the multiple effects of the upper layers in the system.

3.3 Thickness calculation

As seen in the previous section, the thickness of each layer has an significant role in the behavior of the reflectivity over wavelength. For example, Figure 3.6 demonstrated that a change in the thickness of one cell has important effects on the reflectivity of the structure. If predicting the change in reflectivity created by a change in thickness is possible, then analysing the data the other way around should be possible. Using the reflectivity and its oscillations over wavelength should give us interesting insight into the thickness of each layer. In this section, a methodology to extract the various thicknesses in the solar cell structure by using solely the reflectivity measurement will be developed. It will be done non-destructively in the same run as an EQE measurement and will be used to obtain the thicknesses of various layers inside the structure. In the laboratory, the method is referred as 'the etalon effect measurement'.

3.3.1 Thickness measurement in the literature

Measuring precisely the thickness of semiconductor layers can be done using multiple methods. First, during the growth in a molecular beam epitaxy (MBE) reactor, the thickness is commonly measured using the reflection high energy electron diffraction (RHEED) technique. This technique uses grazing angle X-ray radiation to measure the growth of the semiconductors layer-by-layer. However, even though this technique can be very precise, it has to be done during growth [69].

Another common method used to measure the thickness of semiconductors is transmission electron microscopy (TEM). If the instrument is calibrated precisely, the resulting image can yield the thicknesses in the structure. However, this technique is not a feasible measurement to do on MJSC. It is destructive and the sample preparation is complex. Hence, even though TEM measurements can be a very powerful tool to obtain the thickness values in the structure, it is not possible to do it on multiple samples that will be installed in the field.

Optical techniques are often more easily applied. One prominent example is the ellipsometer. It uses polarized light reflected at various angles on the surface of a material. In the said technique, a thin film of the material is usually deposited, and the index of refraction and the extinction coefficient are measured [70]. It is furthermore possible to extract the thickness of the thin film [71]. However, ellipsometry is limited to the surface of a material. It either measures only the top material or only a thin film deposited on top of a substrate.

Another technique, that will be similar to the one introduced in the current thesis, is the use of infrared spectroscopy to infer the thicknesses of semiconductor layers. Pioneered in 1989, it used infrared radiation (from 5 to 20 μm) reflectivity at oblique incidence on Si oxide layers [72]. They fitted a calculated reflectivity on the measured one, putting emphasis on the oscillations present in the spectra.

Then, improving on the technique in 1993, the thicknesses of a 4 layer system was calculated by using the reflectivity measured at normal incidence in the near-infrared region (800 to 1100 nm) [73]. They used a simplified version of the TMM framework, and then fitted the experimental reflectivity by varying the thicknesses of each semiconductor layer in the model. This shows that the model created in the current thesis could be capable of obtaining the thicknesses in the simple case of a 4 layer semiconductor. However, because the MJSC used in this thesis possesses more than 10 layers, each of unknown thicknesses, this technique will not be suitable. There would be too many fitting variables.

Building on this methodology, it is possible to use a Fourier transform to obtain the thickness of the layers. In an American 1998 patent [74], the Filmetrics company describes the use of reflectivity and Fourier transforms to infer the thickness of SiO_2 films deposited on an Si substrate. They first measure the normal angle reflectivity from 300 to 900 nm. Then, they manipulate the data, transforming it using the known refractive index of the SiO_2 material, giving $Z = \frac{n}{\lambda}$. Finally, by applying a numerical Fourier transform on the Z data array, they are capable of deducing the thickness of the wanted film. This technique has multiple applications, especially in the lithography industry.

Even though this technique has been applied solely to thin films on Si in the patent, it is possible to extend it. The mathematical framework to use it shall be developed. Then, it will be applied to measurements of a simple solar cell structure, and afterward extended to the complex MJSC structure.

3.3.2 Etalon effect measurement

The etalon effect measurement uses the reflectivity measurement obtained from an EQE run, applies a Fourier transform in the oscillating region and obtains the thicknesses of various layers in the structure.

The reflectivity of a structure can be calculated by the TMM method, as seen in Section 2.4.3. An important part to notice is that the said reflectivity is dependent on

the optical path that the light travels inside each layer, namely

$$\delta = \frac{2\pi n d}{\lambda}. \tag{3.5}$$

This optical path parameter enters in the equations governing the TMM method as an oscillating exponential. As the frequency of the light (or $\frac{c}{\lambda}$) is continuously varied, the reflectivity will oscillate between maxima and minima. This was highlighted in the previous section.

Taking the simplified equation for the reflectivity, given in Equation 2.45, and expanding it using trigonometric functions, it gives

$$R = \frac{(n_0 - n_2)^2 \left(\cos(2\delta_1) + 1\right) + \left(\frac{n_0 n_2}{n_1} - n_1\right)^2 \left(1 - \cos(2\delta_1)\right)}{(n_0 + n_2)^2 \left(\cos(2\delta_1) + 1\right) + \left(\frac{n_0 n_2}{n_1} + n_1\right)^2 \left(1 - \cos(2\delta_1)\right)}. \tag{3.6}$$

The reflectivity will be periodic as a function of $2\delta_1$, and will not reach infinities when $\cos(2\delta_1) = 0$ or $\cos(2\delta_1) = 1$. It is possible to obtain the frequency at which it is oscillating by using a Fourier transform. Furthermore, in the $2\delta_1$ term, the thickness d of the layer creating the oscillation is present. Hence, in the Fourier transform, the integration shall not be done over the wavelength λ. Instead, the ordinate coordinate in the reflectivity is transformed from λ to $2\frac{n}{\lambda}$, which now corresponds to the time axis in a normal Fourier transform. Then, by integrating over $2\frac{n}{\lambda}$, the frequency at which the reflectivity is oscillating, d, is obtained. Figure 3.7a shows a reflectivity curve calculated using the TMM method, where a simple 2 µm GaAs layer on top of a Ge wafer was assumed. Figure 3.7b demonstrates the transformation of the ordinate from λ to $Z = 2\frac{n}{\lambda}$.

Fast Fourier transform

A Fourier transform is commonly used to change a signal that varies over time into all its frequency components. For example, it can obtain all of the sound frequencies of a voice. It can however be used for most types of data that vary over a certain variable x. For a certain continuous function $f(x)$, the Fourier transform is defined as

$$F(k) = \int_{-\infty}^{\infty} f(x) \mathrm{e}^{-2\pi i k x} dx, \tag{3.7}$$

and with the inverse transformation being

$$f(x) = \int_{-\infty}^{\infty} F(k) \mathrm{e}^{2\pi i k x} dk, \tag{3.8}$$

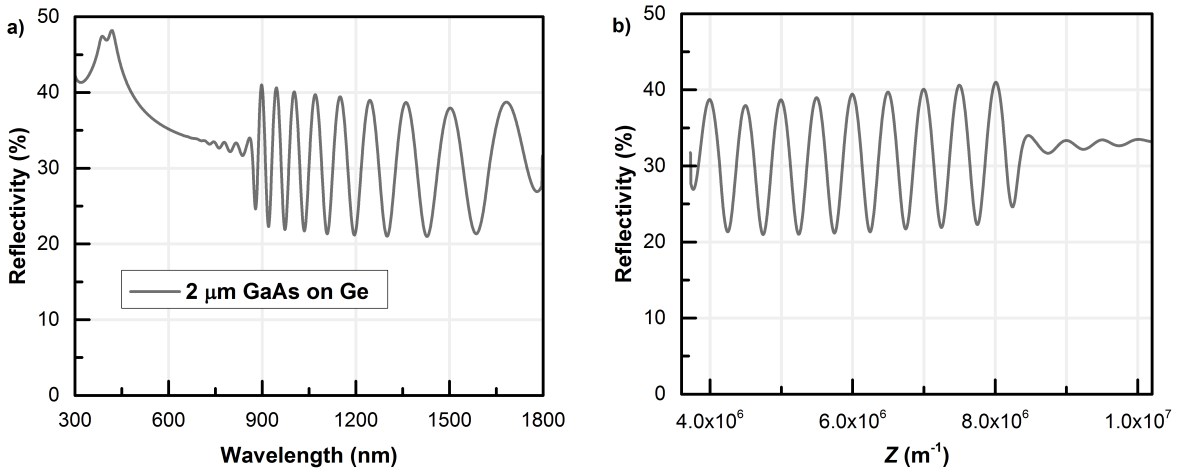

Figure 3.7: a) Reflectivity of a simple 2 μm GaAs layer on top of a Ge wafer. b) The reflectivity, in the new $Z = \frac{2n_{GaAs}}{\lambda}$ coordinate, is periodic and will be used in a Fourier transform to obtain the thickness of the semiconductor layer.

where k is the frequency and $F(k)$ is the function in frequency space. The amplitude of $F(k)$ over frequency k corresponds to the frequencies present in the original $f(x)$ signal.

For example, let's create a signal that varies over Z, given by $f(Z) = R_0 + R_1 \cos(2\pi dZ)$. The Fourier transform of this function gives

$$F(k) = R_1 \left(\delta(k-d) + \delta(k+d)\right) + R_0\delta(k). \tag{3.9}$$

The function $F(k)$ will give a peak centered around the thickness d. The curve will be mirrored in the negative region of k. The constant part of the reflectivity, R_0, will give a peak at a frequency of $k = 0$. Hence, using a Fourier transform in Z on the reflectivity data shall give us a figure in frequency space with peaks corresponding to the thickness contributing to the oscillations.

If, instead of having a continuous function, a discrete set of N points in x each spaced by Δx is given, the discrete Fourier transform is

$$F(k\Delta\nu) = \sum_{n=0}^{N-1} f(n\Delta x)\mathrm{e}^{-i2\pi kn/N}. \tag{3.10}$$

The continuous variables have been replaced, x by $n\Delta x$ and k by $k\Delta\nu$. The spacing in frequency space is now given by

$$\Delta\nu = \frac{1}{N\Delta x}. \tag{3.11}$$

The Fourier transform will give a sequence of the same length of complex numbers in frequency space. In this thesis, the Fourier transform shall always be taken as the absolute value $|F(k)|$. Note that the symmetry present in the continuous Fourier transform of a real function, given as $F(k) = F(-k)$, is different in the discrete case. It will now be given by $F(n\Delta\nu) = F((N-n)\Delta\nu)$. This translate to the absolute of the Fourier transform $|F(k)|$ being symmetric around the folding frequency $k_f = \frac{N\Delta\nu}{2}$ [75].

Even though this formula is adequate to calculate the discrete Fourier transform, it is not used anymore. The fast Fourier transform (FFT), pioneered by Cooley and Tukey in 1965, removes most of the redundancy in the discrete Fourier transform by using a complex method to reorganize the coefficients so that the computing time is optimal. It yields the same values of the discrete Fourier transform, but much more efficiently [75]. One important features of this algorithm is that the number of points, N, needs to be a power of two. If the FFT algorithm is directly applied to raw data, it will often yield results that are difficult to analyse. Important artifacts may arise while using this algorithm.

First, leakage is created because only a finite quantity of data is measured. The Fourier transform is not applied to an infinite number or points, but to a truncated part of an oscillating function. Hence, for the reflectivity seen in Figure 3.7, the FFT will be applied to data ranging from λ=900 to 1800 nm (Z = 3.7 to $8 \cdot 10^6$ m^{-1}) only. This is equivalent to multiplying a rectangular function to an infinitely oscillating function. A property of a Fourier transform, the convolution theorem, is given by

$$\int_{-\infty}^{\infty} f(x) \cdot g(x) \mathrm{e}^{-2\pi i k x} dx = F(k) \otimes G(k). \tag{3.12}$$

It states that the Fourier transform of a product of two functions, $f(x)$ and $g(x)$, is given by the convolution between each individual's function Fourier transform, $F(k)$ and $G(k)$. Hence, in the case of a pure cosine multiplied by a rectangular function, the Fourier transform is the convolution of a Dirac function δ and a sinc function. The rectangular function of width T is shown in Figure 3.8a while the resulting sinc function is shown in Figure 3.8b. Because a truncated portion of the reflectivity is taken, the calculated peaks are widened.

Furthermore, each central peak creates several side peaks, which are lobes. The amplitude of those lobes is non-negligible, being up to 22 % of the amplitude of the main peak. If two frequencies are close to each other, their lobes will distort each other's peaks and skew the data. To diminish the amplitudes of these lobes, an additional function to the data shall be applied. One function that is commonly used and shall be used in

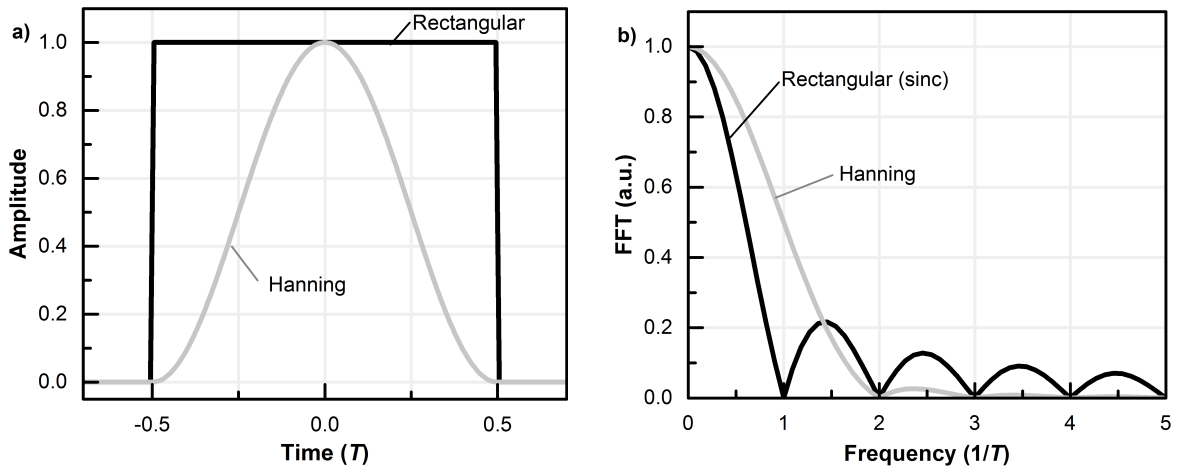

Figure 3.8: Effect of the used window on the lineshape of the FFT. a) The window of width T applied to the initial signal and b) the FFT of the respective signals. Applying the FFT on a rectangular window gives a sinc function, with noticeable lobes. Applying the FFT on a Hanning window gives a peak with a larger FWHM, but negligible lobes.

the current thesis is the Hanning window. Its shape is seen in Figure 3.8, as well as its corresponding Fourier transform. Its corresponding lobes are of a much lower amplitude, with a maximum of 2 %. The truncation of the lobes comes at a cost : the resolution. If the width of the square window is given by T, the FWHM of the sinc function is $0.884/T$, while the FWHM of the Hanning window is $1.44/T$. For the proposed 'etalon effect' method, the Hanning window will be applied in all cases. For measurements involving oscillations between 900 and 1800 nm, the resolution for the Hanning window is 0.4 µm.

The second effect is aliasing. It happens when, at a certain sampling rate, a higher frequency will have the same points as a lower frequency. As mentioned before, the FFT of a discrete set of data is symmetrical. The Fourier spectrum is mirrored at the folding frequency, named the Nyquist frequency, $k_f = \frac{N\Delta\nu}{2}$. This means, for example, that a frequency component that is 5 Hz higher than the Nyquist frequency will give the same data points than a frequency component that is 5 Hz lower. Hence, in a FFT spectrum, if there is some measured frequencies that are higher than the folding frequency, the values will then be folded into the lower frequency range. This folding gives an inaccurate representation of the Fourier transform. For a FFT spectrum to be accurate, the sampling rate of the data needs to be high enough so that the Nyquist frequency is higher than the highest frequency measured. For example, if reflectivities

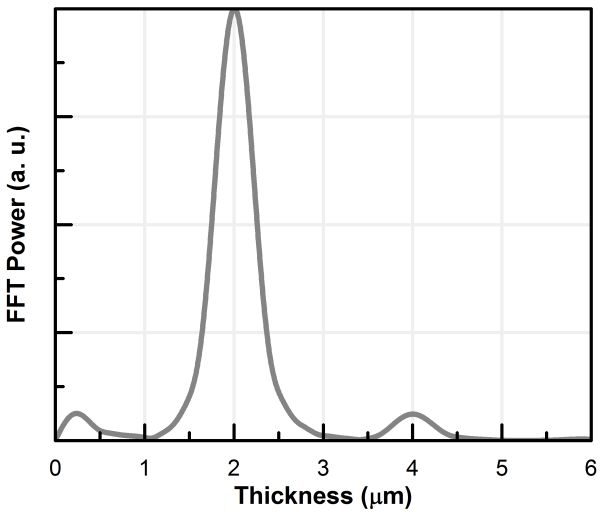

Figure 3.9: Fast Fourier transform of the reflectivity of a 2 μm GaAs layer on top of a Ge substrate, shown in Figure 3.7. The used reflectivity was from 900 to 1800 nm, a Hanning window was applied and 1800 zeroes were used outside the window.

with stepsize of 5 nm and using the GaAs index of refraction are given, the Nyquist 'thickness' is 46 μm. For the same reflectivity but with the InGaP index of refraction, this gives a Nyquist 'thickness' of 51 μm. These values will be the highest thickness values that the current method will be capable of obtaining.

The last effect is named the picket-fence. It happens when the frequency resolution is not high enough, and the spectral peaks are placed between two frequency points. As mentioned before in Equation 3.11, the frequency sampling rate is inversely dependant on the total number of points N. If not enough points are used, the frequency steps in the FFT graph would be too high. For example, using the previous example of the 2 μm GaAs layer, the total number of data points that can be used is 180. This gives a step in the 'thickness' frequency space of 0.5 μm. This would make the peak at 2 μm unresolved. This effect is, however, easily avoidable. The solution is to add a significant number of zeroes before and after the reflectivity in the data table. This allows the FFT algorithm to calculate more points between each frequency sample. This solves the picket-fence problem and allows peaks to be resolved that would otherwise not be seen. It furthermore does not change the spectrum, since those zeroes have no other effect on the FFT. In our case, the number of added zeroes is 10 times the original number of data points. By solving this effect, the resolution of the method is then solely limited by the Hanning window.

The FFT of the reflectivity shown in Figure 3.7 between 900 and 1800 nm is presented in Figure 3.9. The ordinate change $Z = 2\frac{n_{GaAs}}{\lambda}$ was applied, a Hanning window shape was applied to the data, and 1800 zeroes were added to the data array. The peak centered at 2 µm clearly shows that the FFT allows us to retrace the thickness of the semiconductor that created the oscillation in the reflectivity.

In the next section, this technique will be applied to measured reflectivities. It will be shown that the power of this technique is important to verify various semiconductor thicknesses. It shall give us important insights in the structure of MJSCs.

3.3.3 GaAs solar cell's reflectivity

Now that the groundwork to be capable of understanding the reflectivity of a solar cell has been set, it is now possible to apply the etalon effect technique to experimental measurements. The method will first be applied on the single junction GaAs solar cell used beforehand, then extended to MJSCs.

The single junction GaAs solar cell studied here (sample SJ-ref) was introduced in Section 2.4.4. Its structure has been shown in Figure 2.18, and its EQE in Figure 2.19. The measured reflectivity of the solar cell is shown in Figure 3.10a. The solar cell is made out of GaAs layers and a single AlGaAs layer. If the cell was made out purely of GaAs layers, the reflectivity would be governed mostly by the air-GaAs interface. However, the single AlGaAs layer, which acts as a front surface field, creates two optical cavities that should be of interest. The first optical cavity, made out of a 200 nm GaAs is the cap layer. The second optical cavity, made out of the AlGaAs layer, is 40 nm thick. As made evident in the EQE simulation study, the cap layer thickness of 200 nm is uncertain. A thickness of 220 nm was found to be a best fit for the EQE simulation.

The FFT of the reflectivity is shown in Figure 3.10b. It was taken using the reflectivity from 500 to 1800 nm using a Hanning window and with additional zeroes amounting to 10 times the number of data points in the data array. As made evident from the FFT spectrum, the measured reflectivity reflects a thickness of 220 nm and not 200 nm. A simulated reflectivity as well as its associated etalon effect FFT transformation is shown in grey. This simulated component was obtained using the TMM method, with a 220 nm cap layer and the rest of the single junction solar cell structure. The oscillations in the measured reflectivity and the simulated reflectivity correspond well to each other. However, the amplitude of the oscillations are slightly different. This can be corrected by either changing the amplitude of the index of refraction of the AlGaAs layer or the

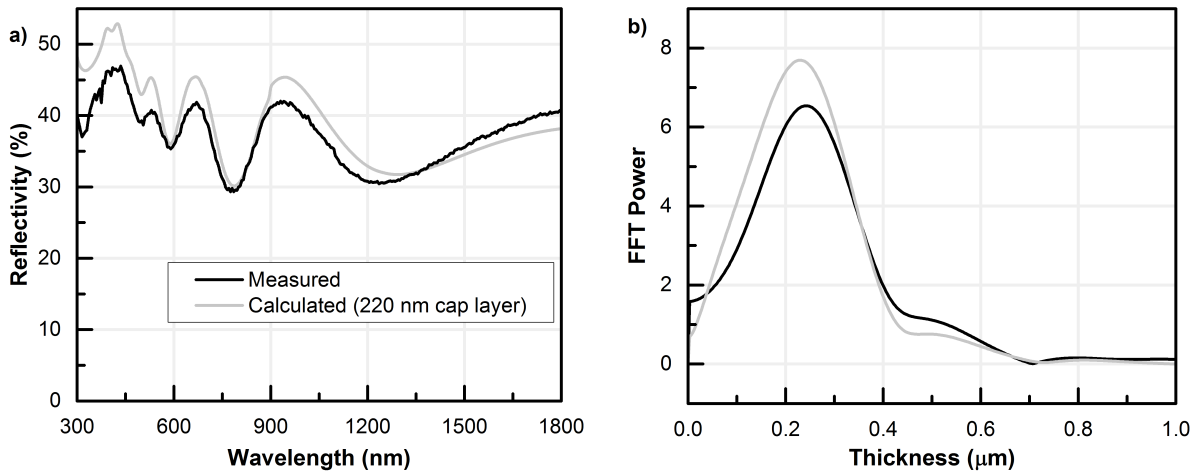

Figure 3.10: a) Measured (black) and calculated (grey) reflectivity of the single junction GaAs solar cell (sample SJ-ref). b) The corresponding FFT of the reflectivities, taken from 500 to 1800 nm using a Hanning window and with additional zeroes amounting to 10 times the number of data points in the data array.

GaAs cap layer. An amplitude change in the index of refraction is expected when one uses high doping for the cap layer [76].

Another optical cavity is present in this solar cell, the 40 nm thick AlGaAs layer. Using the Equation 3.4 to approximate the period of oscillation and a value of $n = 3.1$ at 900 nm, oscillations on the order of $\Delta\lambda = 3300$ nm are expected in the reflectivity. This is well beyond the experimental limit of the method. As calculated earlier, the resolution due to the FHWM of the FFT peak is 0.4 μm when the wavelength range of 900 to 1800 nm is used. This resolution improves to 0.1 μm when the wavelength range is increased to 500 to 1800 nm, which is the case for this single junction solar cell. This resolution allowed the detection of the peak associated to the 220 nm cap layer while not allowing the detection of the peak associated to the AlGaAs layer.

3.3.4 Multijunction solar cell's reflectivity

The MJSC is a far more complex structure than the single junction solar cell. Nevertheless, as seen in Figure 3.5, optical cavities are created by the top and middle subcell. In this section, the etalon effect method will be applied on the simulated reflectivity. Then, after building the methodology to infer the thicknesses of each layers, it will be applied to experimentally measured reflectivity.

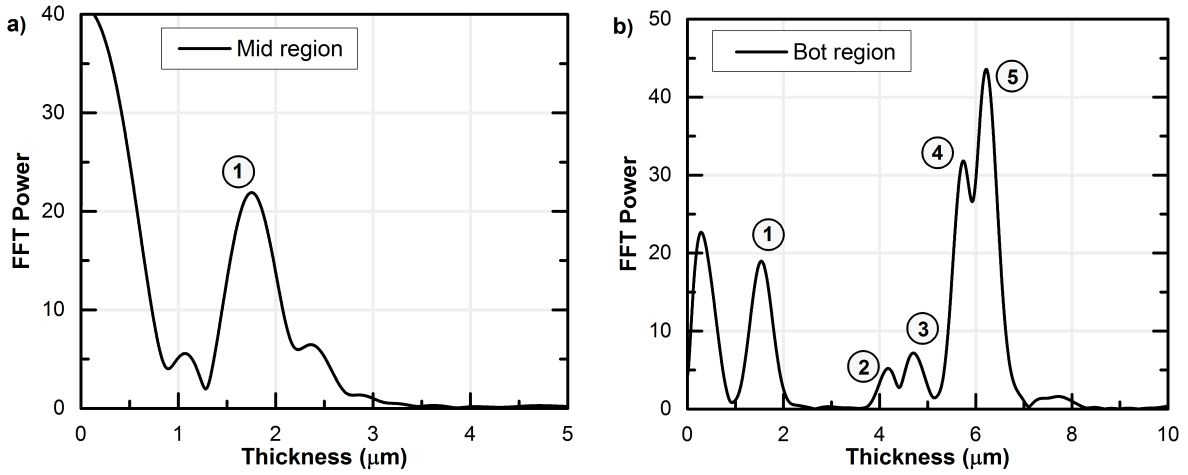

Figure 3.11: FFT of the calculated reflectivity of the standard MJSC in Figure 3.2. a) The FFT applied in the middle subcell's wavelength region, from 670 to 900 nm and using the InGaP's index of refraction. b) The FFT applied in the bottom subcell's wavelength region, from 900 to 1800 nm and using the GaAs index of refraction.

Simulated standard reflectivity

The standard structure yields the reflectivity seen in Figure 3.2. Let's first apply the FFT to the mid region, from 670 to 900 nm. Using this part of the reflectivity, the top subcell's optical cavity thickness is obtained. The ordinate coordinate transformation will be done using the InGaP's index of refraction, $Z = 2\frac{n_{InGaP}}{\lambda}$. The resulting FFT spectrum, using a Hanning window and with 10 times more zeroes added to the original data array, is show in Figure 3.11a.

Two main peaks can be seen. The first peak, which has its maximum point at 0 μm but is 0.6 μm large is due to the ARC coating. The coating implemented in the structure, made out of 79 nm of SiO_2 and 59 nm of Si_3N_4 creates long wavelength oscillations in the reflectivity. The FFT picks those oscillation in the reflectivity, and this is reflected in this low thickness peak. Even though the combined thickness of the coating layers is 138 nm, the fact that the FFT used the index of refraction of InGaP skews the value of their thickness. As mentionned in the previous section, the FFT method has a resolution of 0.1 μm when using the wavelength range of 500 to 1800 nm, which would not be enough to resolve the ARC peak adequately. The results for the ARC are then inaccurate, but still visible in the peak.

The peak labelled 1 in Figure 3.11a comes from the oscillations created by the top subcell. Its maximum is placed at 1.8 μm. It is created by the combination of the

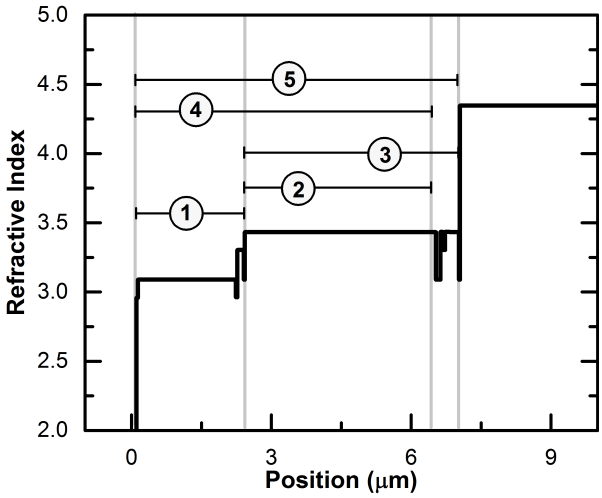

Figure 3.12: Position of the measured optical cavities inside the solar cell. The refractive index is taken at 1200 nm, similarly to Figure 3.5.

complete top subcell (10 nm AlInP and 1630 nm InGaP), the tunnel diode (140 nm AlGaAs) and the middle subcell fsf (20 nm InGaP) for a total of 1800 nm of material. Nevertheless, the value of the peak is a good approximate to obtain the total thickness of the layer.

The FFT is then applied to the reflectivity in the bottom subcell region, from 900 to 1800 nm. The bottom subcell's thickness will be obtained, using the results obtained from the FFT applied in Figure 3.11a. The FFT spectrum is shown in Figure 3.11b, with the ordinate transformation done using $Z = 2\frac{n_{GaAs}}{\lambda}$. The peak associated to the top subcell, labeled as number 1 at 1.5 μm, is seen in a thickness slightly lower than the one obtained earlier. This is because the index of refraction used is different for both FFT.

Four other peaks are of interest in the current structure. The first two peaks, labeled as number 2 and 3, are positioned at 4.2 μm and 4.7 μm respectively. The first peak corresponds to the optical cavitiy created by the top tunnel junction and the GaAs middle subcell (140 nm of AlGaAs, 4000 nm and 100 nm of GaAs). This gives a total of 4240 nm of semiconductor material. The second peak correspond to the optical cavity created by the top tunnel junction, the middle subcell and its bsf (140 nm AlGaAs, 4100 nm GaAs and 100 nm InGaP), the bottom subcell tunnel diode (150 nm GaAs and 50 nm AlGaAs) and the buffer layer of the bottom subcell (200 nm), for a total of 4740 nm of semiconductor material.

The last two peaks, labeled as 4 and 5, are positioned at 5.7 μm and 6.2 μm re-

spectively. These each correspond to similar cavities than the peaks number 2 and 3, but with the top subcell as well. The peak number 4 correspond to the full top subcell (1.5 µm in this transformation of index of refraction) and the GaAs emitter and base (4100 nm) for a total of 5.6 µm worth of effective material. Similarly, the peak number 5 corresponds to all semiconductor material up to the Ge semiconductor, containing the full top subcell (1.5 µm) and the full middle subcell with the GaAs buffer (4.6 µm) for a total of 6.1 µm worth of effective material. Each optical cavity are shown in Figure 3.12. This demonstrates that the thicknesses obtained from the FFT technique corresponds to a good degree of precision to the thicknesses inside the solar cell.

Measured reflectivity

Now that the etalon effect measurement technique has been expanded to the case of a MJSC, it shall be applied to experimentally measured samples. The used samples for the application of this technique are the MJSC-S and the MJSC-920. MJSC-S is a standard InGaP/GaAs/Ge solar cell while MJSC-920 is a quantum dot-enhanced MJSC.

The reflectivity of sample MJSC-S is shown in Figure 3.13a, along with the corresponding FFT of the middle and bottom subcells. The FFT in Figure 3.13b was taken from 670 to 900 nm using the InGaP index of refraction, n_{InGaP}. The peak maximum is placed at 1.5 µm, meaning it has a similar thickness of the top subcell compared to the standard design.

The FFT in Figure 3.13c was taken from 900 to 1800 nm, using the GaAs index of refraction, n_{GaAs}. The peak values are shown in the legend of the figure. The peak number 1, corresponding to oscillations from the top subcell, is placed at 1.4 µm in this index of refraction transformation. The combination of the peaks shows the possible optical cavities created. The addition of peaks 1 and 2 and 3 is equivalent to peaks 4 and 5. This means an optical cavity creates peak 1, from the InGaP top subcell, and another optical cavity creates peaks 2 and 3. The peaks 4 and 5 represent the overall optical cavities created by both top and middle subcells. The reconstruction of the structure, along with the according peak labels, is shown in the fourth part of Figure 3.13.

Using this structure, consisting of 1.56 µm InGaP for the top subcell, 3.3 µm GaAs for the middle subcell, another 50 nm InGaP for the bsf of the middle subcell, 0.6 µm GaAs for the bsf of the middle subcell, the tunnel junction and the fsf of the bottom subcell and 500 µm Ge for the bottom subcell, the reflectivity of the analysed structure can be calculated. The standard ARC (79 nm SiO_2 and 59 nm Si_3N_4) was added as well. The resulting reflectivity is shown in the first part of Figure 3.13. Its corresponding

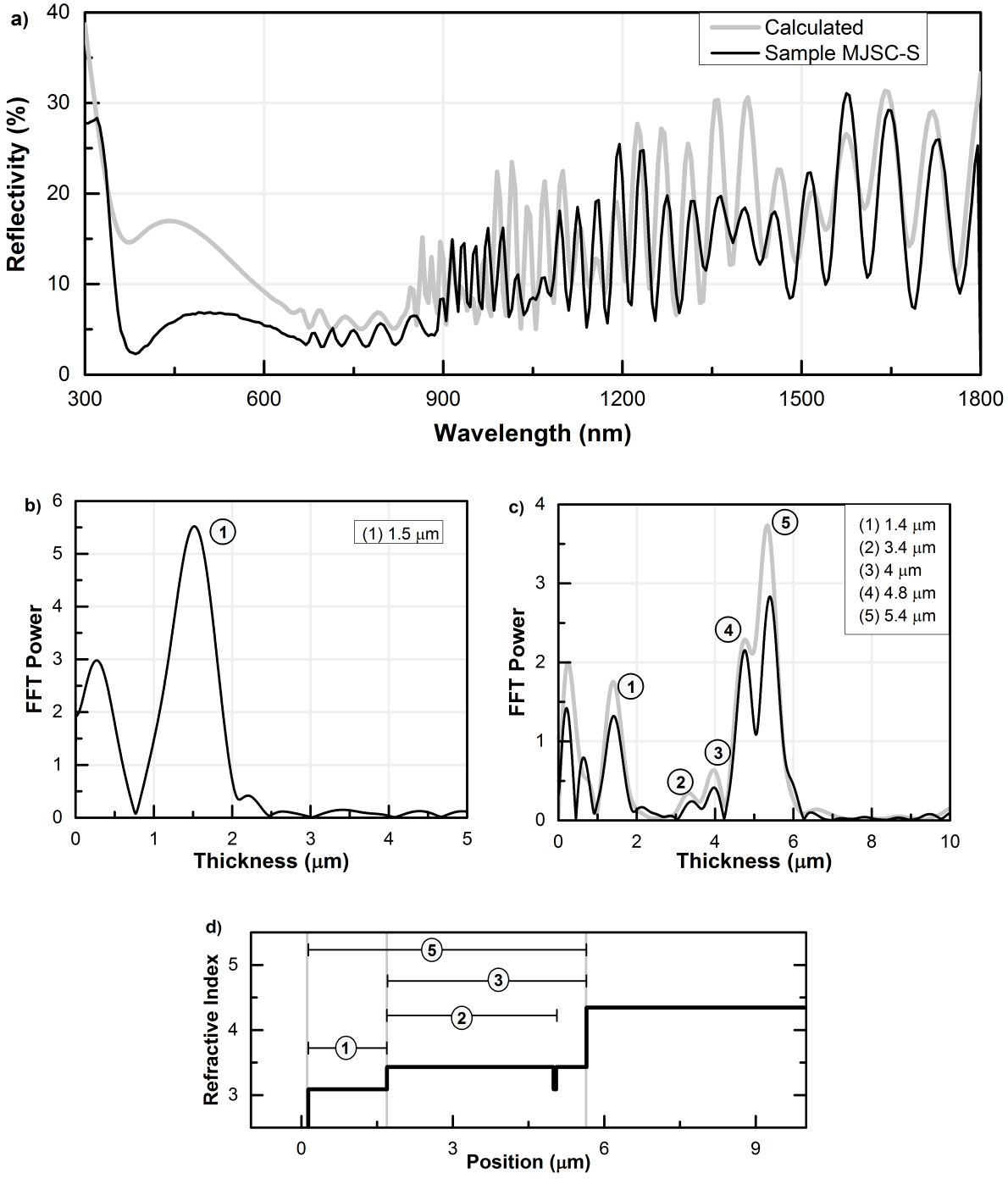

Figure 3.13: a) Experimentally measured and calculated reflectivity of sample MJSC-S. b) FFT of the reflectivity from 670 to 900 nm, using n_{InGaP}, to infer the top subcell's thickness. c) FFT of the reflectivity from 900 to 1800 nm, using n_{GaAs}, to obtain the rest of the thicknesses inside the structure. The FFT of the simulated structure is shown in grey. d) Refractive index at 1200 nm of the structure obtained from the analysis of each peak in the FFT spectrum, which is then used to simulate the reflectivity.

FFT transformation is shown as the light grey curve. The resulting structure and its reflectivity yield satisfying results. Even though the finer structure of the solar cell is not resolved, the fact that the oscillations in the reflectivity are reproduced demonstrates that the thicknesses obtained are correct. The errors therefore originate from the fact that some layers of different materials, for example in the tunnel junctions, are present in the real structure while they are omitted in the model. Furthermore, the n and k data are assumed to be independent of doping in the model while they are expected to vary in the semiconductor structure.

The reflectivity of sample MJSC-920 is shown in Figure 3.14, along with the corresponding FFT of the middle and bottom subcell. Similarly to sample MJSC-S, the FFT in Figure 3.14 was taken from 670 to 900 nm using the InGaP index of refraction, n_{InGaP}. The peak maximum is placed at 1.2 µm, meaning the thickness of the top subcell is smaller than in the standard design.

The FFT in Figure 3.14c was taken from 900 to 1800 nm, using the GaAs index of refraction, n_{GaAs}. Peak number 1, corresponding to oscillations from the top subcell, is situated at 1.0 µm using this index of refraction transformation. The peak values are shown in the legend of the figure. The combination of the peaks shows the possible optical cavities created within the MJSC. The addition of 2 and 3 gives peak 5. The addition of the two peaks labeled 2 also gives the peak number 4. Taking these combinations into account, it is possible to reconstruct the structure. It is shown, along with the according peak labels, in the Figure 3.14d.

Using this structure, composed of 1.1 µm InGaP for the top subcell, 3.1 µm GaAs for the middle subcell, another 50 nm InGaP for the bsf of the middle subcell, 2.55 µm of GaAs forming the tunnel junction and the fsf of the bottom subcell and 500 µm Ge for the bottom subcell, the reflectivity of the analysed structure is calculated. This is shown in Figure 3.14a as the light grey reflectivity curve labeled as 'Calculated' as well as the light grey curve in the FFT Figure 3.14c. Similarly to the sample MJSC-S, some noticeable differences are visible. The oscillations present in the bottom subcell's reflectivity are similar in both curves. However, the amplitude of these oscillation are different, and the position of some major peaks are different in the simulation. Many of these subtle changes in the oscillations can be controlled by changes in the structure of the fsf and bsf of each subcell. However, since there are so many variables, multiple solutions are possible. This demonstrates that the method is relevant to estimate the thicknesses of each subcell, but is not capable of resolving the finer detail in the semiconductor structure.

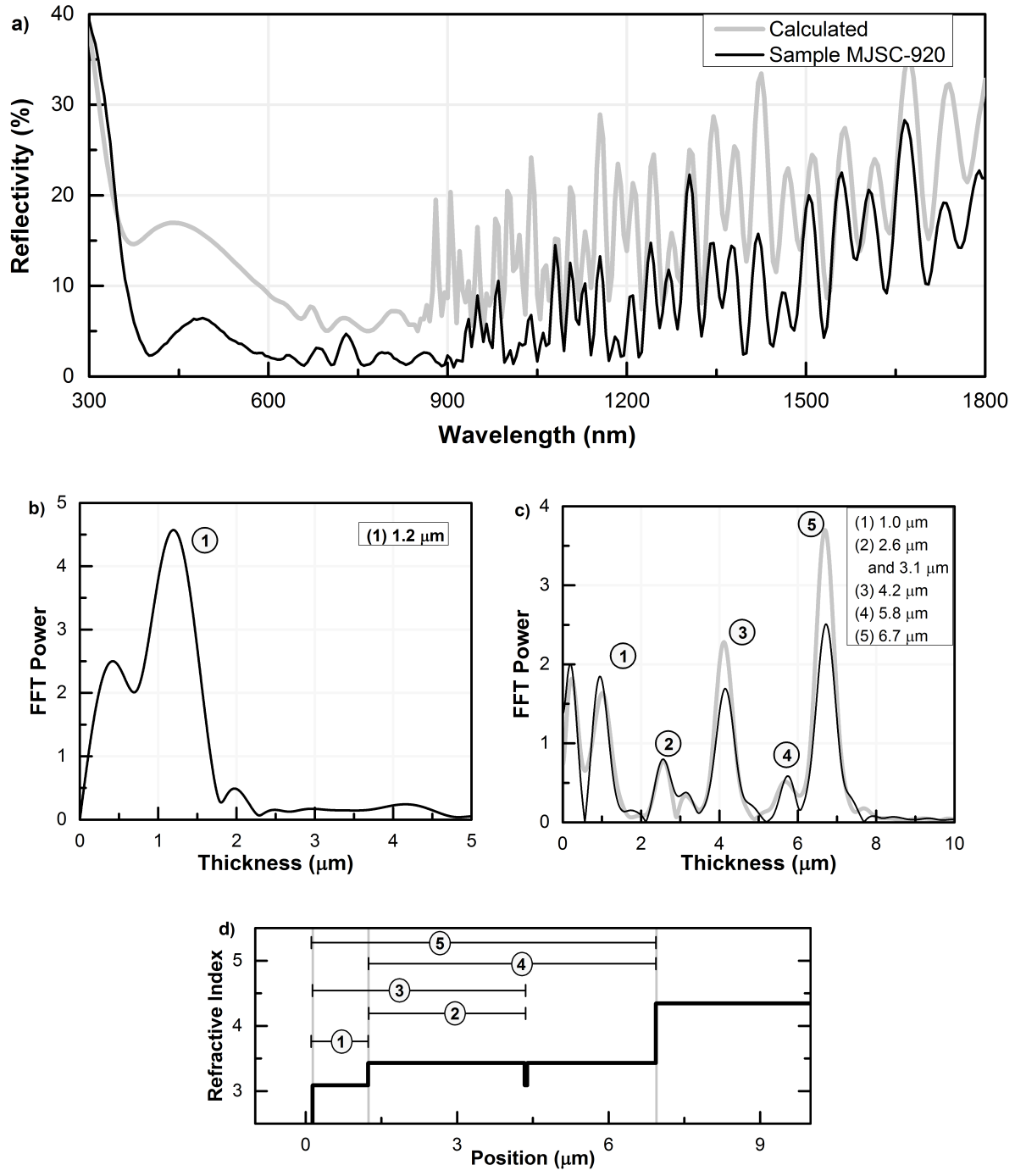

Figure 3.14: a) Experimentally measured and simulated reflectivity of sample MJSC-920. b) FFT of the reflectivity from 670 to 900 nm, using n_{InGaP}, to infer the top subcell's thickness. c) FFT of the reflectivity from 900 to 1800 nm, using n_{GaAs}, to obtain the rest of the thickness inside the structure. The FFT of the simulated structure is shown in grey. d) Refractive index at 1200 nm of the structure obtained from the analysis of each peak in the FFT spectrum, which is then used to simulate the reflectivity.

3.4 Review of results

This chapter provided an in-depth study on the reflectivity of MJSCs. The importance of the addition of an ARC on the overall reflectivity was demonstrated. The effects of the optical cavities inside the solar cell were highlighted in the oscillations created in the reflectivity.

Furthermore, the methods shown in this chapter demonstrate the wealth of information that the reflectivity of a solar cell contains. Not only it is important in maximizing the current output, it can also be used to study the internal structure of the solar cell. The reflectivity measurement in a solar cell can be used to estimate the thicknesses of the semiconductor layers. This was done using the Fast Fourier transform of the reflectivity under a new ordinate, $Z = 2\frac{n}{\lambda}$. In this case, the frequency peaks corresponds to the thickness of the layers creating the oscillation in the reflectivity.

Chapter 4

Spectroscopy of quantum dots in solar cells

Quantum dot-enhanced solar cells have been shown to be a viable alternative to the widely adopted lattice matched MJSC design, InGaP/InGaAs/Ge, where InAs QDs are added to the intrinsic region of the middle subcell [77]. The QDs act to increase the absorption range of the middle subcell, and therefore increase the overall current generated by the device with optimized top subcell bandgap. It does so by capturing light that would normally be absorbed within the current overproducing Ge subcell.

In this chapter, the addition of QDs in a solar cell and its effects on the EQE will be explored. The characteristics of the nanostructures will be reviewed. Then, the semiconductor nanostructures will be simulated using a finite element solver, COMSOL Multiphysics [78]. This simulation shall then be transformed into an absorption coefficient that will be used in the calculation of an EQE. The experimental characterisation of QDs shall then be studied through photoluminescence and electroluminescence and be compared with the respective simulation. Finally, the goal of the chapter is to compare the simulated QD-enhanced EQE to experimentally measured solar cells.

4.1 Quantum dots in solar cells

The addition of QDs in solar cells is an active area of research in photovoltaics. The InAs/GaAs QDs have been mainly discussed in the literature from the point of view of the intermediate band model [79]. This process relies on the probability that the carriers are excited into the QD states by a photon of sufficient energy, and then the subsequent

absorption of another photon to finally excite the electron from the confined intermediate state to the conduction band. The efficiency of this two photon absorption process is predicted to go up to 63 % in a single junction solar cell [10]. Another possible scenario, which is of interest to the current thesis is the absorption of a photon to excite a carrier into the confined QD state, followed by the thermal escape into the conduction band via phonon scattering. The effect of the thermal escape and the depth of the confinement has been studied in a published paper [80].

In GaAs solar cells, most devices demonstrate a lowered V_{oc} when nanostructures are added. This reduction of the V_{oc} is typically significant such that it counteracts the added current from the extended absorption of the QDs. Work has shown improved performance with optimization of the growth thickness of the quantum layers in [81] and [82]. By changing the amount of InAs material grown for the QD, the author of the study changed the sizes of the dot, modifying their absorption properties. The larger QDs absorbed further in the infrared and had an increased photocurrent under 1 sun. However, their effect on the V_{oc} was significant, leading to a lower efficiency. The cell with the smallest QD had a negligible V_{oc} drop and a small photocurrent improvement.

The possibility of bandgap engineering MJSCs using QDs has been studied as well in the literature. The Rochester Institute of Technology (RIT) group has proposed a design containing up to 200 layers of QD in the middle subcell to increase the efficiency [83]. They furthermore demonstrated that the QDs improve the radiation tolerance of these cells in space [84]. Dr. Fafard and Cyrium Technologies have pioneered the commercialization of the QD-enhanced MJSC [77].

The behavior of QDs in MJSC under concentrated light is beneficial. The effects of concentration on the MJSC have been extensively studied for the lattice matched system [85]. The concentration of light increases the efficiency up until the series resistance becomes non-negligible. However, the efficiency variation is different between the QD-enhanced and a standard MJSC. This is explained by a shift in the dominant recombination mechanism in the solar cell. Under operating conditions, at 1000 suns, the QD enhanced cell is expected to have an efficiency of 0.1 to 1.2 % higher than the control case [86]. This dominant recombination shift can be seen as a change in the FF and the V_{oc} over concentration [87].

4.1.1 Quantum dot growth

At 300 K, InAs has a lattice parameter that is 6.7 % larger than GaAs. When InAs is grown epitaxially on top of the GaAs crystal, its atoms are under strain. After a few planar layers of InAs, the strain energy is high enough to cease the planar growth. Islands spontanously form on top of a wetting layer to relieve the stress. This is the Stranski-Krastanov growth process [88]. The onset for the spontaneous island-formation in InAs/GaAs structures is 1.6 monolayers [89]. This phenomenon can be compared to water drops forming on a flat surface. An important difference, however, is that the water droplets do not form a wetting layer.

The growth of a large number of quantum dot layers is limited. Because of the very nature of the Stranski-Krastanov growth process, the QD material has to have a different lattice parameter than GaAs. As the number of QD layers increases, the accumulated strain increases. At a certain threshold, the strain is high enough in the structure to create dislocations. These dislocations propagate through the rest of the growth of the structure, as can be seen in [90]. Being a center for non-radiative recombination, they deteriorate the electrical properties of the solar cell. A possible solution is to introduce layers of semiconductor material of larger lattice constant to balance the strain on the semiconductor structure [91]. For example, the introduction of GaP layers between the InAs QD layers and the GaAs spacer improved the performance of a QD enhanced GaAs solar cell [92].

Another technique used to manipulate the strain is the indium flush technique [33]. This technique was first developed to engineer the size and shape of the QDs while keeping a good crystal quality. The steps involve the normal growth of InAs QDs. After depositing 5 nm of GaAs over a QD layer, the substrate's temperature was raised from 510 to 610 °C for 70 s. Then, the temperature was brought back down to 510 °C and the growth was continued. This eliminated all the possible In atoms left in the topmost semiconductor layers, creating a flatter quantum dot. The technique led to a more homogeneous composition of dots [93]. A TEM image of an example of indum flushed QD layers is shown in Figure 4.1.

An important consequence of this indium flush technique is the relief of strain energy. It allows a good relaxation of the strain in the structure [94]. By using the anneal, the QDs evolve to their equilibrium shape and remove a significant portion of strain. For example, by using the indium flush technique, it was possible to grow up to 50 layers of QDs without dislocations [95].

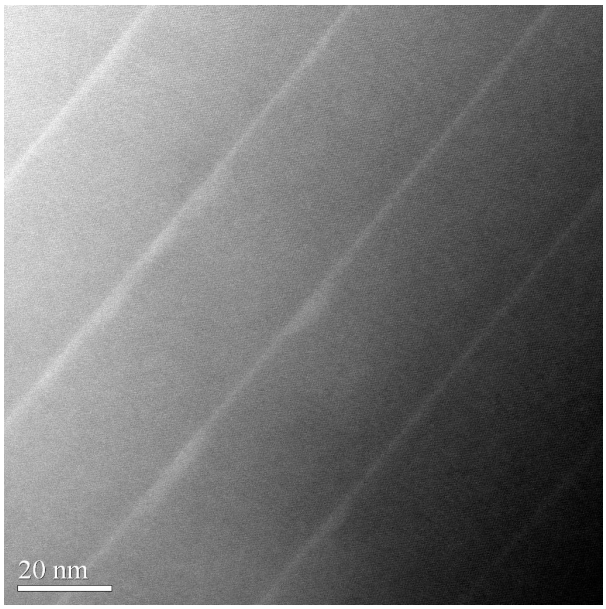

Figure 4.1: Transmission electron microscopy of indium flushed QDs. The InAs layers are shown in lighter gray, with the wetting layer crossing the image from bottom left to top right and a QD in the center of the image. Image courtesy of Jihène Zribi from the Université de Sherbrooke.

The importance of a thermal anneal has been shown as well in [96]. In this technique, instead of annealing after a small GaAs cap layer is grown like the indium flush technique, the full structure is grown and a post-growth thermal anneal is performed. In the cited experiment, 30 layers of QD were grown and compared to a structure that was not annealed. The structure without thermal anneal showed significant dislocations in the structure. Its electrical characteristics were significantly lower than its annealed counterpart. This demonstrates that it is possible to grow a large number of QD layers in a GaAs solar cell, with high quality crystalline structure, as long as the thermal anneal or the indium flush technique is completed. The thermal anneal has been furthermore shown to cause intermixing of Ga inside the InAs semiconductor [97].

For these reasons, it is possible to grow a large number of QD layers while precisely controlling their sizes and energy levels. By using the indium flush and a thermal anneal, it is possible to remove the constraint of using strain compensating layers. It is furthermore possible to have a fine control over the ground state energy of the QDs.

The InAs/GaAs quantum sizes and densities vary widely in the literature. Earlier work on these nanostructures measured QDs of 24 nm diameter and 3 nm height, amount-

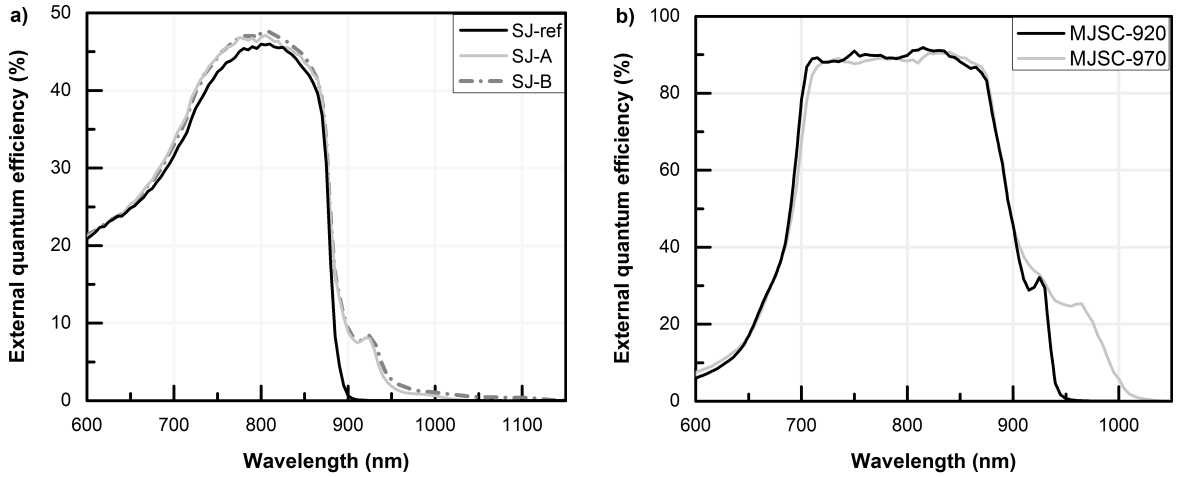

Figure 4.2: The experimentally measured EQEs of a) single junction QD-enhanced solar cells along with the reference GaAs cell, b) QD-enhanced MJSC.

ing to a density of $8.8 \cdot 10^9$ cm^{-2} [89]. However, much higher densities can be achieved, going up to 10^{11} cm^{-2} in some cases [98]. Good control of QD sizes from 12 to 28 nm diameter has been demonstrated as well [99]. For these reasons, the current simulation in the thesis assumes that a continuous control over the QD size is possible. The size and shape of the dots will be mentioned for each simulation.

In this thesis, multiple QD enhanced solar cells shall be studied. The single junction QD-enhanced GaAs solar cells, shown in Section 4.3, were grown at the Université de Sherbrooke as part of the Ph.D. thesis of Jihène Zribi. The single junction GaAs (SJ-ref) with no QD was simulated in Figure 2.20c. Different QDs were grown inside the intrinsic region for samples SJ-A and SJ-B [100]. The reference cell is the GaAs solar cell grown without QDs. Their measured EQEs are shown in Figure 4.2a. Twenty layers of QDs were grown inside the intrinsic region of the solar cell for samples A and B. An indium flush was applied to modify the shape of the QDs. These were applied either after the deposition of 2.5 nm of GaAs (SJ-A) or after deposition of 5 nm of GaAs (SJ-B). This changes the QD absorption peak while keeping the wetting layer absorption peak the same. These curve shall be reproduced by simulating the corresponding QDs structures in Section 4.3.

The QD enhanced MJSCs were grown at Cyrium Technologies and graciously given by Dr. Simon Fafard. Their measured EQEs are shown in Figure 4.2b. They have a noticeably higher EQE value due to a good ARC coating on the surface of the cell. Furthermore, the top subcell (not shown in the figure) absorbs significantly at wavelength

under 700 nm, explaining the different EQE shape compared to the single junction solar cell. The quantity of layers as well as the QD growth procedure is unknown in those structures, as this information is protected by intellectual property. Hence, each of the structure will be named depending on the approximate ground state energy transition (MJSC-920 and MJSC-970). These structures shall be studied extensively through spectroscopy and their EQE will be reproduced in Section 4.4.

4.2 Simulation of quantum dots

The absorption coefficient of the quantum dots is a complex quantity to obtain. It is dependent on the energy levels present in the QDs and well as the wavefunction overlap between the electrons and holes. This section shall introduce the methodology used to simulate the QDs in this thesis.

4.2.1 Conduction and valence band offsets

The simulation of the energy levels in InAs/GaAs QD structures is an elaborate problem. The first seminal paper on the numerical simulation of QDs, published by Grundmann Stier and Bimberg in 1995 [32], demonstrated the importance of strain in the calculation of the energy levels. They calculated the strain induced potential using elastic stress-strain theory. Afterwards, they obtained the energy levels in the system by treating electrons and heavy holes as single particles moving in the potential. They did this calculation using the Schrödinger's equation under the effective mass approximation, and assuming anisotropic masses for the holes.

A more complex 8-band $k \cdot p$ Hamiltonian can be used to calculate the energy levels without the effective mass approximation. Pryor pioneered such research in 1998 [101]. In this framework, the effective mass can be obtained from the dispersion relation by using $\frac{1}{m_e^*} = \frac{\partial^2 E}{\partial k^2}$. The cited author used continuum elasticity to calculate the strain in the structure, which modifies the conduction and valence bands. The heavy-hole band is deeper than the light-hole and split-orbit bands, creating bound states only for the heavy-hole component. He demonstrated that the strain anisotropy is large enough so that the assumption of a heavy hole effective mass is inadequate. However, he demonstrated that the resulting energy levels and electron-hole wavefunctions are similar to the ones calculated using the simpler model of Grundmann.

A basic model was proposed by Califano in 1999 to determine the electronic structures

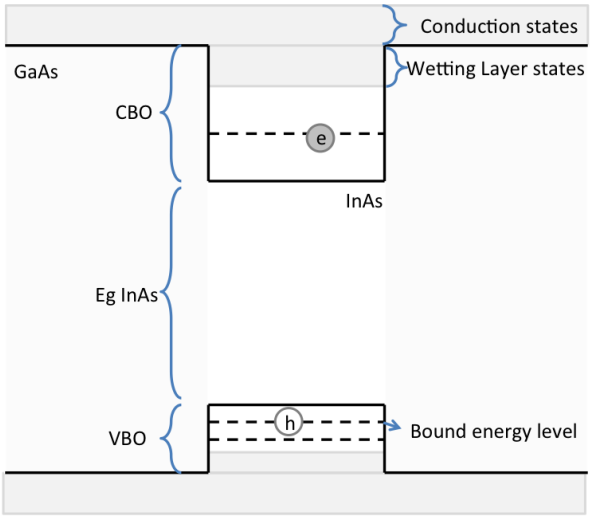

Figure 4.3: Band alignment in the InAs quantum dot in a GaAs matrix. The conduction band offset (CBO) and valence band offset (VBO) determines the depth of the potential barrier for the electrons and hole.

in the QDs [102] . It was composed of a single-band, constant-confining potential model applied to a pyramidal QD shape. They used carrier confining potential, that shall now be referred as band offsets, to approximate the effect of the different bandgaps and the strain. They then assumed constant effective masses for electrons and holes in each of the materials in the system. The 1-band Schrödinger's equation was subsequently solved for the system and for each of the carrier type, electron and hole. They demonstrated that this simplified model recreated adequately the results of the more complex simulations.

This simplified 1-band model shall be used in the current thesis. For a lens-shaped quantum dot, the values for the conduction band offset (CBO), the strained InAs bandgap ($E_{g,InAs}$) and the valence band offset (VBO) are (0.58,0.82,0.36) eV [103, 104]. These CBO and VBO are similar to the ones calculated in [101]. The band offsets are assumed to be temperature independent [105], while the strained bandgap is assumed to follow the Varshni relationship [106]. The Varshni parameters for the strained InAs are $\alpha = 454$ meV/K and $\beta = 210$ K, giving a strained InAs bandgap at room temperature (300 K) of 0.749 eV. The resulting band alignment of InAs and GaAs is shown in Figure 4.3. The transitions in the quantum dot shall be given by calculated energy levels in the valence band and in the conduction band.

4.2.2 COMSOL simulations

In the proposed method, the 1-band Schrödinger's equation shall be numerically solved using COMSOL for the particular shapes of the QD. COMSOL Multiphysics is a finite element solver for general partial differential equations [78]. The finite element method is a numerical methodology that uses variational method to minimize an error function and find an optimal solution. It divides a large domain into a mesh with small elements (see Figure 4.4b) where simplified equations can be solved. The boundary values over the full domain need to be specified and the solver finds the appropriate solutions of the given equation inside the domain. The time independent general equation that COMSOL solves is

$$\nabla \cdot (-c\nabla u - \vec{\alpha}u + \vec{\gamma}) + au + \vec{\beta} \cdot \nabla u = d_a \lambda u, \tag{4.1}$$

where ∇ is the three dimensional gradient, $\vec{\alpha}$, $\vec{\gamma}$ and $\vec{\beta}$ are vectors while c, a, d_a and λ are scalars that can all be dependent on the spatial coordinates [107].

The Schrödinger's equation is then manipulated and transformed into an equation solvable in COMSOL. The method will follow the methodology of [108]. If we have an electron in a semiconductor, its electronic wavefunction and energy can be calculated using the 1-band Schrödinger's equation. It is given by

$$-\frac{\hbar^2}{2}\left(\nabla \cdot \left(\frac{1}{m_e^*}\nabla\psi\right)\right) + V\psi = E\psi, \tag{4.2}$$

where $\hbar$ is the reduced Planck's constant, m_e^* is the effective mass of the electron in the semiconductor, ψ is the electron wavefunction, V is the applied potential on the electron and E is the energy of the electron. A similar calculation is done for the holes using their effective mass m_h^* and corresponding potential. In this 1-band approximation, the complete wavefunction of the electron is given by the multiplication of the calculated wavefunction ψ and the Bloch wavefunction. The applied potential, V, can either come from an electric field applied to the semiconductor or can come from band changes due to the semiconductor heterostructure. In this equation, the wavefunction ψ and potential V are both dependant over position, as well as the effective mass m_e^*.

The shape of the QDs that are simulated are paraboloids, as shown in Figure 4.4a [103, 109]. Because the paraboloid has a rotational symmetry around the axis z, cylindrical coordinates are appropriate. The wavefunction can then be separated into

$$\psi = \chi(z, r)\Theta(\phi), \tag{4.3}$$

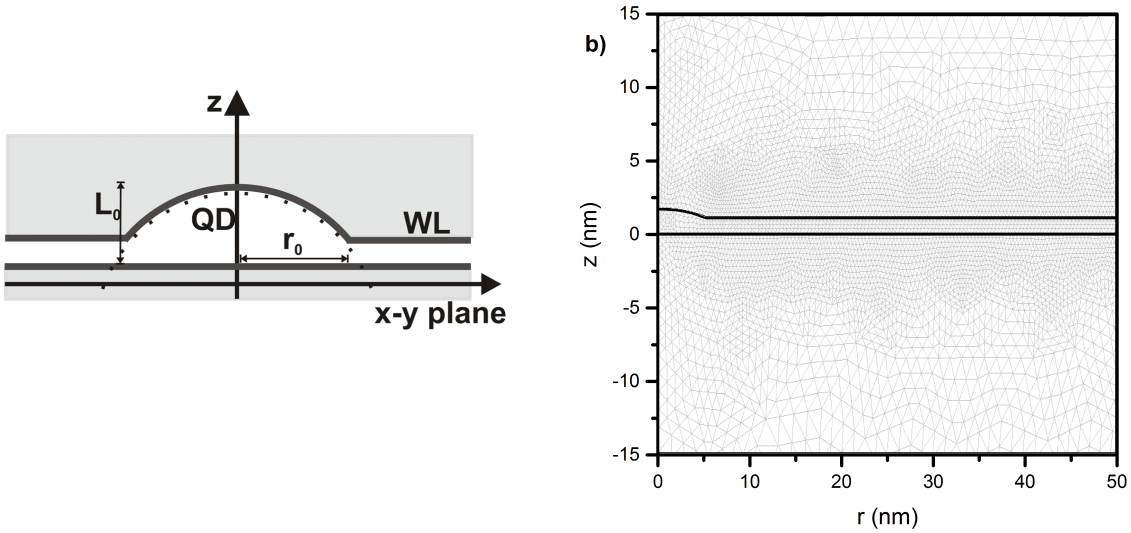

Figure 4.4: a) The QD geometry and b) the mesh used in the COMSOL simulation. 29296 points were used for this mesh structure.

where z is the direction perpendicular to the wetting layer, r is the distance in the plane and ϕ is the azimuthal angle. In cylindrical coordinate, the Schrödinger's equation is given by

$$-\frac{\hbar^2}{2}\left[\frac{\partial}{\partial z}\left(\frac{1}{m_e^*}\frac{\partial\chi}{\partial z}\right)+\frac{1}{r}\frac{\partial}{\partial r}\left(\frac{r}{m_e^*}\frac{\partial\chi}{\partial r}\right)\right]\Theta-\frac{\hbar^2}{2}\frac{\chi}{m_e^* r^2}\frac{\partial^2\Theta}{\partial\phi^2}+V\chi\Theta=E\chi\Theta. \tag{4.4}$$

Rearranging this equation, the terms in Θ are isolated, giving

$$-m_e^* r^2\frac{1}{\chi}\left[\frac{\partial}{\partial z}\left(\frac{1}{m_e^*}\frac{\partial\chi}{\partial z}\right)+\frac{1}{r}\frac{\partial}{\partial r}\left(\frac{r}{m_e^*}\frac{\partial\chi}{\partial r}\right)\right]+\frac{2m_e^* r^2}{\hbar^2}(V-E)=\frac{1}{\Theta}\frac{\partial^2\Theta}{\partial\phi^2}. \tag{4.5}$$

Because of the symmetry in ϕ of the problem, and because the left hand side of the equation is independant of ϕ, the solution for Θ is an oscillatory exponential:

$$\Theta=\mathrm{e}^{-il\phi}\quad\rightarrow\quad\frac{1}{\Theta}\frac{\partial^2\Theta}{\partial\phi^2}=-l^2, \tag{4.6}$$

where l is an integer. The equation is now arranged to be similar to the general partial differential equation,

$$-\frac{\hbar^2}{2}\left[\frac{\partial}{\partial z}\left(\frac{1}{m_e^*}\frac{\partial\chi_l}{\partial z}\right)+\frac{1}{r}\frac{\partial}{\partial r}\left(\frac{r}{m_e^*}\frac{\partial\chi_l}{\partial r}\right)\right]+\left(\frac{\hbar^2}{2m_e^*}\frac{l^2}{r^2}+V\right)\chi_l=E_l\chi_l. \tag{4.7}$$

Parameter	Value	Reference
$E_{0,InAs}$	749 meV	[103, 106]
CBO	580 meV	[103]
$m^*_{e,QD}$	0.053 m_0	[101]
$m^*_{e,GaAs}$	0.0665 m_0	[102]
VBO	360 meV	[103]
$m^*_{h,QD}$	0.341 m_0	[102]
$m^*_{h,GaAs}$	0.3774 m_0	[102]

Table 4.1: Quantum dot band offsets and effective masses used in the COMSOL simulation.

Comparing this equation to Equation 4.1, the coefficients are given by

$$c = \frac{\hbar^2}{2m_e^*}, \quad \alpha = 0, \quad \vec{\gamma} = (0,0), \quad a = \frac{\hbar^2}{2m_e^*}\frac{l^2}{r^2} + V, \quad \vec{\beta} = (-\frac{\hbar^2}{2m_e^* r}, 0), \quad d_a = 1. \quad (4.8)$$

This is now a two dimensional problem, with the spatial coordinates given by r and z. The variables that shall be solved are λ which will give the energy E_l and u which will give the wavefunction χ_l.

The values that are needed are the effective masses, the QD size and the potential V inside the structure. The potential V is defined as zero inside the InAs semiconductor, and $V = \text{CBO}$ in the GaAs semiconductor. The important parameters are given in Table 4.1, as discussed in Section 4.2.1.

The final features that are important to define in the finite element simulation are the boundary conditions. In the simulation problem, the wavefunction must be zero for values of z that are far from the QD and the wetting layer. Conditions imposed on the problem are that $\chi_l = 0$ at the top and bottom boundary of our problem. For all other boundaries, the wavefunction χ does not necessarily equal to 0. However, the wavefunction slope, given by $\frac{1}{m_e^*}\nabla\psi$, needs to be continuous [110].

Let's have a look at the boundary conditions available in COMSOL. The conditions that are available on the domain boundaries are given by

$$\vec{n} \cdot (c\nabla u + \alpha u - \vec{\gamma}) + qu = g - h^T\mu, \quad (4.9)$$

$$hu = r \quad (4.10)$$

where $\vec{n}$ is the unit normal vector that is perpendicular to the boundary, q, g, h, r are new constants that can be defined by the user, h^T is the transpose of h, and μ is a Lagrange multiplier. The other constants were defined in Equation 4.8.

Two boundaries where the wavefunction needs to be forced to 0 are the top and the bottom. The coefficients in those cases are defined as

$$q = 0, \quad g = 0, \quad h = 1, \quad \text{and} \quad r = 0. \tag{4.11}$$

It forces the Equations 4.9 and 4.10 to give

$$\vec{n} \cdot (c\nabla u) = 0, \quad u = 0, \tag{4.12}$$

which means it forces the wavefunction to be zero and its slope to be zero at this interface.

The other boundaries are the left and the right. They both are non-trivial, and shall be observed carefully. The boundary on the left, where $r = 0$, is the axis of symmetry of the quantum dot. In Equation 4.7, the term $\frac{\hbar^2}{2m_e^*}\frac{l^2}{r^2}\chi_l$ diverges when $r = 0$. This means that the wavefunction χ_l needs to be zero when l is not zero.

For the cases when $l = 0$, this term does not diverge. However, the solution for the wavefunction in the azimuthal angle is the same on all angles, giving $\Theta(\phi) = \Theta(\phi + \pi)$. This means that for a point that is positioned infinitesimally close to the axis of rotation,

$$\lim_{\epsilon \to 0} \psi(z, \epsilon, \phi) = \lim_{\epsilon \to 0} \psi(z, \epsilon, \phi + \pi). \tag{4.13}$$

In the two dimensions the simulation is employing, this means that the value of the wavefunction must not vary when it approaches the axis of rotation. This shall be applied by setting the gradient $\vec{n} \cdot \vec{\nabla}\chi_l = 0$ and forcing $u \neq 0$. This is done by imposing $\nabla u = 0$ and $h = 0$ $(0 \cdot u = 0)$.

For the boundary to the right of the domain, the conditions are similar. The wavefunction either approaches 0 for a bound quantum dot state or a non-zero value for a quantum well state. The solution for a pure quantum well state in cylindrical coordinate is given by [108]

$$\psi = A_{nk} Z_{nk}(z) J_n(kr) \mathrm{e}^{in\phi}, \tag{4.14}$$

where Z_{nk} is the wavefunction in the z direction, A_{nk} is a constant that normalizes the wavefunction, and $J_n(kr)$ is the Bessel function of the first kind at a certain wavevector k. The Bessel function can oscillate between values of $+1$ and -0.4 at a certain r, depending on the particular wavevector k. Because it is impossible to impose a boundary condition at a certain r to vary between two values, our solution space will then be limited. By

Parameter	Symbol	Value
QD density	ρ	$1.25 \cdot 10^{10}$ cm^{-2}
QD radius	r	5.2 nm
QD height	L	1.71 nm
QW thickness	T	1.11 nm

Table 4.2: Nanostructure parameters and dimensions for the MJSC-920 design.

applying the condition $\vec{n} \cdot \vec{\nabla}\chi_l = 0$, the solution is placed at a maximum or a minimum of the Bessel function. This means that this boundary condition will find only solutions where the wavevector k satisfies the condition of the minimum or maximum of the Bessel function at the boundary. This solution to the boundary condition problem only works for domain sizes that are much larger than the QD size. This ensures that the solutions where χ_l is non-zero at the boundary are quantum-well like.

For those two boundaries, the coefficients are

$$q = 0, \quad g = 0, \quad h = 0, \quad \text{and} \quad r = 0. \tag{4.15}$$

These coefficients forces the Equations 4.9 and 4.10 to give

$$\vec{n} \cdot (c\nabla u) = 0, \quad 0 \cdot u = 0. \tag{4.16}$$

The second equation, where $0 = 0$, states that the wavefunction given by u can be non-zero. The first equation states that the slope of the wavefunction is zero.

One last step necessary to complete the simulation is the wavefunction normalization. Because the wavefunction u in the calculation is not normalized, it is necessary to complete it afterwards. It is done by applying

$$\chi_l = \frac{u}{\int |u| d\Omega}, \tag{4.17}$$

where Ω is the domain of the simulation and $|u|$ is the absolute value of the calculated wavefunction u. By applying this transformation, the final wavefunction is normalized and gives $|\psi| = 1$. It is done practically by integrating the absolute value of the wavefunction $\int |u|^2 r dr dz$ over the spatial coordinate using Matlab, and multiplying it by 2π to take into account the ϕ spatial coordinate.

Figure 4.4a shows the structure of the simulated quantum dot. The dimensions for the simulated nanostructures are given in the Table 4.2. These quantities will be related

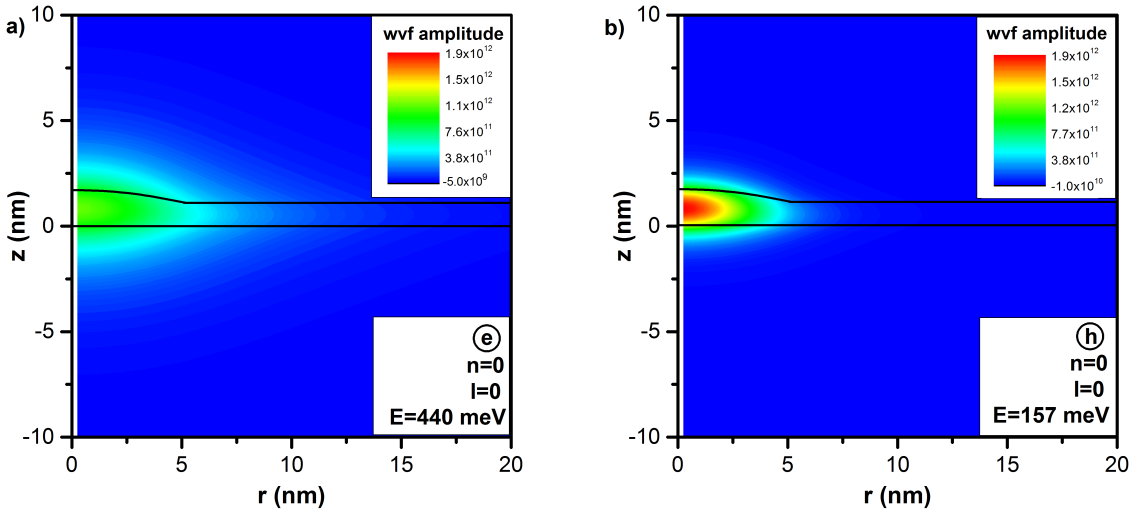

Figure 4.5: a) The electron and b) hole ground state wavefunction for the MJSC-920 simulated design. The principal number is $l = 0$ and the wavefunction is at the ground state $n = 0$ energy level.

to the experimentally measured sample MJSC-920. Figure 4.4b shows the discrete mesh created by the software, with 29296 mesh points. The size of the domain was from $z = -20$ nm to $z = 20$ nm and from $r = 0$ nm to $r = 150$ nm. It was chosen to obtain a better view of the extended wetting layer wavefunctions, as seen later in the current section in Figure 4.8.

Figure 4.5 shows the electron and hole ground state wavefunctions. The wavefunction was zoomed into $z = -10$ nm to $z = 10$ nm and $r = 0$ nm to $r = 20$ nm instead of showing the complete domain size for clarity purpose. For each simulation, only the ground state ($n = 0$) was bound for the quantum number $l = 0$. The wavefunction (wvf) amplitude, shown in the legend, ranges from $-1.0 \cdot 10^{10}$ to $1.9 \cdot 10^{12}$ for the hole. The maximum wavefunction amplitude for the electron is $1.1 \cdot 10^{12}$. The energy of the carriers are $E = 440$ meV over the InAs conduction band for the electron and $E = 144$ meV under the InAs valence band for the hole. The electron wavefunction is significantly more extended than the hole wavefunction. The significantly heavier effective mass of the hole explains this behavior. The wavefunction for both carriers are equal to 0 for large r and are maximal at the center of the QD.

The electron-hole wavefunction overlap, given by $|M| = |\langle\psi_e|\psi_h\rangle|$, is important. It is calculated similarly to the normalization of the wavefunction, using the integral

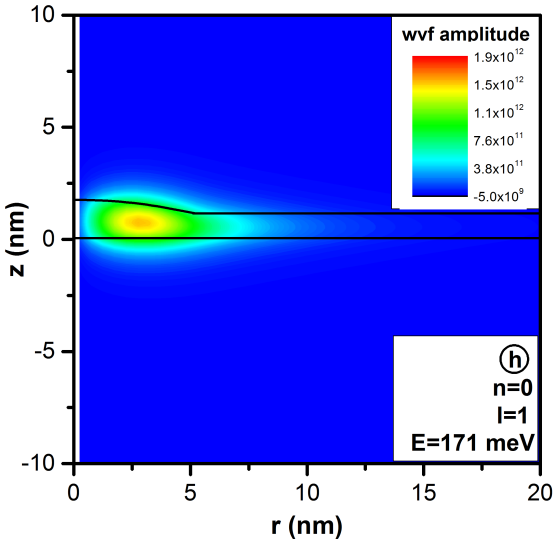

Figure 4.6: Quantum dot hole wavefunction for the $l = 1$ quantum number in the MJSC-920 simulated design.

$2\pi \int \chi_e \chi_h r dr dz$. For the $n = 0$ case, because the wavefunctions are not equal, the wavefunction overlap will not be 1. The result of the integration in this case gives $|M| = |\langle \psi_e | \psi_h \rangle| = 0.86$. It is similar to wavefunction overlap calculated using more rigorous techniques [111].

For this particular QD geometry, no bound state for electrons was found for non-zero values of l. However, one bound state was found for the holes, at $n = 0$ an $l = 1$. The corresponding wavefunction is shown in Figure 4.6. This is consistent with a rigourous simulation of the wavefunction, in [109]. As stated earlier, the wavefunction needs to be zero at $r = 0$ for the solution to have physical meaning. The wavefunction is situated towards the edge of the QD and is equal to 0 at the axis of symmetry. Because the quantum number is $l = 1$ for this wavefunction, the wavefunction overlap with the electron ground state will be zero. A similar range of wavefunction amplitude label as Figure 4.5 is used for comparison purpose. The maximum wavefunction amplitude is $1.5 \cdot 10^{12}$ in this case.

The solutions where the value of the wavefunction at the right boundary are zero are assumed to be QD bound states. The solutions where the wavefunction is non-zero at the boundary are assumed to be quantum well-like states. Figure 4.7 shows the first quantum well-like wavefunction for an electron and a hole. The wavefunction amplitude ranges

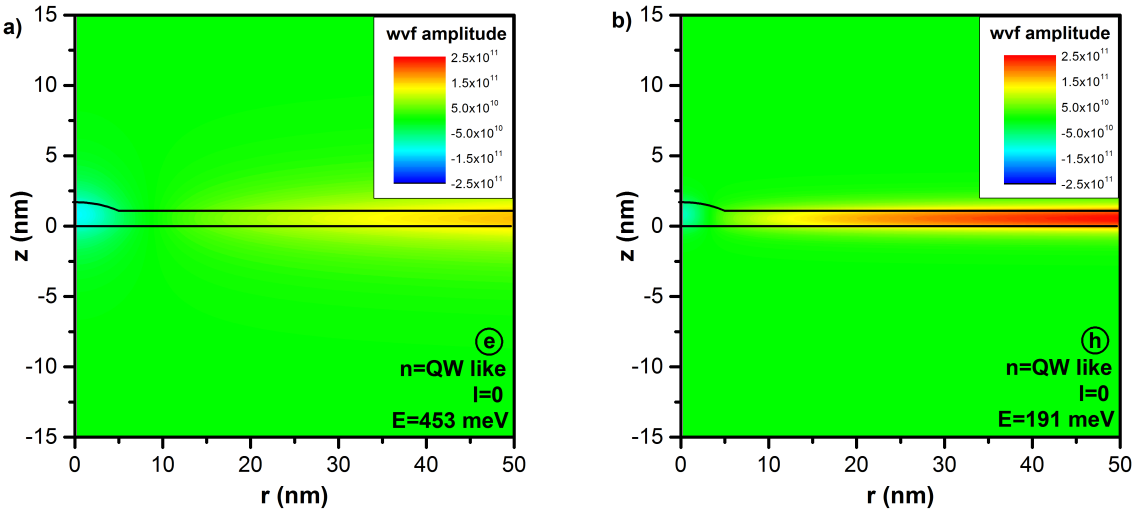

Figure 4.7: a) Quantum well electron and b) hole wavefunctions in the MJSC-920 simulated design. The principal number is $l = 0$ and the wavefunction is at the lowest QW energy level.

from $-2.5 \cdot 10^{11}$ to $2.5 \cdot 10^{11}$ for the electron and for the hole. The energy of the carriers are $E = 453$ meV over the InAs conduction band for the electron and $E = 191$ meV under the InAs valence band for the hole. The wavefunction overlap in this case gives $M = |\langle\psi_e|\psi_h\rangle| = 0.86$. If the wavefunction has a Bessel function shape, the corresponding wavevector is $k = 2.6 \cdot 10^7$ m^{-1}. Hence, the wavefunction shall extend indefinitely in the plane. In the real structure, the ground state quantum well-like wavefunction will have a wavevector that starts at $k = 0$. However, the simulated wavefunction is assumed to be equivalent to the ground state.

The quantum-well like wavefunction is expected to have a shape similar to the Bessel function. However, because Figure 4.7 represents the calculated quantum well-like state of the lowest energy, only one oscillation is seen. Figure 4.8 represents a quantum well-like wavefunction of higher energy but of the same quantum number, with a wavevector of $k = 1.1 \cdot 10^8$ m^{-1}. The wavefunction oscillates in a Bessel-like shape. It is interesting to note that a peak of high intensity is seen at the center of the QD at $r = 0$. Hence, the calculated wavefunction will extend indefinitely in the plane.

The energy of the possible transitions can then be calculated using the resulting energy levels in the simulation and the strained InAs energy. For example, the $n = 0$ state has an energy transition given by the sum of the bound electron energy (440 meV),

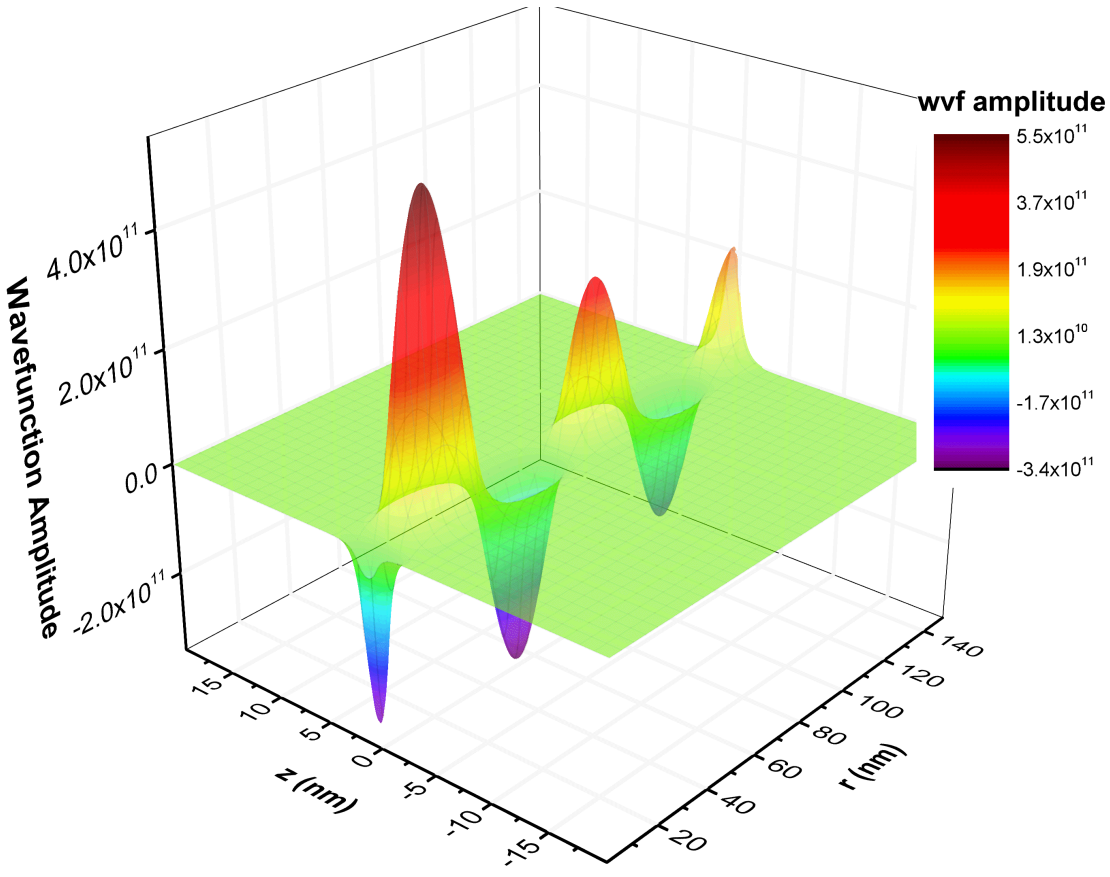

Figure 4.8: Three dimensional figure of the excited quantum well wavefunction in the MJSC-920 simulated design as a function of height z and radius r. The principal number is $l = 0$ and the wavevector is $k = 1.1 \cdot 10^8$ m^{-1}.

the strained InAs bandgap at 300 K (749 meV) and the bound hole energy (157 meV). This particular transition has an energy of 1.346 eV (921 nm). In a similar fashion, it is possible to calculate the energy level of the quantum-well like transitions. In this case, the transition has an energy of 1.379 eV (899 nm). Using these simulated values, it is now possible to calculate the absorption of these nanostructures.

4.2.3 Absorption coefficient

In the previous section, the wavefunctions and energy levels of carriers in QDs were simulated. A procedure to link those quantities to the absorption coefficient is derived in this section.

The first published absorption coefficient of the InAs/GaAs nanostructures was in 1997 by Cusack [112]. They first used the valence force field methodology to calculate the strain induced potential surrounding the quantum dots. The shape of the quantum dots they assumed was a pyramidal shaped structure of 20 nm width and 2.5 nm height. They then used a four-band Hamiltonian to solve for the wavefunction and energy levels in the structure. They demonstrated that the resulting absorption coefficient is dependent on the direction of the light, and that normal incident light is absorbed strongly. They calculated an absorption coefficient amplitude for their ground state transition of $1.5 \cdot 10^4$ cm^{-1}.

A more complete calculation was completed in 2008 by Tomić [113]. In this study, where they focus on the possibility of intraband transitions for the operation of intermediate band solar cell, they use a 8-band Hamiltoninan to solve Schrödinger's equation. They simulated truncated pyramidal QDs with a 6 nm base and a 3 nm height. Their calculation leads to an absorption coefficient of the order of $3 \cdot 10^3$ cm^{-1}, with a well defined transition at 1.3 eV. Tomić published an extension of this work in 2014 [114]. Again, using a 8-band Hamiltonian, they studied the coupling between the wavefunction of neighbouring QDs. Similarly to the earlier study, they obtained an absorption coefficient amplitude for the ground state transition of $5 \cdot 10^3$ cm^{-1}.

To the best of our knowledge, the only reported experimentally measured absorption coefficient of InAs/GaAs QD was published by Vorobjev in 2007 [115]. Their measured structures were InAs QDs with a 5 nm $In_{0.12}Ga_{0.88}As$ layer grown on top, creating larger QDs. Their ground state transition energy was placed at 1.07 eV at 77K, at a significantly lower energy than the other reported values. Using an incoming light beam aimed at 45° of the sample, the photons passed six times through the QD layer before being collected.

They measure the absorbance of the single layer of QD at 77 K, giving $\alpha \cdot L = 3 \cdot 10^{-4}$. Using their reported QD height of $L = 5.5$ nm, this leads to an absorption coefficient of $\alpha = 5.5 \cdot 10^4$ cm^{-1} for the ground state transition.

With those values in mind,the methodology to calculate the absorption coefficient shall now be derived. This part of the thesis was done in conjunction of a simulation study of quantum dots incorporated in the Sentaurus environment. A very similar derivation can be found in Alex Walker's Ph.D. thesis [40]. The resulting absorption coefficient was used in several papers [80, 116, 117, 118].

The absorption coefficient is defined as the ratio of energy removed from an incident beam of light per unit time and unit volume. It is given by

$$\alpha = \hbar\omega \cdot \frac{R_{i\to f}}{{}^{c}\!/_{n} U_E}, \tag{4.18}$$

where $R_{i\to f}$ is the transition rate due to absorption of photons, ${}^{c}\!/_{n} U_E$ is the energy flux, ${}^{c}\!/_{n}$ is the speed of light in the material and U_E being the energy density of the photon beam.

The transition rate of carriers can be described using quantum mechanics. The transition of electrons from the valence band initial state $|i\rangle$ to the conduction band final state $|f\rangle$ of energy E_f is given by the Fermi's golden rule

$$R_{i\to f} = \frac{2\pi}{\hbar} \sum_f |\langle f|H'|i\rangle|^2 f_i(E_i)\left(1 - f_f(E_f)\right) \tag{4.19}$$

where H' is the perturbed Hamiltonian arising from the interaction of the light, f_i is the Fermi-Dirac probability of having an electron present at energy E_i and $1 - f_f(E_f)$ is the probability of having a hole at energy E_f. The summation $\sum_f$ over all final states f needs to be completed to take into account all possible transitions at the particular energy E_f.

If expanding the Hamiltonian, completing the integration over final and initial states and entering the transition rate back into the definition of the absorption coefficient, the absorption coefficient is now [119]

$$\alpha = A \sum_{\vec{k}} \delta(E_f(\vec{k}) - E_i(\vec{k}) - \hbar\omega) \tag{4.20}$$

where $\delta(E_f - E_i - \hbar\omega)$ is the Dirac delta function forcing the transition to occur between two energy states that equals the photon energy, $\vec{k}$ is the wavevector of the electron, and the constant A is given by

$$A = \frac{\pi q^2 \hbar}{cn\varepsilon_0 m_0^2 \hbar\omega} |P_{cv}|^2. \tag{4.21}$$

In this constant, q is the elementary charge, n is the index of refraction of the material, ε_0 is the vacuum permittivity, m_0 is the electron mass and $|P_{cv}|$ is the dipole matrix element. The dipole matrix element, given by

$$|P_{cv}| = |\langle f|\hat{e}\cdot\vec{p}|i\rangle| \tag{4.22}$$

where $\hat{e}$ is the polarization vector and $\vec{p}$ is the momentum operator, is a quantity that is different for each semiconductor material and can be calculated through numerical methods. In the literature, this matrix element is given by the Kane energy parameter, $E_P = \frac{2|P_{cv}|^2}{m_0}$. The Kane parameter is 22.2 eV for InAs and 25.7 eV for GaAs [120]. A complete derivation is given in appendix A.

The summation over wavevector $\vec{k}$ in Equation 4.20 can be transformed into an integral over energy by using the joint density of states ($JDOS$),

$$\sum_{\vec{k}} \quad \rightarrow \quad \int JDOS(E_{fi})dE_{fi}. \tag{4.23}$$

The absorption coefficient is then given by the combination of the constant A and the joint density of state,

$$\alpha = A\cdot JDOS(\hbar\omega). \tag{4.24}$$

For example, the joint density of states for a bulk material is given by

$$JDOS_{3D}(E) = \frac{\mu\sqrt{2\mu(E-E_g)}}{\pi^2\hbar^3}, \tag{4.25}$$

where E_g is the bandgap of the semiconductor and μ is the reduced effective mass $\frac{1}{\mu} = \frac{1}{m_e^*} + \frac{1}{m_h^*}$.

The absorption coefficient comes from multiple components. First of all, the GaAs layers separating each QD layers contributes to absorption in the structure. These will have the GaAs absorption coefficient. Then, each QD layer is created by the wetting layer and the parabolic QDs. The absorption coefficients of the wetting layer will first be derived, then QDs and then subsequently of the whole structure. Equation 4.24 will be the main equation governing the absorption coefficient of our structures.

The wetting layer, created by the growth of few monolayers of InAs on top of GaAs, creates a potential barrier that is a quantum well. It confines the electrons and holes in the z direction, while no confinements are imposed in the plane. The $JDOS$ of a quantum well is given by

$$JDOS_{QW} = \frac{1}{L}\frac{\mu}{\pi\hbar^2}\sum_n \mathcal{H}(E-En), \tag{4.26}$$

where $\mathcal{H}$ is the Heaviside function, L is the thickness of the quantum well and E_n are the n possible energy transitions calculated for the quantum well.

For each transition n, there is a corresponding wavefunction overlap integral $M = |\langle\psi_e|\psi_h\rangle|$ that was calculated in the previous section. The dipole matrix element, $|P_{cv}|$, contains both the electron and the hole wavefunctions. In the case that was derived earlier, the bulk wavefunction was used. However, in the confined case, the wavefunction of the carriers is defined as the product of the envelope wavefunction ψ and the Bloch wavefunction u. The wavefunctions are now given by $|\Psi_e\rangle = |\psi_e\rangle|u_c\rangle$ and $|\Psi_h\rangle = |\psi_h\rangle|u_v\rangle$. The dipole matrix element is now given by

$$|P_{cv}|^2 = |\langle\psi_e|\langle u_c|\hat{e}\cdot\vec{p}|u_v\rangle|\psi_h\rangle|^2 = |\langle\psi_e|\psi_h\rangle|^2|\langle u_c|\hat{e}\cdot\vec{p}|u_v\rangle|^2 + |\langle\psi_e|\hat{e}\cdot\vec{p}|\psi_h\rangle|^2|\langle u_c|u_v\rangle|^2. \quad (4.27)$$

Because the Bloch wavefunctions u_v and u_c are orthogonal, their overlap is equal to zero, $|\langle u_c|u_v\rangle| = 0$. The dipole matrix element, in our case, is then given by

$$|P_{cv}|^2 = |\langle\psi_e|\psi_h\rangle|^2|\langle u_c|\hat{e}\cdot\vec{p}|u_v\rangle|^2 = |M|^2|P_{cv,bulk}|^2, \quad (4.28)$$

where $|M|^2$ is calculated in the COMSOL simulations.

The wetting layer (WL) absorption coefficient is then given

$$\alpha_{WL} = A\cdot\frac{1}{L}\frac{\mu}{\pi\hbar^2}\sum_n |M_{QW}|^2\mathcal{H}(\hbar\omega - En), \quad (4.29)$$

which gives a stepwise absorption coefficient for each energy level present in the quantum well. Similarly, for a single quantum dot, the absorption coefficient will be given by

$$\alpha_{QD} = \frac{A}{V_{dot}}\cdot\sum_n g_s|M_{QD}|^2\delta(\hbar\omega - E_n), \quad (4.30)$$

where E_n are the possible transitions inside the quantum dot, $|M_{QD}|^2$ is the square of the wavefunction overlap between electron and hole, g_s is the degeneracy of the energy level n and V_{dot} is the volume of the quantum dot. A similar formula was derived in [114].

In the structure, the absorption coefficient of the ensemble of the quantum dot is important. The density of the QDs in the plane has to be taken into account. To generalize the one dot absorption coefficient in Equation 4.30, the absorption coefficient has to be multiplied by the absorption cross section and by the density [121]. Assuming that the absorption cross-section of the QD is equal to its surface area S_{QD},

$$\alpha_{QD} = \frac{A}{V_{dot}}\rho\cdot S_{QD}\sum_n g_s|M_{QD}|^2\delta(\hbar\omega - E_n), \quad (4.31)$$

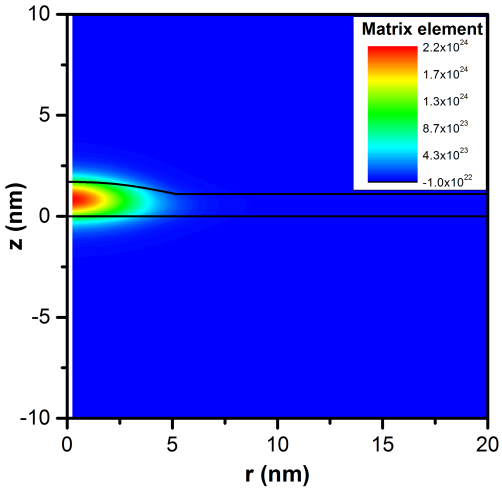

Figure 4.9: Multiplication of the electron and hole wavefunction in the MJSC-920 simulated design. The integration of this quantity gives the optical matrix element $|M|^2$.

where the surface area of a paraboloid dot is $S_{QD} = \pi r^2$ and the density of the quantum dots is denoted ρ. Figure 4.9 shows the multiplication of the electron and hole wavefunction in the quantum dot. Since the multiplication of the electron-hole wavefunction gives a matrix element that is confined to the QD shape, assuming that the absorption cross-section of the QD is equivalent to the surface area of the dot is a good approximation. The amplitude of the matrix element, as shown in the legend, ranges from $-1 \cdot 10^{22}$ to $2.2 \cdot 10^{24}$.

In the current case, either the photons will hit the QD inside its absorption cross-section, or go through only the WL when it is outside the absorption cross-section. As seen in Figure 4.8, a quantum well like wavefunction extends throughout the full plane, QD included. This means that if a photon of enough energy is travelling through the structure, it has a chance to create a transition at any place in the well.

In our system, the size distribution of quantum dots is non-negligible. Because of the spontaneous process of the quantum dot growth, their sizes and shapes will range in a distribution of different QD types. The calculated energy levels E_n will now be considered as a distribution of energies centered around this value. If a distribution of energies of probability $P(E)$ is given, the absorption coefficient of the ensemble of QDs ($\bar{\alpha}_{QD}$) will be [122]

$$\bar{\alpha}_{QD} = \int P(E)\alpha_{QD}dE. \tag{4.32}$$

The distribution of energy levels is considered as a standard normalized Gaussian distribution, given by

$$P(E) = \frac{1}{\sqrt{2\pi}\xi E_n} \mathrm{e}^{-\frac{(\frac{E}{E_n}-1)^2}{2\xi^2}}, \tag{4.33}$$

where E_n is the energy level of the transition and ξ is the relative standard deviation of the said energy level. If this probability distribution is applied to the absorption coefficient of the quantum dots, the equation becomes

$$\bar{\alpha}_{QD} = \frac{A}{V_{dot}\sqrt{2\pi}\xi} \rho \cdot S_{QD} \sum_n \frac{g_s |M_{QD}|^2}{E_n} \mathrm{e}^{-\frac{(\frac{\hbar\omega}{E_n}-1)^2}{2\xi^2}}. \tag{4.34}$$

In the quantum dot of interest, the degeneracy factor g_s is given by $2(l+1)$, where 2 spins and $l+1$ wavefunctions are given in the cylindrical coordinate. It is important to note that the A coefficient, given in Equation 4.21, is a quantity that varies over wavelength. It is inversely proportional to the index of refraction of the material, n_{InAs} in our case. It is furthermore inversely proportional to the energy of the photon, $\hbar\omega$.

The wetting layer is also subject to variation of its thickness over the span of the solar cell. Similarly, if the probability distribution over energies given in Equation 4.33 is applied, the absorption coefficient of the wetting layer is given by

$$\bar{\alpha}_{WL} = A\frac{1}{L}\frac{\mu}{\pi\hbar^2} \sum_n \frac{|M_{QW}|^2}{\sqrt{2\pi}\xi E_n} \int \mathrm{e}^{-\frac{(\frac{E}{E_n}-1)^2}{2\xi^2}} \mathcal{H}(\hbar\omega - E_n) dE. \tag{4.35}$$

A variable transformation and the integral of a Heaviside function with a squared exponential are completed and the final equation for the absorption coefficient of the wetting layer is obtained,

$$\bar{\alpha}_{WL} = A\frac{\mu}{2\pi\hbar^2 L} \sum_n |M_{QW}|^2 \left(1 - \mathrm{erf}\left(\frac{1-\frac{\hbar\omega}{E_n}}{\sqrt{2\xi^2}}\right)\right), \tag{4.36}$$

where erf is the error function, which looks like a smoothed Heaviside function. In the case of the absorption coefficient of the wetting layer, E_n represents the energy levels present in the quantum well. Furthermore, the optical matrix element of the quantum well, $|M_{QW}|$, is dependent on the polarization of the incoming light. Using unpolarized light, the matrix element is integrated over all directions of the polarization vector and gives $|M_{QW}|^2 = 1.5 \cdot |\langle\psi_e|\psi_h\rangle|^2$ [123].

Now that the absorption coefficient of the quantum dots and the quantum well are given, it is necessary to investigate the property of conduction like states. These states are

Transition (n_e, n_h, l)	Energy	Overlap	Deviation
$E_{QD,\,0,0,0}$	1.35 eV (920 nm)	0.86	0.005
$E_{QW,\,0,0,0}$	1.39 eV (888 nm)	0.86	0.015
E_{bulk}	1.42 eV (873 nm)	1	0.01

Table 4.3: Components used in the calculation of the total absorption coefficient in Equations 4.34 and 4.36.

placed above the CBO and VBO in the InAs structure. They are highlighted in Figure 4.3. In this energy range, it is assumed that the absorption coefficient has bulk-like property of the InAs material. The transition between the quantum well-like absorption coefficient and the bulk-like absorption coefficient appears at the GaAs bandgap, at 873 nm. This transition will be applied in a continuous fashion, with an error function similar to the one applied to Equation 4.36.

It is now possible to calculate the absorption coefficient for the QDs contained in the MJSC-920 design. The wavefunctions of the carriers in those nanostructures were shown in the previous section. The transition energies, their wavefunction overlap $|M|$ and their relative standard deviation ξ of the nanostructures are shown in Table 4.3. The quantum numbers for each transition is the energy levels for the electrons n_e and the holes n_l and the principal quantum number l. These were calculated for 300 K. The resulting absorption coefficient of the QD structure is shown in Figure 4.10.

The absorption coefficient at the QD peak is $1.9 \cdot 10^4$ cm^{-1}. It compares well with the absorption coefficients simulated in the literature, $1.5 \cdot 10^4$ cm^{-1} from [112] and $5 \cdot 10^3$ cm^{-1} from [114]. Furthermore, it is similar to the experimentally measured absorption coefficient, $\alpha = 5.5 \cdot 10^4$ cm^{-1}, obtained in [115].

4.2.4 Emission

Radiative recombination in the solar cell is a phenomenon that can be used extensively to study its material properties. This is completed by filling the conduction band with electrons and the valence band with holes. Then, by radiative recombination, the carriers recombine and emit photons.

Electroluminescence (EL) is the phenomenon where material emits light in response to

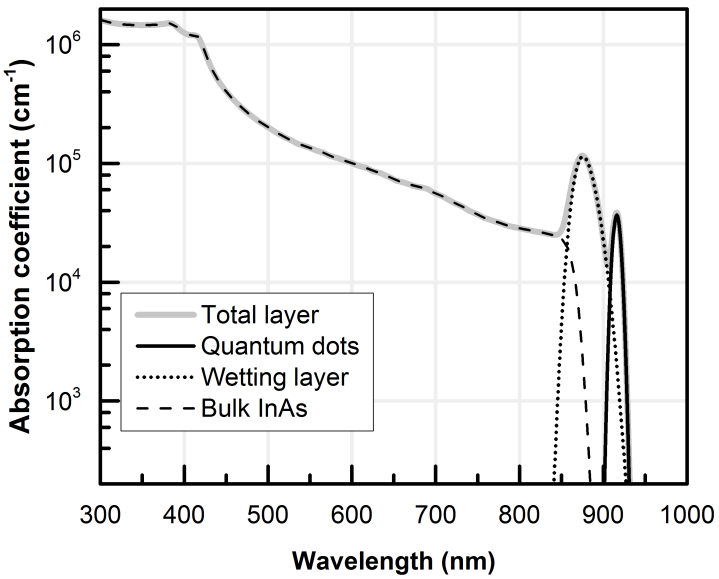

Figure 4.10: Absorption coefficient of QDs contained in the MJSC-920 design calculated in Equations 4.34 and 4.36.

an electric current. In the case of the solar cell, an electric current is driven in forward bias through the semiconductor p-n junction. The said current recombines either radiatively or non-radiatively, mainly in the space-charge region. The radiative recombination can then be collected by a spectrometer. The spectral distribution of the luminescence will be dictated by the bandedge of the semiconductor.

Photoluminescence (PL) is the optical counterpart of electroluminescence. It involves irradiating the semiconductor material with light of energy higher than its bandgap. Each absorbed photon creates an electron-hole pair that relaxes to the lowest available point in the conduction and valence band. The pair subsequently recombines by emitting a photon. The emitted light is then captured by a spectrometer that shows the intensity distribution over wavelength. Again, similarly to the electroluminescence, the spectrum will be dependent on the band structure of the semiconductor.

By using the Fermi's Golden rule, it is possible to evaluate the emission of these nanostructures when their density of states is filled with carriers. For the case of the solar cell, the spontaneous emission rate (r_{sp}) is given by [124, 125]

$$r_{sp}(\hbar\omega) = \alpha(\hbar\omega)\frac{(\hbar\omega)^2}{\pi^2\hbar^3c^2} f_c(E_c)\cdot(1-f_v(E_v)), \tag{4.37}$$

where α is the absorption coefficient of the semiconductor, $f_c(E_c)$ is the probability that an electron is found in the conduction band at the energy E_c, $(1-f_v(E_v)$ is the probability

that a hole is found in the valence band at the energy E_v, $\Delta\mu$ is the quasi-Fermi level split in the semiconductor and $\hbar\omega$ is the photon energy. The quasi quasi-Fermi level split in the semiconductor is given by $\Delta\mu = F_n - F_p$, where F_n and F_p are the electron and hole quasi-Fermi level. The Fermi functions are given by

$$f_c(E_c) = \frac{1}{\mathrm{e}^{\frac{E_c - F_n}{k_\mathrm{B}T}} + 1} \quad \text{and} \quad f_v(E_v) = \frac{1}{\mathrm{e}^{\frac{E_v - F_p}{k_\mathrm{B}T}} + 1} \tag{4.38}$$

This quasi-Fermi level split is either induced by the applied voltage on the structure or by the accumulation of electrons in the conduction band and holes in the valence band by illumination.

Assuming that the semiconductor is undoped, the Fermi functions can be approximated to

$$f_c(E_c) \cdot (1 - f_v(E_v)) \approx \frac{1}{(\mathrm{e}^{\frac{\hbar\omega - \Delta\mu}{2k_\mathrm{B}T}} + 1)^2}. \tag{4.39}$$

For the case of the electroluminescence, the photon emission happens in the space-charge region. Hence, to obtain the complete photon current emitted outside the semiconductor, one has to integrate over the region where photons are emitted and take into account the reflectivity at the surface [124]. The total emission rate (R_{tot}) during EL is given by

$$R_{tot}\left(\hbar\omega\right) = a\left(\hbar\omega\right) \frac{\left(\hbar\omega\right)^2}{\pi^2\hbar^3c^2} \frac{1}{\left(\mathrm{e}^{\frac{\hbar\omega - \Delta\mu}{2k_\mathrm{B}T}} + 1\right)^2}, \tag{4.40}$$

where a is the absorptivity of the region where the emission takes place, the space-charge region in this case. The absorptivity is given by

$$a = (1 - R) \cdot (1 - \mathrm{e}^{\alpha x_{scr}}) \tag{4.41}$$

where R is the reflectivity of the semiconductor structure, α is the absorption coefficient of the space-chage region and x_{scr} is its thickness.

The contribution of each component is shown in Figure 4.11. The EL is given by the multiplication of the absorptivity a, the prefactor given by $\frac{(\hbar\omega)^2}{\pi^2\hbar^3c^2}$ and the Fermi-Dirac distribution given by $\frac{1}{\left(\mathrm{e}^{\frac{\hbar\omega - \Delta\mu}{2k_\mathrm{B}T}} + 1\right)^2}$. The absorption coefficient was assumed to be the one shown in Figure 4.10. Twenty layers of QDs were simulated inside the structure of the single junction GaAs solar cell. The quasi-Fermi level split originating from the excitation was assumed to be 1.5 V. The scale of the EL and the prefactor were changed for clarity purposes. As can be seen in the figure, the EL shape is determined mostly by the quasi-Fermi level position and the absorptivity.

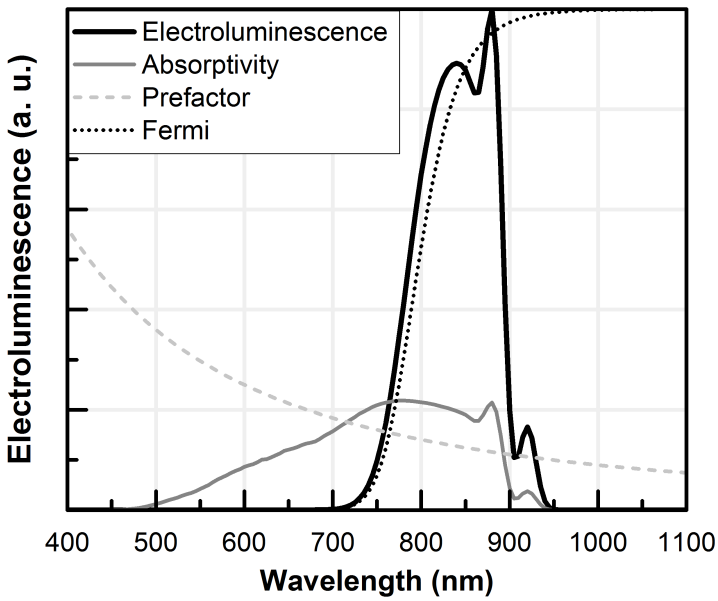

Figure 4.11: Calculated electroluminescence of 20 layers of QDs in the single junction GaAs cell, demonstrating the effect of each component in the calculation.

The ASD FieldSpec Spectroradiometer [126] is used to obtain the spectrum of the EL. It detects light in the range of 300 to 2500 nm and is calibrated for the light guide used. It can be used for detection of broadband source, with a resolution of 7 nm.

The measured EL spectrum of the single junction GaAs solar cell (SJ-ref) is shown in Figure 4.12. It was taken for a current of 100 mA applied to the solar cell. The calculated spectrum using Equation 4.40 is shown as well. Both peaks were normalized for comparison purposes. The EL peaks have a similar shape. Both spectra have a similar width of the peak.

Hence, for a given absorption coefficient of the nanostructure, it is possible to calculate the expected emission, either from PL or from EL. It shall be used to compare the QD simulation results to an experimentally measured spectrum. Then, after confirmation that the simulated absorption coefficient gives emission properties that corresponds to the measured spectrum, it shall be applied to the EQE simulation.

4.3 Quantum dot-enhanced single-junction solar cell

In the QD-enhanced single junction solar cells that are studied in the current thesis, two different shapes of QDs are used. As mentioned in Section 4.1.1, the QDs were either

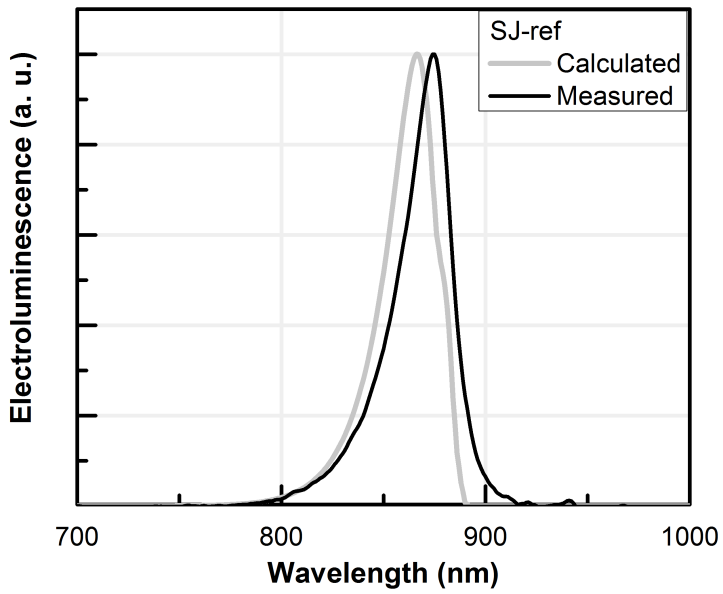

Figure 4.12: Measured and calculated electroluminescence of the single junction GaAs solar cell (SJ-ref), with 100 mA applied.

Parameter	Symbol	Value
QD density	ρ	$5 \cdot 10^{10}$ cm^{-2}
QD radius	r	5.5 nm
QD height	L	2.5 nm
QW thickness	T	1.3 nm

Table 4.4: Nanostructure parameters and dimensions for the SJ-A design.

indium flushed after a 2.5 nm GaAs layer (sample SJ-A) or a 5 nm GaAs layer (sample SJ-B). The number of layers grown is 20 layers of QDs in a 660 nm intrinsic layer.

A TEM measurement of a QD receiving a 2.5 nm indium flush is shown in Figure 4.13. The approximate values for the QD parameters obtained from this TEM are shown in Table 4.4. The surface density of the QDs were measured by Jihène Zribi by an atomic force microscopy (AFM) measurement. A density of $5 \cdot 10^{10}$ cm^{-2} was measured.

4.3.1 Absorption coefficient

The resulting structure was simulated in COMSOL, using the band offsets and effective masses shown previously in Table 4.1 . In the simulation, one bound electron wavefunc-

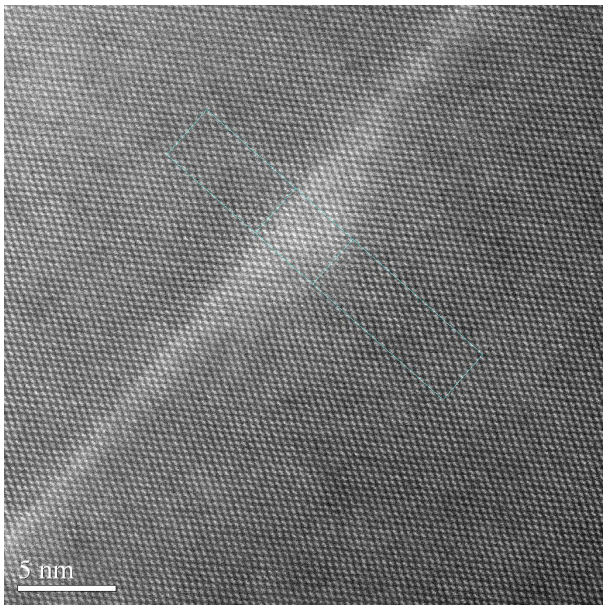

Figure 4.13: TEM of a single indium flushed QD after deposition of a 2.5 nm GaAs layer in the single junction solar cell. Courtesy of Jihène Zribi from the Université de Sherbrooke.

tions for $l = 0$ is obtained. Furthermore, three bound hole wavefunctions, two for $l = 0$ and one for $l = 1$, are simulated. The $l = 1$ wavefunction will not make transitions with the other electron wavefunctions since it has a different quantum number. The transition between a bound state and a quantum well state are assumed to be negligible [127].

The resulting energy transitions, at 300 K, are shown in Table 4.5. The quantum numbers for each transition is the energy levels for the electrons n_e and the holes n_l and the principal quantum number l. These quantities are then used to obtain the related absorption coefficient for the 2.5 nm QD layers (sample SJ-A). The resulting absorption coefficient is shown in Figure 4.14a.

The other type of QDs that were grown in the single junction solar cells are QDs that have received an indium flush at 5 nm. The said indium flush did not change the optical property of the QDs that were grown without the flush. However, their properties started to change as soon as the indium flush was done at 4 nm [128]. For this reason, the height of these dots was assumed to be 4 nm, while keeping the radius and the quantum well (QW) height the same. These dimensions are summarized in Table 4.6. The resulting structure was simulated in COMSOL, using similar band offsets and effective masses as before. In the simulation, bound electron wavefunctions are obtained at $l = 0$ and at

Transition (n_e, n_h, l)	Energy	Overlap	Deviation
$E_{QD,\,0,0,0}$	1.23 eV (1005 nm)	0.91	0.02
$E_{QD,\,0,1,0}$	1.29 eV (961 nm)	0.35	0.02
E_{QW}	1.34 eV (925 nm)	0.76	0.02
E_{bulk}	1.42 eV (873 nm)	1	0.01

Table 4.5: Energy transitions and wavefunction overlap used in the calculation of the absorption coefficient of the QDs in the SJ-A design at 300 K.

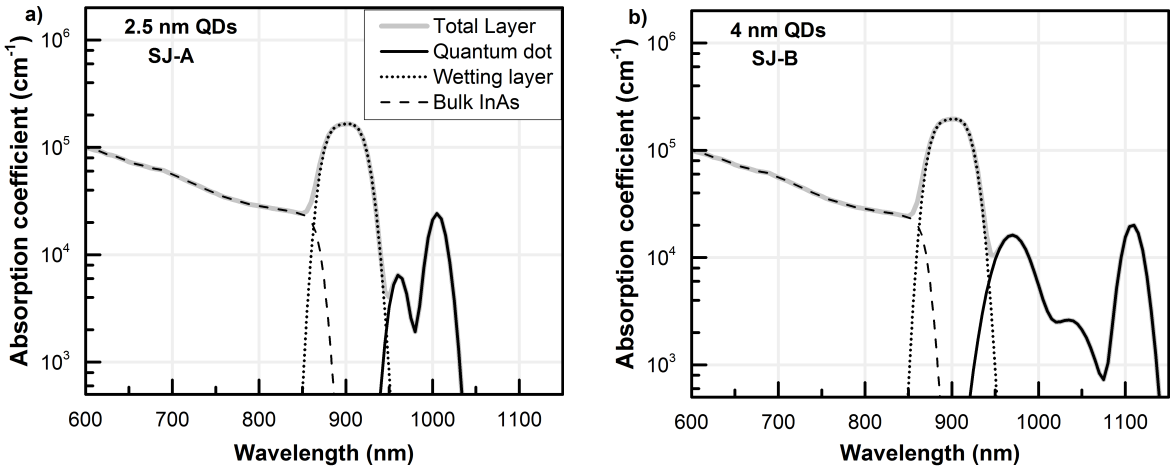

Figure 4.14: Absorption coefficient of the QDs (a)2.5 nm height for SJ-A and b) 4 nm height for SJ-B) grown in the single junction GaAs solar cell.

Parameter	Symbol	Value
QD density	ρ	$5 \cdot 10^{10}$ cm^{-2}
QD radius	r	5.5 nm
QD height	L	4 nm
QW thickness	T	1.3 nm

Table 4.6: Nanostructure parameters and dimensions for the SJ-B design.

$l = 1$. Furthermore, four bound hole wavefunctions are obtained, two for $l = 0$, one for $l = 1$ and one for $l = 2$. The $l = 2$ wavefunction shall not make transitions with the other electron wavefunctions since it has a different quantum number. The transition between a bound state and a quantum well state are assumed to be negligible.

The resulting energy transition components, at 300 K, are shown in Table 4.7. These quantities are then used to obtain the related absorption coefficient for the 4 nm QD layers (sample SJ-B). The resulting absorption coefficient is shown in Figure 4.14b.

Comparing the two absorption coefficient, notable differences appear. First, three peaks associated to QD transitions are visible in the absorption coefficient of the sample SJ-B while only 2 are seen for the sample SJ-A. It is because the SJ-B QDs are large enough to contain a $n_e = 1$ electronic state. In this case, the transition between the $n_e = 1$ and $n_h = 1$ states is possible, while it was not present in the SJ-A case.

Both absorption coefficient shows a peak that corresponds to a transition between the $n_e = 0$ and $n_h = 1$ states. This peak has a significantly lower wavefunction overlap. In a quantum system with a paraboloic potential, these transition between different quantum numbers would be forbidden. However, because our potential profile is different, these transitions become allowed.

Both samples have a ground QD transition of similar amplitude in absorption coefficient. The difference in wavefunction overlap ($|M| = 0.95$ for SJ-B and $|M| = 0.91$ for SJ-A) originates from the difference in the confinement of the wavefunctions. In the SJ-A case, the electron wavefunction is more extended in space than in the SJ-B case, giving rise to a lesser wavefunction overlap.

Transition (n_e, n_h, l)	Energy	Overlap	Deviation
$E_{QD,\ 0,0,0}$	1.12 eV (1108 nm)	0.95	0.02
$E_{QD,\ 0,1,0}$	1.19 eV (1037 nm)	0.36	0.02
$E_{QD,\ 0,0,1}$	1.28 eV (969 nm)	0.80	0.02
E_{QW}	1.34 eV (925 nm)	0.90	0.01
E_{bulk}	1.42 eV (873 nm)	1	0.01

Table 4.7: Energy transitions and wavefunction overlap used in the calculation of the absorption coefficient of of the QDs in the SJ-B design

4.3.2 Electroluminescence

The EL of the two QD-enhanced single junction solar cells were measured by the calibrated ASD spectrometer. A constant current of 100 mA was applied at room temperature, and the corresponding spectrum was obtained by aiming the collecting fiber of the spectrometer at the sample. The resulting spectrum for the samples containing the 2.5 nm QDs (SJ-A) and the 4 nm QDs (SJ-B) are shown in Figures 4.15a and b respectively. The maximum of the calculated peak is placed at a longer wavelength. This is due to a calculated energy level that is lower than the actual energy level in the system. The position of the measured energy peak for the SJ-A design is 1006 nm (1.23 eV) while the calculated peak is placed at 1023 nm (1.21 eV). The position of the measured energy peak for the SJ-B design is 1113 nm (1.11 eV) while the calculated peak is placed at 1126 nm (1.10 eV). The difference between the two peaks, on the order of 20 meV, is considered small because of the multiple approximations needed to calculate the energy levels in the QDs, such as assuming constant potentials in the structure and a 1-band effective mass approximation.

The interesting feature that is visible in the SJ-A solar cell's spectrum is the secondary peak seen in the 930 nm region. The peak, visible in both the measured and the calculated spectrum, is due to the non-negligible population of the quantum well state by the EL. A third peak is visible in the measured spectrum, at 875 nm, while it is not seen in the calculated spectrum. The peak comes from luminescence from the bulk GaAs semiconductor. Another important difference between the measured and calcu-

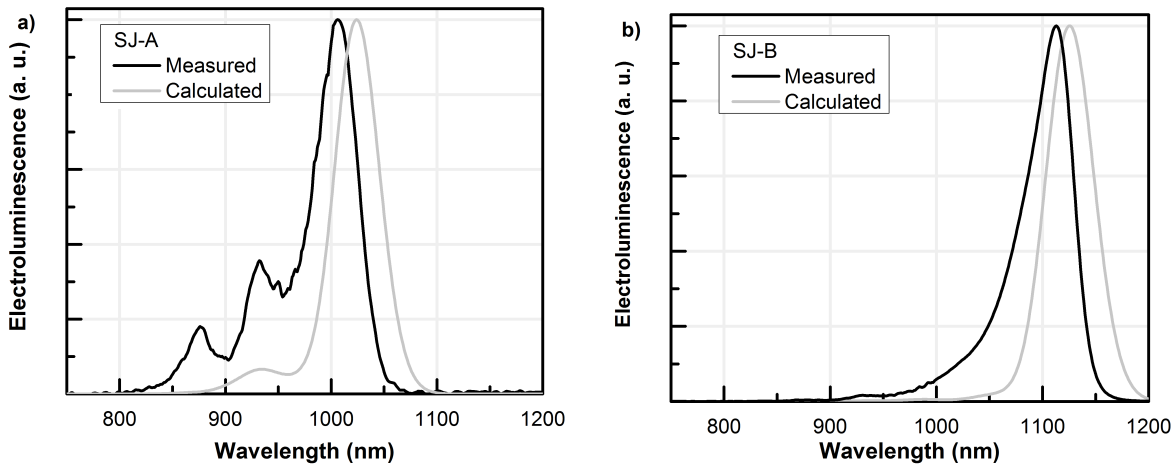

Figure 4.15: Measured and calculated electroluminescence of the QD enhanced single junction solar cells of a) sample SJ-A and b) SJ-B. The current that was applied to the cell was 100 mA. The spectrums were normalized to the highest value of the 20 layer spectrum.

lated spectrum in both the SJ-A and the SJ-B cells is the linewidth. In both cases, the calculated spectrum had a much more abrupt low-wavelength tail.

The calculated model assumes that the carriers always populate the lowest energy levels possible, while there is a non-negligible probability that the carriers escape the QD at any given time [129]. Furthermore, in the measured case, the carriers have a non-negligible lifetime in the excited states. For example, it has been calculated that the intraband relaxation between the excited p orbital and the ground s state is on the order of 10 ps [129]. Because of this, carriers that populates higher energy levels has a higher chance to radiatively recombine than in the calculated case. This is one reason why the measured EL demonstrates a higher intensity for the low-wavelength tail.

Furthermore, as will be evidenced by the EQE study done in the next section, the 1-band effective mass model underestimates the quantity of excited states present in the system. As evidenced in [127], multiple energy levels are bound in the system. They are calculated by the 8-band Hamiltonian, which takes into account the interactions between each carrier states. There is furthermore a possibility that the strain-induced potentials in the QDs creates localised states over the CBO, the so-called strain-induced localised states [130]. Finally, possible valence band mixing or coupling between quantum well and dot increase the quantity of available energy levels between the ground state and the quantum well state [66]. This demonstrates the limits of the 1-band model used in this

thesis. Even though it is capable of deriving the ground state energy level and absorption coefficient to a good approximation, it is limited in its capacity to calculate the excited energy levels and their effects on the luminescence properties.

4.3.3 External quantum efficiency

The absorption coefficient derived in the previous section can now be applied in the simulation of the quantum efficiency of solar cells. The quantum dots are grown in the intrinsic region, or space-charge region, of the solar cell. The simulation of the EQE in this layer of the solar cell is calculated using Equation 2.36, as

$$\mathrm{EQE}_{scr}(\lambda) = q\left(1 - R\left(\lambda\right)\right)\mathrm{e}^{-\alpha(\lambda)x_i}, \tag{4.42}$$

where $x_i = x_{scr} + w_i$ is the total intrinsic region thickness, with the thickness of the additional intrinsic region growth, w_i, and the space-charge region x_{scr} created in the base and emitter layers calculated in Equation 2.27. The absorption coefficient α is given either for the GaAs spacer layers or the QD layers.

For example, Figure 2.20c shows the EQE simulation of the GaAs solar cell (SJ-ref) shown in Section 2.4.4. The effect of the addition of 20 layers of QDs is now simulated. These QD layers will use the properties introduced earlier in the COMSOL simulation as well as their corresponding absorption coefficient. The effective thickness of the QD layers is 1.3 nm. For 20 layers of QDs, 26 nm of the effective QD medium has to be calculated. The intrinsic layer thickness for the 20 layers QD enhanced solar cell is 660 nm. The equation governing the EQE of the intrinsic region of the GaAs solar cell is now

$$\mathrm{EQE}_{scr}(\lambda) = q\left(1 - R\left(\lambda\right)\right)\mathrm{e}^{-\alpha_{GaAs}\cdot 634\mathrm{nm}}\mathrm{e}^{-\alpha_{QD}\cdot 26\mathrm{nm}}. \tag{4.43}$$

In this equation, it is assumed that no recombination losses due to the confinement potential occurs. Hence, in the simulation, all of the carriers absorbed by the nanostructures will escape the confinement and be collected.

The resulting calculated EQE of the sample SJ-A (20 layers, 2.5 nm height dot), along with the original measured EQE in light grey, is shown in Figure 4.16. The measured EQE of the single junction GaAs subcell without added QD (SJ-ref) is shown as well for comparison purpose. The addition of the QDs increases the absorption range of the solar cell towards longer wavelength.

As can be seen in a), the amplitude of the EQE in the bulk region (mainly from 700 to 800 nm) is increased for the QD-enhanced cell compared to the reference case. This

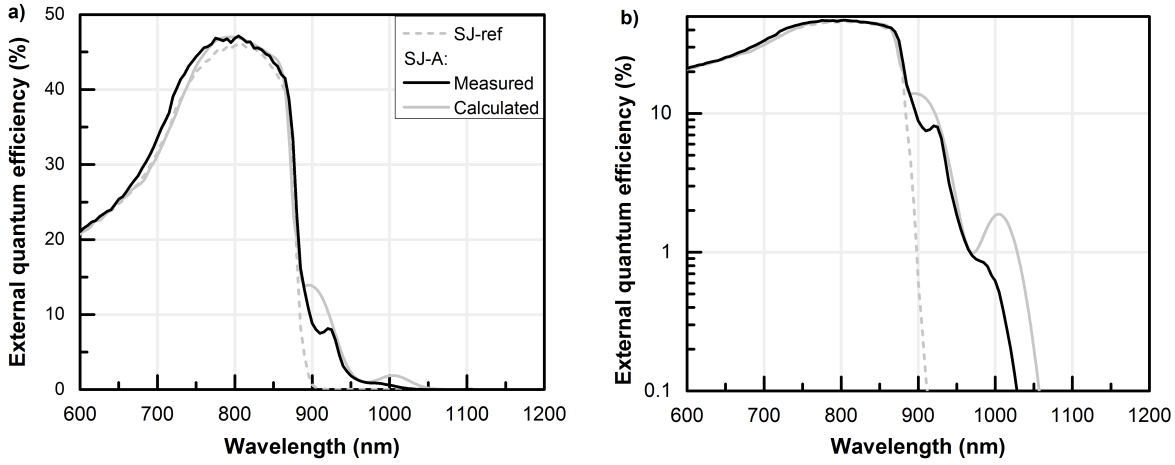

Figure 4.16: Measured and calculated EQE of the QD enhanced single junction solar cell sample SJ-A (20 layers, 2.5 nm height QDs) compared to the reference single junction GaAs solar cell (SJ-ref). a) is the normal scale to show the general EQE trend while b) is on a logarithmic scale to emphasis the nanostructure's effect.

is due to the addition of the InAs layers in the intrinsic region of the cell in both the measured and the calculated case. The InAs nanostructures have a higher absorption coefficient than GaAs, and create this small increase in the EQE in this region.

The shape of the EQE in the nanostructure region, from 900 to 1100 nm, follows the same trend for both the measured and the calculated regime. Both EQE showcase a wetting layer peak, situated around 920 nm, and a QD peak situated around 1000 nm. One important difference, however, lies in the amplitude of both peaks. The measured peaks are significantly lower than the calculated one, as emphasised by the logarithm scale in Figure 4.16b. The assumption that all carriers created in the space-charge region are collected as current is the principal cause of this difference. As demonstrated in [80], the addition of nanostructures creates a non-negligible amount of recombination in those layers which reduces the amplitude of the EQE peaks. In [66], where the effect of the addition of quantum wells in GaAs solar cell was studied, they added a multiplicative factor f for the carriers created in the nanostructures to take the non-negligible recombination into consideration. However, since there is no analytic relationship between the recombination rate and the said multiplicative factor, the methodology will refrain from using it as a fitting tool. Hence, the calculated EQE overestimates the contribution from the nanostructures.

The Figure 4.17 shows the calculated and measured EQE of SJ-B (20 layers, 4 nm

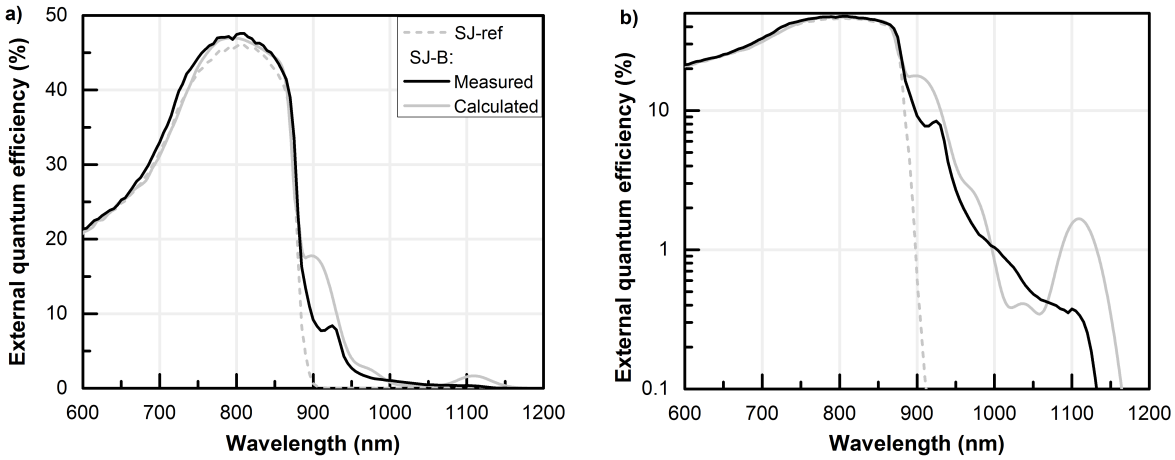

Figure 4.17: Measured and calculated EQE of the QD enhanced single junction solar cell SJ-B (20 layers, 4 nm height QDs) compared to the reference single junction GaAs solar cell (SJ-ref). Subfigure a) is the normal scale to show the general EQE trend while b) is on a logarithmic scale to emphase the nanostructure's effect.

height dot). Similarly to the 2.5 nm QD height sample, the amplitude in the bulk region is higher for the QD enhanced sample. Furthermore, both the measured and the calculated EQE follows a similar trend in the 900 to 1200 nm region, with the quantum well peak positioned at 925 nm and a QD peak at 1100 nm. Again, the simulated QD and QW peaks are significantly higher in amplitude than the measured peaks, due to the recombination rates in the nanostructures not reflected in the simulation.

An interesting difference arises in the region between the QW and the QD peaks, from 950 to 1050 nm. In this region, the calculated EQE does not follow the smooth line of the measured EQE. The oscillations in this region are principally due to the excited peaks (the cross-transition at 1037 nm and the $l = 1$ transition at 969 nm) seen in Table 4.7. It furthermore has a lesser value between 1000 and 1050 nm. This seems to contradict the conclusion that the calculated EQE is overestimated. However, as was demonstrated in the previous section on EL, the 1-band simulation underestimates the available energy levels above the ground state energy level. This shall increase the absorption coefficient, and the EQE, in the 950 to 1050 nm region. Hence, the model is not adequate to accurately predict states that lie between the ground state energy level and the quantum well energy level.

4.4 Quantum dot-enhanced multijunction solar cell

In this section of the chapter, the QD-enhanced MJSC shall be studied. Two different samples, with different QD sizes, are examined. These samples are labeled as a function of their QD peak in the EQE, with MJSC-920 having a QD peak at approximately 920 nm and MJSC-970 at 970 nm. These were graciously given by Cyrium Technologies as part of the SUNRISE research project.

The complete structure of these cells is unknown, and no TEM measurement is available. For this reason, it is not possible to infer the QD sizes and simulate their corresponding energy levels. Hence, the extensive use of PL spectroscopy will allow us to estimate the QD structure and its corresponding absorption coefficient. These shall then be used to calculate the EQE and compare to the experimentally measured EQE shown in Figure 4.2.

4.4.1 Photoluminescence of quantum dots

The PL setup present in the SUNLAB was built as a collaboration effort between the author and Jamie Brar as part of the work for her masters thesis [44]. In simple words, the experimental setup consists of a laser which is directed towards the solar cell sample. The solar cell emits light that is then collected and directed towards a spectrometer that measures the corresponding spectrum.

Experimental setup

Figure 4.18 shows the schematic of the experimental setup. Two continuous wave lasers are installed on the optical table. The first is a 500 mW ND:YAG 532 nm solid state laser from Changchun Optoelectronics Technology (MLL532). The second is a 100 mW solid state 785 nm laser from Pavillion Integration Corporation (W785-100FS). The power of these lasers was controlled by the addition or removal of reflective neutral density filters (Newport FR-ND) placed in front of the lasers. Combinations of multiple optical densities, ranging from optical density (OD) 3 to 0.1 are used to precisely control the power on the sample.

The chosen laser beam is directed towards a beamsplitter. The said beamsplitter is an OD 0.3 reflective neutral density filter, which transmits $10^{-0.3} \approx 50\%$ of the light and reflects $\sim 50\%$. A silicon photodiode coupled with a power meter is placed behind the beamsplitter to continuously measure the laser power that is received on the sample

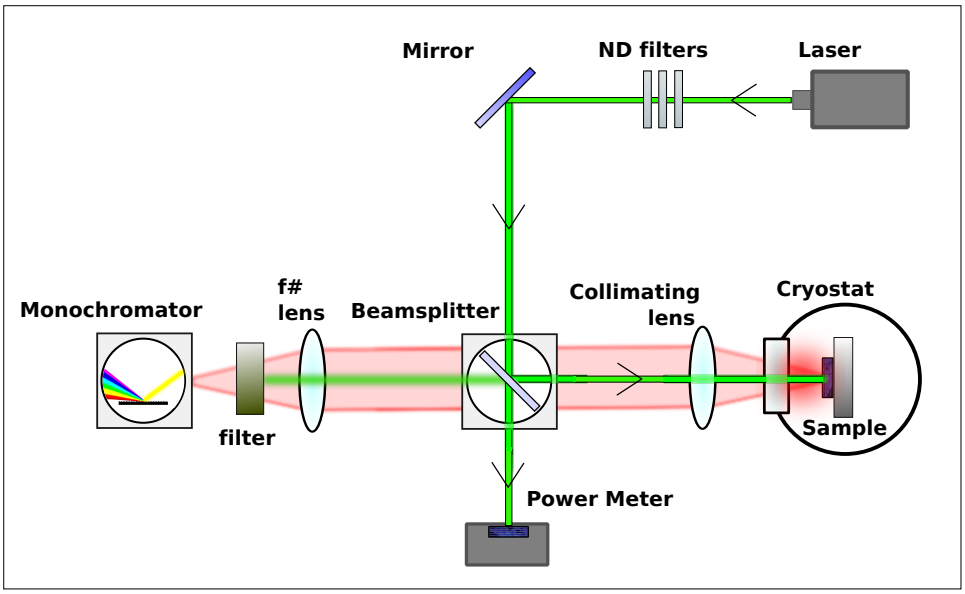

Figure 4.18: Schematic of the photoluminescence experimental setup.

(Newport 842-PE with 918D-SL-OD3). A conversion factor is used to estimate the difference between the measured power behind the beamsplitter and the actual power hitting the sample. The beamsplitter redirects half of the laser beam towards a focusing lens.

A biconvex lens of 7.56 cm focal length is placed in front of the cryostat containing the solar cell sample. This lens is used to focus the $\sim$ 2 mm laser beam into a focused 80 µm diameter point [44].

The solar cell sample is mounted in a cryostat from Cryo Industries of America (ND 1100H). It consists of a copper cold finger that is the sample holder which is connected to a liquid nitrogen reservoir. This holder contains a 50 ohm heater coupled to a resistance temperature detector. The structure is placed in a isolated cavity in which a high vacuum is created. A turbo pump coupled to a mechanical pump (Agilent turbo-V 81-M and DS42) is used to evacuate all air down to a pressure of 1 mTorr in the cryostat. This ensures that no possible condensation is created on the sample surface when it is brought to liquid nitrogen temperatures. The temperature of the sample was controlled continuously between 77 K and 400 K by the liquid nitrogen and the temperature controller (CryoCon 32B). The laser beam has to go through an UV grade fused silica window before hitting the solar cell sample.

The light hitting the semiconductor is absorbed and PL is emitted. The emitted light is recollected by the 7.56 nm lens and directed towards the beamsplitter. Again,

half of the light passes through and the other half is lost. The light is finally collected by the f# matching lens, which focuses the photoluminescence in the spectrometer. As mentioned in Section 2.3.1, a well matched lens is necessary for the optimal operation of the spectrometer, which is 10 cm in this case.

For the measurement with the 532 nm laser light, a 550 nm longpass filter (Edmund Optics NT62-984) is installed directly after the focusing lens. This filters all the light that is of lower wavelength than 550 nm, and has a flat transmission at wavelengths between 550 and 1600 nm. The PL taken using the 532 nm laser light is not shown in the current thesis, but demonstrated similar behavior as the 785 nm one.

Finally, the emitted PL is collected by the spectrometer. In this thesis, a Horiba Jobin Yvon iHR320 spectrometer coupled with a liquid nitrogen cooled charge coupled device (CCD) detector and a liquid nitrogen cooled InGaAs array detector was used. For the experiments shown in the thesis, solely the CCD detector was used. The functioning principles is similar to the spectrometer described in Section 2.3.1 for the EQE system. Three diffraction gratings are available: grating I with 600 grooves/nm and a 1000 nm blaze, grating II with 600 grooves/nm and a 1500 nm blaze and grating III with 1200 grooves/nm and a 500 nm blaze. The grating I was used for all the measurements in the current thesis.

For each measured spectrum of PL, the stray light spectrum has to be substracted. This stray light spectrum is taken when the laser is turned on, but without the semiconductor sample. Most of the stray light created by the laser inside the spectrometer is measured. Each subsequent PL spectrum is measured, and the stray light spectrum is subtracted.

Figure 4.19a shows a raw photoluminescence spectrum. It consists of 15 averaged spectra taken with the CCD detector and an integration time of 0.01 s. The spectrum is from the MJSC-920 sample, illuminated with the green laser beam of 793 μW. Even though the QD peak is observed, the shape of the spectrum is influenced by multiple other constituents of the setup. The emitted light has to pass through the UV grade silica window, the 7.56 cm collecting lens, the OD 0.3 beamsplitter, the 10 cm f# lens and the 550 nm longpass filter before being collected in the spectrometer. Furthermore, in the spectrometer, the mirrors, the 500 nm blazed grating and the CCD detector all have different spectral efficiencies. Because of these components, the raw collected photoluminescence spectrum shall be different than the one emitted.

These spectral modifications are corrected by calibrating the system using a calibrated white light source (Newport 6334 QTH 250 W source). The spectrum of the said white

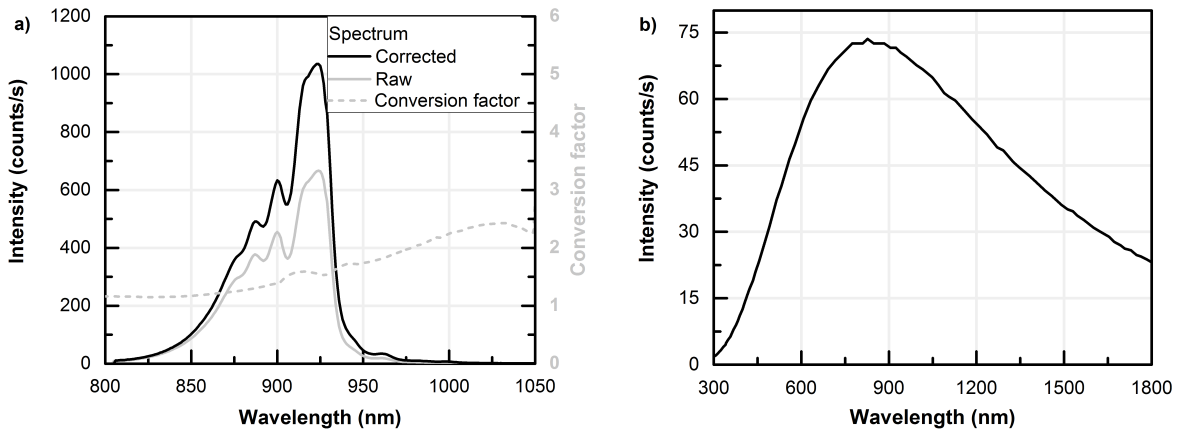

Figure 4.19: a) Raw spectrum of QD photoluminescence from sample MJSC-920, along with the conversion factor used to obtain the corrected spectrum. b) QTH white light source spectrum used to calculate the conversion factor.

light source is shown in Figure 4.19b and corresponds to a 3500 K blackbody radiation source. Hence, before each photoluminescence measurements, a spectrum of the white light source is obtained, and the resulting collected raw data is used to calculate a calibration curve for the system. Figure 4.19a shows the corrected spectrum on top of the raw photoluminescence data with the corresponding conversion factor as the dashed line.

Sample MJSC-970

To ensure a maximal PL collection efficiency of the QDs in the middle subcell, the top-most layers in the MJSCs were removed in the samples. The ARC and top subcell were removed through chemical etching, courtesy of Artur Turala at the Nanofabrication and Nanocharacterization Research Center at the Université de Sherbrooke. The photoluminescence of the samples was obtained by shining a laser directly onto the middle subcell layers.

To investigate the different energy levels in the nanostructures, intensity dependent photoluminescence is completed. By increasing the intensity of the laser beam, the quantity of electron-hole pairs created increases proportionally. Hence, by having a higher intensity laser hitting the semiconductor sample, the quasi-Fermi level split $\Delta\mu$ increases. By increasing the quasi-Fermi level split, luminescence from the higher energy level states in the system becomes visible.

The intensity dependent photoluminescence of the first sample, the MJSC-970 solar

cell, is shown in Figure 4.20a. The sample was installed in the cryostat and cooled down to 77 K. The solar cell sample was excited by the 785 nm laser over intensities ranging from 1.11 to 310 μW. The spectrum was obtained using the grating I and the CCD detector, 0.01 s of integration time and averaged over 15 measurements. Each spectrum was corrected for the spectral dependence of the optics in the system using the white light source.

The main QD peak at 77 K is placed at 920 nm. This means that the ground state energy transition is at 1.34 eV. At lower intensities of illumination, a non-negligible peak is measured at 874 nm. This corresponds to an excited state in the QD. As the intensity of the laser beam increases, the electron-hole pairs completely fill the QD energy levels and an emission peak starts to be measured at 850 nm. This demonstrates the filling of the ground state energy level. This emission comes from the wetting layer energy states.

By looking carefully at the main QD peak, one can notice oscillations in the curve. These are not unique energy levels. As evidenced by Equation 4.40, the reflectivity of the structure has an influence on the luminescence. In fact, light emitted by the quantum dots undergoes constructive and destructive interference by the reflection from the front and the back of the GaAs layers. Hence, the oscillations observed in the PL spectrum are due to the internal reflections inside the structure.

Because no size measurements on these quantum dots are available, contrarily to the single junction QD samples, assumptions concerning their physical properties need to be made. The Table 4.8 shows the physical parameters used in COMSOL to obtain a similar ground state and wetting layer state energy emission at 77 K. The resulting energy levels in the system are given in Table 4.9. For this geometry, only states for the quantum number $l = 0$ are bound, and only one excited hole energy level at $n_h = 1$ is bound. It is interesting to note that even though only the ground state of the QD was used to obtain the structure, the excited state at 876 nm corresponds to the one measured in the PL spectra.

It is important to remember that the label MJSC-970 is for the absorption property at 300 K. The variation of the energy levels over temperature is the next topic of investigation.

The calculated emission property of the nanostructures using Equation 4.40 is shown in Figure 4.20b for quasi-Fermi level splits ranging from $\Delta\mu = 1.24$ to 1.42 eV. It was calculated using the standard MJSC structure, with 100 QD layers incorporated into the intrinsic region of the middle subcell. The resulting spectra demonstrate similar behavior as the measured data in Figure 4.20a. At low intensities, solely the QD peak is observed.

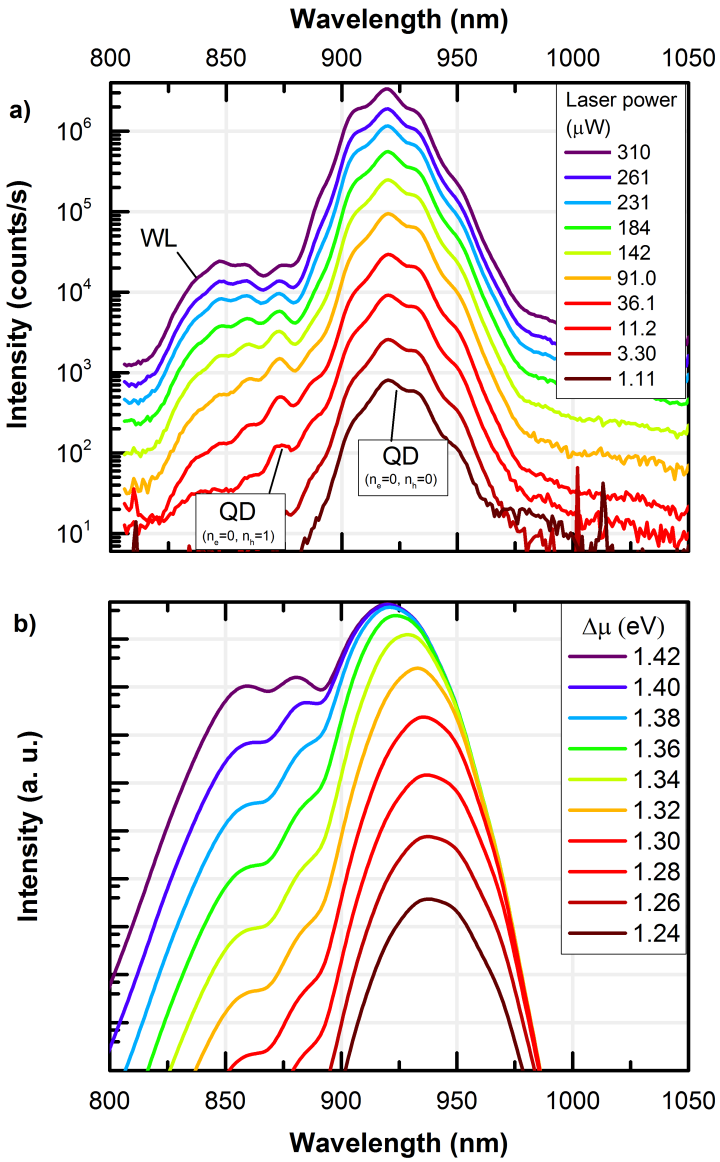

Figure 4.20: a) Intensity dependant PL of the MJSC-970 sample at 77 K. The labels represent the QD ground transition ($n_e = 0$ and $n_h = 0$), the QD excited transition ($n_e = 0$ and $n_h = 1$) and the transition from the WL. b) Calculated PL of the MJSC-970 sample at 77 K over different excitation intensities. The quasi-Fermi level split $\Delta\mu$ is given in eV.

Parameter	Symbol	Value
QD density	ρ	$1.25 \cdot 10^{10}$ cm^{-2}
QD radius	r	5.2 nm
QD height	L	2.3 nm
QW thickness	T	1.11 nm

Table 4.8: Nanostructure parameters and dimensions for the MJSC-970 design.

Transition (n_e, n_h, l)	Energy	Overlap	Deviation
$E_{QD,\,0,0,0}$	1.34 eV (920 nm)	0.90	0.01
$E_{QD,\,0,1,0}$	1.41 eV (876 nm)	0.16	0.01
E_{QW}	1.46 eV (846 nm)	0.70	0.01
E_{bulk}	1.51 eV (823 nm)	1	0.01

Table 4.9: Energy transitions and wavefunction overlap used in the calculation of the emission and absorption properties of the MJSC-970 quantum dots at 77 K.

As the intensity of the laser is increased and the quasi-Fermi level split is increased, the energy transition at 876 nm becomes apparent. Furthermore, the QW energy transition becomes apparent for quasi-Fermi level split of 1.30 eV and higher.

An important difference is observed at higher laser intensities and higher quasi-Fermi level splits. In the calculated figure, as the quasi-Fermi level split increases for values of 1.40 eV and higher, the QD peak stops increasing in intensity, whereas the other peaks increases. On the other hand, the measured QD peak continues to increase even though the QW peak becomes visible.

This difference comes from the limitation of the laser in the experiment. The focused laser beam has a Gaussian shape. Hence, the intensity of the laser beam is different between the center of the beam and the outer limit. As the power of the laser is increased, the QDs placed in the middle of the beam will have a higher quasi-Fermi level split than the ones at the outter limit. For this reason, the QDs in the middle will become 'saturated' first and their emission peak will stop increasing in intensity like the calculated figure. However, when this happens, the QD situated in the outskirts of the laser beam have less power impinging on them, and hence have a lesser quasi-Fermi level split. At this intensity, those QDs will not be saturated and their emission peak shall still be increasing. For this reason, the QD peak can increase in intensity over laser power even though the quasi-Fermi level split allow transitions from the higher energy transitions in the system.

Now that the nanostructures optical properties have been simulated at low temperatures, these quantities shall be simulated towards higher temperatures. Figure 4.21a displays the behavior of the measured photoluminescence of MJSC-970 over temperature. Similarly to the intensity dependent photoluminescence, the MJSC-970 cell was installed in the cryostat and cooled down to 77 K. The spectrum was obtained using the grating I and the CCD detector, 0.01 s of integration time and averaged over 15 measurement and finally corrected for the spectral dependence of the optics in the system using the white light source. Each spectrum is taken at a different temperature, ranging from 100 to 300 K. Spectra were taken up to 400 K and demonstrated a similar trend as observed in the figure. However, they are not shown, for clarity purpose.

The QD photoluminescence peak shifts towards longer wavelengths as the temperature is increased. This is due to the bandgap dependence over the temperature. The strained InAs bandgap follows the Varshni relationship.

The intensity of the main QD peak decreases over temperature. Equation 4.40 governs

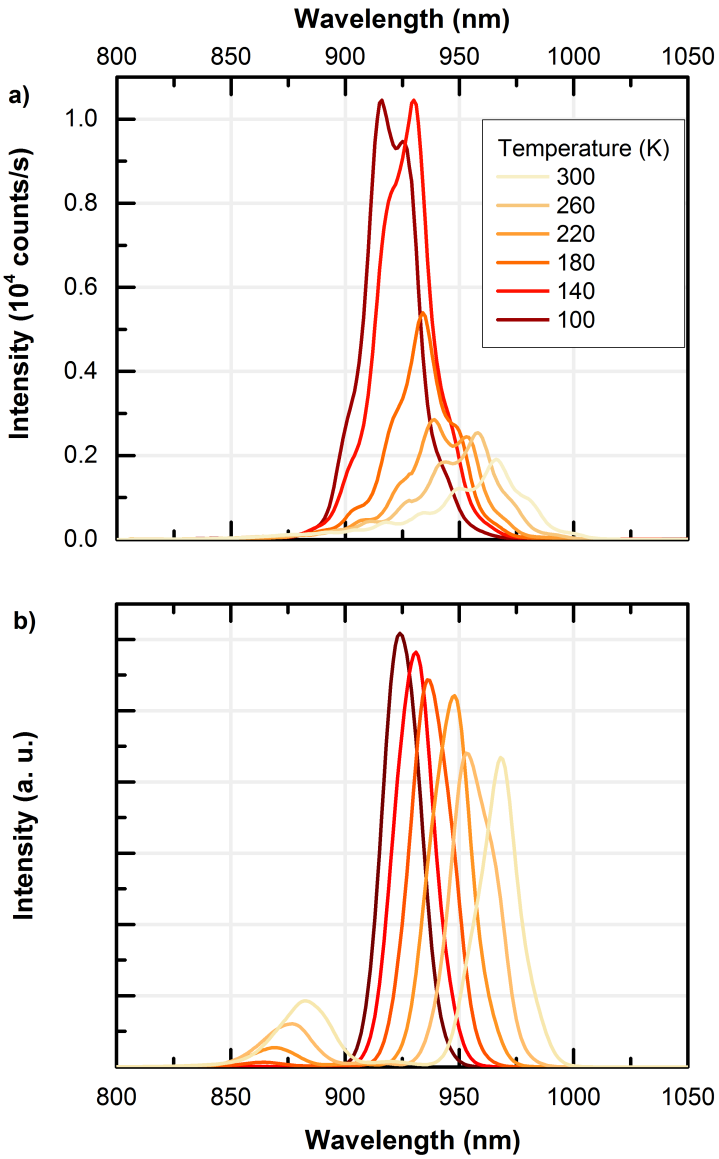

Figure 4.21: a) Measured temperature dependent PL of the MJSC-970 sample excited by 300 µW 785 nm laser light. b) Calculated temperature dependent PL of the MJSC-970 sample. The used quasi-Fermi level split $\Delta\mu$ is 1.36 eV.

the emission from the semiconductor and the Fermi-Dirac term, $\frac{1}{\left(e^{\frac{\hbar\omega-\Delta\mu}{2k_BT}}+1\right)^2}$, should make the emission increase as the temperature is increased. For all temperatures, the laser intensity was kept the same. Hence, the quantity of electron-hole pairs created by the laser is constant throughout the temperature range studied. For this reason, the quasi-Fermi level split $\Delta\mu$ decreases as well as the temperature is increased. To a first approximation, the quasi-Fermi level split shall follow a Varshni relationship that is similar to the bandgap of the semiconductor.

The calculated emission spectrum as a function of temperature is shown in Figure 4.21b. The quasi-Fermi level split used in the equation was 1.36 eV for the initial 77 K spectrum. It was subsequently adjusted at each temperature so that the total emitted photons is the same for all temperature. It was done by calculating the carrier concentration for the quasi-Fermi level split of 1.36 eV at 77 K, then subsequently calculating the quasi-Fermi level split necessary to recreate the same carrier concentration over different temperatures. The QD peak follows the same trend in both the calculated and the experimental case. The position of the calculated peak is placed at 971 nm at 300 K while the experimental peak is at 967 nm. This result will be useful when the emission peaks will be correlated with the EQE of the MJSC.

One major difference lies in the higher emission energies. The experimental photoluminescence at 300 K is maximal at 967 nm and continuously decreases at smaller wavelengths. The calculated luminescence, on the other hand, has 2 major peaks, one for the QD and one for the QW. This demonstrates again that the model does not take into account multiple available energy levels between the ground QD energy and the QW energy levels. This was highlighted in Section 4.3 for the electroluminescence of single junction GaAs solar cell.

Another interesting difference is the intensity of the QD peak. From the 100 K to the 300 K spectrum, the amplitude of the QD peak decreases by 82 % in the experimental measurement while it only decreases by 29 % in the calculated case. The main reason comes from the increased non-radiative recombination at higher temperatures. As the temperature is increased, carriers are allowed to thermally escape from the QD into the GaAs barrier material, where they have a higher probability of being lost to non-radiative recombination [131]. This quenching occurs at a certain activation energy that correlates with the barrier height [132]. Hence, a more complete model would take into account the possibility of exchange of carriers between the GaAs and the QD layers.

Now that the calculated emission properties have been shown to corresponds to the

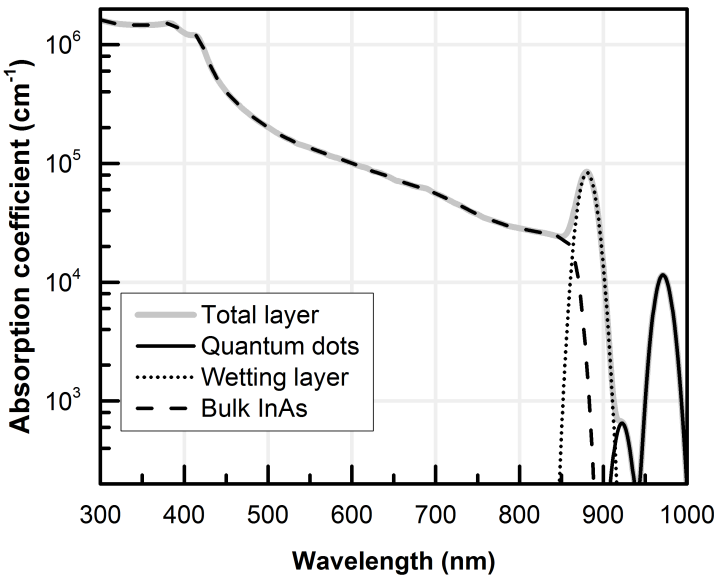

Figure 4.22: Absorption coefficient of QDs contained in the MJSC-970 design calculated in Equations 4.34 and 4.36.

measured PL, the absorption coefficient of the nanostructures can be derived. In Section 4.2.3, the absorption coefficient of the QDs contained in the MJSC-920 design was obtained. In a similar procedure, the absorption coefficient of the nanostructures in the MJSC-970 design is calculated. The transition energies, the wavefunction overlap $|M|$ and the relative standard deviation ξ of the nanostructures are shown in Table 4.9. These are used in Equations 4.34 and 4.36. The resulting absorption coefficient of the QD structure is shown in Figure 4.22.

Sample MJSC-920

The intensity dependent photoluminescence of the final sample, the MJSC-920 solar cell, is shown in Figure 4.23a. The sample was installed in the cryostat and cooled down to 77 K. The solar cell sample was excited by the 785 nm laser over intensities ranging from 1.22 to 309 μW. The spectra were obtained using the grating I and the CCD detector, 0.01 s of integration time and averaged over 15 measurements. Each spectrum was corrected for the spectral dependence of the optics in the system using the white light source.

In this case, the main QD peak is placed at a wavelength of 868 nm, or 1.43 eV. This energy peak is measured at 77 K, while at room temperature the emission peak shall translate to approximatively 920 nm. Contrarily to the MJSC-970 sample, the wetting

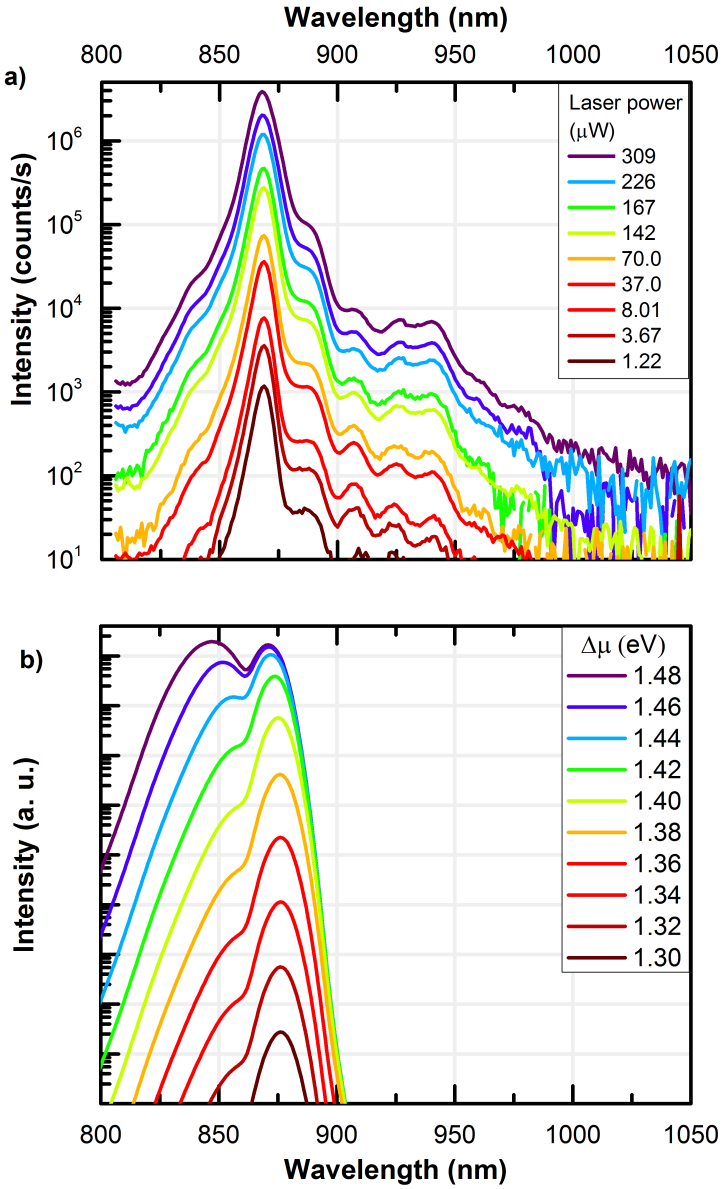

Figure 4.23: a) Measured intensity dependant photoluminescence of the MJSC-920 Sample at 77 K. b) Calculated PL over different excitation intensities of the MJSC-920 sample at 77 K . The quasi-Fermi level split $\Delta\mu$ is given in eV.

layer energy peak is not clearly observed from the intensity dependent PL. While it is expected to be placed at 850 nm, only a small increase in this energy level range is seen in the spectra. For this particular experiment, the quasi-Fermi level split created by the laser is not large enough to effectively saturate the energy levels in the QDs.

Furthermore, there are interesting features in the luminescence spectrum in the higher wavelength range. Non-negligible emission is observed in the wavelength range between 900 and 950 nm. This emission comes from larger nanoislands. It is possible, under certain growth conditions, that a bimodal composition of QD sizes is created [82]. The creation of small and large dots of different densities depends mainly on the InAs coverage and its growth rate [133]. To have emission in this wavelength range, according to COMSOL simulations, their radii need to be at least 20 nm if their height is kept the same as the smaller dots. These larger QDs are of significantly lower densities, and shall have a negligible contribution to the EQE of the solar cell.

The COMSOL simulations of these types of QDs was completed in the Section 4.2.3 of this thesis. It was used to derive the absorption coefficient given in Figure 4.10. This particular QD size was used as a demonstration because the main product from Cyrium showcases similar QDs compared to this MJSC-920 sample. Only one energy state is bound, at quantum numbers $n_h = 1$, $n_e = 0$ and $l = 0$. For the transition at 77 K, the QD peak is placed at 875 nm and the QW peak is placed at 846 nm.

The calculated emission property of the nanostructures using Equation 4.40 is shown in Figure 4.23b for quasi-Fermi level splits ranging from $\Delta\mu = 1.30$ to 1.48 eV. It was calculated again using the standard MJSC structure, with 100 QD layers incorporated into the intrinsic region of the middle subcell. In this case, the QW energy level present at 850 nm becomes important at higher quasi-Fermi level, unlike what was measured. No emission at wavelengths in the range of 950 nm is observed since the larger QD ensemble is not taken into account in the simulation.

An important difference between the two simulations is the fact that only one energy transition in the QD is calculated for the MJSC-920 calculation, while the MJSC-970 had one additional energy transition at higher energies (1.41 eV). Comparing the MJSC-920 Figure 4.23 and the MJSC-970 Figure 4.20, at higher intensities the MJSC-970 spectrums has an additionnal peak at 876 nm. This additional transition reproduces more accurately the behavior of the experimentally measured photoluminescence in this wavelength region. Again, this demonstrates the limitation of the model to calculate allowed excited energy transitions in the QDs.

The measured PL of MJSC-920 over different temperature is shown in Figure 4.24a.

The experimental measurement is completed similarly to the temperature dependant PL of MJSC-970.

The calculated emission spectrum as a function of temperature is shown in Figure 4.24b. The quasi-Fermi level split used in the equation was 1.36 eV for the initial 77 K spectrum. Similarly to the MJSC-920 calculation, it was subsequently adjusted at each temperature so that the total emitted photons is the same for all temperature.

The QD peak follows the same trend in both the calculated and the experimental case. The position of the calculated peak is placed at 923 nm at 300 K while the experimental peak is at 924 nm. Again, the calculated emission property demonstrates similar properties as the MJSC-970 Figure 4.21. The calculated luminescence has 2 major peaks, one for the QD and one for the QW, while the measured case shows continuous luminescence from the QD ground state to lower wavelengths. The decrease in the QD's peak intensity is only 48 % while it is 87 % for the experimental case.

4.4.2 External quantum efficiency

Now that the QD absorption model has been introduced and that it reproduces the behavior of the emission of solar cell over intensities and temperature, it shall now be applied to the EQE simulation. The comparison of the calculated emission properties to the measured spectra was necessary to create an adequate model for the absorption coefficient.

The measured EQE of sample MJSC-970 is shown in Figure 4.25a, along with the 300 K PL spectrum. A clear correlation between the emission property of the QDs and their absorption is observed in the figure. The emission peak, centered at 967 nm, corresponds to the absorption peak centered at 966 nm in the EQE. The continuous absorption from the quantum dots between the bandgap of the GaAs matrix, at 873 nm, and the QD ground state is an indication that the density of states over the ground state energy level is non-negligible.

Both PL and EQE peaks associated to the QDs are expected to be at similar energies. Differences between the position of the ground QD energy peak of the photoluminescence and the photocurrent have been measured in the literature [134]. They are due to the carrier redistribution among the QDs. In PL measurements, if the thermal energy is high enough, the carriers can redistribute themselves into different QDs. In a layer with different QD sizes, the carriers generally distribute themselves into the lower energy QDs first. Hence, if only the QDs of the lowest ground energy level are populated, the PL peak

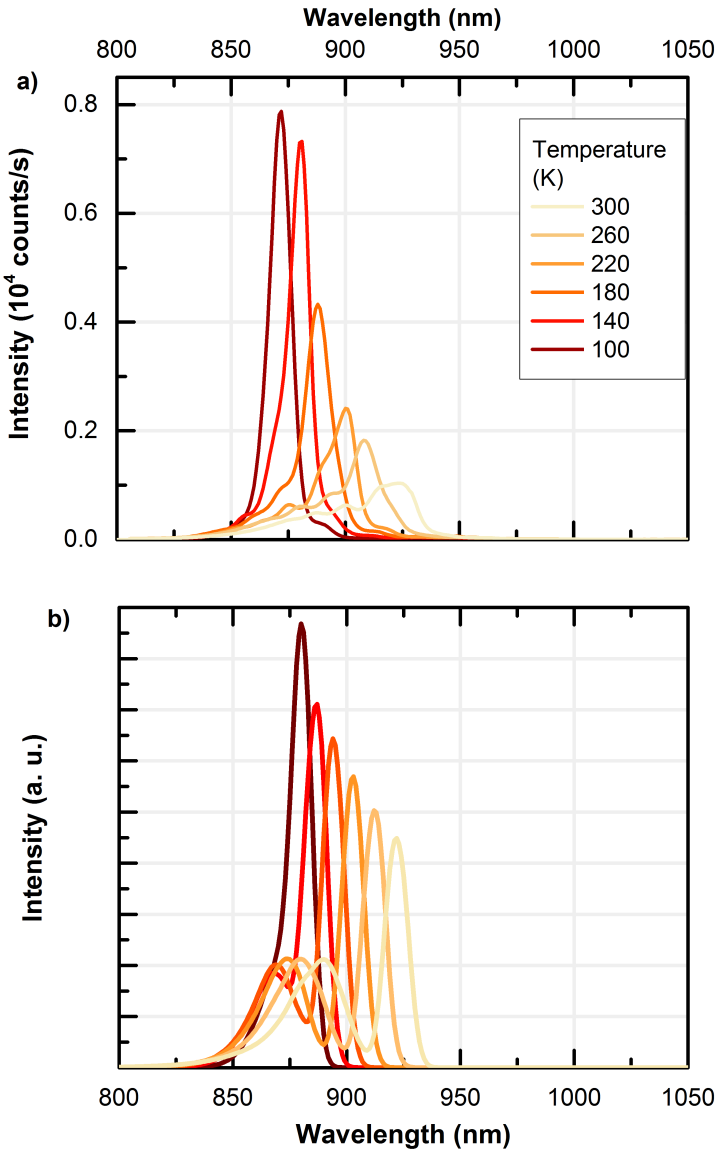

Figure 4.24: a) Measured temperature dependant photoluminescence of the MJSC-920 sample excited by 300 µW 785 nm laser light. b) Calculated photoluminescence of the C920 sample over different temperature. The used quasi-Fermi level split $\Delta\mu$ is 1.36 eV.

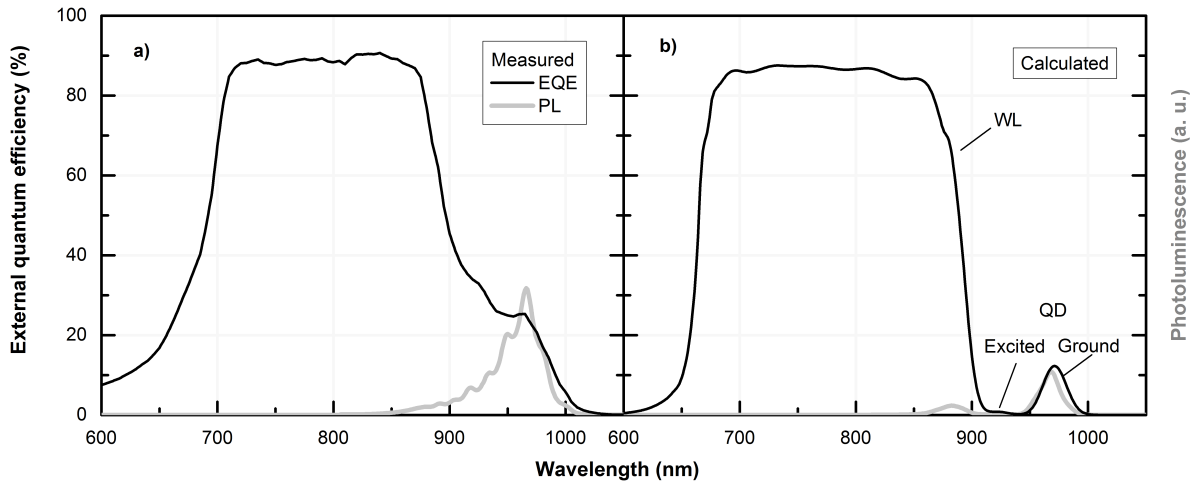

Figure 4.25: a) The measured EQE of MJSC-970 along with its corresponding PL spectrum. b) The calculated EQE, using the standard structure in Table 2.7 and the QD's absorption coefficient shown in Figure 4.22.

will be centered towards lower energies, while the absorption peak will be unaffected. The expected energy difference between those two peaks is 10 meV, or approximatively 6 nm in this wavelength range.

In the current PL experiment, however, the QD was illuminated with a high power laser. The ground state energy level is saturated for the measurement at 300 uW. Hence, carrier redistribution is not possible in our luminescence measurement, and the PL peak is expected to be at the same energy as the EQE peak.

The calculated EQE of the middle subcell of sample MJSC-970 along with the calculated PL is shown as well in Figure 4.25b. It was calculated using the standard multijunction solar cell structure given in Table 2.7, with the exception of the addition of an intrinsic layer in the middle subcell. This intrinsic layer was assumed to be 1 μm thick, and contains 100 layers of QDs. To conserve the total thickness of the standard solar cell, the GaAs base of the middle subcell was reduced by 1 μm.

The calculated EQE shows a clear peak in the QD ground state region, and subsequently goes down to 0. It then has a small peak of 1 % at the second bound energy transition at 925 nm. It finally goes back up to values similar to the bulk GaAs EQE in the wavelength range of the quantum well transition, at 890 nm. The difference between the calculated and measured EQE demonstrates the importance of taking into account the energy states between the ground QD state and the wetting layer state.

The amplitude of the calculated QD peak is significantly lower than the measured

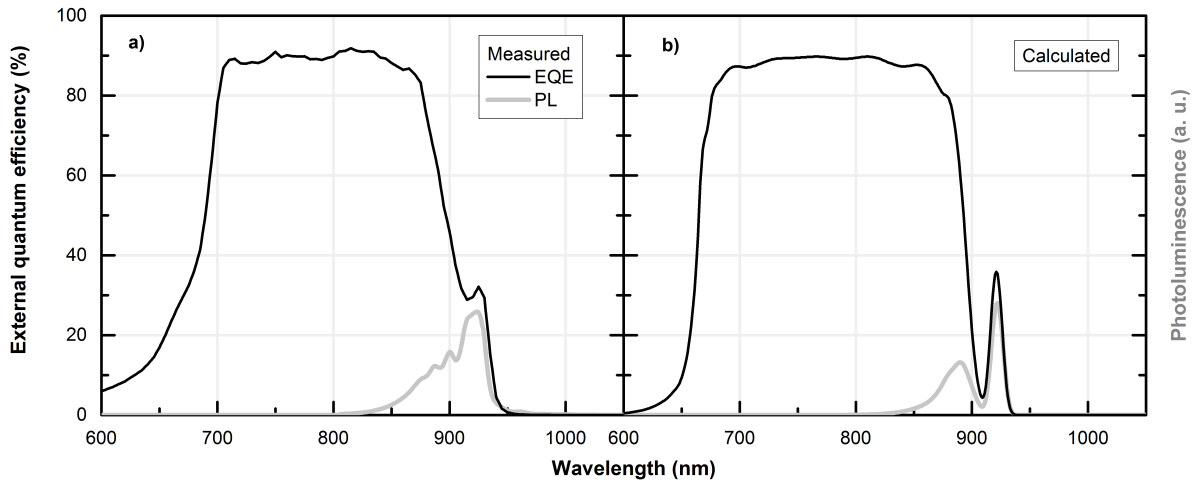

Figure 4.26: a) The measured EQE of MJSC-920 along with its corresponding PL spectrum. b) The calculated EQE, using the standard structure in Table 2.7 and the QD's absorption coefficient shown in Figure 4.10

QD peak. However, because of the unknown number of layers in the structure and the unknown QD density, the 100 layers and density of $1.25 \cdot 10^{10}$ cm^{-2} were chosen was an arbitrary quantity. These values correlate well within the more sophisticated Sentaurus-based simulations completed in the laboratory [40]. The amplitude of the QD peak is expected to vary significantly as a function of these two quantities.

The resulting EQE of the C920 sample and its corresponding 300 K photoluminescence is shown in Figure 4.26. Both the measured EQE and PL peaks are positioned at 925 nm. This time, the calculated EQE demonstrate a behavior that is much more close to the experimentally measured EQE. The QD peak is placed at 921 nm, then drop slightly before the wetting layer absorption increases the EQE. Because the QD peak is much closer to the QW peak in this case, the quantity of allowed energy transition is less in this case. For this reason, the model reproduces accurately the EQE of the QD enhanced solar cell for high QD energies.

Using this developped absorption coefficient, it is possible to quantify the contribution of the QDs in the middle subcell's EQE. In the calculated QD-enhaced EQE of MJSC-920, the addition of 100 layers of QDs increased the J_{sc} of this subcell by 1.2 mA/cm^2. For the MJSC-970 desgin, the J_{sc} increase was 0.93 mA/cm^2. Interestingly, the smaller increase in current from the MJSC-970 design comes from the contribution of the AM1.5D spectrum. As can be seen in Figure 1.7, the direct solar spectrum has an absorption band in the 930-970 nm region. For this reason, the QDs that absorb in the 920 nm region are

better suited for the absorption of the solar spectrum than the QDs that absorb in the 970 region.

Using a more sophisticated simulation technique, it is possible to calculate the contribution of these layers to the overall efficiency of the device, as in [116]. It is not possible using the model proposed in this thesis, since no recombination was assumed in the QDs. The goal of the current chapter was to explain and derive the contribution of the QDs to the EQE of the GaAs subcell.

4.5 Conclusion

This chapter studied an important feature in the EQE that was not taken into account in the initial model, the QD absorption peak. As highlighted in the EQEs shown in Figure 2.24, the absorption of the standard middle subcell extends only up to 900 nm. However, as demonstrated by the experimentally measured EQE of QD-enhanced MJSCs shown in Figure 4.2, the addition of QDs can extend the absorption range up to 970 nm.

The electronic structure of InAs/GaAs QDs was obtained using a finite element solver, COMSOL. The simulation was completed by assuming strain dependant conduction and valence band offsets and the 1-band effective mass Schrödinger's equation. The electron and hole wavefunctions for each QD sizes were obtained and their corresponding wavefunction overlap and energy levels were calculated. Subsequently, those quantities were used to calculate the absorption coefficient of the nanostructures. Furthermore, the equations calculating the emission properties of the QDs were derived.

The QD model was subsequently applied to a single-junction QD-enhanced GaAs solar cell. The EL of the solar cell was measured, and the simulated emission properties were compared to the experiment. Subsequently, the measured EQE of the QD-enhanced GaAs solar cells demonstrated the additionnal photon absorption by the QDs. The model accurately reproduced the behavior of QDs in the EQE of the solar cell.

Then, the QD-enhanced MJSC was studied. First, because no physical measurements of the QDs were available for the samples, their properties were obtained differently. The intensity dependent PL was measured and the QD ground energy levels and the QW energy level were obtained. Then, using these values, their size and absorption properties were derived using the COMSOL simulation. The emission properties over intensities and over temperature were calculated and compared to the experimentally measured spectra. Finally, the measured EQE of the solar cells were compared to the calculated EQEs with their corresponding QDs. The model reproduced the EQE of the

QD enhanced solar cell MJSC-920. However, the MJSC-970 sample demonstrated the limitation of the model in calculating the excited energy levels.

The absorption coefficient derived in this thesis was used extensively in the complete numerical simulation of QD-enhanced solar cell in Sentaurus. This simulation work was part of Alex Walker's thesis [40]. It was first used to demonstrate the increased performance of the MJSC due to the addition of QDs in the middle subcell [80]. Then, the optimal number of QD layers in the system was derived in [116]. The behavior of the carrier dynamics in the QD enhanced MJSC over concentration was shown in [118]. Finally, the importance of the correct positioning of the QD layers was demonstrated in [117].

Chapter 5

The bottom subcell artifact

An important component of the EQE of a MJSC is the 'bottom subcell artifact'. It consists of a non-zero value for the EQE of the bottom subcell when it is probed in the middle subcell wavelength region. As seen in Figure 5.1, where the EQE of sample MJSC-920 is shown, it is visible as the EQE of the bottom subcell in the wavelength range of 600 to 900 nm. On paper, the bottom subcell should not be absorbing photons that are in this wavelength range. The middle subcell is thick enough to absorb all of these photons, and none should be capable of reaching the bottom subcell.

This artifact either comes from internal voltage biasing between each subcell or comes from light coupling between the middle and bottom subcell. In this chapter, each hypothesis is studied. An experimental procedure using the fill-factor bias (FF-bias), proposed by Cyrium Technologies [39], is used to independently separate the effect of both the internal biasing and the light coupling.

5.1 Internal voltage biasing

In an EQE measurement, light bias is applied to the solar cell so that the subcell of interest is current-limiting. The additional chopped monochromatic light will be absorbed by the measured subcell and will create an additional alternating photocurrent that can be measured.

During the operation of an EQE measurement, the external voltage applied on the MJSC and the operating voltage of each subcell are different. If the total voltage is 0, it does not necessarily mean that the internal applied voltage on each subcell is 0. Because the sum of each subcell's voltage is equal to the total voltage, they are correlated. If 2

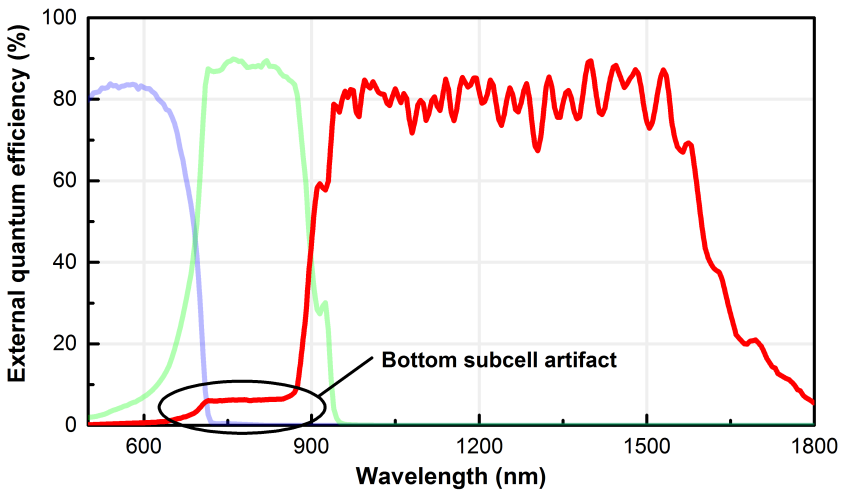

Figure 5.1: External quantum efficiency of sample MJSC-920, where the bottom subcell's artifact is highlighted.

subcells are illuminated while the 3$^{\text{rd}}$ is not illuminated, the 2 subcells will operate near their V_{oc} while the 3$^{\text{rd}}$ will be reverse biased by $V = V_1 + V_2$. Hence, it is possible that this internal biasing will have an effect on the measured photocurrent.

The initial explanation of the EQE measurement artifact was published by Meusel in 2003 [37]. They calculate the J-V curve of each subcell under bias illumination. They did so using the 2 diode model, including the series and shunt resistances, given by

$$J(V) = J_{light} - J_{01}\left(\mathrm{e}^{\frac{qV+JR_s}{k_{\mathrm{B}}T}} - 1\right) - J_{02}\left(\mathrm{e}^{\frac{qV+JR_s}{k_{\mathrm{B}}T}} - 1\right) - \frac{V + JR_s}{R_{shunt}}, \tag{5.1}$$

where J_{light} is the photo-generated current density, J_{01} is the dark current density coming from radiative recombination, J_{02} is the dark current density generated by the Schockley-Read-Hall (SRH) recombination in the junction, R_s is the series resistance and R_{shunt} is the shunt resistance [9]. This technique shall be reproduced in this chapter to explain and study the internal voltage biasing .

For a given voltage, the current density J that solves the Equation 5.1 is found by a root of nonlinear function numerical technique. Then, each individual J-V curve is calculated numerically with step-wise increase in voltage. The triple junction J-V curve is calculated by adding the voltages of each subcells,

$$V_{MJSC}(J) = V_{top}(J) + V_{mid}(J) + V_{bot}(J). \tag{5.2}$$

This creates the full J-V curve under illuminated bias. Then, to calculate the EQE, the measured subcell's photocurrent is increased by $\Delta J = 0.5$ mA/cm^2. The MJSC's

Subcell	Top	Middle	Bottom
J_{01} (A/cm^2)	10^{-24}	10^{-17}	10^{-7}
J_{02} (A/cm^2)	$1.7 \cdot 10^{-15}$	$1.6 \cdot 10^{-9}$	10^{-5}
J_{light} (A/cm^2)	0.128	0.124	0.187
R_s (Ω cm^2)	0.001	0.004	0.009
R_{shunt} (Ω)	20000	50000	2000

Table 5.1: *J-V* curve parameters used in the two-diode model calculations.

J-V curve is then recalculated under this new applied photocurrent. To obtain the EQE, the original and the new MJSC curves are substracted, giving the alternating current that would be measured, and subsequently dividing the result by the initial applied photocurrent of 0.5 mA/cm^2. This quantity will be refered as the photocurrent proportion, $\frac{\Delta J}{\Delta J_{photo}}$. Ideally, this quantity would be 1 if all the photocurrent created by the subcell is converted into the measured EQE. For the subcells not under test, this quantity should be 0.

The parameters used to trace each individual *J-V* curves are shown in Table 5.1. They are obtained by using an experimental fitting procedure that will be introduced in Section 5.3 of this chapter.

Figure 5.2a shows the top, middle and bottom subcell's *J-V* curves under light bias as the blue, green and red curves respectively. The total MJSC *J-V* curve, calculated by the sum of each subcell's voltage, is shown in light grey. The dashed lines are the *J-V* curves under the additional oscillating photocurrent for the EQE measurement. For demonstration purposes, the shunt resistance of the bottom subcell was decreased to 500 Ω and the middle subcell's series resistance was increased to 40 Ω. This additionnal series resistance is not realistic. An added series resistance would be applied for the complete structure. However, in this case, it is only applied to the middle subcell to demonstrate the difference between having a large series resistance (middle) or a negligible series resistance (top). Because the bottom subcell is measured, its photocurrent was reduced to 2 mA/cm^2. An additional photocurrent of 0.5 mA/cm^2 is used to measure the bottom subcell's EQE.

It is assumed that the measurement is taken at $V = 0$. Hence, the measured EQE shall be equivalent to the difference in current measured at $V = 0$ on the MJSC's *J-V* curve. Under these conditions, the applied voltage on each subcell is shown as the dots

on the *J-V* curves. The voltage applied on the MJSC is $V = 0$ while the internal applied voltages are $V = 1.30$ for the top subcell, $V = 0.56$ for the middle subcell and $V = -1.86$ for the bottom subcell.

Figure 5.2b shows the bottom subcell's *J-V* curve near the operating voltage point while Figure 5.2c shows the top and middle *J-V* curves near their operating voltage points. The arrow labeled as 1 shows the increase of 0.5 mA in the bottom subcell's photocurrent. Looking at the top subcell's curve in Figure 5.2c, the increase in the photocurrent has negligible effect on its operating voltage. On the other hand, the operating voltage of the middle subcell is decreased by approximately 0.02 V because of the additional series resistance. This decrease in the operating voltage of the middle subcell leads to a decrease in the operating voltage of the bottom subcell highlighted by the arrow 2 in Figure 5.2b. Because the bottom subcell has a non-negligible shunt resistance, the decrease in voltage leads to a decrease in the current density, as shown by the arrow 3. In this case, the reduction in photocurrent by the bottom subcell is 0.047 mA/cm^2. The measured current is then $\Delta J = 0.453$ mA/cm^2 while the applied current was $\Delta J_{photo} = 0.5$ mA/cm^2. This means that the photocurrent proportion is $\frac{\Delta J}{\Delta J_{photo}} = 90.6\%$ and that the measured EQE is 10.4 % smaller than the real EQE of the bottom subcell.

As highlighted by the difference between the middle and top subcell's curve, an additional series resistance will have an important effect on the measured artifact. The top subcell's effect on the operating voltage is negligible compared to the middle subcell's effect. This is because the added series resistance in the middle subcell creates the noticeable slope on the *J-V* curve while the small resistance in the top subcell creates this near-vertical *J-V* curve in this region. Hence, to decrease the artifact, one wants to reduce the series resistance in the system.

Furthermore, the small shunt resistance in the bottom subcell is essential in creating the artifact. If the bottom subcell had a large shunt resistance, the curve in Figure 5.2b would be horizontal. Hence, even if the applied voltage changes, the photocurrent will not be different. The smaller the shunt resistance, the larger the amplitude of arrow 3, which outlines the drop in current due to the shunt. This will lead to a more important artifact.

In the current case, the calculated difference in current was completed at an applied voltage of $V = 0$. However, as highlighted in Section 2.3.4, it is necessary to apply a voltage to the MJSC for an accurate measurement. Figure 5.3 shows the evolution of the calculated alternating current ΔJ divided by the applied photocurrent ΔJ_{photo} over

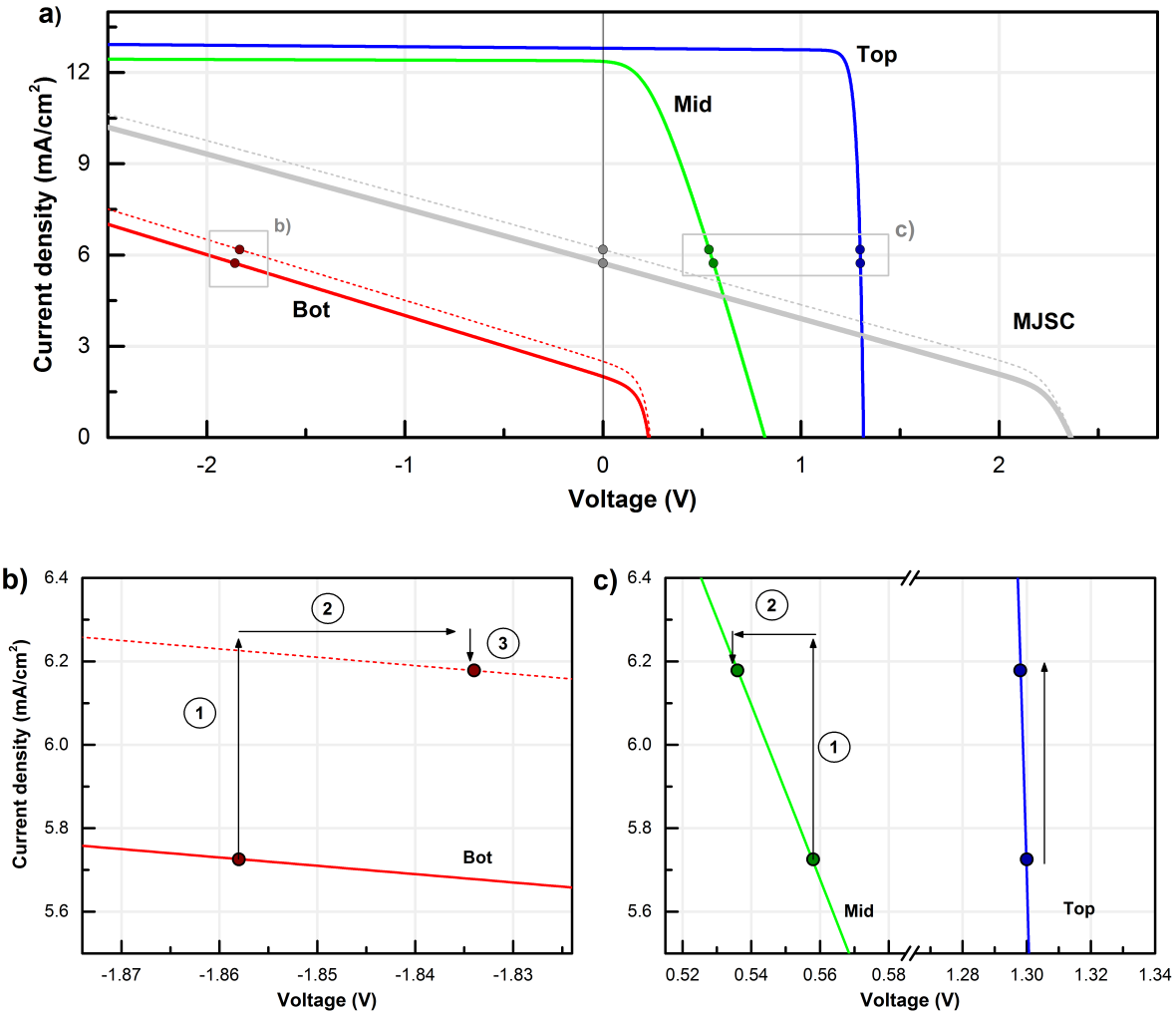

Figure 5.2: a) J-V curves of the MJSC while the bottom subcell's EQE is measured, demonstrating the artifact created by the shunt resistance. b) The bottom subcell's J-V curve near the operating voltage point. c) The top and middle J-V curves near their operating voltage point. The circled numbers and arrows are used to describe the behavior of the cell during an EQE measurement. These are throughly described in the text.

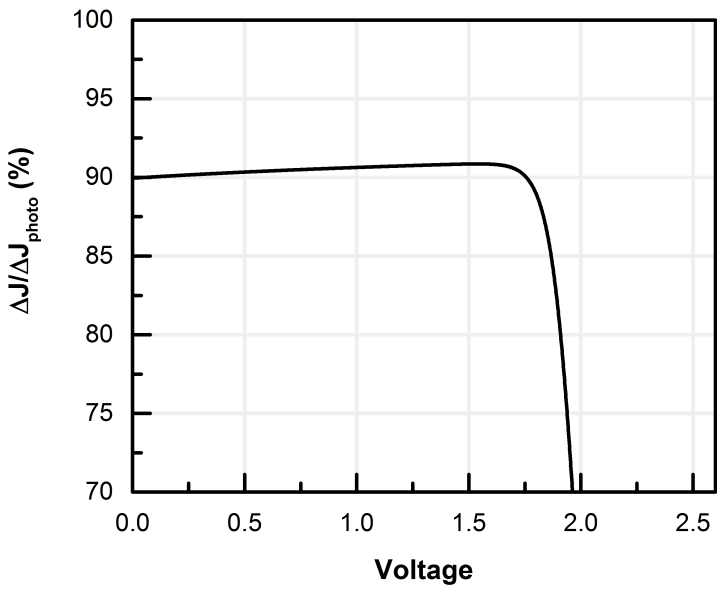

Figure 5.3: Calculated photocurrent proportion of the bottom subcell artifact in the bottom subcell's wavelength range for a shunted bottom subcell over different applied voltage.

voltage. As highlighted by the *J*-*V* curves in Figure 5.2, the calculated photocurrent proportion is 90.6 % at an applied voltage of 0. As the voltage is increased, the proportion increases up to 91.2 % at 1.9 V and decrease rapidly afterwards for increasing voltage. It therefore becomes clear that this must be corrected to account for this missing 8.8 %, assuming the cell can be properly biased.

These *J*-*V* curves explain the behavior of the EQE when the bottom subcell is measured. The bottom subcell's measured EQE is reduced when there is a small shunt resistance in the bottom subcell and a non-negligible series resistance in the MJSC. However, this does not yet explain the presence of the bottom subcell's artifact in the 600 to 900 nm region. Figure 5.4a shows the *J*-*V* curves when the light bias is applied to measure the bottom subcell, but the alternating probing light is in a wavelength range that is absorbed by the middle subcell. Like Figure 5.2, the bottom subcell is the current limiting subcell. However, as shown by the dashed lines representing the *J*-*V* curves under the additional alternating light, the probing light is fully absorbed by the middle subcell.

Again, Figure 5.4b shows the bottom subcell's *J*-*V* curve near the operating voltage point, while Figure 5.4c shows the top and middle *J*-*V* curves near their operating voltage points. This time, the increase in photocurrent caused by the probing light shifts the

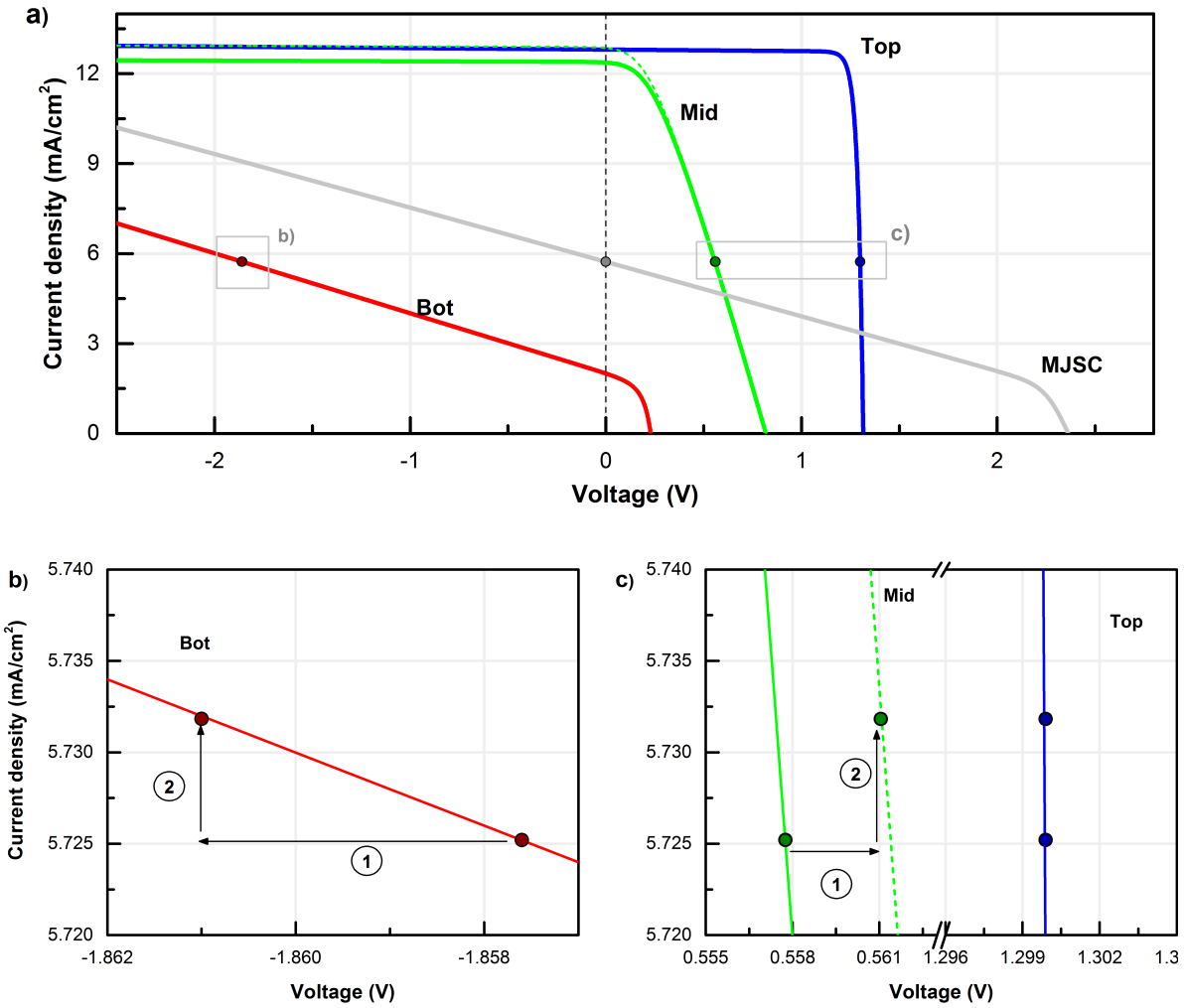

Figure 5.4: a) J-V curves of the MJSC while the bottom subcell's EQE is measured in the middle subcell's absorption range, demonstrating the artifact created by the shunt resistance. b) The bottom subcell's J-V curve near the operating voltage point. c) The top and middle J-V curves near their operating voltage point.

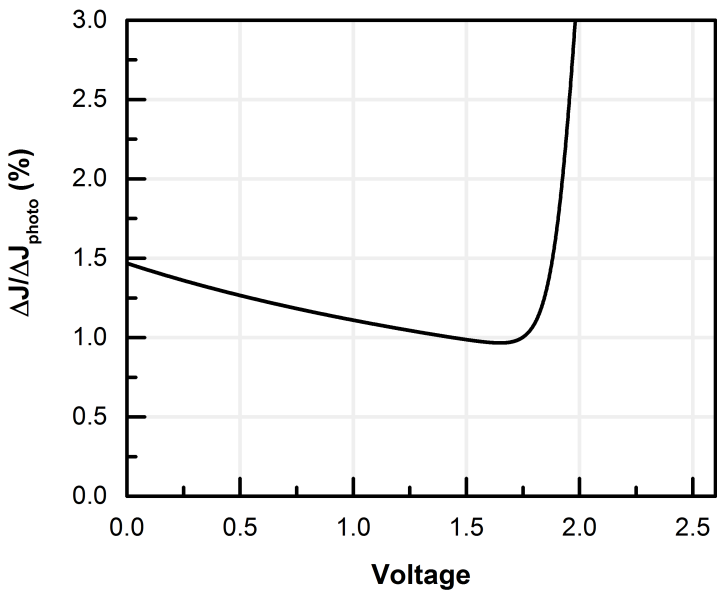

Figure 5.5: Calculated photocurrent proportion of the bottom subcell artifact in the middle subcell's wavelength range for a shunted bottom subcell as a function of applied voltage.

middle subcell's J-V curve upwards. This increase in photocurrent increases the voltage at the operating point by 0.003 V. This can be seen in Figure 5.4c as arrow 1. This change in the operating voltage of the middle subcell then changes the operating voltage of the bottom subcell by the same amount.

As seen in Figure 5.4b, the decrease in the operating voltage of the bottom subcell leads to an increase in photocurrent of 0.007 mA/cm^2. This is shown by the arrow 2. Although the bottom subcell absorbed no light from the alternating light, it still creates a non-zero photocurrent. In this case, the photocurrent proportion will give 1.5 % of the middle subcell's EQE.

Figure 5.5 shows the evolution of the calculated alternating current ΔJ divided by the applied photocurrent ΔJ_{photo} over voltage for the EQE of the bottom subcell when it is measured in the wavelength range that is absorbed by the middle subcell. As the voltage is varied, the proportion decreases from 1.5 % down to 1 % at 1.7 V and increase rapidly afterwards.

This demonstrates that the artifact can arise from internal coupling between each subcell's J-V curve. If the series resistance is negligible, it is possible to derive a method to remove the artifact [135]. The bottom subcell's EQE measured in the middle subcell's

wavelength region will be dictated by the said middle subcell's EQE. If the notation from [135] is used, the bottom subcell's EQE in the middle wavelength range is given by

$$EQE_{measured} = EQE_{mid} \cdot sf, \tag{5.3}$$

where sf is a scaling factor. Furthemore, they demonstrated that the bottom subcell's EQE is reduced by the same amount, as in

$$EQE_{measured} = EQE_{bot} \cdot (1 - sf), \tag{5.4}$$

where EQE_{bot} is the real bottom subcell's EQE.

Hence, to correct for the bottom subcell's artifact, one must use the middle subcell's EQE. The procedure is applied on the measured EQE of sample MJSC-920 in Figure 5.6. First, the middle and bottom subcell EQEs are compared in the wavelength region of 600 to 800 nm. The middle subcell's EQE is fitted to the bottom subcell's artifact by using the scaling factor sf. The artifact is removed by subtracting the middle subcell's EQE multiplied by the scaling factor from the bottom subcell's EQE. Finally, the reduction of the measured EQE by the artifact is corrected by multiplying it by $\frac{1}{1-sf}$. In equation form, this gives

$$EQE_{bot} = (EQE_{measured} - EQE_{mid} \cdot sf) \cdot \frac{1}{1 - sf} \tag{5.5}$$

The scaling factor sf necessary to correct for the artifact in Figure 5.6 is 8 %.

Comparing this procedure to the calculated artifact arising from the *J-V* curves, the correction is not necessarily similar in both cases. For the simulated *J-V* curves, 1.5 % of the middle subcell's EQE from the bottom subcell has to be removed, and the bottom subcell's EQE has to be divided by 0.9. These numbers do not correspond to a scaling factor sf that should be similar in both cases. This difference arises from the fact that the series resistance of the subcells was neglected in the derivation of the sf in [135]. Hence, this correction procedure is not adequate when significant series resistance is present in the system.

Second, the assumption that the bottom subcell's *J-V* curve is dependent on a shunt resistance is not always correct. The low bandgap of germanium generates a low reverse breakdown voltage [37]. The creation of a nucleating layer on the Germanium layer needed in the growth of the MJSC can create a non-linear effect on the *J-V* curve. This creates a slow reverse bias breakdown of the bottom subcell [136]. Hence, in reverse bias, the *J-V* curve of the bottom subcell does not necessarily follows the qualitative

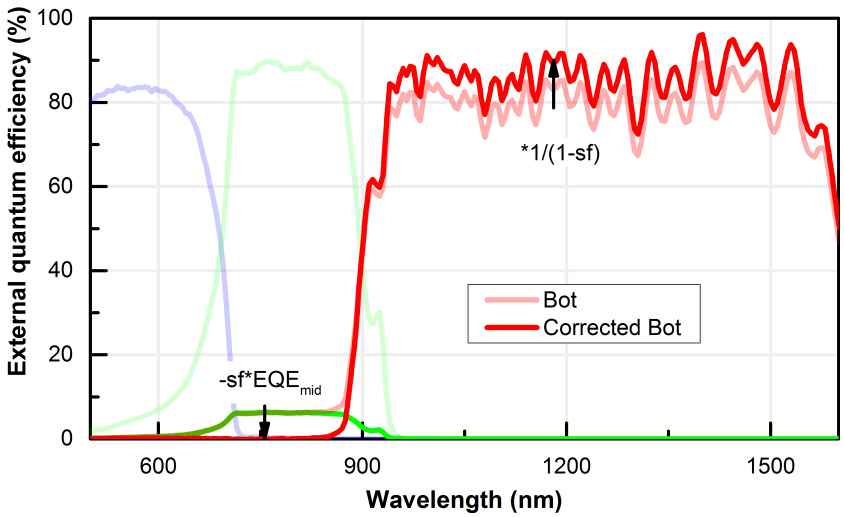

Figure 5.6: Correction procedure to remove the artifact for the bottom subcell EQE of sample MJSC-920.

behavior observed in Figure 5.2. The reverse breakdown of the bottom subcell is not easily simulated since it is highly growth dependent, and its shape is hidden in the common 1 sun J-V curve measurement.

Finally, the amplitude of the measured artifact in the middle subcell region does not correlate with the results obtained earlier. By using the J-V curves of each subcell, an artifact arose in the EQE because of the shunt resistance in the bottom subcell. An artifact of the order of 1 % was calculated for the middle subcell, but for unusually small shunt resistances. In common measurements of the EQE, such as the one seen in Figure 5.6, the artifact is on the order of 7 %. This amplitude varies between MJSC.

A possible answer to these problems is the possibility of light coupling between the middle subcell and the bottom subcell. In the following section of this chapter, the literature on light coupling will be reviewed. Then, the FF-bias experiment will be used to resolve the problem that arises from the correction procedure previously described.

5.2 Light coupling

During the EQE measurement of the bottom subcell, the top and middle subcells are forward biased. This condition commonly creates a large amount of radiative recombination. If the probing light is absorbed by the middle subcell, it is possible that the excited carriers will radiatively recombine. This additional light could then subsequently be re-

emitted towards the bottom subcell and create signal that would be picked as an EQE. It is believed that a part of the artifact, if not the entirety, is due to photon coupling between the middle and the bottom subcell [38]. GaAs is a highly efficient emitter, and world record solar cells of single junction actually exploits its high radiative efficiency to obtain very high V_{oc} [137].

Recent work has been performed extensively in the literature to demonstrate this light coupling. An important demonstration has been completed in 2007 by Baur [138]. In this work, a simple n-GaAs layer was grown on top of an electrically active Ge subcell. It was a GaAs double heterostructure on top of a Ge photodetector. This inactive GaAs layer is surrounded by two thin InGaP layers to ensure that the minority carriers cannot diffuse to the bottom subcell. With this structure, they measure the EQE of the bottom subcell, and still observe the artifact in the middle subcell region. Because the GaAs layer is electrically inactive, the internal voltage biasing does not have any effect on the behavior of the EQE. The measured artifact is then due to light coupling between the high quality GaAs layer and the Ge sub-cell.

They furthermore radiated the GaAs layer with high energy protons, giving rise to a higher non-radiative recombination rate in the GaAs layer. This completely removed the artifact present in the middle subcell region for this solar cell. This work convincingly shows that radiative coupling between subcells is important in understanding the artifact.

In 2012, Derkacs [139] used dual junction solar cells and their isotypes to demonstrate the light coupling between each of them. They grew three different samples, based on a GaAs/GaInNAsSb solar cell. They had a GaAs isotype, a dual junction cell and a GaInNAsSb isotype. The isotypes were single junction cells, but with the similar semiconductor structure than the dual junction cell. The same material is grown, but with significantly different dopings to ensure that parts are electrically inactive. They measure the current of each cell under illumination of a 808 nm (1.53 eV) laser, which is completely (99.2 %) absorbed by the GaAs subcell. As expected, the bottom subcell isotype sample had a short circuit current of 1% of the laser illumination, which is equivalent to the amount of light that goes through the GaAs inactive region. Interestingly, the dual junction tandem cell did not have a similar behavior. Instead, it had an illuminated-like J-V curve, with light coupling going up to 35 % between the two subcells.

The NREL group has studied the impact of light coupling in MJSC extensively. Steiner and Geisz have published a study of the luminescent coupling between each subcell in 2012 [140]. They measured radiative coupling between each subcell by measuring the J_{sc} of the MJSC while increasing the light illumination corresponding to the top

and middle subcells. In this experiment, the middle subcell LED is kept below 1 sun illumination while the top subcell LED corresponds to 1 sun illumination. The J_{sc} of the MJSC increases approximately linearly with the LED bias light corresponding to the middle subcell. This demonstrates that the middle subcell is light coupled to the bottom subcell. However, they did not take into account the internal voltage biasing. As demonstrated in the previous section, even if the bottom subcell does not absorb any light, the possibility of a small shunt resistance could recreate this increase in J_{sc}.

Using this experimental technique, they derived the methodology to correct for the luminescent coupling [141]. Even though the luminescent coupling is a real effect on the EQE, it is necessary to remove it. Under the normal operation of the solar cell, when it is illuminated by the AM1.5D spectrum, the individual subcells are expected to be current matched. In this configuration, since all subcells operate near their maximum power point, negligible luminescence coupling between each subcells is expected. Their proposed methodology to remove the artifact related to the light coupling is the same as the one proposed by [135] and shown in Equation 5.5. They remove the middle subcell's EQE multiplied by a scaling factor from the bottom subcell's EQE and subsequently multiply its EQE by the corresponding factor. They correct as well for the middle subcell's EQE when there is light coupling from the top subcell in a similar fashion.

Their demonstration was completed for inverted metamorphic solar cells. As mentionned in Chapter 1, this design uses substrate removal techniques and has a bottom subcell made out of InGaAs. In this case, the bottom subcell's J-V curve behavior is optimal. They furthermore demonstrate that it is possible to adequatly measure the light coupling in a Ge based MJSC. However, their method shows that the reverse breakdown behavior of the Ge subcell has a non-negligible effect on the luminescent coupling. They determined empirically that adding 1.5 V to the experiment minimized this behavior. Hence, from the conclusion of this paper, the artifact present in the bottom subcell's EQE either comes from the luminescent coupling or the internal voltage biasing from the subcells. Both effects are corrected in the same way.

Li demonstrated the effect of both the shunt and the luminescence coupling as a function of biasing light [38]. However, the method was not complete enough to quantitatively differentiate the contribution of each component. Using their model, they developed a pulsed voltage bias method and a pulsed light bias method to minimize the EQE artifact [142, 143].

5.3 The fill-factor bias measurement

As seen in the previous section, the EQE artifact has been studied extensively in the literature. However, the quantitative extraction of the contribution of each effect has not been shown. Furthermore, the reverse bias breakdown of the bottom subcell has been neglected by most techniques. The current section will demonstrate the possibility of using an experimental technique to independently separate the effect of both the internal biasing and the luminescence coupling. The experimental procedure is the fill factor bias experiment (FF-bias), proposed by Cyrium Technologies [39].

The apparatus consists of 3 light sources, one for each subcell. Each of these light sources is tailored to be exclusively absorbed by their corresponding subcell. Their intensity can be continuously controlled between values of 0 to 1 sun.

For a single measurement, the intensities of the three light sources are set to 1 sun. Subsequently, the intensity of the light associated to the subcell under test is varied between 0 and 1 sun. For each intensity increment, a full MJSC J-V curve is measured. The resulting measurement, as seen in Figure 5.9 and 5.10, demonstrate curves that are highly dependent of the subcell's internal J-V curve. It is possible to complete this measurement for each of the subcells under test to obtain a complete picture of each subcell. This experimental technique was implemented initially to assess the quality of each subcell through the measurement of their respective FFs. This created the name of the apparatus, 'the fill-factor bias measurement' (FF-bias).

By measuring the J-V curve as a function of the illumination of each subcell, it is possible to extract each subcell's characteristic. This technique shall then be used to obtain the shunt behavior of the bottom subcell as well as the light coupling from the middle to the bottom subcell.

The FF-bias setup was built at the SUNLAB using multiple optical components. The solar cell was installed on a metallic stage and the electrical contacts were created using electrical probes. The light bias used to illuminate the top subcell was a 505 nm high power LED source coupled to a continuous power supply. This continuous power supply took an input from 0 to 5 Volts and subsequently applied a maximum of 700 mA to the high power LED. Figure 5.7a shows the spectrum of the LED source as a function of applied current. Similarly, for the middle subcell, a 780 nm LED source was used. Again, a continuous power supply used an input of 0 to 5 Volts to apply a maximum of 1000 mA to the LED. Figure 5.7b shows the according spectrum of the LED.

The bottom subcell's biasing light was an Oriel 1600 W solar simulator coupled with

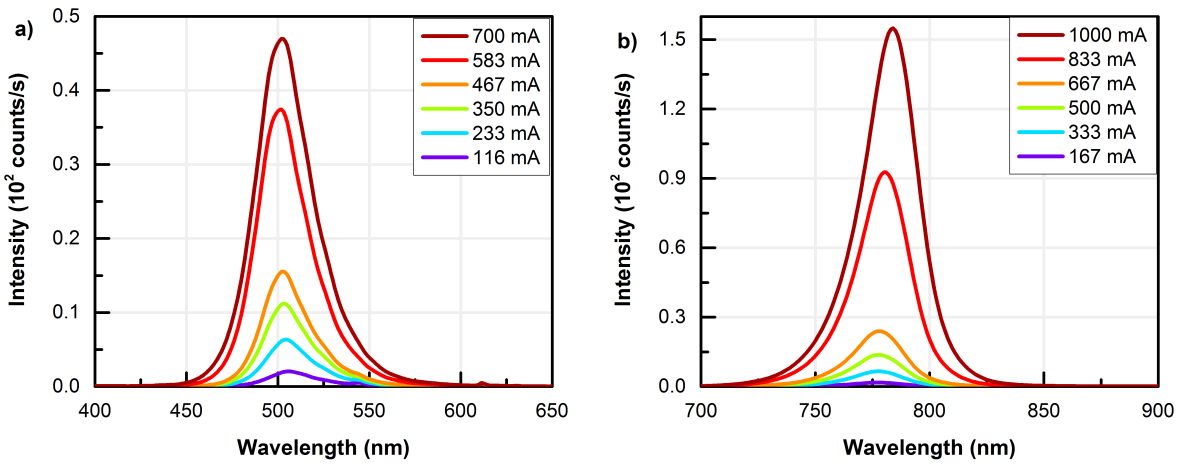

Figure 5.7: a) Spectra of the biasing high power 505 nm LED for the top subcell, driven by currents ranging from 116 to 700 mA. b) Spectra of the biasing high power 780 nm LED for the middle subcell, driven by currents ranging from 167 to 1000 mA

a long wave pass 1000 nm filter (20CGA-1000). The filter removed all the light that was of a wavelength lower than 1000 nm. To control the intensity of the light going onto the solar cell, a combination of neutral density filters were used, similarly to the PL measurement in Section 4.4.1. The resulting spectra of the light source is shown in Figure 5.8, using filters of optical densities ranging from OD 0.2 to OD 3.0.

To calculate the equivalent intensity going onto the cell, calibrated reference isotype solar cells were used. These isotypes are single junction solar cells that are grown with a similar structure than a MJSC. This ensures that they have similar EQEs than their MJSC's counterpart, and hence have a similar response to different specta. Each irradiation intensity was converted to their value in number of suns (with the AM1.5D spectrum). The *J*-*V* curves were measured from 0 to 3 V using a Keithley 2420 sourcemeter.

Using these spectra, setting the intensity of the middle and bottom subcell's light sources to 1 sun, the top subcell's light source was varied to obtain its corresponding FF-bias curves. These are shown in Figure 5.9a for the sample MJSC-920. The FF-bias curves in Figure 5.9b are obtained by setting the top and bottom subcell's light source to 1 sun and subsequently by varying the middle subcell's light intensity.

The top subcell's FF-bias measurement behaves as expected. Its calculated J_{sc} under the AM1.5D spectrum is 12.8 mA/cm^2. As the bias light intensity is increased, the *J*-*V* curve linearly increases up to its J_{sc} at 1 sun. The V_{oc} of the device increases

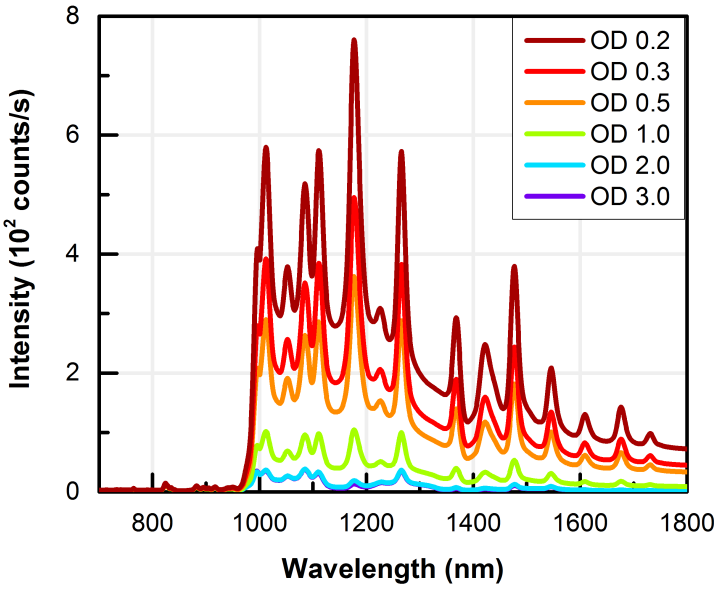

Figure 5.8: Spectra of the Oriel 1600 W solar simulator coupled with a 1000 nm long-wave pass filter and neutral density filters, used to bias the bottom subcell in the FF-bias measurement.

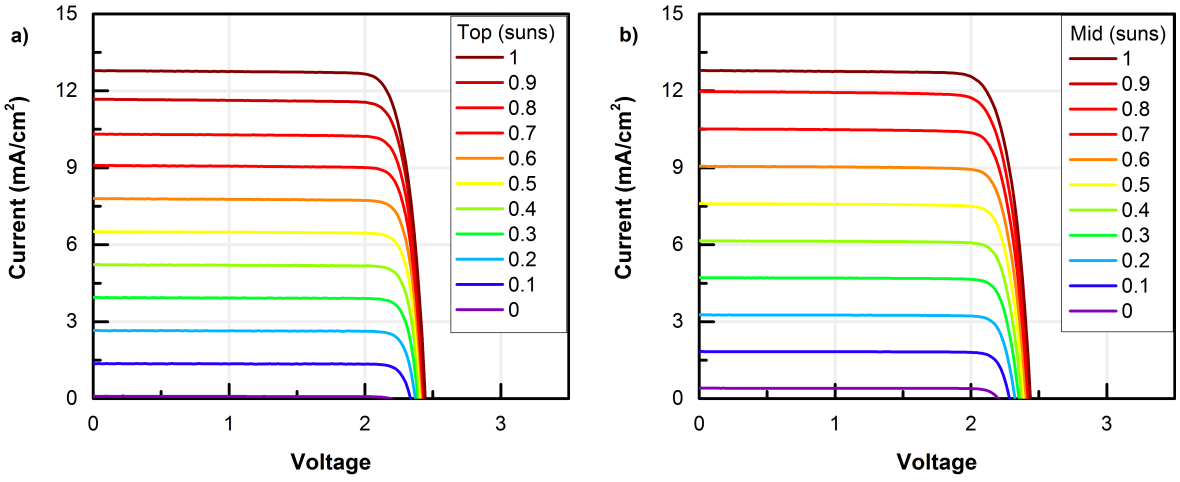

Figure 5.9: J-V curves as a function of light bias intensity of the sample MJSC-920 during the FF-bias experiment. a) The top subcell FF-bias measurement, with the 505 nm LED intensities varying from 0 to 1 sun. b) The middle subcell FF-bias measurement, with the 780 nm LED intensities varying from 0 to 1 sun.

logarithmically up to 2.44 V. The shape of the *J-V* curve is ideal and no shunt resistance is present for this subcell. Its measured EQE is then expected to be ideal.

The middle subcell's FF-bias measurement is similar to the top subcell's measurement. However, an important difference arises at 0 sun intensity. The *J-V* curve has a non-zero current at this intensity. It is expected to be zero since no light is applied on the said subcell. At $V = 0$, the measured current density is 0.4 mA/cm^2. Carefully looking at the top subcell's EQE of MJSC-920 in Figure 5.6, the middle subcell's EQE is 3 % at 505 nm. This either comes from light coupling or from light that is actually not absorbed by the top subcell. The thickness of the top subcell in this sample was derived in the Figure 3.14 in Chapter 3. The top subcell's thickness is 1.2 µm. Using the absorption coefficient of InGaP at 505 nm ($\alpha_{InGaP} = 5.35 \cdot 10^4$ cm^{-1}), the amount of light that is absorbed by the top subcell at this wavelength is 99.8 %. This means that at this wavelength, the amount of light that reaches the middle subcell is 0.2 %. Hence, when the top subcell is biased at 1 sun while the middle subcell is biased at 0 sun, the light coupling between the top subcell and the middle subcell is approximately 2.8 %. Since the J_{sc} of the top subcell is 12.8 mA/cm^2, the middle subcell will create 3 % of it, 0.38 mA/cm^2. This corresponds to the measured *J-V* curve at 0 suns in Figure 5.9b. The *J-V* curve subsequently increases linearly with the applied light bias.

The bottom subcell's measured FF-bias is shown in Figure 5.10. It was obtained by setting the top and middle subcell's light source to 1 sun, and then subsequently changing the neutral density filters in front of the bottom subcell's biasing light source. The J_{sc} of this subcell is 18.7 mA/cm^2. The *J-V* curves of the MJSC are current limited by the top and middle subcells at higher light bias intensities. As highlighted beforehand, multiple components influence the *J-V* curves. The two important ones that are highlighted in this thesis are the reverse bias breakdown of the bottom subcell and the light coupling between the middle and bottom subcells.

Comparing the resulting *J-V* curves of Figure 5.10 to the calculated bottom subcell's *J-V* curve in Figure 5.2, they are not similar. While the calculated *J-V* curve shows a straight line from $V = 0$ to $V = -2$, the measured *J-V* curve demonstrate a curved behavior. This can be explained by the fact that the Ge subcell has a reverse bias breakdown. The small bandgap of the germanium as well as the growth of a nucleation layer increase the chance of observing such breakdown in this subcell [136]. Hence, in this case, the calculation of the bottom subcell's artifact by assuming a small shunt resistance in the bottom subcell is incorrect.

The calculation of the internal *J-V* curves in the MJSC done in Section 5.1 shall now

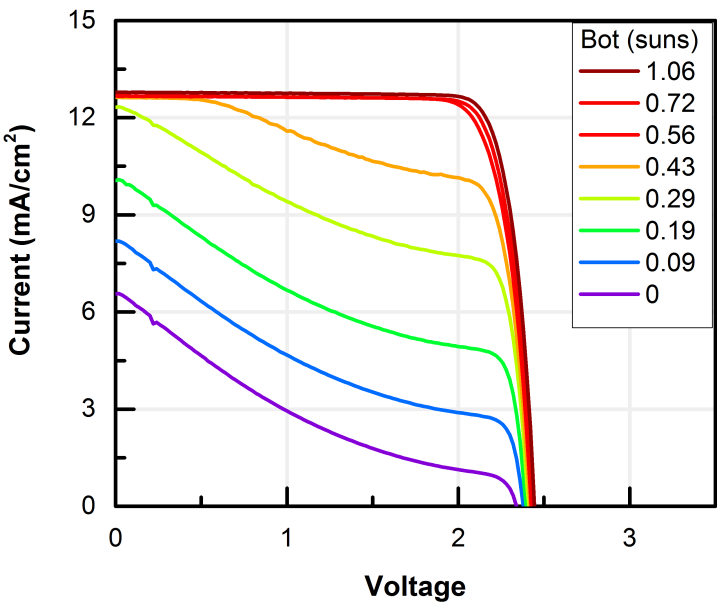

Figure 5.10: Measured J-V curves as a function of light bias intensity of the sample MJSC-920 during the bottom subcell FF-bias experiment.

be revisited. This time however, the reverse bias breakdown and the light coupling will be included. The MJSC J-V curves again are calculated using Equations 5.1 and 5.2. The light coupling is calculated as an additional constant term in the J_{sc} of each subcell. Hence, in Equation 5.1, J_{sc} becomes $J_{sc} + J_{LC}$ where J_{LC} is the light coupling current density. The J-V curves are calculated for each of the light conditions in the FF-bias experiment.

The individual subcell's values in Table 5.1 were obtained by fitting the calculated J-V curves to the measured curves in Figures 5.9a and b and Figure 5.10. The top subcell's parameters were first obtained by fitting the J-V curve of the 0.1 sun curve in Figure 5.9a. It was assumed that the middle and bottom subcells were operating near their V_{oc}. The fit was obtained by varying each parameter in Table 5.1 to create an array of different J-V curves. The J-V curve with the least MSE compared to the experimentally measured curve was chosen as the fitted curve.

Subsequently, the middle subcell's parameters were obtained by doing a similar fit to the 0 sun curve in Figure 5.9b. The additional light coupling from the top subcell was calculated as well in this fitting procedure. The obtained light coupling was calculated to be of 0.4 mA/cm^2, or 3.1 %.

The bottom subcell's J-V curve is more complex to fit. First, light coupling between

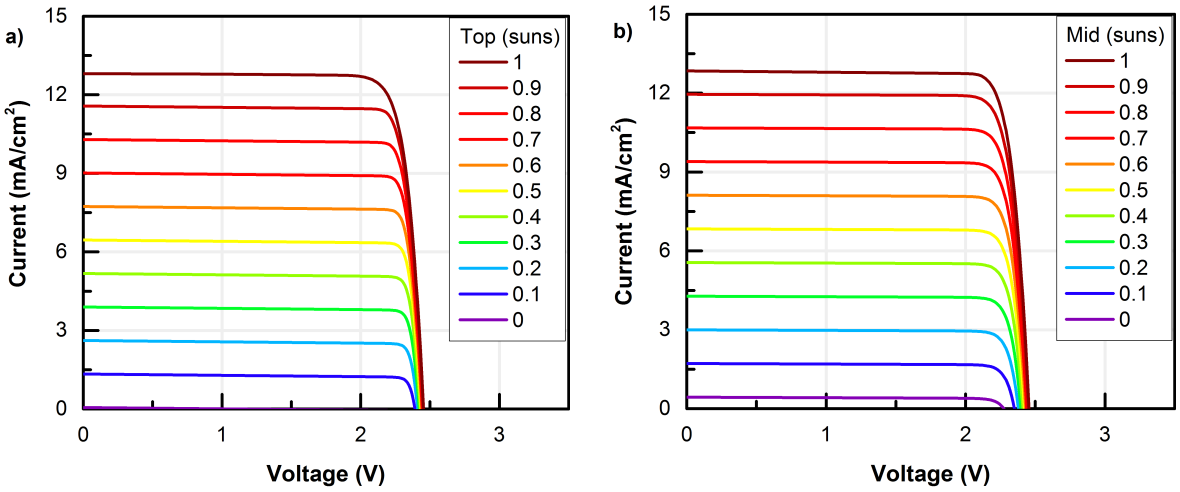

Figure 5.11: Calculated J-V curves as a function of light bias intensity of the sample MJSC-920 reproducing the a) top and b) middle subcell FF-bias experiment.

the middle subcell and the bottom subcell is observable. By estimating that the internal V_{oc} of the top and middle subcells are similar to the calculated ones using Table 5.1 (1.32 V and 0.83 V respectively), the J_{sc} of the bottom subcell is seen when $V = 2.15$ is applied to the MJSC. The measured current at $V = 2.15$ when 0 sun is applied to the bottom subcell is $J = 0.1$ mA/cm^2 . Similarly to the top subcell, the middle subcell's thickness was obtained in Chapter 3. The total thickness of GaAs that was measured using the FFT of the reflectivity was approximately 5.8 μm. Using the absorption coefficient of GaAs at 780 nm ($\alpha_{GaAs} = 1.53 \cdot 10^4$ cm^{-1}), the amount of light that is absorbed by the middle subcell at this wavelength is 99.9 %. The 780 nm biasing light is completely absorbed by the middle subcell, and the J_{sc} is created by light coupling.

Secondly, the shunt resistance approximation is inadequate. To adequately fit the measured J-V curve, it is necessary to replace the shunt resistance by a diode in reverse breakdown in series with a resistance. To fit the bottom subcell's J-V characteristics, the J-V curves were calculated for the 0 sun case in Figure 5.10. An additional resistive reverse breakdown diode as well as light coupling from the middle subcell were added to the circuit calculation. The best fitted curve had the parameters that fit into the two-diode model shown in Table 5.1. The light coupling from the middle subcell was 1 mA/cm^2, or 8 %. The resistive reverse breakdown diode has an ideality factor of $n = 10$, a dark current of $J_0 = 10^4$ mA/cm^2 and a resistance of 200 Ω. These values have no physical meaning, and solely serve to fit the curve.

The calculated J-V curves for the top and middle subcell's FF-bias experiment are

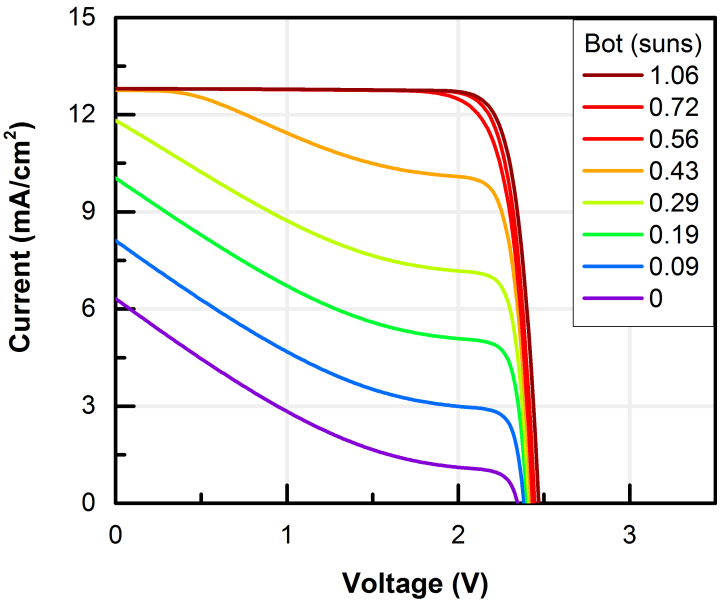

Figure 5.12: Calculated J-V curves as a function of light bias intensity of the sample MJSC-920 reproducing the bottom subcell FF-bias experiment.

shown in Figure 5.11a and b respectively. They show similar behavior as the measured curves in Figure 5.9b.

The calculated J-V curves for the bottom subcell's FF-bias experiment are shown in Figure 5.12. They accurately reproduce the behavior of the bottom subcell over different light bias intensities.

The model is capable of calculating the internal J-V curves of the sample MJSC-920 under different illumination conditions. It is then possible to estimate the contribution of each component, namely the light coupling and the internal voltage biasing, to the bottom subcell's artifact. The light coupling measured in Figure 5.10 and calculated in Figure 5.12 creates an artifact of 8 %. This means that the bottom subcell's EQE in the middle subcell's region will be 8 % times the middle subcell's EQE due to light coupling. This further means that the measured bottom subcell's EQE in the bottom subcell's region will be 92 % of the real EQE due to light coupling.

Furthermore, It is possible to calculate the contribution of the internal voltage biasing. By using a similar procedure as the one presented in Section 5.1, the effect of the bottom subcell's J-V curve on the measured EQE is calculated. Figure 5.13a shows the amplitude of the photocurrent proportion $\frac{\Delta J}{\Delta J_{photo}}$ as a function of applied voltage. When $V = 0$ is applied on the MJSC, the internal voltage biasing reduces the amplitude of the measured

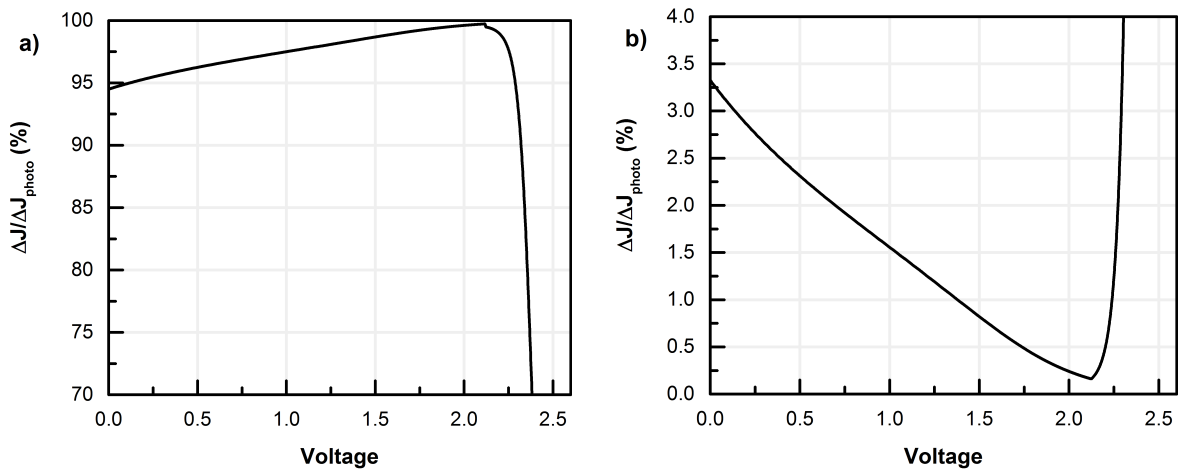

Figure 5.13: Calculated bottom subcell artifact as a function of voltage using the J-V curves derived from the FF-bias measurement. a) Reduction of the EQE amplitude due to the artifact. b) Artifact present in the middle subcell's region.

EQE down to 94.5 %. As evidenced by this figure, the optimal voltage to measure the EQE is 2.1 V. At this voltage, the measured EQE is 99.7 % of the real EQE.

Figure 5.13b shows the amplitude of the photocurrent proportion $\frac{\Delta J}{\Delta J_{photo}}$ in the wavelength range that is absorbed by the middle subcell as a function of applied voltage. When $V = 0$ is applied to the MJSC, the measured EQE will be 3.3 % of the middle subcell's EQE. Again, the optimal voltage to measure the EQE is 2.1 V, with an artifact of 0.2 %.

The internal voltage biasing artifact is not accurately resolved by using the scaling factor procedure shown in Equation 5.5. As highlighted by Figure 5.13, the measured artifact in the bottom subcell's region when $V = 0$ is applied is 94.5 % while it is 3.3 % in the middle subcell region. Hence, to correct for this artifact, a scaling factor of $sf = 3.3\%$ is needed in the middle subcell region and a scaling factor of $sf = 5.5\%$ is needed in the bottom subcell's region. This cannot be completed solely by fitting the middle subcell's EQE to the bottom subcell's artifact, as shown in Figure 5.6. It can, however, be resolved by completing the FF-bias measurement.

The measured EQE in Figure 5.6 was not measured at $V = 0$. As mentioned in Chapter 2, the applied voltage for the bottom subcell's EQE is 2 V. In this case, the measured artifact in the bottom subcell's region when $V = 2$ is applied is 99.6 % while it is 0.2 % in the middle subcell region. This is considered negligible compared to the light coupling artifact.

In this case, the calculated scaling factor to fit the middle subcell's EQE to the bottom subcell's artifact is 8 %. This corresponds to the light coupling of 8 % between the middle subcell and the bottom subcell that was measured in the FF-bias experiment. Hence, it is adequate to apply the scaling factor procedure to remove the artifact in the middle subcell's region and to increase the bottom subcell's EQE from 92 to 100 %. However, it was necessary to complete the FF-bias experiment to ensure that in the studied sample, the internal voltage biasing was negligible. If the measurement demonstrated that the internal voltage biasing was significant, a separate correction procedure would need to be applied for each EQE region.

This study demonstrated that as long as an adequate voltage biasing was applied, the internal voltage biasing is negligible in MJSC. It is however necessary to measure the internal J-V curves to ensure that the bottom subcell's reverse bias breakdown is small. If the bottom subcell's reverse bias breakdown is strong, it shall have an important effect on the measured EQE artifact.

5.4 Conclusion

This chapter highlighted the bottom subcell's artifact. This artifact has two effects on the EQE of the bottom subcell. First, it creates a non-zero EQE in the region where the middle subcell would absorb the incoming light. Secondly, it creates a reduced EQE amplitude for the bottom subcell.

This artifact arises from two different physical processes. First, it was demonstrated that the internal biasing between each subcell's J-V curves can contribute to the artifact. This internal voltage biasing arises when the bottom subcell has a small shunt resistance. Second, the possibility of light coupling between the subcells was discussed. In the light conditions for an EQE measurement, the incoming probing light can be absorbed by the middle subcell and subsequently be re-emitted towards the bottom subcell. When measuring the bottom subcell, both physical processes creates a non-zero EQE in the middle subcell region. Furthermore, they both create a reduced EQE amplitude.

The standard procedure to correct for this artifact is to use a scaling factor and the middle subcell's EQE to remove the artifact in the middle subcell's region and to correct the EQE amplitude. This was shown in Equation 5.5 and Figure 5.6. However, this procedure does not decipher the contribution of each physical process in the artifact.

The analysis of the FF-bias experiment permits the quantification each physical process. In this measurement, the MJSC's J-V curve is measured under different light

conditions. To measure the FF-bias of the top subcell, a light source of 1 sun is applied to the middle and bottom subcell while the top subcell light biasing source is varied from 0 to 1 sun. The measured J-V curve is highly dependent on the top subcell's J-V curve since it is the current-limiting one. The measurement is subsequently applied for the middle and bottom subcells with according light bias.

As seen in Figure 5.9, the top and middle subcells behave as expected. A two-diode model was fitted to their J-V curves. However, as seen in Figure 5.10, the bottom subcell had a non-negligible reverse-bias breakdown. Its J-V curve was fitted using a two-diode model with a resistive reverse breakdown diode. Furthermore, a light coupling of 8 % between the middle and bottom subcells was measured under particular conditions.

Using these newly fitted J-V curves, the effect of each physical process in the bottom subcell's artifact was estimated. For the measured EQE at $V = 2$, the contribution for the light coupling was 8 % and the contribution from the internal voltage biasing was 0.2 %. If the EQE was measured at $V = 0$, the internal voltage biasing created an artifact of the order of 3.3 % in the middle subcell region and of 94.5 % in the amplitude in the bottom subcell's region. In this case, the correction procedure shown in Equation 5.5 is not adequate.

This demonstrated the importance of correctly applying the adequate voltage when the bottom subcell's EQE is measured. This ensures that the artifact arising from the internal voltage biasing becomes negligible. This leaves only the light coupling, which is easily corrected using the appropriate procedure. It is important to note that luminescent coupling between the top and middle subcell is possible as well [141]. Such coupling, when present, is corrected similarly.

Chapter 6

Conclusion

The EQE measurement of a solar cell is an essential tool for the thorough characterisation of the solar cell structure. The analysis of this measurement gives important insight in the physical processes governing the electrical and optical behavior of this device.

This thesis analysed indepth the EQE of single and multi-junction solar cells. First, the experimental procedure and instrumentation was explained in Chapter 2. The main equations governing the behavior of the EQE were introduced. A model was developed and fitted to a single junction GaAs solar cell (cell SJ-ref). It was furthermore demonstrated that the model reproduced the behavior of a MJSC's EQE.

The following chapters subsequently studied in detail the important features that are obtained in the EQE of a MJSC. In Chapter 3, the reflectivity of the semiconductor structure was studied. It was demonstrated that the design of a standard MJSC created optical cavities composed of material with different refractive indexes. Those cavities created interference effects visible in the reflectivity of the structure. A novel technique was introduced, the etalon effect measurement, which used a fast Fourier transform to calculate the thicknesses of the optical cavities. Using this method, it was possible to determine the thicknesses of the top and middle subcells of MJSC samples MJSC-S and MJSC-920.

In Chapter 4, the effect of adding QDs in the middle subcell of a MJSC on the EQE was described. The semiconductor nanostructures were first simulated using a finite element solver. Their absorption and emission properties were subsequently derived. Then, QDs grown in single junction (SJ-A and SJ-B) and in MJSC (MJSC-920 and MJSC-970) were characterised. Their PL and their EL spectra were measured, and further compared with their calculated emission properties. Then, the QD enhanced

EQE of each structure was measured and compared with the calculation. The calculation of the absorption properties of the nanostructures explained adequately their effect on the EQE. Adequately describing the effect of the nanostructures on the EQE has multiple benefits. When coupled with semiconductor simulation techniques, it can be used to predict the increase in J_{sc} created by the addition of QDs.

Finally, in Chapter 5, the bottom subcell's artifact was studied. This artifact creates a non-zero bottom subcell EQE in the middle subcell's wavelength region. It furthermore creates a lower amplitude for the bottom subcell than the real EQE. The origin of the artifact comes from two possible physical processes: the internal voltage biasing and the light coupling. Then, the FF-bias experimental technique was introduced. It was used to separate the contribution from the two physical processes on the artifact. The reverse bias breakdown of the bottom subcell was measured and its effect on the artifact was quantified. In the measured solar cell (MJSC-920), under optimal voltage biasing, the light coupling contributed to an artifact of 8 % while the internal voltage biasing was negligible.

Future research shall concentrate on newer MJSC designs. Four junctions and even five junctions [144] designs have been proposed to further increase the efficiency of solar cells. The technique proposed in Chapter 2, using the reflectivity to calculate the thicknesses of the semiconductor layers in the solar cell, could be extended to these solar cells. Furthermore, the possibility of adding QDs in different subcells of a five junction cell design is an important concept that would need an extensive study. The added flexibility that the nanostructures introduce in the current matching process can possibly significantly improve the design possibilities in those types of cells. The work introduced in this thesis on QDs can conceivably be extended to different materials and demonstrate the added benefit that these nanostructures might have in these MJSCs.

The FF-bias methodology proposed in Chapter 5 should yield important insights for these types of structures. In some proposed designs, the third junction of a four junction lattice matched MJSC (InGaP/GaAs/GaInAsN/Ge) is a dilute nitride cell, which is known to yield reduced material quality [145]. The measurement of the individual subcells in those devices, and furthermore the electrical influence between each subcell should be an important step in the research of these cells.

The analysis of the MJSC's EQE presented in this thesis gives a complete picture of the importance of this measurement. As was mentioned in Chapter 1, the CPV industry is a young industrial sector. Scientific research plays a major role in the field, and efficiency increase is a vital path to ensure that the technology gets implemented

in today's world for renewable energy production. Hence, the methodology presented in this thesis, using the EQE as a tool to investigate the properties of each component in the solar cell, is an essential step for the research community. It was demonstrated that using the reflectivity gave insight in the structural details of the solar cell, that the addition of nanostructures in the middle subcell could tailor its absorption properties, which could assist in current matching the MJSC, and that using the FF-bias measurement technique gives strong insights into the light coupling and the electrical behavior of each subcell. These are important insights in the operation of the solar cells that should catalyze the design towards higher efficiencies.

Appendix A

Derivation of the absorption coefficient

This annex will outline the methods and equations needed to obtain an analytical set of equations to be able to calculate the absorption coefficient of quantum wells as well as of the parabolic quantum dots. We will first define the absorption coefficient, then obtain the rate of transition in a quantum mechanical fashion. We will apply these results to obtain the absorption coefficient of the nanostructures present in the system, namely a quantum well and quantum dots. We will then extend the analysis to a broad Gaussian distribution of energy levels. The results shown in this appendix are used in chapter 4. It was derived using [125].

The absorption coefficient is defined as the ratio of energy removed from the incident beam per unit time and unit volume, or, in a more common fashion

$$I(x) = I_0 \mathrm{e}^{-\alpha x}, \tag{A.1}$$

where I is the incident flux of energy per unit time per unit area and α is the absorption coefficient. In a solid, the absorption coefficient will be related to the rate of the absorbed photons. This can be written as

$$\alpha = \hbar\omega \frac{R_T}{{}^{c}\!/_{n} U_E}, \tag{A.2}$$

where R_T, is the rate of transitions due to absorption, ${}^{c}\!/_{n} U_E$ is the energy flux, ${}^{c}\!/_{n}$ is the speed of light in the material and U_E being the energy density of the photon beam. We will consider an electric field, in complex notation

$$\vec{E}(x,t) = Re[\vec{E}(x)\mathrm{e}^{-i\omega t}] = \frac{1}{2}\left(\vec{E}(x)\mathrm{e}^{-i\omega t} + \vec{E}^{*}(x)\mathrm{e}^{i\omega t}\right), \tag{A.3}$$

where we are assuming that the electric field has the form of a plane wave $\vec{E}(x) = \vec{E}_0 e^{i(\vec{q}\cdot\vec{r})}$. For an electromagnetic wave, the time averaged energy density is given by (in SI units)

$$U_E = \frac{1}{2}(\varepsilon E^2 + {}^1\!/_\mu B^2). \tag{A.4}$$

Assuming that we have a non-magnetic material,

$$U_E = \frac{n^2 \varepsilon_0}{2} |\vec{E}_0|^2. \tag{A.5}$$

If we assume to have quantization of photons, the energy density at energy E is simply related to the number of photons per energy mode N_E,

$$U_E = N_E \cdot \hbar\omega. \tag{A.6}$$

Back into the absorption coefficient, we obtain

$$\alpha = \frac{R_T}{{}^c\!/_n N_E}. \tag{A.7}$$

It is important to note here that E is the photon energy while $|\vec{E}_0|$ is the amplitude of the electric field. We now have to define the transition rate R_T.

The transition of carriers from the valence band initial state $|i\rangle$ to a final state $|f\rangle$ of energy E_f is given by the Fermi's golden rule

$$R_{i\to f} = \frac{2\pi}{\hbar} \sum_f |\langle f|H'|i\rangle|^2 f_i(E_i)\left(1 - f_f(E_f)\right), \tag{A.8}$$

where H' is the perturbed Hamiltonian arising from the interaction of the light, f_i is the Fermi-Dirac probability of having an electron present at energy E_i and $1 - f_f(E_f)$ is the probability of having a hole at the energy E_f. The summation $\sum_f$ over all final states f needs to be completed to take into account all possible transitions at the particular energy E_f.

The full Hamiltonian under an electromagnetic field is given by

$$H = \frac{1}{2m_0}(P + qA)^2 + V(r), \tag{A.9}$$

where the vector potential A is obtained from the electric field $\vec{E} = -\frac{\partial \vec{A}}{\partial t}$. If we expand the square, and we assume the term in A^2 to be negligible, we can get the Hamiltonian

$$H = H_0 + H' = \frac{1}{2m_0} P^2 + V(r) + \frac{q}{m_0} P \cdot A, \tag{A.10}$$

where H' is the perturbed Hamiltonian creating the optical transition. We can now evaluate the matrix element of the transition by

$$|\langle f|H'|i\rangle|^2 = \frac{q^2}{m_0^2}|\langle f|P\cdot A|i\rangle|^2. \tag{A.11}$$

In the case of an initial electronic state in the valence band and the final state in the conduction band, the wavefunction will be given by Bloch functions

$$\begin{aligned} |i\rangle &= u_v(r)\cdot \mathrm{e}^{i\vec{k}_v\vec{r}}\cdot \mathrm{e}^{-\frac{iE_vt}{\hbar}}, \\ |f\rangle &= u_c(r)\cdot \mathrm{e}^{i\vec{k}_c\vec{r}}\cdot \mathrm{e}^{-\frac{iE_ct}{\hbar}}, \end{aligned} \tag{A.12}$$

where u_c and u_v are the Bloch wavefunction, $\vec{k}_v$ and $\vec{k}_c$ are the wavevector of the carrier and E_v and E_c are the intial and final energy states in the valence and conduction band. The integration over time inside the matrix element will involve conservation of energy

$$\int \mathrm{e}^{-\frac{iE_ct}{\hbar}}\mathrm{e}^{-i\omega t}\mathrm{e}^{-\frac{iE_ct}{\hbar}}dt \quad \rightarrow \delta(E_c - E_v - \hbar\omega). \tag{A.13}$$

The matrix element will be (with $\hat{e}$ being the direction of the polarization)

$$|\langle f|P\cdot A|i\rangle|^2 = \frac{|E_0|^2}{4\omega^2}\left|\int u_c^*\mathrm{e}^{i(\vec{q}-\vec{k_c})\cdot\vec{r}}\hat{e}\cdot\vec{p}u_v\mathrm{e}^{i\vec{k_v}\cdot\vec{r}}dr\right|^2. \tag{A.14}$$

We operate $\vec{p}$ on the last part of the equation (where $\vec{p} = -\hbar\nabla$)

$$\vec{p}\cdot u_v\mathrm{e}^{ik_vr} = \mathrm{e}^{ik_vr}\vec{p}\cdot u_v + \hbar k_v u_v\mathrm{e}^{ik_vr}. \tag{A.15}$$

Since u_v and u_c are orthogonal, the integration over space of the second term will give 0. The matrix element becomes

$$|\langle f|P\cdot A|i\rangle|^2 = \frac{|E_0|^2}{4\omega^2}\left|\int \mathrm{e}^{i(\vec{q}-\vec{k_c}-\vec{k_v})\cdot\vec{r}}u_c^*\cdot\hat{e}\cdot u_v dr\right|^2. \tag{A.16}$$

We now change the integral so that it is only inside the unit cell instead of over the whole space ($\vec{R}_j$ is a lattice vector), giving

$$|\langle f|P\cdot A|i\rangle|^2 = \frac{|E_0|^2}{4\omega^2}\left|\sum_j \mathrm{e}^{i(\vec{q}-\vec{k_c}-\vec{k_v})\cdot\vec{R}_j}\int_{\text{unitcell}}\mathrm{e}^{i(\vec{q}-\vec{k_c}-\vec{k_v})\cdot\vec{r}'}u_c^*\cdot\hat{e}\cdot u_v dr'\right|^2. \tag{A.17}$$

The summation over the lattice vector gives a Kronecker delta,

$$\sum_j \mathrm{e}^{i(\vec{q}-\vec{k_c}-\vec{k_v})\cdot\vec{R}_j} = \delta_{\vec{q},\vec{k_c}-\vec{k_v}}. \tag{A.18}$$

We will now assume the photon wavevector ($\vec{q}$) to be small compared to the electrons. This is equivalent to the dipole approximation. We apply the delta function on the equation,

$$|\langle f|P\cdot A|i\rangle|^2 = \frac{|E_0|^2}{4\omega^2}\left|\int_{\text{unitcell}} u_c^*(\vec{k})\cdot\hat{e}\cdot u_v(\vec{k})dr'\right|^2. \tag{A.19}$$

This integral is the one we call the momentum matrix element, $|P_{cv}|$. Continuing our integration of the equation, we obtain

$$|\langle f|P\cdot A|i\rangle|^2 = \frac{|E_0|^2}{4\omega^2}\left|P_{cv}\right|^2, \tag{A.20}$$

$$R_{i\to f} = \frac{2\pi}{\hbar}\sum_f \frac{q^2}{m_0^2}\frac{|\vec{E}_0|^2}{4\omega^2}|P_{cv}|^2\delta(E_c - E_v - \hbar\omega)f_i(E_i)\left(1-f_f(E_f)\right). \tag{A.21}$$

We are now able to see the possible link to the absorption coefficient. Remembering the definitions of the photon energy flux, it is possible to relate our transition rate to the number of photons

$$U_E = \frac{n^2\varepsilon_0}{2}|E_0|^2 = N_E\cdot\hbar\omega,$$

$$R_{i\to f} = \frac{2\pi}{\hbar}\sum_f \frac{q^2}{m_0^2}\frac{U_E}{2n^2\varepsilon_0\omega^2}|P_{cv}|^2\delta(E_{cv} - \hbar\omega)f_i(E_i)\left(1-f_f(E_f)\right).$$

We then obtain the absorption coefficient

$$\alpha = \hbar\omega\frac{R_T}{{}^c\!/_n U_E} = \hbar\omega\frac{2\pi}{\hbar}\sum_f \frac{q^2}{m_0^2}\frac{U_E}{{}^c\!/_n U_E 2n^2\varepsilon_0\omega^2}|P_{cv}|^2\delta(E_{cv}(\vec{k}) - \hbar\omega)f_i(E_i)\left(1-f_f(E_f)\right),$$

$$\alpha = \frac{\pi q^2\hbar}{cn\varepsilon_0 m_0^2\hbar\omega}\sum_k |P_{cv}|^2\delta(E_{cv}(\vec{k}) - \hbar\omega)f_i(E_i)\left(1-f_f(E_f)\right).$$

The probability of finding carriers in a certain state is related to the Fermi statistics. We have the probability of finding an electron in the valence band, $f_i(E_i)$, and the probability of finding a hole in the valence band $(1-f_f(E_f))$. Under the assumption of low illumination, these factors can be approximated to be equal to 1. Now, to obtain the complete absorption coefficient, we need to sum over all possible final state in k space.

The summation can be transformed into an integration over energy with the joint density of states (JDOS)

$$\sum_{\vec{k}} \quad \to \int D_j(E_{cv}dE_{cv}), \tag{A.22}$$

where the density of states can be calculated with

$$D_j(E_{cv}) = \frac{1}{4\pi^3}\int \frac{dS_k}{|\nabla_k(E_{cv})|}. \tag{A.23}$$

The joint density of states for various sizes of materials are as follow :

$$JDOS_{3D} = \frac{\mu\sqrt{2\mu(E-E_g)}}{\pi^2\hbar^3}$$

$$JDOS_{2D} = \frac{\mu}{L\pi\hbar}\sum_n \mathcal{H}(E-E_n)$$

$$JDOS_{1D} = \frac{1}{LT\pi}\sqrt{\frac{2\mu}{\hbar^2(E-E_n)}}$$

$$JDOS_{0D} = \frac{1}{V_{dot}} g_s\delta(E-E_n) \tag{A.24}$$

where μ is the reduced effective mass given by $\frac{1}{\mu} = \frac{1}{m_e^*} + \frac{1}{m_h^*}$, E_g is the bandgap of the semiconductor, E_n is the energy transition possible in the nanostructures, L is the thickness of the quantum well or the nanowire and T is the width of the 1D nanowire.

The joint density of state can now be implemented in the absorption coefficient

$$\alpha = A\int \delta(E_{cv}-\hbar\omega)JDOS(E)dE_{cv},$$

$$\alpha = A\cdot JDOS(\hbar\omega), \tag{A.25}$$

where the coefficient A is given by

$$A = \frac{\pi q^2\hbar}{cn\varepsilon_0 m_0^2\hbar\omega}|P_{cv}|^2. \tag{A.26}$$

We can now derive the absorption coefficient of a quantum well with its corresponding joint density of states and the general absorption coefficient formula.

For each transition in a nanostructure, there is a corresponding wavefunction overlap integral $|M| = |\langle\psi_e|\psi_h\rangle|$. In the A coefficient, the dipole matrix element, $|P_{cv}|$, contains both the electron and the hole wavefunctions. It is defined as $|P_{cv}| = |\langle u_c|\hat{e}\cdot\vec{p}|u_v\rangle|$, where u_c and u_v are the Bloch wavefunction in the conduction and valence bands. In the confined case, the wavefunction of the carriers is defined as the product of the envelope wavefunction ψ and the Bloch wavefunction u. The wavefunctions are now given by $|\Psi_e\rangle = |\psi_e\rangle|u_c\rangle$ and $|\Psi_h\rangle = |\psi_h\rangle|u_v\rangle$. The dipole matrix element is now given by

$$|P_{cv}|^2 = |\langle\psi_e|\langle u_c|\hat{e}\cdot\vec{p}|u_v\rangle|\psi_h\rangle|^2 = |\langle\psi_e|\psi_h\rangle|^2|\langle u_c|\hat{e}\cdot\vec{p}|u_v\rangle|^2 + |\langle\psi_e|\hat{e}\cdot\vec{p}|\psi_h\rangle|^2|\langle u_c|u_v\rangle|^2. \tag{A.27}$$

Because the Bloch wavefunctions u_v and u_c are orthogonal, their overlap is equal to zero, $|\langle u_c|u_v\rangle| = 0$. The dipole matrix element, in our case, is then given by

$$|P_{cv}|^2 = |\langle\psi_e|\psi_h\rangle|^2|\langle u_c|\hat{e}\cdot\vec{p}|u_v\rangle|^2 = |M|^2|P_{cv,bulk}|^2. \tag{A.28}$$

In a real world device, broadening of the step function is usually seen. We will assume that the energy transition E_n in the well follows a Gaussian distribution. The probability distribution is then

$$P(E) = \frac{1}{\sqrt{2\pi}\xi E_n}\mathrm{e}^{-\frac{(\frac{E}{E_n}-1)^2}{2\xi^2}}, \tag{A.29}$$

We can then apply the probability distribution to the absorption coefficient

$$\bar{\alpha}_{QW} = A\cdot\int P(E)JDOS(E)dE,$$

$$\bar{\alpha}_{QW} = A\cdot\frac{\mu}{\pi L\hbar^2}\int\sum_n|M_{QW}|^2\frac{1}{\sqrt{2\pi}\xi E_n}\mathrm{e}^{-\frac{(\frac{E}{E_n}-1)^2}{2\xi^2}}\mathcal{H}(\hbar\omega-E)dE.$$

The properties of the Heaviside function are given by

$$\mathcal{H}(\hbar\omega-E) = \begin{cases}1 & \hbar\omega\geq E\\ 0 & \hbar\omega<E\end{cases}.$$

Hence, we can transform our Heavyside function to

$$\bar{\alpha}_{QW} = A\cdot\frac{\mu}{\pi L\hbar^2}\int_{-\infty}^{\infty}\sum_n|M|^2\frac{1}{\sqrt{2\pi}\xi E_n}\mathrm{e}^{-\frac{(\frac{E}{E_n}-1)^2}{2\xi^2}}\mathcal{H}(\hbar\omega-E)dE,$$

$$\bar{\alpha}_{QW} = A\cdot\frac{\mu}{\pi L\hbar^2}\int_{-infty}^{\hbar\omega}\sum_n|M|^2\frac{1}{\sqrt{2\pi}\xi E_n}\mathrm{e}^{-\frac{(\frac{E}{E_n}-1)^2}{2\xi^2}}dE,$$

$$\bar{\alpha}_{QW} = A\cdot\frac{\mu}{\pi L\hbar^2}\int_{y_n}^{\infty}\sum_n|M|^2\frac{1}{\sqrt{2\pi}\xi E_n}E_n\sqrt{2}\xi\mathrm{e}^{-y^2}dy,$$

$$\bar{\alpha}_{QW} = A\cdot\frac{\mu}{\pi L\hbar^2}\sum_n|M|^2\frac{1}{\sqrt{\pi}}\frac{\sqrt{\pi}}{2}\,\mathrm{erf}(y)|_{-\infty}^{y_0},$$

$$\bar{\alpha}_{QW} = A\cdot\frac{\mu}{\pi L\hbar^2}\sum_n|M|^2\frac{1}{2}\left(1-\mathrm{erf}\left(\frac{1-\frac{\hbar\omega}{E_n}}{\sqrt{2\xi^2}}\right)\right). \tag{A.30}$$

Similarly, the quantum dot absorption coefficient is given by

$$\alpha_{QD} = A\cdot JDOS_{0D}(\hbar\omega),$$

$$\alpha_{QD} = \frac{A}{V_{dot}} \cdot \sum_n |M_{QD}|^2 g_s \cdot \delta(\hbar\omega - E_n), \tag{A.31}$$

where E_n are the transition energy of the quantum dots, g_s is the degeneracy of the energy level and V_{dot} is the volume of the quantum dot. This absorption coefficient is for a single dot. In our system, we have a distribution of a certain density of dot. For a density ρ of quantum dots of cross section S_{QD}, the absorption coefficient is

$$\alpha_{QD} = \frac{A}{V_{dot}} \cdot S_{QD} \cdot \rho \sum_n |M_{QD}|^2 g_s \cdot \delta(\hbar\omega - E_n). \tag{A.32}$$

Again, due to the random distribution of quantum dot size, we shall apply a distribution to the energy levels. By applying the Gaussian distribution to the energy levels, we obtain

$$\alpha_{QD} = \frac{A}{V_{dot}} \cdot S_{QD} \cdot \rho \sum_n |M_{QD}|^2 g_s \frac{1}{\sqrt{2\pi}\xi E_n} \cdot \mathrm{e}^{-\frac{(\frac{\hbar\omega}{E_n}-1)^2}{2\xi^2}}. \tag{A.33}$$

These are the absorption coefficients that shall be used in the calculation of the complete structure.

Bibliography

[1] A. E. Becquerel, "Mémoire sur les effets électriques produits sous l'influence des rayons solaires," *Comptes Rendus*, vol. 9, no. 567, 1839.

[2] D. M. Chapin, C. S. Fuller, and G. L. Pearson, "A new silicon p-n junction photocell for converting solar radiation into electrical power," *Journal of Applied Physics*, vol. 25, no. 5, pp. 676–677, 1954.

[3] F. Treble, "Milestones in the development of crystalline silicon solar cells," *Renewable Energy*, vol. 15, no. 14, pp. 473–478, 1998.

[4] BSW-Solar, "100 gigawatts of installed solar power capacity," *BSW-Solar Press Releases*, December 6, 2012.

[5] European Photovoltaic Industry Association, *Solar Photovoltaics Competing in the Energy Sector - On the road to competitiveness*, 2011.

[6] National Renewable Energy Laboratory, *2010 Solar Technologies Market Report*, November 2011.

[7] M. A. Green, "Third generation photovoltaics: solar cells for 2020 and beyond," *Physica E: Low-dimensional Systems and Nanostructures*, vol. 14, no. 1, pp. 65–70, 2002.

[8] "Arnprior solar project profile," *EDF Press Releases*, January 2011.

[9] J. Nelson, *The physics of solar cells*, vol. 57. Imperial College Press, 2003.

[10] A. Luque and A. Marti, "Increasing the efficiency of ideal solar cells by photon induced transitions at intermediate levels," *Physical Review Letters*, vol. 78, no. 26, pp. 5014–5017, 1997.

[11] A. Shalav, B. S. Richards, and M. A. Green, "Luminescent layers for enhanced silicon solar cell performance: Up-conversion," *Solar energy materials and solar cells*, vol. 91, no. 9, pp. 829–842, 2007.

[12] R. K. Jones, J. H. Ermer, C. M. Fetzer, and R. R. King, "Evolution of multijunction solar cell technology for concentrating photovoltaics," *Japanese Journal of Applied Physics*, vol. 51, no. 10, 2012.

[13] M. A. Green, K. Emery, Y. Hishikawa, W. Warta, and E. D. Dunlop, "Solar cell efficiency tables (version 43)," *Progress in Photovoltaics: Research and Applications*, vol. 22, no. 1, pp. 1–9, 2014.

[14] A. Luque, "Will we exceed 50% efficiency in photovoltaics?," *Journal of Applied Physics*, vol. 110, no. 3, p. 031301, 2011.

[15] S. R. Forrest, "The limits to organic photovoltaic cell efficiency," *MRS Bulletin*, vol. 30, no. 01, pp. 28–32, 2005.

[16] R. R. King, D. Bhusari, A. Boca, D. Larrabee, X.-Q. Liu, W. Hong, C. M. Fetzer, D. C. Law, and N. H. Karam, "Band gap-voltage offset and energy production in next-generation multijunction solar cells," *Progress in Photovoltaics: Research and Applications*, vol. 19, no. 7, pp. 797–812, 2011.

[17] J. M. Olson, D. J. Friedman, and S. Kurtz, *Chapter 9: High-Efficiency III-V Multijunction Solar Cells*, pp. 359–411. Handbook of Photovoltaic Science and Engineering, John Wiley & Sons, Ltd, 2005.

[18] J. M. Olson, T. Gessert, and M. M. Al-Jassim, "$GaInP_2$/GaAs-A current and lattice-matched tandem cell with a high theoretical efficiency," in *Proceedings of the 18th Photovoltaic Specialists Conference (PVSC)*, vol. 1, pp. 552–555, October 1985.

[19] J. M. Olson, S. R. Kurtz, A. E. Kibbler, and P. Faine, "A 27.3% efficient $Ga_{0.5}In_{0.5}P$/GaAs tandem solar cell," *Applied Physics Letters*, vol. 56, no. 7, pp. 623–625, 1990.

[20] N. Fatemi, "EMCORE solar panels power the orbital-built LDCM satellite," *EMCORE Press Releases*, February 19, 2013.

[21] M. D. Yandt, J. F. Wheeldon, C. E. Valdivia, S. Chow, O. Thériault, A. Johnson, F. Szadkowski, M. Armstrong, L. Motte, T. Cassidy, *et al.*, "A new on-sun test facility at the SUNRISE quantum-dot-enhanced CPV module demonstration system," in *AIP Conference Proceedings*, vol. 1407, p. 224, 2011.

[22] I. Vurgaftman, J. Meyer, and L. Ram-Mohan, "Band parameters for iii–v compound semiconductors and their alloys," *Journal of Applied Physics*, vol. 89, no. 11, pp. 5815–5875, 2001.

[23] R. R. King, D. C. Law, K. M. Edmondson, C. M. Fetzer, G. S. Kinsey, H. Yoon, R. A. Sherif, and N. H. Karam, "40% efficient metamorphic GaInP/GaAs/Ge multijunction solar cells," *Applied Physics Letters*, vol. 90, no. 18, p. 183516, 2007.

[24] W. Guter, J. Schone, S. P. Philipps, M. Steiner, G. Siefer, A. Wekkeli, E. Welser, E. Oliva, A. W. Bett, and F. Dimroth, "Current-matched triple-junction solar cell reaching 41.1% conversion efficiency under concentrated sunlight," *Applied Physics Letters*, vol. 94, no. 22, p. 223504, 2009.

[25] J. F. Geisz, S. Kurtz, M. W. Wanlass, J. S. Ward, A. Duda, D. J. Friedman, J. M. Olson, W. E. McMahon, T. E. Moriarty, and J. T. Kiehl, "High-efficiency GaInP/GaAs/InGaAs triple-junction solar cells grown inverted with a metamorphic bottom junction," *Applied Physics Letters*, vol. 91, no. 2, p. 023502, 2007.

[26] M. Wilkins, "Design of multi-junction solar cells on silicon substrates using a porous silicon compliant membrane," Master's thesis, University of Ottawa, 2013.

[27] D. Liao and A. Rockett, "Epitaxial growth of Cu(In,Ga)Se_2 on GaAs (110)," *Journal of Applied Physics*, vol. 91, no. 4, pp. 1978–1983, 2002.

[28] A. Walker, A. Coathup, O. Thériault, H. M. Myers, J. F. Wheeldon, Z. Mi, I. Shih, and K. Hinzer, "Modeling of $CuIn_xGa_{1-x}Se_2$ solar cells for applications in multijunction solar cell technologies," in *Next Generation Solar, Photovoltaics Canada*, 2012.

[29] N. J. Ekins-Daukes, D. B. Bushnell, J. P. Connolly, K. W. Barnham, M. Mazzer, J. S. Roberts, G. Hill, and R. Airey, "Strain-balanced quantum well solar cells," *Physica E: Low-dimensional Systems and Nanostructures*, vol. 14, no. 1, pp. 132–135, 2002.

[30] N. Bilodeau, "JDSU acquires critical assets from quantasol for CPV solar offering," *JDSU Press releases*, 2011.

[31] B. Hemish, "Cyrium technologies introduces customized CPV solar cells to meet demanding and unique applications," *Cyrium Press releases*, August 3, 2010.

[32] M. Grundmann, N. N. Ledentsov, R. Heitz, L. Eckey, J. Christen, J. Böhrer, D. Bimberg, S. S. Ruvimov, P. Werner, U. Richter, *et al.*, "InAs/GaAs quantum dots radiative recombination from zero-dimensional states," *physica status solidi (b)*, vol. 188, no. 1, pp. 249–258, 1995.

[33] Z. Wasilewski, S. Fafard, and J. McCaffrey, "Size and shape engineering of vertically stacked self-assembled quantum dots," *Journal of Crystal Growth*, vol. 201202, pp. 1131 – 1135, 1999.

[34] S. Fafard, Z. R. Wasilewski, C. N. Allen, K. Hinzer, J. P. McCaffrey, and Y. Feng, "Lasing in quantum-dot ensembles with sharp adjustable electronic shells," *Applied Physics Letters*, vol. 75, no. 7, pp. 986–988, 1999.

[35] B. Riel, "Quantum dots: higher CPV efficiencies, same production cost," *Future Photovoltaics*, vol. 1, pp. 78–84, 2010.

[36] K. Emery, *Chapter 16 : Measurement and characterization of solar cells and modules*, pp. 701–752. Handbook of Photovoltaic Science and Engineering, John Wiley & Sons, Ltd, 2005.

[37] M. Meusel, C. Baur, G. Letay, A. W. Bett, W. Warta, and E. Fernandez, "Spectral response measurements of monolithic GaInP/Ga(In)As/Ge triple-junction solar cells: Measurement artifacts and their explanation," *Progress in Photovoltaics: Research and Applications*, vol. 11, no. 8, pp. 499–514, 2003.

[38] J.-J. Li, S. H. Lim, C. R. Allen, D. Ding, and Y.-H. Zhang, "Combined effects of shunt and luminescence coupling on external quantum efficiency measurements of multijunction solar cells," *IEEE Journal of Photovoltaics*, vol. 1, no. 2, pp. 225–230, 2011.

[39] S. Fafard, C. E. Valdivia, and S. G. Wallace, "The fill-factor bias measurement for advanced triple-junction solar cell characterization and quality control," in *AIP Conference Proceedings*, vol. 1477, p. 118, 2012.

[40] A. Walker, *Bandgap engineering of multi-junction solar cells using nanostructures for enhanced performance under concentrated illumination*. PhD thesis, University of Ottawa, 2013.

[41] Oriel Instruments, Newport, *IQE200 Series : Intelligent Quantum Efficiency Systems*, 2012. Rev. 02.

[42] Oriel Instruments, Newport, *Oriel product training; spectral irradiance*, 2006. Section one, `http://assets.newport.com/webDocuments-EN/images/Light_Sources.pdf`.

[43] J. M. Lerner and A. Thevenon, *The optics of spectroscopy*. Horiba Scientific, 1988. `http://www.horiba.com/us/en/scientific/products/optics-tutorial/`.

[44] J. Brar, "Photoluminescence spectroscopy of CdSe/$Cd_{0.5}Zn_{0.5}S$ core/shell colloidal quantum dots," Master's thesis, University of Ottawa, 2011.

[45] E. Hecht, *Optics*. Addison-Wesley Longman, 2002.

[46] Oriel Instruments, Newport, *Oriel product training; monochromators and spectrographs*, 2006. Section three, `http://assets.newport.com/webDocuments-EN/images/Monochromators_Spectrographs.pdf`.

[47] Oriel Instruments, Newport, *Oriel amplifier for QE light bias; User's manual*, 2012. Model 70714.

[48] Oriel Instruments, Newport, *Merlin^{TM}radiometry systems; User's manual*, 2011. Model 70100.

[49] T. Larason and J. Houston, "Spectroradiometric detector measurements: ultraviolet, visible, and near-infrared detectors for spectral power," *NIST Special Publication*, vol. 250, p. 41, 2008.

[50] K. D. Stock, R. Heine, and H. Hofer, "Spectral characterization of Ge trap detectors and photodiodes used as transfer standards," *Metrologia*, vol. 40, no. 1, p. S163, 2003.

[51] T. Takamoto, E. Ikeda, H. Kurita, and M. Ohmori, "Over 30% efficient InGaP/GaAs tandem solar cells," *Applied Physics Letters*, vol. 70, no. 3, pp. 381–383, 1997.

[52] M. Sotoodeh, A. H. Khalid, and A. A. Rezazadeh, "Empirical low-field mobility model for III–V compounds applicable in device simulation codes," *Journal of Applied Physics*, vol. 87, no. 6, pp. 2890–2900, 2000.

[53] J. Piprek, *Semiconductor optoelectronic devices: Introduction to physics and simulation*. Academic Press, 2003.

[54] M. Schubert, V. Gottschalch, C. M. Herzinger, H. Yao, P. G. Snyder, and J. A. Woollam, "Optical constants of $Ga_xIn_{1-x}P$ lattice matched to GaAs," *Journal of Applied Physics*, vol. 77, no. 7, pp. 3416–3419, 1995.

[55] E. D. Palik, *Handbook of Optical Constants of Solids*, vol. 1, ch. 15. Access Online via Elsevier, 1998.

[56] E. D. Palik, *Handbook of Optical Constants of Solids*, vol. 1, ch. 17. Access Online via Elsevier, 1998.

[57] G. Ghosh, "Dispersion-equation coefficients for the refractive index and birefringence of calcite and quartz crystals," *Optics Communications*, vol. 163, no. 1, pp. 95–102, 1999.

[58] B. Harbecke, "Coherent and incoherent reflection and transmission of multilayer structures," *Applied Physics B*, vol. 39, no. 3, pp. 165–170, 1986.

[59] T. Bååk, "Silicon oxynitride; a material for GRIN optics," *Applied Optics*, vol. 21, no. 6, pp. 1069–1072, 1982.

[60] H. Kato, S. Amour, H. Nakanishi, and K. Onrsuml, "Optical properties of $(Al_xGa_{1-x})_{0.5}In_{0.5}P$ quaternary alloys," *Japanese Journal of Applied Physics*, vol. 33, pp. 186–192, 1994.

[61] E. D. Palik, *Handbook of Optical Constants of Solids*, vol. 2, ch. 24. Access Online via Elsevier, 1998.

[62] V. Palankovski and R. Quay, *Analysis and simulation of heterostructure devices*. Springer New York, 2004.

[63] S. Sato, H. Miyamoto, M. Imaizumi, K. Shimazaki, C. Morioka, K. Kawano, and T. Ohshima, "Degradation modeling of InGaP/GaAs/Ge triple-junction solar cells irradiated with various-energy protons," *Solar Energy Materials and Solar Cells*, vol. 93, no. 6, pp. 768–773, 2009.

[64] J. S. Blakemore, "Intrinsic density $n_i(t)$ in GaAs: Deduced from band gap and effective mass parameters and derived independently from Cr acceptor capture and emission coefficients," *Journal of Applied Physics*, vol. 53, no. 1, pp. 520–531, 1982.

[65] F. J. Morin and J. P. Maita, "Conductivity and hall effect in the intrinsic range of germanium," *Physical Review*, vol. 94, no. 6, p. 1525, 1954.

[66] M. Paxman, J. Nelson, B. Braun, J. Connolly, K. Barnham, C. Foxon, and J. Roberts, "Modeling the spectral response of the quantum well solar cell," *Journal of Applied Physics*, vol. 74, no. 1, pp. 614–621, 1993.

[67] A. Boucherif, R. Arès, and V. Aimez, "APECS: Milestone 3 deliverables," tech. rep., CRN²-UdeS-4CPV, 2013.

[68] S. M. Sze and K. K. Ng, *Physics of semiconductor devices*. John Wiley & Sons, 2006.

[69] W. Braun, *Applied RHEED: reflection high-energy electron diffraction during crystal growth*. No. 154, Springer, 1999.

[70] G. Friedbacher and H. Bubert, *Surface and Thin Film Analysis: A Compendium of Principles, Instrumentation, and Applications*. John Wiley & Sons, 2011.

[71] M. Ghezzo, "Thickness calculations for a transparent film from ellipsometric measurements," *Journal of the Optical Society of America*, vol. 58, no. 3, pp. 368–368, 1968.

[72] P. Grosse, "Fourier transform IR analysis of thin solid films," *TrAC Trends in Analytical Chemistry*, vol. 8, no. 6, pp. 222–226, 1989.

[73] A. Zeng, J. Eldridge, C. Lavoie, and T. Tiedje, "Characterization of GaAs/$Ga_{1-x}Al_xAs$ multilayer systems by infrared spectroscopy at normal incidence," *Solid state communications*, vol. 87, no. 11, pp. 1039–1044, 1993.

[74] S. A. Chalmers, "Rapid and accurate thin film measurement of individual layers in a multi-layered or patterned sample," 2001. US Patent 6,204,922.

[75] G. Bergland, "A guided tour of the fast fourier transform," *Spectrum, IEEE*, vol. 6, no. 7, pp. 41–52, 1969.

[76] D. Sell, H. Casey Jr, and K. Wecht, "Concentration dependence of the refractive index for n-and p-type GaAs between 1.2 and 1.8 eV," *Journal of Applied Physics*, vol. 45, no. 6, pp. 2650–2657, 1974.

[77] S. Fafard, "Solar cell with epitaxially grown quantum dot material," 2011. US Patent 7,863,516.

[78] "COMSOL Multiphysics, Version 3.5 a," *COMSOL Inc, Burlington, MA*, 2008.

[79] A. Martí, N. López, E. Antolin, E. Cánovas, C. Stanley, C. Farmer, L. Cuadra, and A. Luque, "Novel semiconductor solar cell structures: The quantum dot intermediate band solar cell," *Thin Solid Films*, vol. 511, pp. 638–644, 2006.

[80] A. W. Walker, O. Thériault, J. F. Wheeldon, and K. Hinzer, "The effects of absorption and recombination on quantum dot multijunction solar cell efficiency," *IEEE Journal of Photovoltaics*, vol. 3, no. 3, pp. 1118–1124, 2013.

[81] D. Guimard, R. Morihara, D. Bordel, K. Tanabe, Y. Wakayama, M. Nishioka, and Y. Arakawa, "Fabrication of InAs/GaAs quantum dot solar cells with enhanced photocurrent and without degradation of open circuit voltage," *Applied Physics Letters*, vol. 96, no. 20, p. 203507, 2010.

[82] C. G. Bailey, D. V. Forbes, R. P. Raffaelle, and S. M. Hubbard, "Near 1 V open circuit voltage InAs/GaAs quantum dot solar cells," *Applied Physics Letters*, vol. 98, no. 16, p. 163105, 2011.

[83] S. M. Hubbard, C. Bailey, S. Polly, C. Cress, J. Andersen, D. Forbes, and R. Raffaelle, "Nanostructured photovoltaics for space power," *Journal of Nanophotonics*, vol. 3, no. 1, pp. 031880–031880, 2009.

[84] C. Kerestes, C. D. Cress, B. C. Richards, D. V. Forbes, Y. Lin, Z. Bittner, S. J. Polly, P. Sharps, and S. M. Hubbard, "Strain effects on radiation tolerance of triple-junction solar cells with InAs quantum dots in the GaAs junction," *IEEE Journal of Photovoltaics*, vol. 4, no. 1, pp. 224–232, 2014.

[85] G. S. Kinsey, P. Hebert, K. E. Barbour, D. D. Krut, H. L. Cotal, and R. A. Sherif, "Concentrator multijunction solar cell characteristics under variable intensity and temperature," *Progress in Photovoltaics: Research and Applications*, vol. 16, no. 6, pp. 503–508, 2008.

[86] O. Thériault, A. Walker, J. F. Wheeldon, and K. Hinzer, "Effects of quantum dot layers on the behavior of multijunction solar cell operation under concentration," in *proceedings of the 8th International Conference on Concentrating Photovoltaics*, pp. 20–23, American Institute of Physics, 2012.

[87] T. Sogabe, Y. Shoji, M. Ohba, K. Yoshida, R. Tamaki, H.-F. Hong, C.-H. Wu, C.-T. Kuo, S. Tomić, and Y. Okada, "Intermediate-band dynamics of quantum dots solar cell in concentrator photovoltaic modules," *Scientific reports*, vol. 4, 2014.

[88] D. Bimberg, M. Grundmann, and N. N. Ledentsov, *Quantum dot heterostructures*. John Wiley & Sons, 1999.

[89] D. Leonard, M. Krishnamurthy, C. Reaves, S. P. Denbaars, and P. Petroff, "Direct formation of quantum-sized dots from uniform coherent islands of InGaAs on GaAs surfaces," *Applied Physics Letters*, vol. 63, no. 23, pp. 3203–3205, 1993.

[90] A. Marti, N. Lopez, E. Antolin, E. Canovas, A. Luque, C. Stanley, C. Farmer, and P. Diaz, "Emitter degradation in quantum dot intermediate band solar cells," *Applied Physics Letters*, vol. 90, no. 23, p. 233510, 2007.

[91] V. Popescu, G. Bester, M. C. Hanna, A. G. Norman, and A. Zunger, "Theoretical and experimental examination of the intermediate-band concept for strain-balanced (In,Ga)As/Ga(As,P) quantum dot solar cells," *Physical review B*, vol. 78, no. 20, p. 205321, 2008.

[92] R. Laghumavarapu, M. El-Emawy, N. Nuntawong, A. Moscho, L. Lester, and D. Huffaker, "Improved device performance of InAs/GaAs quantum dot solar cells with GaP strain compensation layers," *Applied Physics Letters*, vol. 91, no. 24, pp. 243115–243115, 2007.

[93] S. Fafard, Z. Wasilewski, C. N. Allen, D. Picard, M. Spanner, J. McCaffrey, and P. Piva, "Manipulating the energy levels of semiconductor quantum dots," *Physical Review B*, vol. 59, no. 23, p. 15368, 1999.

[94] Q. Mo, T. Fan, Q. Gong, J. Wu, Z. Wang, and Y. Bai, "Effects of annealing on self-organized InAs quantum islands on GaAs (100)," *Applied Physics Letters*, vol. 73, no. 24, pp. 3518–3520, 1998.

[95] H. Liu, M. Gao, J. McCaffrey, Z. Wasilewski, and S. Fafard, "Quantum dot infrared photodetectors," *Applied Physics Letters*, vol. 78, no. 1, pp. 79–81, 2001.

[96] F. Tutu, I. Sellers, M. Peinado, C. Pastore, S. Willis, A. Watt, T. Wang, and H. Liu, "Improved performance of multilayer InAs/GaAs quantum-dot solar cells using a high-growth-temperature GaAs spacer layer," *Journal of Applied Physics*, vol. 111, no. 4, p. 046101, 2012.

[97] C. Lobo, R. Leon, S. Fafard, and P. Piva, "Intermixing induced changes in the radiative emission from III–V quantum dots," *Applied Physics Letters*, vol. 72, no. 22, pp. 2850–2852, 1998.

[98] A. Babiński, J. Jasiński, R. Bożek, A. Szepielow, and J. Baranowski, "Rapid thermal annealing of InAs/GaAs quantum dots under a GaAs proximity cap," *Applied Physics Letters*, vol. 79, no. 16, pp. 2576–2578, 2001.

[99] I. Mukhametzhanov, Z. Wei, R. Heitz, and A. Madhukar, "Punctuated island growth: An approach to examination and control of quantum dot density, size, and shape evolution," *Applied physics letters*, vol. 75, no. 1, pp. 85–87, 1999.

[100] J. Zribi, B. Ilahi, D. Morris, V. Aimez, and R. Arès, "Chemical beam epitaxy growth and optimization of InAs/GaAs quantum dot multilayers," *Journal of Crystal Growth*, vol. 384, pp. 21–26, 2013.

[101] C. Pryor, "Eight-band calculations of strained InAs/GaAs quantum dots compared with one-, four-, and six-band approximations," *Physical Review B*, vol. 57, no. 12, p. 7190, 1998.

[102] M. Califano and P. Harrison, "Presentation and experimental validation of a single-band, constant-potential model for self-assembled InAs/GaAs quantum dots," *Physical Review B*, vol. 61, no. 16, p. 10959, 2000.

[103] B. Riel, "An introduction to self-assembled quantum dots," *American Journal of Physics*, vol. 76, no. 8, pp. 750–757, 2008.

[104] M. Korkusiński and P. Hawrylak, "Electronic structure of vertically stacked self-assembled quantum disks," *Physical Review B*, vol. 63, no. 19, p. 195311, 2001.

[105] R. Teissier, D. Sicault, J. Harmand, G. Ungaro, G. Le Roux, and L. Largeau, "Temperature-dependent valence band offset and band-gap energies of pseudomorphic GaAsSb on GaAs," *Journal of Applied Physics*, vol. 89, no. 10, pp. 5473–5477, 2001.

[106] J. Chen, A. Markus, A. Fiore, U. Oesterle, R. Stanley, J. Carlin, R. Houdré, M. Ilegems, L. Lazzarini, L. Nasi, *et al.*, "Tuning InAs/GaAs quantum dot properties under Stranski-Krastanov growth mode for 1.3 μm applications," *Journal of Applied Physics*, vol. 91, no. 10, pp. 6710–6716, 2002.

[107] "COMSOL multiphysics modeling guide: Version 3.5," *COMSOL AB*, 2007.

[108] R. Melnik and M. Willatzen, "Bandstructures of conical quantum dots with wetting layers," *Nanotechnology*, vol. 15, no. 1, p. 1, 2004.

[109] A. Wojs, P. Hawrylak, S. Fafard, and L. Jacak, "Electronic structure and magneto-optics of self-assembled quantum dots," *Physical Review B*, vol. 54, no. 8, p. 5604, 1996.

[110] F. L. Claude Cohen-Tannoudji, Bernard Diu, *Mécanique quantique*. Hermann, 1997.

[111] A. Andreev and E. OReilly, "Optical matrix element in InAs/GaAs quantum dots: Dependence on quantum dot parameters," *Applied Physics Letters*, vol. 87, no. 21, pp. 213106–213106, 2005.

[112] M. Cusack, P. Briddon, and M. Jaros, "Absorption spectra and optical transitions in InAs/GaAs self-assembled quantum dots," *Physical Review B*, vol. 56, no. 7, p. 4047, 1997.

[113] S. Tomić, T. S. Jones, and N. M. Harrison, "Absorption characteristics of a quantum dot array induced intermediate band: Implications for solar cell design," *Applied Physics Letters*, vol. 93, no. 26, p. 263105, 2008.

[114] S. Tomić, T. Sogabe, and Y. Okada, "In-plane coupling effect on absorption coefficients of InAs/GaAs quantum dots arrays for intermediate band solar cell," *Progress in Photovoltaics: Research and Applications*, 2014.

[115] L. Vorobjev, N. Fedosov, V. Y. Panevin, D. Firsov, V. Shalygin, M. Grozina, A. Andreev, V. Ustinov, I. Tarasov, N. Pikhtin, *et al.*, "Interband light absorption and

Pauli blocking in InAs/GaAs quantum dots covered by InGaAs quantum wells," *Semiconductor Science and Technology*, vol. 22, no. 7, p. 814, 2007.

[116] A. Walker, O. Thériault, and K. Hinzer, "The dependence of multijunction solar cell performance on the number of quantum dot layers," *IEEE Journal of Quantum Electronics*, vol. 50, no. 3, pp. 198–203, 2014.

[117] A. W. Walker, O. Thériault, and K. Hinzer, "Positioning and doping effects on quantum dot multi-junction solar cell performance," *Progress in Photovoltaics: Research and Applications*, 2014.

[118] A. W. Walker, O. Thériault, and K. Hinzer, "Carrier dynamics in quantum-dot multijunction solar cells under concentration," *Journal of Photovoltaics*, 2014.

[119] S. Tomić, "Theory of quantum dot arrays for solar cell devices," in *Quantum Dot Solar Cells*, pp. 113–134, Springer, 2014.

[120] C. Pryor, "Geometry and material parameter dependence of InAs/GaAs quantum dot electronic structure," *Physical Review B*, vol. 60, no. 4, p. 2869, 1999.

[121] S. Sauvage, P. Boucaud, J.-M. Gérard, and V. Thierry-Mieg, "In-plane polarized intraband absorption in InAs/GaAs self-assembled quantum dots," *Physical Review B*, vol. 58, no. 16, p. 10562, 1998.

[122] D. Ferreira and J. Alves, "The effects of shape and size nonuniformity on the absorption spectrum of semiconductor quantum dots," *Nanotechnology*, vol. 15, no. 8, p. 975, 2004.

[123] C.-S. Chang and S. Chuang, "Universal curves for optical-matrix elements of strained quantum wells," *Applied Physics Letters*, vol. 66, no. 7, pp. 795–797, 1995.

[124] P. Wurfel, "The chemical potential of radiation," *Journal of Physics C: Solid State Physics*, vol. 15, no. 18, p. 3967, 1982.

[125] H. B. Bebb and E. Williams, "Transport and optical phenomena," *Semiconductors and Semimetals*, vol. 8, 1972.

[126] ASD Inc., *FieldSpec Wide-Res Spectroradiometer*, 2012.

[127] V. Popescu, G. Bester, and A. Zunger, "Coexistence and coupling of zero-dimensional, two-dimensional, and continuum resonances in nanostructures," *Physical Review B*, vol. 80, no. 4, p. 045327, 2009.

[128] "Jihène Zribi, personal communication," 2013.

[129] G. A. Narvaez, G. Bester, and A. Zunger, "Carrier relaxation mechanisms in self-assembled (In,Ga)As/GaAs quantum dots: Efficient P→S Auger relaxation of electrons," *Physical Review B*, vol. 74, no. 7, p. 075403, 2006.

[130] V. Popescu, G. Bester, and A. Zunger, "Strain-induced localized states within the matrix continuum of self-assembled quantum dots," *Applied Physics Letters*, vol. 95, no. 2, p. 023108, 2009.

[131] E. Le Ru, J. Fack, and R. Murray, "Temperature and excitation density dependence of the photoluminescence from annealed InAs/GaAs quantum dots," *Physical Review B*, vol. 67, no. 24, p. 245318, 2003.

[132] S. Fafard, S. Raymond, G. Wang, R. Leon, D. Leonard, S. Charbonneau, J. Merz, P. Petroff, and J. Bowers, "Temperature effects on the radiative recombination in self-assembled quantum dots," *Surface Science*, vol. 361, pp. 778–782, 1996.

[133] S. Lee, S. Noh, J. Choe, and E. Kim, "Evolution of bimodal size-distribution on InAs coverage variation in as-grown InAs/GaAs quantum-dot heterostructures," *Journal of Crystal Growth*, vol. 267, no. 3, pp. 405–411, 2004.

[134] W.-H. Chang, T. Hsu, C. Huang, S. Hsu, C. Lai, N. Yeh, T. Nee, and J.-I. Chyi, "Photocurrent studies of the carrier escape process from InAs self-assembled quantum dots," *Physical Review B*, vol. 62, no. 11, p. 6959, 2000.

[135] G. Siefer, C. Baur, and A. W. Bett, "External quantum efficiency measurements of germanium bottom subcells: Measurement artifacts and correction procedures," in *proceedings of the 35th IEEE Photovoltaic Specialists Conference (PVSC)*, pp. 000704–000707, 2010.

[136] D. L. King, B. R. Hansen, J. M. Moore, and D. J. Aiken, "New methods for measuring performance of monolithic multi-junction solar cells," in *proceedings of the 28th IEEE Photovoltaic Specialists Conference (PVSC)*, pp. 1197–1201, 2000.

[137] B. M. Kayes, H. Nie, R. Twist, S. G. Spruytte, F. Reinhardt, I. C. Kizilyalli, and G. S. Higashi, "27.6% conversion efficiency, a new record for single-junction solar cells under 1 sun illumination," in *proceedings of the 37th IEEE Photovoltaic Specialists Conference (PVSC)*, pp. 4–8, IEEE, 2011.

[138] C. Baur, M. Hermle, F. Dimroth, and A. W. Bett, "Effects of optical coupling in III-V multilayer systems," *Applied Physics Letters*, vol. 90, no. 19, p. 192109, 2007.

[139] D. Derkacs, D. T. Bilir, and V. A. Sabnis, "Luminescent coupling in GaAs/GaInNAsSb multijunction solar cells," *IEEE Journal of Photovoltaics*, vol. 3, no. 1, pp. 520–527, 2013.

[140] M. A. Steiner and J. F. Geisz, "Non-linear luminescent coupling in series-connected multijunction solar cells," *Applied Physics Letters*, vol. 100, no. 25, p. 251106, 2012.

[141] M. A. Steiner, J. F. Geisz, T. E. Moriarty, R. M. France, W. E. McMahon, J. M. Olson, S. R. Kurtz, and D. J. Friedman, "Measuring IV curves and subcell photocurrents in the presence of luminescent coupling," *IEEE Journal of Photovoltaics*, vol. 3, no. 2, pp. 879–887, 2013.

[142] J.-J. Li, C. R. Allen, S. H. Lim, and Y.-H. Zhang, "Elimination of artifacts in external quantum efficiency measurements of multijunction solar cells using a pulsed voltage bias," *IEEE Journal of Photovoltaics*, vol. 3, no. 2, pp. 769–775, 2013.

[143] J.-J. Li and Y.-H. Zhang, "Elimination of artifacts in external quantum efficiency measurements for multijunction solar cells using a pulsed light bias," *IEEE Journal of Photovoltaics*, vol. 3, no. 1, pp. 364–369, 2013.

[144] D. C. Law, R. King, H. Yoon, M. Archer, A. Boca, C. Fetzer, S. Mesropian, T. Isshiki, M. Haddad, K. Edmondson, *et al.*, "Future technology pathways of terrestrial III–V multijunction solar cells for concentrator photovoltaic systems," *Solar Energy Materials and Solar Cells*, vol. 94, no. 8, pp. 1314–1318, 2010.

[145] D. Friedman and S. R. Kurtz, "Breakeven criteria for the GaInNAs junction in GaInP/GaAs/GaInNAs/Ge four-junction solar cells," *Progress in Photovoltaics: Research and Applications*, vol. 10, no. 5, pp. 331–344, 2002.